Topics in Numerical Relativity: the periodic standing-wave approximation, the stability of constraints in free evolution, and the spin of dynamical black holes

Thesis by

Robert Owen

In Partial Fulfillment of the Requirements

for the Degree of

Doctor of Philosophy

California Institute of Technology

Pasadena, California

2007

(Defended May 17, 2007)

Abstract

This thesis concerns numerical relativity, the attempt to study Einstein's theory of gravitation using numerical discretization. The goal of the field, the study of gravitational dynamics in cases where symmetry reduction or perturbation theory are not possible, finally seems to be coming to fruition, at least for the archetypal problem of the inspiral and coalescence of binary black hole systems. This thesis presents three episodes that each bear some relationship to this story.

Chapters 2 and 3 present previously published work in collaboration with Richard Price and others on the so-called *periodic standing-wave* (PSW) approximation for binary inspiral. The approximation is to balance outgoing radiation with incoming radiation, stabilizing the orbit and making the problem stationary in a rotating frame. Chapters 2 and 3 apply the method to the problem of co-orbiting charges coupled to a nonlinear scalar field in three dimensions.

Chapters 4, 5, and 6 concern the stability of constraint fields in conventional numerical relativity simulations. Chapter 4 (also previously published work, in collaboration with the Caltech numerical relativity group, along with Michael Holst and Lawrence Kidder) presents a method for immediately correcting violations of constraints after they have arisen. Chapters 5 and 6 present methods to "damp" away constraint violations dynamically in two specific contexts. Chapter 5 (previously published work in collaboration with the Caltech numerical relativity group and Lawrence Kidder) presents a first-order linearly degenerate symmetric hyperbolic representation of Einstein's equations in generalized harmonic gauge. A representation is presented that stabilizes all constraints, including those that appear when the system is written in first-order form. Chapter 6 presents a generalization of the Kidder-Scheel-Teukolsky evolution systems that provides much-improved stability. This is investigated with numerical simulations of a single black hole spacetime.

Finally, chapter 7 presents work in progress to implement code to calculate the spin of black holes in numerical simulations. This requires a well-defined generalization of the concept of "rotation generators" on topological two-spheres that may not have any true Killing vectors. I present a new method for defining these fields, and results of a numerical code that computes them.

Acknowledgements

This thesis would not have been possible without the help of a large number of people, and I'm in a sentimental mood, so I'm going to try to name as many as I can.

First and foremost, I thank my advisors: Lee Lindblom, my guide, mentor, editor, adversary, and advocate, who has seen me through most of my work over the last five years, and put up with more flakiness than I should have expected him to; Richard Price, my teacher, friend, collaborator and idol, who first proved to me that physics at its best should make us laugh; and Kip Thorne, the spiritual leader of the Tapir group and of a significant fraction of the relativity community, a man from whom I would have learned much more, if only I'd had the energy to keep up. Thanks also go to Curt Cutler and Ken Libbrecht, for serving on my candidacy and defense committes, and also JoAnn Boyd, Shirley Hampton, and Donna Driscoll, for help with administrative matters.

I also thank the rest of my collaborators, both at Utah and at Caltech. I'm lucky to be able to say that there are too many of them to list, but there are a few that I mustn't overlook. I thank Mark Scheel and Harald Pfeiffer for frequent discussions and advice, and for bringing with them to Caltech the finest code that has ever been written for numerical relativity. I also thank Chris Beetle, for igniting my interest in mathematical relativity, and Ben Bromley, for teaching me most of what I know about computers and numerics. I especially want to thank Maria Cranor, for her friendship and her infectious passion for science, for frequently reminding me that I can do physics, that I should do physics, and that I want to do physics. I've needed plenty of reminding.

I thank my fellow relativity students for their friendship and comradery: Drs. Boyle, Chu, Cohen, Fang, Keppel, Li, Lovelace, Mandel, Matthews, Pan, Savov, Suyu—particularly Geoffrey and Ilya, with whom I got to talk a lot of physics and always intended to collaborate on something. Maybe later. I also thank the organizers and attendees of the Tapir grad student lunches, for sitting so patiently when I tried to argue that twistor theory is relevant for astrophysics.

If I think too hard about it, I can start to view the printing of this thesis as an important moment in the story of my life, so I want to thank a few people on a personal level as well. First, my mother and my brother, the most important people in my life and the best people I've ever known, and Charles and Sarah, for making them so happy. I also thank my extended family, particularly my aunt Karen and uncle Bish, without whose influence I might never have imagined postgraduate

education.

I thank my old friend Joe Sosa, for all the time we've spent hanging out, doing nothing, and also Mark, Nick, Joseph, Marie, Anthony, and Gabrielle, for treating me like a member of the family.

I am grateful for the help of a number of fantastic and inspiring teachers, a few of whom come to mind immediately: Cade Monroe, Jim Kurshner, Charlie Jui, Bill Sutherland, Mike Salamon, Karel Kuchař.

I thank Esa-Pekka Salonen and the LA Philharmonic, despite the fact that they've turned Caltech into the second best thing about living in this town. I also thank Steve Reich, another person I've never met, for proving to me that there are still interesting things for us to do, as long as we're clever enough to find them.

The work that I have put toward this thesis, and in fact all of the work I ever expect to do, is dedicated to the memory of my father. We lived together for about a decade and a half. I can't say that time was good, I won't say it was bad, but unlike any other period of my life, I know that it was real.

Contents

List of Figures

List of Tables

Chapter 1

Introduction

It's an exciting time to be a relativist. Once-esoteric concepts such as black holes and gravitational lenses are now fully understood to exist in the "real" world. Theoretical and experimental cosmology have entered the mainstream. Gravitational-wave astronomy is about to follow. And most important for this thesis, the *general* solution of Einstein's field equations finally seems to be approaching our grasp.

For many years, exact solutions of Einstein's equations were only available in cases of extreme symmetry or algebraic speciality [39]. Various perturbative approaches were developed, providing an enormous amount of insight into the nature of gravitational dynamics, but the truly *strong-field* dynamics have remained far from reach until very recently. The stunning complexity and nonlinearity of the field equations puts the dynamics of strong gravitational fields on a pedestal that can only be reached today with the help of careful computer simulations. This is the regime of *numerical relativity*.

The field of numerical relativity has progressed in small steps—sometimes forward, sometimes backward—over a very long period of time. It has come to require a simultaneous command of state-of-the-art computational, numerical, and analytical methods, sometimes to the unfortunate exclusion of physical insight. This gargantuan effort, however, is finally beginning to pay off, with multiple methods now available for handling the archetypal problem of numerical relativity: binary black holes [36, 13, 14, 15, 6, 7, 38, 12].

This thesis is evidence of this revolution of the field, in that the philosophy driving the work can be divided somewhat cleanly into three phases: before (chapters 2 and 3), during (chapters 4, 5, and 6), and after (chapter 7).

1.1 The periodic standing-wave approximation for nonlinear scalar fields

Chapters 2 and 3 relate to to a program spearheaded in recent years by Richard Price [37], called the *periodic standing-wave* (PSW) approximation. The most ambitious of this project's original goals stemmed from what in retrospect looks like an extreme pessimism regarding the near-term prospects for the conventional approach to numerical relativity: integrating evolution equations in time. One major difficulty with that approach has to do with competing timescales. At the short end, there is the ringing timescale of the individual holes, of order GM/c^3. At the long end, there is the timescale of the essential dynamics: the inspiral. This is several times greater than even the orbital period $\sqrt{r^3/GM}$, for a binary separation of radius r. If an evolution code is to become numerically unstable, it will do so on the ringing timescale, for which the numerical time step is adapted, rendering the much longer-term physical dynamics out of reach. Even if the code remains stable (and nowadays, most of them do), the mismatch of the evolution time step from the more interesting inspiral timescale presents an ineffiency of the standard approach of integrating the evolution equations in time.

The periodic standing-wave approximation ignores the shorter timescale. In fact it ignores *all* timescales. The orbit is approximated as being exactly periodic, or in fact, exactly *stationary* in a corotating frame of coordinates. Once this ansatz is imposed, the four-dimensional evolution problem simplifies to a boundary-value problem on the three-dimensional manifold of Killing orbits[1]. Once such a stationary solution is found, the slow, secular inspiral can be inferred adiabatically[2]. This adiabatic assumption breaks down, of course, when the holes finally plunge toward one another, but there is a significant period of time (multiple orbits [33, 22]) in which the inspiral remains slow but the evolution is too nonlinear for a post-Newtonian expansion.

It now appears that this late inspiral stage can be handled very well by modern evolution codes, so the PSW approximation is no longer necessary as a go-between from early post-Newtonian calculations to late numerical plunge simulations. However, it could conceivably still be useful. The basic inefficiency posed by the mismatch of timescales remains even in modern numerical codes. Removing it will require the implementation of stable implicit time-stepping algorithms, a substantial effort for such complicated codes. It is possible that once the machinery is finally

[1] Technically, it is not expected that the full general relativity problem would be solved by the standard method for stationary spacetimes: projection onto the manifold of Killing orbits [39]. That method is severely complicated in this case by the existence of a light cylinder in the helical Killing congruence. An alternative method, involving the use of harmonic gauge and the imposition of symmetry at each stage of an iterative algorithm, is being implemented [8]. This technical issue will not arise in this thesis, which goes no further than the much simpler case of a nonlinear scalar field toy theory.

[2] Being slightly more precise for a moment: the inspiral can be inferred in a sequence of timeslices of "outgoing-wave" solutions. A basic ingredient of the periodic standing-wave approximation is the method by which one transforms a standing-wave solution to one with outgoing waves at infinity. Once this is done, one can calculate the gravitational-wave flux at infinity to infer the rate of change of binding energy. From this, one can hope to infer the rate of change of the orbital separation.

in place to handle the late inspiral with PSW methods, their efficiency may be competitive with implicit evolution.

Another possible payoff for PSW calculations is that they could provide ideal initial data for conventional evolutions. Einstein's theory defines not only the evolution of geometry, but also *constraint equations* that must be satisfied throughout each spatial slice. The initial data, from which an evolution begins, must satisfy the constraint equations for the simulation to be physically meaningful. York and collaborators (see, e.g., [35]) have set these constraint equations as an elliptic system, amenable to standard numerical techniques; however, there are subtleties related to how they should be solved for *particular* spatial configurations of physical interest. The equations involve freely specifiable data, relating to a background conformal geometry on the initial spatial slice. These free data can be chosen at will, and the elliptic equations will provide a solution for any (reasonable) data. Choosing the *correct* free data for a given physical situation is not easy. In particular, the naive (and standard) choice, a flat conformal geometry, has been shown to be incompatible with rotational [23] or rectilinear [41] motion of even single black holes. Spinning or boosted configurations that come from flat conformal geometry are necessarily accompanied by a substantial amount of "junk radiation," unphysical gravitational waves present only to allow the spacetime to be initially conformally flat. This junk radiation quickly radiates in the evolution and contaminates the simulation that was intended. Correcting this problem of junk radiation will require new choices of conformal data, better representing the tidal structure of the binary black holes. Lovelace [31, 20] has begun a systematic study of modified initial conformal geometry, and has found promising signs. Letting the conformal geometry simply be a superposition of two individual boosted black hole geometries, he has substantially reduced the junk radiation in binary evolutions, particularly its high-frequency components. Results from PSW calculations, which already represent the exact spacetime geometry apart from the slow secular inspiral, could reduce this junk radiation much further, if needed.

Chapters 2 and 3 present the results of most of my work with the periodic standing-wave collaboration. Both relate to a toy model used to lay down ideas and machinery before attacking the full equations of general relativity. This toy model is of binary point charges coupled to a nonlinear scalar field on Minkowski spacetime:

$$\Box\psi + \lambda F(\psi) = \text{Source}, \tag{1.1}$$

where F is some nonlinear function of the scalar field, λ is a freely specifiable constant, and the source is two co-orbiting point charges, represented by delta functions with angular velocity Ω relative to the inertial coordinate system. This equation is then reduced by imposing the symmetry

condition that the field should rotate rigidly with the source:

$$\partial_t \psi = -\Omega \partial_\phi \psi. \tag{1.2}$$

Using this equation, the time derivatives appearing in (1.1) are replaced with angular derivatives. This leaves a purely spatial differential equation, but one of a curious sort: it is not purely elliptic or hyperbolic. In an interior region, where the vector that generates the symmetry, $\partial_t + \Omega\partial_\phi$, is timelike, the reduced equation is elliptic. Outside of this region the symmetry vector is spacelike and the reduced equation is hyperbolic. This mixed character represents the first major complication of the method, since all well-known numerical methods for efficiently solving differential equations assume global hyperbolicity or ellipticity. For this reason, we approached this helically-reduced wave equation very cautiously, by direct finite-difference discretization. I wrote most of this numerical code.

I used standard second-order finite-difference stencils to reduce the partial differential equation to a system of coupled nonlinear algebraic equations. The field was defined on a mesh of grid points, and the differential equation was approximated at each grid point using differences of the field values at the given grid point and its neighbors. If there are n grid points, this results in a system of n coupled algebraic equations for the n unknown values of the field. These coupled equations were then solved by a Newton-Raphson scheme, in which the equations are iteratively linearized and solved, resulting in successively better approximations to the true solution. These linearized systems were handled at each step using standard LAPACK [19] libraries for the direct numerical solution of linear systems. Ben Bromley assisted greatly in the interfacing of my code with the LAPACK routines.

As well as writing the code defining the discretized equations and the Newton-Raphson iteration, I also wrote code to calculate the "exact" solution of the linear ($\lambda = 0$) problem from a series expansion involving spherical harmonics and Bessel functions. Later elements of the chapter, involving the procedure for extracting an "outgoing" solution from a "standing-wave" solution, are mostly due to the efforts of my co-authors. The text of chapter 2 was written by Richard Price for publication as [2], of which I was listed as a co-author, and is reprinted verbatim.

Chapter 3 refines the methods of chapter 2 to provide significantly improved numerical results. Rather than solving our equations in spherical coordinates, we worked in an adapted coordinate system that is much better suited to the structure of a binary charge configuration. This adapted coordinate system provided automatic refinement of the numerical grid near the two source charges, while reducing to standard spherical coordinates far away. Unfortunately, we faced subtle complications with the application of my finite-difference code in this adapted coordinate system, and quickly moved on to a new numerical approach that was more robust and made better use of the

adapted coordinates. We called this new approach, the "eigenspectral method." It is a kind of compromise between a spectral expansion (in our specially-adapted angular coordinates), and a finite-difference method. The spectral decomposition was made not into conventional spherical harmonics, but rather onto the eigenbasis of the discretization of the angular laplacian on our coordinate grid. This spectral representation was then truncated to filter out physically irrelevant short-distance features. Loosely speaking, this means the eigenspectral code is a finite-difference code with automatic multipole filtering. This automatic filtering cured the numerical instabilities present in my more conventional finite-difference code.

The implementation and use of the eigenspectral code was almost entirely carried out by Benjamin Bromley and Richard Price. The most important elements of chapter 3 for this thesis are therefore those that relate to comparison with my finite-difference code, particularly the confirmation of certain results from chapter 2 in Table 3.49. I also carried out some analytical work relevant for chapter 3, such as (in parallel with others, for cross-checking) calculating the coefficients necessary to express the helically-reduced wave equation in our adapted coordinates. The text of chapter 3 was written by Richard Price, and published as [10], of which I was a co-author. It is reprinted verbatim as chapter 3.

Since the publication of the work presented in chapters 2 and 3, the helically-reduced scalar wave problem has been investigated further by others. Yoshida et al. [42] compared our finite-difference and eigenspectral codes with others recently developed at Milwaukee, systematically investigating an expanded class of nonlinearities, better representing the nonlinear terms to be expected in general relativity. Lau and Price [27] developed a multidomain pseudospectral code for this problem, similar in many ways to the code used by the Caltech and Cornell numerical relativity groups. Beetle, Bromley, and Price [9] investigated the helical symmetry reduction of linearized gravity, and simple nonlinear generalizations, using the eigenspectral code. They have also begun calculations in full general relativity, and hope to have results relevant to the wider numerical relativity community very soon.

1.2 The stability of constraint fields in free evolution

As we noted in the previous section, Einstein gave us two types of equations: *evolution equations*, that prescribe the change of the geometry from one time slice to the next, and *constraint equations*, purely spatial differential equations that must be satisfied throughout each time slice. The standard analogy is with Maxwell theory, for which the evolution equations are (in vacuum):

$$\partial_t \vec{E} = -\mathrm{curl}\vec{B}, \tag{1.3}$$

$$\partial_t \vec{B} = \mathrm{curl}\vec{E}, \tag{1.4}$$

and the constraint equations are:

$$\begin{aligned} \mathrm{div}\vec{E} &= 0, & (1.5)\\ \mathrm{div}\vec{B} &= 0. & (1.6) \end{aligned}$$

If a constrained evolution system is to be sensible, the evolution must be compatible with the constraints. That is to say, if a constraint-satisfying field configuration is integrated forward using the evolution equations, the result must be constraint satisfying as well. It is trivial to show that the Maxwell evolution equations are compatible with the constraints:

$$\begin{aligned} \partial_t(\mathrm{div}\vec{E}) &= \mathrm{div}(\partial_t\vec{E}) & (1.7)\\ &= -\mathrm{div}(\mathrm{curl}\vec{B}) & (1.8)\\ &= 0, & (1.9) \end{aligned}$$

by the standard vector calculus identity. The same result obviously holds for the divergence of $\vec{B}$.

This compatibility has led the numerical relativity community to the widespread adoption of a technique called *free evolution*, in which the constraint equations are solved only to obtain initial data, and then these data are integrated forward in time using only the evolution equations. In principle this is a sensible strategy. After all, the evolution preserves the constraints in general relativity as well. However, this compatibility is not quite as strong as in Maxwell theory.

Consider a theory with some number of constraints, $c^A = 0$, for certain quantities indexed by uppercase Latin letters. In the case of Maxwell theory, $c^1 = \mathrm{div}\vec{E}$, and $c^2 = \mathrm{div}\vec{B}$. The above calculation demonstrated that in this case the evolution equations imply that the constraint fields evolve as $\partial_t c^A = 0$. That is, the constraints of Maxwell theory are preserved exactly. Notice, however, that it would be just as sensible for a constrained evolution system to imply

$$\partial_t c^A = M^A{}_B c^B, \qquad (1.10)$$

for some matrix M on the vector space of constraints. In fact, the evolution of the constraints could be something even more complicated, involving spatial derivatives of the c^A. The only thing that matters for compatibility is that when the constraints are satisfied, $c^A = 0$, the right side of this constraint evolution system vanishes so that the constraints will continue to be satisfied.

When constraints evolve according to (1.10), the eigenvectors of the matrix M will grow (or decay) exponentially, at a rate equal to their corresponding eigenvalue. When one of these eigenvalues is positive, the corresponding eigenvector is said to define a *constraint-violating instability* of the evolution system. As long as this constraint is precisely satisfied in the initial data, it will

continue to be satisfied upon (ideal) evolution, but if it is even slightly violated, or if the evolution algorithm is not exactly precise, then the instability will be triggered. In the numerical context, nothing is exact, so if constraint-violating instabilities are present in the evolution equations, they will *always* be triggered. Constraint-violating instabilities arise in practice from this nasty collusion between analytical and numerical issues. They are instabilities of the *continuum* evolution equations, but they are triggered by the presence of *numerical* approximations. Chapters 4, 5, and 6 present three different strategies for dealing with these instabilities. The first strategy is to "correct" constraint violations after they have arisen, the second and third employ carefully designed evolution equations meant to remove constraint-violating instabilities before they even reach the numerical code.

1.2.1 Optimal constraint projection for hyperbolic evolution systems

Chapter 4 is a paper originally published by members of the Caltech numerical relativity group, including myself, along with Michael Holst (of U.C. San Diego) and Lawrence Kidder (of Cornell). The subject of this paper is called *optimal constraint projection*. This technique can be thought of as gently beating constraint violations into submission, ensuring that the hammer does no more damage than it absolutely needs to do.

Consider the problem of a rigid pendulum swinging in a plane, under the influence of gravity. Any freshman physics student could apply Newton's laws to derive the pendulum's equation of motion, an ordinary differential equation for the unknown function $\theta(t)$.

What if, instead, the student decided to work not in polar coordinates, but in cartesian coordinates? The result would be a system of coupled ordinary differential equations for the coordinates $x(t)$ and $y(t)$. These two functions cannot present more information than the single function $\theta(t)$, so they must satisfy a constraint. Indeed, if the pendulum is rigid and has length R, they must satisfy[3]

$$c(t) := [x(t)]^2 + [y(t)]^2 - R^2 = 0. \tag{1.11}$$

The requirement that this constraint be satisfied at all times implies another constraint on phase space:

$$\dot{c}(t) := x\dot{x} + y\dot{y} = 0. \tag{1.12}$$

If the student were to integrate the equations for $x(t)$ and $y(t)$ numerically, then he or she might eventually find that the constraints $c(t)$ and $\dot{c}(t)$ become nonzero. Assuming the student has had a proper education up to that point, he or she would know that the Pythagorean theorem must take priority over the numerical integrator, and would suspend the integration, fiddle with x and

[3] In this example, I am ignoring the effects of tidal gravity, and assuming the Pythagorean theorem holds in its classic form.

y until finding values that again lie on a circle of radius R, and a velocity tangent to this circle, and then let the integration resume. In the language of chapter 4, the student would have carried out a *constraint projection*.

If the student is particularly sensible, she will not just choose any point on the circle for the new values of x and y. She will retain some level of faith in her evolution equations, and choose the point on the circle that is *closest* to what her evolution equations have given her. She will project normal to the circle. In the language of chapter 4, she will have carried out an *optimal constraint projection*.

This cartoon description of constraint projection can be generalized considerably. Imagine an evolution system for some number of fields u^α on spacetime. Greek letters, here, index the various fields being evolved, not spacetime coordinates. Just as the phase space coordinates x, y, $\dot{x}$, and $\dot{y}$ of the previous example coordinatize the manifold $\mathbb{R}^4$, the fields u^α live in a manifold as well: the dynamical field bundle. This is the vector bundle whose base is the spatial domain, and whose fibers are given by the vector space of evolved fields u^α at the associated point.

Now imagine that this evolution system has some number of constraints c^A that can be written in terms of the u^α and their derivatives. When the c^A are written in this manner, the conditions $c^A = 0$ define a submanifold of the field bundle. This submanifold, called the *constraint manifold*, is analogous to the submanifold of phase space where $c(t)$ and $\dot{c}(t)$ vanish in the pendulum problem. The analogue of finding the nearest point on the circle, the geometric concept of "projecting the u^α normal to the constraint manifold," implies differential equations for the projected values of the u^α. Hopefully, these equations will be elliptic, and can be solved numerically.

In chapter 4, this abstract formalism is developed and applied to a specific model problem. This requires a constrained evolution system that is both simple, and unstable. Simplicity is necessary both to make the abstract concept as clear as possible for this "proof of concept" paper, and also to ensure that the actual differential equations can be written as an elliptic system without too formidable an effort of analytical massaging. Instability, of course, is necessary to demonstrate that the projection method can stand up to a nontrivial test. Instability is necessary to simulate the situation that arises in numerical relativity.

This combination of simplicity and instability is surprisingly rare. For example, the Maxwell equations are quite simple, and their optimal constraint projection turns out to involve nothing more complicated than Poisson equations. Unfortunately, as we've seen above, the constraint fields are exactly conserved in the evolution, even when they are nonzero.

Another simple system that has a simple constraint projection procedure is derived from the scalar wave equation, $\Box\psi = 0$. This equation has no constraints, but one appears if we write the

equation as a first-order system:

$$\partial_t \psi = \pi, \tag{1.13}$$

$$\partial_t \pi = \delta^{ij} \partial_i \phi_j, \tag{1.14}$$

$$\partial_t \phi_i = \partial_i \pi, \tag{1.15}$$

$$\mathcal{C}_i := \partial_i \psi - \phi_i = 0. \tag{1.16}$$

The quantities π and ϕ_i have been introduced to stand in for the temporal and spatial derivatives of ψ. The constraint $\mathcal{C}_i$ is nonzero if ϕ_i is not properly representing the gradient of ψ.

Unfortunately, the constraint evolution equation is again too stable:

$$\partial_t \mathcal{C}_i = \partial_t \partial_i \psi - \partial_t \phi_i = \partial_i \partial_t \psi - \partial_t \phi_i = \partial_i \pi - \partial_i \pi = 0. \tag{1.17}$$

My main contribution to the constraint projection project, an idea that will be relevant to chapters 5 and 6 as well, was to note that we can add a term proportional to the constraint to the right side of one of the evolution equations, equation (1.15), making it $\partial_t \phi_i = \partial_i \pi + \gamma \mathcal{C}_i$, i.e.,

$$\partial_t \phi_i = \partial_i \pi + \gamma \partial_i \psi - \gamma \phi_i, \tag{1.18}$$

where γ is a freely-specifiable parameter. This modification does not alter the physical, constraint-satisfying solution space for which $\mathcal{C}_i = 0$, but it strongly affects the behavior of constraint-violating modes. For the evolution of the constraint, one immediately finds,

$$\partial_t \mathcal{C}_i = -\gamma \mathcal{C}_i. \tag{1.19}$$

Thus, for negative values of γ, the constraint will grow exponentially on a timescale $-1/\gamma$.

This all seems a little too easy. Might there be some sort of technicality that makes the terms proportional to γ illegal? The only such technicality that could apply is the condition that the system must remain hyperbolic. For the time being, I will postpone the formal definitions of the various types of hyperbolicity that are relevant to this problem. These definitions will be given, when necessary, in the later chapters. Suffice it to say, the hyperbolicity of a system of equations is determined by the nature of certain linear operators (called "characteristic matrices") that can be read off from the principal part of the evolution system. The principal part of an evolution system is obtained by ignoring all terms in the system except the highest-order derivatives. The principal part of the scalar wave system is therefore given by:

$$\partial_t \psi \simeq 0, \tag{1.20}$$

$$\partial_t \pi \simeq \delta^{ij} \partial_i \phi_j, \tag{1.21}$$

$$\partial_t \phi_i \simeq \partial_i \pi + \gamma \partial_i \psi. \tag{1.22}$$

The γ parameter changes the principal part of the evolution system, so it could indeed ruin hyperbolicity. However, it appears in a very special way, such that the modification to the system turns out not to be relevant. If we define the new field

$$\bar{\pi} := \pi + \gamma \psi, \tag{1.23}$$

then the principal part of the evolution system becomes:

$$\partial_t \psi \simeq 0, \tag{1.24}$$

$$\partial_t \bar{\pi} \simeq \delta^{ij} \partial_i \phi_j, \tag{1.25}$$

$$\partial_t \phi_i \simeq \partial_i \bar{\pi}. \tag{1.26}$$

This is the same as the principal part of the *unmodified* evolution system, so the effect that the γ term has had on the principal part of the evolution system can be removed by a linear change of variables. This linear change of variables has the geometric meaning of a change of basis on the bundle of dynamical fields, but the abstract structure of the characteristic matrices that determines hyperbolicity is basis-independent. My modification of the evolution equations, therefore, has no effect on the hyperbolicity of the system.

After convincing myself that this system is both hyperbolic and unstable, I quickly wrote a simple finite-difference evolution code to investigate the numerical situation. The result is shown in Fig. 1.1, the first ever demonstration of optimal constraint projection for the unstable scalar wave system. This simple finite-difference simulation was only meant to demonstrate the instability of the system, and the effectiveness of the projections. Far more detailed numerical investigations of constraint projection for this unstable scalar wave system are presented in chapter 4, but they are almost entirely attributable to my co-authors. The text of chapter 4 was written by Lee Lindblom, and published as [25] with myself as a co-author. It is reprinted verbatim as chapter 4.

1.2.2 A new generalized harmonic evolution system

While working as a postdoc with the Caltech numerical relativity group, Frans Pretorius developed a very unconventional code for numerical relativity. Perhaps the most surprising of his design choices was the way that he fixed the spacetime coordinate freedom of general relativity—a way called the *generalized harmonic* method.

The most common approach to numerical relativity begins with some variant of what are now

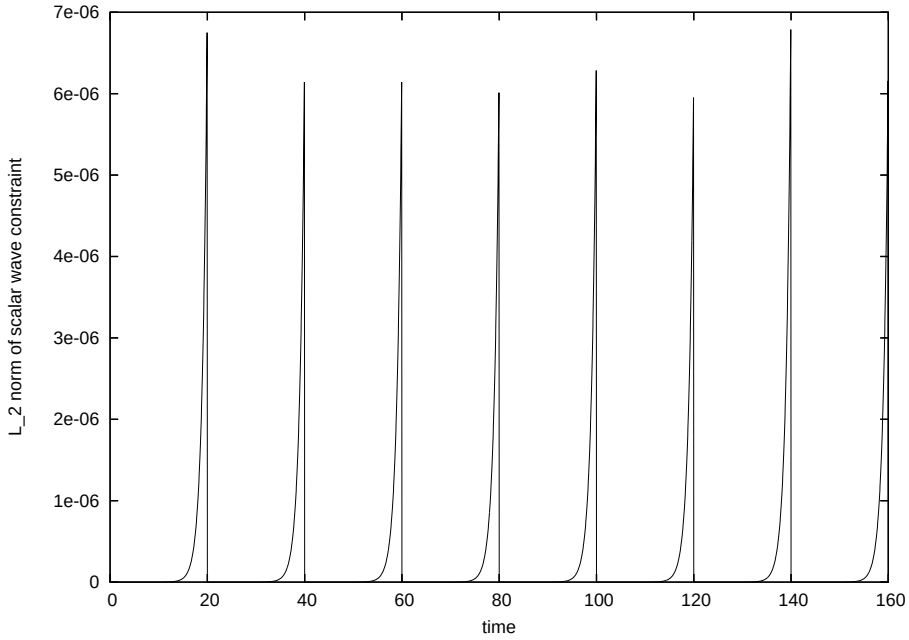

Figure 1.1: Constraint norm $||c|| := \left(\int \delta^{ij}\mathcal{C}_i\mathcal{C}_j d^3x\right)^{1/2}$ for the unstable scalar wave system with $\gamma = -1$ and projections at every 20 time units. The vertical scaling is linear, to emphasize the rapid constraint growth. These results came from a simple finite-difference numerical code, so they are second-order convergent in the grid spacing. Chapter 4 presents detailed numerical tests carried out by my co-authors, using a far more accurate pseudospectral code.

referred to as the ADM equations, originally due to Arnowitt, Deser, and Misner [3, 40]. I will leave the detailed discussion of the ADM formalism for the next section and chapter 6, and merely say that the essential difference between the ADM formalism and the generalized harmonic formalism amounts to how one chooses to fix coordinates. In the ADM formalism, one fixes a function N, called the "lapse," which relates coordinate time to proper time for observers travelling normal to the spatial slice, and a vector N^i, called the "shift," which fixes the velocity of the spatial coordinates, relative to the hypersurface-normal observers. In the generalized harmonic formalism, this geometrically-inspired gauge fixing is abandoned. Instead, one specifies what the d'Alembertians of the spacetime coordinates should be, in the evolved spacetime. In symbols, the generalized harmonic gauge condition (coordinate fixing condition) is:

$$\Box x^\mu = H^\mu, \tag{1.27}$$

where the x^μ are the spacetime coordinates, treated as four scalar fields when acted upon by the curved-space d'Alembertian operator $\Box$, and the H^μ are predetermined functions on spacetime. In truly harmonic gauge, $H^\mu = 0$. The generalization allows the H^μ to be nonzero, so that *arbitrary* coordinates can be specified.

This may seem like a bizarre way to fix a coordinate system. Its motivation lies in the remarkable way that it simplifies the principal part of Einstein's equations. In generalized harmonic gauge, the principal part is simply:

$$\psi^{\rho\sigma}\partial_\rho\partial_\sigma\psi_{\mu\nu} \simeq 0, \tag{1.28}$$

where $\psi_{\mu\nu}$ is the spacetime metric and $\psi^{\mu\nu}$ its inverse[4]. The Einstein equations therefore reduce (at principal order) to independent wave equations for each component of the spacetime metric. As long as the metric remains Lorentzian, this is a *manifestly* hyperbolic system! In chapter 6 we will encounter some of the complexity of ensuring hyperbolicity in the ADM formalism, and will come to appreciate just how special equation (1.28) truly is.

With his specially designed code, using these generalized-harmonic evolution equations (along with a very important modification suggested by Carsten Gundlach, described in chapter 5), Pretorius was able to carry out the first ever simulation of multiple orbits, coalescence, and ringdown of a binary black hole system [36]. There is no absolute dividing line, at which one might say that the "modern age" of numerical relativity began, but Pretorius's first presentation of these results is as good a choice as any[5].

The portion of the Caltech/Cornell numerical relativity group working with our backbone spec-

[4] In numerical relativity, it is common to reserve the letter g for the metric on three-dimensional spatial slices.

[5] Later papers [13, 6], introducing the formalism of "moving punctures," have been more influential, if only because the moving puncture formalism provides similar stability, and is easier to implement in most of the existing numerical relativity codes.

tral code has long insisted on using hyperbolic evolution equations [26], so upon seeing Pretorius's results, we quickly began to investigate whether we could use a generalized harmonic formalism ourselves. For an evolution system to be compatible with our numerical code, it must (for technical reasons) be put in a form that involves derivatives only up to first order with respect to space and time. In the previous section we saw how the second-order wave equation can be written as a first-order system, by promoting all first derivatives to independent fields. The same applies here; introducing fields $\Pi_{\mu\nu}$ and $\Phi_{i\mu\nu}$, equation (1.28) becomes

$$\begin{aligned} \partial_t \psi_{\mu\nu} - N^k \partial_k \psi_{\mu\nu} &\simeq 0, & (1.29)\\ \partial_t \Pi_{\mu\nu} - N^k \partial_k \Pi_{\mu\nu} + N g^{ki} \partial_k \Phi_{i\mu\nu} &\simeq 0, & (1.30)\\ \partial_t \Phi_{i\mu\nu} - N^k \partial_k \Phi_{i\mu\nu} + N \partial_i \Pi_{\mu\nu} &\simeq 0, & (1.31)\\ \mathcal{C}_{i\mu\nu} := \partial_i \psi_{\mu\nu} - \Phi_{i\mu\nu} &= 0, & (1.32) \end{aligned}$$

where $\Pi_{\mu\nu}$ is defined essentially as the time derivative of $\psi_{\mu\nu}$; $\Phi_{i\mu\nu}$ is defined by the new constraint (1.32); and N, N^i, and g_{ij} are shorthand for particular components of $\psi_{\mu\nu}$, defined compactly in the expression:

$$ds^2 = \psi_{\mu\nu} dx^\mu dx^\nu = -N^2 dt^2 + g_{ij}(dx^i + N^i dt)(dx^j + N^j dt). \quad (1.33)$$

This first-order representation of the generalized-harmonic Einstein system was presented by Alvi in [1]. In chapter 5 we generalize this system to cure two serious ills.

First, equation (5.22) implies a frightening evolution equation for N^i, whose principal part is[6]:

$$\partial_t N^i - N^k \partial_k N^i \simeq 0. \quad (1.34)$$

Equations of this form cause shocks to develop in hydrodynamical simulations. To cure this ill, we substitute the constraint $\mathcal{C}_{k\mu\nu}$, to transform the $\partial_k \psi_{\mu\nu}$ appearing in equation (5.22) into $\Phi_{k\mu\nu}$. This substitution, due to my collaborators, may appear very minor and unconvincing, but it turns out to make the system *linearly degenerate*, a quality implying that shocks should not be expected to develop from smooth initial data [30].

The second flaw in Alvi's evolution system, (5.22) – (1.32), is that the newly introduced constraints, $\mathcal{C}_{i\mu\nu}$, may become unstable in nontrivial simulations. We have already seen a cure for this disease. My modification of the scalar wave equation presented in the previous section, that makes that system unstable, can be applied with a coefficient of the opposite sign in order to *stabilize* the system. In the same way, a term proportional to $\mathcal{C}_{i\mu\nu}$ can be added to equation (5.24) to stabilize

[6] Although in the ADM formalism, the shift vector N^i is nondynamical and specified *a priori*, in the generalized harmonic formalism it is merely a component of the spacetime metric, evolved like any other.

this constraint.

A complication arises, however, on the subject of hyperbolicity. The argument given in the previous section, that hyperbolicity is preserved because the modifications to the principal part can be removed by a linear change of variables, is spoiled in this case by the substitution made to ensure linear degeneracy. For some time, we labored under the sad impression that linear degeneracy would be incompatible with constraint stability, that we would have to choose one or the other.

I discovered a resolution for this conflict. In retrospect it should have been obvious. In this business, the answer is always: substitute the constraint. The constraint has already been substituted into Eqs. (5.22) and (5.24). In chapter 5, we will see that a careful substitution of $\mathcal{C}_{i\mu\nu}$ into (5.23) allows us to recover hyperbolicity, while preserving linear degeneracy and constraint stability.

These issues, involving the stabilization of $\mathcal{C}_{i\mu\nu}$, represent my main contribution to the work presented in chapter 5. Lee Lindblom and Mark Scheel are most responsible for the herculean calculation verifying the hyperbolicity of the resulting constraint evolution system, presented in section 5.4.1. They used a computer algebra system to verify this hyperbolicity in general, and I then repeated their calculation by hand, restricted to the special case of linearized perturbations of flat spacetime. In this process I uncovered a few errors, not in the computer algebra results, but in their transcription into the manuscript. The numerical results presented in chapter 5 are entirely due to my co-authors. Lee Lindblom wrote the text of chapter 5, which was published as [29], and is reprinted verbatim.

1.2.3 Constraint damping in the KST evolution systems

The first-order generalized harmonic evolution system presented in chapter 5 is a powerful tool for numerical relativity, and indeed the Caltech and Cornell groups are using it for essentially all of our binary black hole simulations. But it still has a few drawbacks, strong enough that it is reasonable for us to keep an eye on what might be possible in the ADM formalism.

For example, there is the difficulty of fixing coordinate gauge in the generalized harmonic formalism. While in principle any coordinate system can be determined by fixing the functions H^μ, in practice choosing coordinates that avoid such difficulties as physical and coordinate singularities is a difficult problem. Decades of research have been applied to the study of gauge conditions (coordinate conditions) in the ADM formalism, but it is a difficult problem to translate any of this knowledge over to the generalized harmonic context.

Second, there is the sheer size of the space of fields. In the first-order generalized harmonic system, we evolve all components of $\psi_{\mu\nu}$, $\Pi_{\mu\nu}$, and $\Phi_{i\mu\nu}$, a total of fifty fields! This large number of fields implies significant memory and storage requirements, and more importantly, a considerable number of processor cycles per time step.

The spectral code used by the Caltech and Cornell numerical relativity groups requires that

the evolution equations be first-order in all derivatives, and symmetric hyperbolic[7]. The conventional ADM evolution equations satisfy neither of these conditions, but in 2001, Kidder, Scheel, and Teukolsky [26] generalized them to present a twelve-parameter family of first-order symmetric hyperbolic evolution systems, referred to as the "KST" systems. These involve only thirty dynamical fields, just over half as many as are present in the generalized harmonic formalism. These are the components of the metric g_{ij} on the spatial slices, the extrinsic curvature K_{ij} of these slices in spacetime, and a three-index field D_{kij} introduced to take the place of the spatial derivatives of g_{ij}. Coordinates are fixed in the KST systems in (essentially) the familiar ADM language, in terms of the lapse and shift. Lindblom and Scheel [28] have shown how to implement certain popular gauge conditions in the KST formalism, and more recently, Paschalidis [34] has demonstrated that the "1 + log" slicing condition, currently used by most other numerical relativity groups, can be implemented in the KST system in a remarkably simple way. Mathews et al. [21] are currently investigating the implementation of 1 + log slicing in the generalized harmonic formalism, and have found it to be quite a tricky endeavor.

In chapter 6, I sketch the structure of the KST evolution systems, and generalize them by introducing a new modification intended to stabilize their constraints. This modification is directly analogous to the modifications described above for the scalar wave and generalized harmonic systems, but its implementation is considerably more complicated. I demonstrate that these modifications do not alter the hyperbolicity of these evolution systems, nor the evolution systems implied for their constraints. I also demonstrate that in a certain region of the space of freely-specifiable parameters, these modifications are able to stabilize all constraint violating modes, even some that we might not expect. I then demonstrate, with numerical simulations, that this "constraint damping" modification is quite effective for stabilizing simulations of single-black-hole spacetimes. The research presented in chapter 6 is entirely my own, as is the text, which has been submitted for publication in Physical Review D, and is available as an online preprint [32].

1.3 The spin of dynamical black holes

Now that numerical relativists are able to simulate interesting, dynamical spacetimes, including what was once referred to as the holy grail of the field, binary black holes, it is time for us to start extracting some physics. The first obvious target is spin: the spin angular momentum of the individual black holes in a binary configuration, and the nonlinear coupling of these spins to one another and to the orbital angular momentum of the binary system.

The problem that one immediately encounters in this situation is that to talk about the spin of the individual black holes in a binary configuration, the spin must be mathematically defined in a

[7] The precise definition of symmetric hyperbolicity will be given in chapters 4 and 5.

quasilocal manner. That is, there must be some prescription for computing the angular momentum within a closed 2-surface, ignoring everything outside.

In 1993, Brown and York [11] presented such a quasilocal prescription for various "charges" including angular momentum. A few years later, the same prescription appeared in the work of Ashtekar and collaborators [4, 5] in their theory of "isolated and dynamical horizons." This definition of quasilocal spin angular momentum has now become standard in the numerical relativity community [15, 16, 17, 24, 18].

The quasilocal spin is defined as the integral over a two-surface (normally an apparent horizon) of the azimuthal component of a certain vector field. The azimuthal vector field defining this component is well-defined in the presence of rotation symmetry: it is merely taken to be one of the rotation generators. In a binary black hole system, where the spacetime has no rotation symmetries, one must generalize the concept of rotation symmetry in order to keep the quasilocal spin well defined. The question of how this should be done is still somewhat open.

In chapter 7, I discuss existing proposals for defining generalized rotation generators. Then I present a new proposal that, while computationally somewhat demanding, provides what I argue is an ideal solution to the problem. This involves the eigenvalue problem for a certain fourth-order differential operator that is defined by the intrinsic geometry of the surface. The results of this eigenvalue problem provide three independent vector fields of zero expansion and minimum shear. I also present results from a code that carries out this eigenvalue problem numerically. The research presented in chapter 7 is entirely my own, as is the text.

Bibliography

[1] Kashif Alvi. First-order symmetrizable hyperbolic formulations of Einstein's equations including lapse and shift as dynamical fields. *Class. Quantum Grav.*, 19:5153–5162, 2002.

[2] Zeferino Andrade, Christopher Beetle, Alexey Blinov, Benjamin Bromley, Lior Burko, Maria Cranor, Robert Owen, and Richard H. Price. The periodic standing-wave approximation: Overview and three dimensional scalar models. *Phys. Rev. D*, 70:064001, 2003. gr-qc/0310001.

[3] R. Arnowitt, S. Deser, and Charles W. Misner. The dynamics of general relativity. In *Gravitation: An Introduction to Current Research*, L. Witten, Ed., Wiley, New York, 1962, pages 227–265.

[4] Abhay Ashtekar, Christopher Beetle, and Jerzy Lewandowsky. Mechanics of rotating isolated horizons. *Phys. Rev. D*, 64:044016, 2001.

[5] Abhay Ashtekar and Badri Krishnan. Dynamical horizons and their properties. *Phys. Rev. D*, 68:104030, 2003.

[6] John G. Baker, Joan Centrella, Dae-Il Choi, Michael Koppitz, and James van Meter. *Phys. Rev. Lett.*, 96:111102, 2006.

[7] John G. Baker, Joan Centrella, Dae-Il Choi, Michael Koppitz, and James van Meter. *Phys. Rev. D*, 73:104002, 2006.

[8] Christopher Beetle, Benjamin Bromley, and Richard H. Price. (in preparation).

[9] Christopher Beetle, Benjamin Bromley, and Richard H. Price. The periodic standing-wave approximation: eigenspectral computations for linear gravity and nonlinear toy models. *Phys. Rev. D*, 74:024013, 2006. gr-qc/0602027.

[10] Benjamin Bromley, Robert Owen, and Richard H. Price. The periodic standing-wave approximation: nonlinear scalar fields, adapted coordinates, and the eigenspectral method. *Phys. Rev. D*, 71:104017, 2005. gr-qc/0502034.

[11] J. David Brown and James W. York. Quasilocal energy and conserved charges derived from the gravitational action. *Phys. Rev. D*, 47:1407–1419, 1993.

[12] Bernd Brügmann, José A. González, Mark Hannam, Sascha Husa, Ulrich Sperhake, and Wolfgang Tichy. Calibration of moving puncture simulations. 2006. gr-qc/0610128.

[13] Manuella Campanelli, Carlos O. Lousto, Pedro Marronetti, and Yosef Zlochower. Accurate evolutions of orbiting black-hole binaries without excision. *Phys. Rev. Lett.*, 96:111101, 2006.

[14] Manuella Campanelli, Carlos O. Lousto, and Yosef Zlochower. *Phys. Rev. D*, 73:061501(R), 2006.

[15] Manuella Campanelli, Carlos O. Lousto, and Yosef Zlochower. *Phys. Rev. D*, 74:041501, 2006. gr-qc/0604012.

[16] Manuella Campanelli, Carlos O. Lousto, and Yosef Zlochower. Spin-orbit interactions in black-hole binaries. *Phys. Rev. D*, 74:084023, 2006. astro-ph/0608275.

[17] Manuella Campanelli, Carlos O. Lousto, Yosef Zlochower, Badri Krishnan, and David Merritt. Spin flips and precession in black-hole-binary mergers. gr-qc/0612076.

[18] Matthew Caudill, Gregory B. Cook, Jason D. Grigsby, and Harald P. Pfeiffer. Circular orbits and spin in black-hole initial data. *Phys. Rev. D*, 74:064011, 2006. gr-qc/0605053.

[19] E. Anderson et al. *LAPACK Users' Guide*. Society for Industrial and Applied Mathematics, Philadelphia, 1999.

[20] Geoffrey Lovelace et al. (in preparation).

[21] Keith Matthews et al. (in preparation).

[22] Michael Boyle et al. (in preparation).

[23] Alcides Garat and Richard H. Price. Nonexistence of conformally flat slices of the kerr spacetime. *Phys. Rev. D*, 61:124011, 2000. gr-qc/0002013.

[24] Frank Herrmann, Ian Hinder, Deirdre Shoemaker, Pablo Laguna, and Richard Matzner. Gravitational recoil from spinning binary black hole mergers. 2007. gr-qc/0701143.

[25] Michael Holst, Lee Lindblom, Robert Owen, Harald P. Pfeiffer, Mark A. Scheel, and Lawrence E. Kidder. Optimal constraint projection for hyperbolic evolution systems. *Phys. Rev. D*, 70:084017, 2004.

[26] L. E. Kidder, M. A. Scheel, and S. A. Teukolsky. Extending the lifetime of 3d black hole computations with a new hyperbolic system of evolution equations. *Phys. Rev. D*, 64(6):064017, Sep 2001.

[27] Stephen R. Lau and Richard H. Price. Multidomain spectral method for the helically reduced wave equation. gr-qc/0702050.

[28] Lee Lindblom and Mark A. Scheel. Dynamical gauge conditions for the Einstein evolution equations. *Phys. Rev. D*, 67:124005, 2003.

[29] Lee Lindblom, Mark A. Scheel, Lawrence E. Kidder, Robert Owen, and Oliver Rinne. A new generalized harmonic evolution system. *Class. Quantum Grav.*, 23:S447–S462, 2006.

[30] T. P. Liu. Development of singularities in the nonlinear waves for quasilinear hyperbolic partial differential equations. *J. Diff. Equations*, 33(1):92–111, 1979.

[31] Geoffrey Lovelace. *Topics in Gravitational Wave Physics.* PhD thesis, California Institute of Technology, 2007.

[32] Robert Owen. Constraint damping in first-order evolution systems for numerical relativity. gr-qc/0703145.

[33] Yi Pan, Alessandra Buonnano, John G. Baker, Joan Centrella, Bernard J. Kelly, Sean T. McWilliams, Frans Pretorius, and James R. van Meter. A data-analysis driven comparison of analytic and numerical coalescing binary waveforms: nonspinning case. arXiv:0704.1964v1.

[34] Vasileios Paschalidis. Mixed Hyperbolic – Second-Order Parabolic Formulations of General Relativity. arXiv:0704.2861.

[35] Harald P. Pfeiffer and James W. York. Extrinsic curvature and the Einstein constraints. *Phys. Rev. D*, 67:044022, 2003. gr-qc/0207095.

[36] Frans Pretorius. Evolution of binary black hole spacetimes. *Phys. Rev. Lett.*, 95:121101, 2005.

[37] Richard H. Price. Binary inspiral: finding the right approximation. *Class. Quantum Grav.*, 21:S281–S293, 2004.

[38] Mark A. Scheel, Harald P. Pfeiffer, Lee Lindblom, Lawrence E. Kidder, and Saul Teukolsky. Solving Einstein's equations with dual coordinate frames. *Phys. Rev. D*, 74:104006, 2006.

[39] Hans Stephani, Dietrich Kramer, Malcolm Maccallum, Cornelius Hoenselaers, and Eduard Herlt. *Exact Solutions of Einstein's Field Equations*. Cambridge University Press, New York, 2003.

[40] James W. York, Jr. Kinematics and dynamics of general relativity. In *Sources of Gravitational Radiation*, Larry Smarr, Ed., Cambridge University Press, Cambridge, England, 1979, pages 83–126.

[41] James W. York, Jr. Energy and momentum of the gravitational field. In *Essays in General Relativity*, F.J̃. Tipler, Ed., Academic, New York, 1980, pages 39–58.

[42] Shin'ichirou Yoshida, Benjamin Bromley, Jocelyn S. Read, Koji Uryu, and John L. Friedman. Models of helically symmetric binary systems. *Class. Quantum Grav.*, 23:S599–S614, 2006. gr-qc/0605035.

Chapter 2

The periodic standing-wave approximation: overview and three-dimensional scalar models

Originally published as Phys.Rev. D70 (2004) 064001.

The periodic standing-wave method for binary inspiral computes the exact numerical solution for periodic binary motion with standing gravitational waves, and uses it as an approximation to slow binary inspiral with outgoing waves. Important features of this method presented here are: (i) the mathematical nature of the "mixed" partial differential equations to be solved, (ii) the meaning of standing waves in the method, (iii) computational difficulties, and (iv) the "effective linearity" that ultimately justifies the approximation. The method is applied to three-dimensional nonlinear scalar model problems, and the numerical results are used to demonstrate extraction of the outgoing solution from the standing-wave solution, and the role of effective linearity.

2.1 Introduction

Background

The inspiral and merger of a binary pair of compact objects (holes or neutron stars) is one of the most promising sources of signals detectable by gravitational wave observatories. For the ground-based detectors LIGO [1], VIRGO [2], GEO600 [3], and TAMA [4], binary merger, especially of intermediate-mass black holes [5] is an exciting possibility; for the space-based LISA detector [6, 7], the detection of inspiral/merger of supermassive holes is highly probable, and is one of the primary scientific targets.

The need for theoretical waveforms for the inspiral/merger has driven the effort to find a computational solution for the details of the process, but the difficulty of the task has made this problem

also a measure of the usefulness of numerical computation in general relativity. The hope has been that numerical codes evolving initial data can compute the orbital motion using Einstein's equations and, in the case of neutron stars, using hydrodynamical equations. These evolution codes would have, as an intrinsic feature, the loss of energy by the binary due to outgoing wave energy, and the gradual inspiral due to this loss.

An important reason for the limited progress on this problem is the matter of timescales. Near a black hole, the timescale on which the gravitational field can change is GM/c^3, where M is the mass of the hole; for a neutron star the timescale is several times longer. The time step in evolution codes is governed by this short timescale. (More precisely, the spatial grid near the compact objects must be smaller than GM/c^2, and to satisfy the Courant condition, the time step must be no larger than $1/c$ times this grid size.) By contrast, the timescale $\sqrt{r^3/GM}$, for orbital motion at radius r, is much larger than this, and the timescale for the interesting dynamics, the radiation-reaction driven inspiral, is much greater yet. The consequence of this incompatibility of timescales is that a very large number of time steps is needed in order to see the physics of interest. And computing a large number of time steps is not yet possible. Instabilities [8, 9] operating at the short timescale prevent the code from giving useful answers about the long timescale.

The origin of the difficulty suggests its cure: an approximation method that avoids the short timescales. Here we describe such a method: a solution for periodic sources and fields. We assume that the compact objects, and their fields, rotate with a constant angular velocity (to be denoted Ω below). This approximation will fail of course, in the very latest stages of inspiral merger, when the orbit decays rapidly due to a secular instability or the dynamics of the final merger. But that last stage is, by its very nature, rapid; its timescale is only several times that of the shortest timescale of the problem. This last stage, then, can plausibly be handled by numerical evolution codes. Indeed, evolution codes, especially with perturbation theory handling the final ringdown [10], are already near to doing this. Our goal, then, is a method that can approximate the solution up to the time that numerical evolution codes can take over the task that only they can handle. Our approach is not entirely new; it is similar in underlying motivation to a method introduced by Detweiler and collaborators [11, 12], but our approach is very different in its details and its implementation. It is also very closely related to the approach being used by Friedman and his collaborators [13].

Periodic motion and outgoing waves are, of course, impossible in Einstein's theory, both intuitively and mathematically[1]. For this reason, we will solve for standing waves (to be defined and discussed below) in the gravitational field. Our periodic standing-wave (PSW) approach, then, will be to find exact (numerical) periodic standing-wave solutions of the Einstein field equations and to use these exact solutions as approximations to the physical problem of slow inspiral with outgoing

[1] A periodic binary would have no secular change in its energy, but gravitational waves intuitively remove energy. This argument can be made mathematically complete using the conservation law for $H^{\alpha\beta\mu\nu}$, as defined in Misner et al. [14].

waves.

The most basic ideas behind this periodic standing-wave solution have already been introduced in a previous paper [15], but the implementation there was applied only to two-dimensional models and was limited in other ways; in particular, that paper did not discuss the general meaning of standing waves. An general overview of the PSW project has also been given [16]. Here we present a more specific discussion, along with numerical results for three-dimensional models. This paper is meant to serve as the introduction to the PSW, with subsequent papers presenting more detailed information on particular methods, and progress on solving the physical problem.

Effective linearity and uses of the method

A key idea in our approach is the relationship of standing waves to outgoing waves. In a linear field theory, a definition of standing waves is that they are half the sum of an outgoing solution and ingoing solution. Here, as in [15], we shall call this sum LSIO for linear superposition of (half) ingoing and (half) outgoing solutions. In a linear theory, such a superposition is itself a solution. In our nonlinear field model theories, it will turn out that—despite strong nonlinearities—this continues to be very nearly true. This *effective linearity*, the approximate equality of the LSIO and a true standing-wave solution, has already been demonstrated for simple two-dimensional models, and results for three dimensional nonlinear models will be presented below. More importantly, the basis for effective linearity appears to be robust. This basis lies in the fact that the strong nonlinearities in our model theories (and in the physical problem) are confined to the near-field regions around the sources. In these nonlinear near-field regions the solution is insensitive to the distant boundary conditions; it is substantially the same for ingoing boundary conditions as for outgoing. In this near-field region then, the LSIO will be very nearly a solution despite strong nonlinearities, since we are superposing nearly identical solutions. Outside this strong-field near zone the model theories, and the physical theory, are nearly linear, so that again the LSIO is a solution. The LSIO will therefore be a good approximation to a solution everywhere.

Below, we shall choose our definitions of standing-wave solution to be close to that of a LSIO, and our approximation to a large extent is based on interpreting a standing-wave solution to be approximately a LSIO. In the weak-field region this LSIO can be deconstructed into outgoing and ingoing pieces and this deconstruction can be continued to the strong-field source region. (In the source region, the outgoing piece is simply half the solution.) By doubling the outgoing piece thus extracted from the standing-wave solution, we thereby arrive at an approximation to the outgoing solution for a nonlinear problem. It is in this manner that we will extract an approximation of an outgoing solution from a computed standing-wave solution.

This is an appropriate place to point out, though not for the last time, the importance of model problems. In Einstein's theory there is no obvious meaning to the periodic outgoing solution, so

one cannot make statements about it, let alone carry out numerical studies. Statements and computations *are* possible for nonlinear model problems, so that tests of effective linearity with such models are crucial.

The outgoing solutions extracted from our exact periodic solutions can serve two purposes. First, we can use a quasi-stationary sequence of outgoing approximations as a model for the slow physical inspiral. In this approach the mass of the system, measured in a weak wave zone far from the orbiting sources, decreases due to the loss of energy in outgoing radiation. When we find the system energy as a function of orbit radius, and we compute the outgoing radiation, we can infer the rate at which the orbital radius decreases. The difficulty, as with any such quasi-stationary sequence, is how to know that we are comparing the "same" system at different radii. In the case of neutron stars the answer is clear; baryon number is an unchanging tag that identifies neutron stars to be the same. For black holes, the equivalent tag would be some local mass. The concept of an isolated horizon [17] might give us that local mass.

The second use for our extracted outgoing solutions is to provide initial data for evolution codes. A spacelike slice of our extracted outgoing field will be an excellent approximation to the physical initial data, and should be very nearly a solution to the initial value equations. With little change our extracted outgoing initial data, can be made into exact (numerical) initial data through the use of York's decomposition [18, 19].

These two purposes of our solution are not distinct. The natural end point for a quasi-stationary sequence of PSW solutions is the "last orbit," the final stage of motion at almost constant radius. This stage may end due to a secular instability, like that of a particle in a black hole spacetime, or due to the imminence of the merger, the formation of the final black hole. In either case, this end point must be handled by a numerical evolution code, and in either case, the quasi-stationary sequence will provide ideal initial data for the continuation of the problem by numerical evolution.

The nature of the mathematical problem

In the standard approach to computing binary inspiral, initial data are evolved forward in time. In our approach, with periodic symmetry imposed, there is no evolution in the usual sense, and there is not the usual concept of initial data. Rather we must satisfy boundary conditions at large radius: outgoing, ingoing, or standing-wave boundary conditions in model problems, and only standing-wave conditions in general relativity. The boundary value problems that we must solve differ in two important ways from common boundary value problems. First, our partial differential equations (PDEs) are of *mixed* type. They are of elliptical character in some regions and hyperbolic character in others; this will be particularly clear in the model problem to be presented below. We will argue that the mixed character causes no fundamental difficulty, and will demonstrate this with the model problems. The mixed character, however, does complicate the use of some of the

most efficient numerical means of solving boundary value problems. Second, we must define what we mean by "standing-wave boundary conditions." Unlike outgoing and ingoing conditions, there is no simple local condition corresponding to what we will mean by standing waves in a nonlinear problem. We will present two fundamentally different candidates for the standing-wave condition, and here will present results of computations with one those of those two choices. (The alternative choice of standing-wave condition is best implemented with a special numerical method, and will be presented elsewhere [20].)

Stepping back from such details, one may be led to ask more fundamental questions about the whole approach. Such questions arise especially because the PSW spacetime we compute has some awkward features. Since the exact PSW solution contains an infinite amount of gravitational wave radiation, it cannot be expected to be meet the asymptotic flatness conditions of the theorems about the fall-off of fields. But the spacetime *is* asymptotically flat in that the spacetime curvature decreases with increasing distance from the binary source. Another sign that the PSW spacetime has rough edges is that it must not have regular null infinities; Gibbons and Stewart [21] have shown that spacetimes with well-behaved Scri+ and Scri– cannot be periodic.

It is useful, before diving into details, to clarify what the relationship is between the slightly singular spacetime we will be computing, and the physical problem that really interests us. To make this connection we can think of the binary system going through several orbits at almost constant radius. A weak wave zone exists at some distance from the orbit during this epoch of the motion. The stippled region in Fig. 2.1 shows the relevant region as part of the larger physical spacetime. In this limited region the source motion and the fields are almost periodic, and it is in this region only that we hope to approximate the physical fields by the outgoing fields extracted from the computed PSW solution. The imperfect asymptotic structure of the PSW spacetime is therefore irrelevant to its physical usefulness.

In the remainder of this paper we will first present, in Sec. 2.2, the mathematical details of a nonlinear model with which we clarify many aspects of the PSW approximation. We then discuss, in Sec. 2.3, the numerical methods needed to find PSW solutions, especially those aspects of the numerical methods that are idiosyncratic to the special features (mixed character, standing-wave boundary conditions, nonlinearities) of our problem. In this section also, results are presented of the numerical methods. The results are discussed, and put into the context of the next steps in this project [20], in Sec. 2.4.

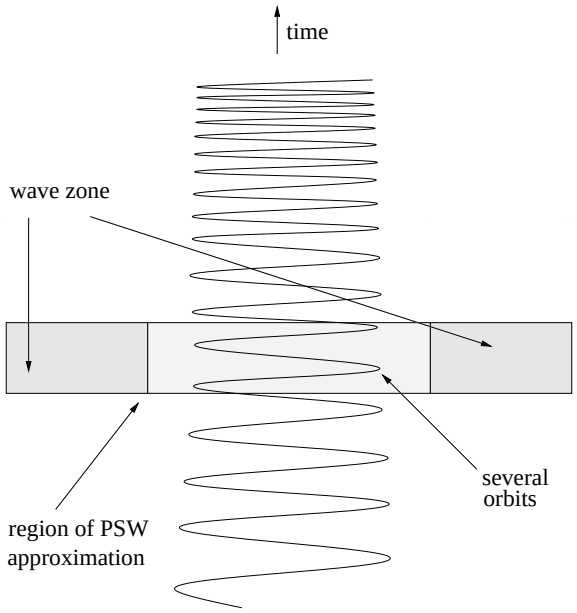

Figure 2.1: The PSW solution is meant to be an approximation to the physical spacetime only in a limited region.

2.2 Periodic solutions, standing waves, and model problems

Mixed PDEs and well-posedness

As stated above, we seek a solution to Einstein's equations in which the sources and the fields rotate rigidly. The mathematical statement of this rigid rotation is that there is a helical Killing vector, a Killing vector that is timelike close to the sources and spacelike far from the sources. (For more on helical Killing symmetry see [22].) For fields in flat spacetime our Killing vector $\vec{\xi}$ takes the form

$$\vec{\xi} = \partial_t + \Omega\partial_\phi \tag{2.1}$$

in spherical or cylindrical spatial coordinates, and

$$\vec{\xi} = \partial_t + \Omega\left(x\partial_y - y\partial_x\right) \tag{2.2}$$

in Cartesian spatial coordinates. The parameter Ω, which must be a constant, can be thought of as the rotation rate of the source and fields with respect to an inertial reference frame. For the flat spacetime case, the null surface $\vec{\xi}\cdot\vec{\xi} = 0$ is a cylinder of radius $1/\Omega$ coaxial with the rotation axis. (Here and below we use units in which $G = c = 1$.) This cylinder separates the inner region of timelike $\vec{\xi}$ from the outer region of spacelike $\vec{\xi}$, as shown in Fig. 2.2. Since this surface, in a sense, represents the points at which the rigidly rotating fields are moving at c, we call this surface the

"light cylinder," in analogy with pulsar electrodynamics.

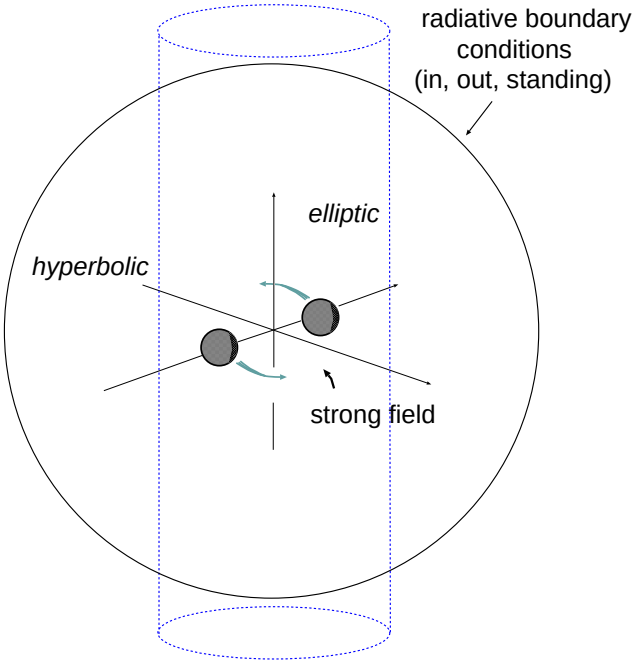

Figure 2.2: The "light cylinder" separating the elliptic and hyperbolic regions of the problem intersects the large spherical surface on which numerical boundary conditions are imposed.

One immediate advantage of the helical symmetry is that it reduces the number of independent variables, thereby greatly reducing the computational difficulty of a problem. In our simple flat spacetime models this reduction is most easily understood by the fact that helically symmetric scalars cannot depend in an arbitrary way on the spherical Minkowski coordinates t, r, θ, ϕ but can depend only on t and ϕ in the combination $\varphi \equiv \phi - \Omega t$. Thus, in the t, r, θ, φ system the Killing vector is $\vec{\xi} = \partial_t$. These ideas are clarified with a simple flat spacetime model theory for a scalar field Ψ

$$\Psi_{;\alpha;\beta} g^{\alpha\beta} + \lambda F = S \; . \tag{2.3}$$

The term $F(\Psi, x^\alpha)$ is included to allow for nonlinearity; the constant λ adjusts the strength of the nonlinearity. In order for a helically symmetric solution Ψ to exist, the explicit coordinate dependence of F must be compatible with the symmetry. That is, F can have explicit coordinate dependence only on r, θ, and φ. The most natural choice for a model would be one in which there is no coordinate dependence, one in which the background spacetime is featureless. We include the possibility of spatial dependence for convenience below. Changing the spatial dependence will help to clarify the accuracy of the PSW approximation when nonlinearities are important.

In the application of the PSW method to holes, an inner boundary condition will be used at a small, approximately spherical surface. For simplicity here, however, we use an explicit source

term,

$$S = \frac{\delta(r-a)}{a^2}\,\delta(\theta-\pi/2)\left[\delta(\varphi)+\delta(\varphi-\pi)\right]\,, \tag{2.4}$$

representing two points, each of unit scalar charge, in equatorial circular orbits, with radius a and angular velocity Ω. This source term S obeys the symmetry property that is necessary if a periodic solution is to exist: its Lie derivative vanishes along the Killing orbit $\vec{\xi}$.

If we are interested only in helically symmetric solutions, then the field equation (2.3) reduces to

$$\frac{1}{r^2}\frac{\partial}{\partial r}\left(r^2\frac{\partial\Psi}{\partial r}\right)+\frac{1}{r^2\sin\theta}\frac{\partial}{\partial\theta}\left(\sin\theta\frac{\partial\Psi}{\partial\theta}\right)+\left[\frac{1}{r^2\sin^2\theta}-\Omega^2\right]\frac{\partial^2\Psi}{\partial\varphi^2}+\lambda F(\Psi,r,\theta,\varphi)=S(r,\theta,\varphi)\,. \tag{2.5}$$

The mixed character of this PDE shows clearly in the coefficient of $\partial_\varphi^2\Phi$. The light cylinder is at $r\sin\theta = 1/\Omega$ where this coefficient changes sign. Inside the light cylinder ($r\sin\theta < 1/\Omega$) the equation is elliptical; outside it is hyperbolic. For outgoing solutions of this equation we impose an outer boundary condition $\partial_r\Psi = -\partial_t\Psi$, or equivalently $\partial_r\Psi = \Omega\partial_\varphi\Psi$, on a spherical surface with a radius large compared to $1/\Omega$. As illustrated in Fig. 2.2, this spherical surface is well outside the light cylinder in the equatorial plane, so our boundary conditions are imposed on a surface that passes through both the elliptic and hyperbolic regions of the problem.

Problems with boundary conditions on closed surfaces are common in the case of elliptical PDEs. We argue here that our boundary value problem with mixed PDEs may be unusual, but is well posed [23]. Again, a simple model problem will help to clarify issues. We set the nonlinearity parameter λ to zero in Eq. (2.5) so that we can solve the resulting linear equation as an infinite series. If we choose a Dirichlet condition

$$\Psi|_{r=r_{\max}} = 0\,, \tag{2.6}$$

at a finite radius $r_{\max}$, then the solution to this linear problem can be written in terms of spherical Bessel functions j_ℓ, n_ℓ as

$$\Psi = \sum_\ell \sum_{m=\text{even}} \frac{2m\Omega Y^*_{\ell m}(\pi/2,0)Y_{\ell m}(\theta,\varphi)}{j_\ell(m\Omega r_{\max})} j_\ell(m\Omega r_<)\left[n_\ell(m\Omega r_>)j_\ell(m\Omega r_{\max})-n_\ell(m\Omega r_{\max})j_\ell(m\Omega r_>)\right]\,. \tag{2.7}$$

Here $r_<(r_>)$ indicates the smaller (greater) of the quantities r, a. Vanishing of the $j_\ell(m\Omega r_{\max})$ denominator means that the the "cavity" $r \le r_{\max}$ has a resonant mode at frequency Ω. In the case that $r_{\max}$ has one of the resonant values, the solution to the boundary value problem is not unique. Such values of r are of zero measure, but are dense in the set of all r choices. This means that the cavity is always arbitrarily close to a resonance, if sufficiently high angular modes are computed. A consequence of this is that a numerical computation does not converge. (Computed solutions de-

pend on the computational grid size, and become larger with increasing angular resolution.) The difficulty is not just one of computational practice. The boundary value problem is fundamentally ill posed as a representation of fields in an infinite space. There is no meaningful $r_{\max} \to \infty$ limit of Eq. (2.7).

Problems with mixed elliptic and hyperbolic regions are of some interest in aerodynamics [24], but there are few general results on well-posedness. In those results that do exist, the nature of the boundary conditions plays a pivotal role. We have found that this applies to our periodic solutions also. If we replace the Dirichlet conditions of Eq. (2.7) with the Sommerfeld condition

$$(\partial_r \Psi - \Omega \partial_\varphi \Psi)_{r=r_{\max}} = 0\,, \tag{2.8}$$

then the problem is found to be well posed. This is particularly clear for the linear problem, where the closed form solution takes the form

$$\Psi = \Psi_{\rm out} + \Psi_{\rm extra}\,. \tag{2.9}$$

Here $\Psi_{\rm out}$ is the usual "outgoing at infinity" solution

$$\Psi_{\rm out} = \sum_\ell \sum_{m={\rm even}} -2im\Omega Y^*_{\ell m}(\pi/2,0) Y_{\ell m}(\theta,\varphi) j_\ell(m\Omega r_<) h^{(1)}_\ell(m\Omega r_>) \tag{2.10}$$

and

$$\Psi_{\rm extra} \equiv \sum_\ell \sum_{m={\rm even}} -2im\Omega Y^*_{\ell m}(\pi/2,0) Y_{\ell m}(\theta,\varphi)\ \gamma_{\ell m}\ j_\ell(m\Omega r_<) j_\ell(m\Omega r_>) \tag{2.11}$$

with

$$\gamma_{\ell m} \equiv -\left(\frac{h^{(1)}_\ell(z) + i\, dh^{(1)}_\ell(z)/dz}{j_\ell(z) + i\, dj_\ell(z)/dz} \right)_{z=m\Omega r_{\max}}\,. \tag{2.12}$$

Since the spherical Hankel function has the asymptotic form $h^{(1)}_\ell(z) = (-i)^{(\ell+1)} e^{iz}[1/z + \mathcal{O}(1/z^2)]$, it follows that $|\gamma_{\ell m}|$ is of order $1/r_{\max}$. Thus, $\Psi \to \Psi_{\rm out}$, as $r_{\max} \to \infty$, suggesting that the linear problem is well posed [25].

Numerical results confirm this suggestion. With the boundary condition in Eq. (2.8), we have encountered no fundamental difficulty computing convergent solutions to both the linear and non-linear versions of Eq. (2.5), and have confirmed that solutions do not depend on the particular (large) value chosen for $r_{\max}$.

Standing waves: iterative method

The solutions we will be computing in Einstein's theory, of course, are standing-wave solutions, but there are no actual "standing-wave boundary conditions" analogous to the Sommerfeld condition

in Eq. (2.8) for outgoing waves. It is useful, therefore, to explore the meaning of standing-wave solutions with our model nonlinear theories. As pointed out in Sec. 2.1, our paradigm for standing waves is the LSIO of a linear theory, the linear superposition of half ingoing and half outgoing solutions. We shall extend this definition of standing wave to nonlinear theories in two ways. The first is an extension of the Green function method of [15], and is called there the TSGF (time symmetric Green function) method. For the problem in Eq. (2.3) this method starts by writing the field equation in the form

$$\mathcal{L}[\Psi](\Psi) = \sigma_{\rm eff}[\Psi]\,. \tag{2.13}$$

Here the operator $\mathcal{L}[\Psi]$ depends on Ψ but—once Ψ is fixed—can be considered to be linearly operating on Ψ. Similarly $\sigma_{\rm eff}$ depends on Ψ, but—once Ψ is fixed—is to be considered a fixed inhomogeneous term in the equation, an effective source term. There is no unique way of putting the field equation into the form of Eq. (2.13) for a nonlinear model problem, or for general relativity. The quasi-linearity of general relativity, and of our nonlinear models, means that at least the principal part of $\mathcal{L}$ is always unambiguous. There are also some obvious guidelines to follow. In particular, $\mathcal{L}$ and $\sigma_{\rm eff}$ should become Ψ-independent in the weak field limit.

To iterate for an outgoing solution, for example, one would find an approximate outgoing solution $\Psi^n_{\rm out}$, and then would solve

$$\mathcal{L}[\Psi^n_{\rm out}](\Psi^{n+1}_{\rm out}) = \sigma_{\rm eff}[\Psi^n_{\rm out}]\,, \tag{2.14}$$

for outgoing boundary conditions. The result would be the improved approximation $\Psi^{n+1}_{\rm out}$ to the outgoing waves. To find standing waves, this method is modified as follows. An approximation $\Psi^n_{\rm stnd}$ is found to the standing-wave solution. The equation

$$\mathcal{L}[\Psi^n_{\rm stnd}](\Psi^{n+1}) = \sigma_{\rm eff}[\Psi^n_{\rm stnd}]\,, \tag{2.15}$$

is then solved with the outgoing boundary conditions of Eq. (2.8) to give $\Psi^{n+1}_{\rm stout}$ and is next solved with ingoing boundary conditions $\Omega \to -\Omega$ in Eq. (2.8)] to give $\Psi^{n+1}_{\rm stin}$. The new approximation for the standing-wave solution is taken to be

$$\Psi^{n+1}_{\rm stnd} = \tfrac{1}{2}\,\Psi^{n+1}_{\rm stout} + \tfrac{1}{2}\,\Psi^{n+1}_{\rm stin}\ . \tag{2.16}$$

We take the $n \to \infty$ limit of $\Psi^{n+1}_{\rm stnd}$ in Eq. (2.16) to be our computed standing-wave solution.

We shall call the iterative method just described "direct iteration." This sort of direct iteration is useful in solving for the root of an equation $x = f(x)$ only if f is slowly varying. In iteration for Ψ the equivalent condition applies to $\mathcal{L}^{-1} \circ \sigma_{\rm eff}$, where $\mathcal{L}^{-1}$ is the Green function, the inverse of $\mathcal{L}$

for the boundary conditions (ingoing or outgoing) of interest. For direct iteration to converge the dependence of $\mathcal{L}^{-1} \circ \sigma_{\rm eff}$ on Ψ must be weak and this is the case only for nonlinearities of moderate strength. For strong nonlinearities another technique must be used.

In Newton-Raphson iteration, one uses the iteration Ψ^n to make linear approximations for $\mathcal{L}$ and $\sigma_{\rm eff}$. Equation (2.13) then takes the form

$$\mathcal{L}[\Psi^n](\Psi) + (\Psi - \Psi^n) \times \left[\frac{\partial \mathcal{L}[\Psi]}{\partial \Psi}\right]_{\Psi=\Psi^n} (\Psi^n) = \sigma_{\rm eff}[\Psi^n] + (\Psi - \Psi^n) \times \left[\frac{\partial \sigma_{\rm eff}}{\partial \Psi}\right]_{\Psi=\Psi^n} . \qquad (2.17)$$

This equation is linear in Ψ, and its solution is taken to be the next iteration Ψ^{n+1}. By choosing appropriate boundary conditions we can use this scheme to iterate an outgoing or ingoing solution. For our standing-wave solution, we follow the same general scheme as with direct iteration. Using the $n^{\rm th}$ standing-wave approximation as Ψ^n in Eq. (2.17) we solve using both in- and outgoing boundary conditions. As in Eq. (2.16), the $n+1^{\rm th}$ standing-wave approximation is taken to be half the sum of the ingoing and outgoing solutions found this way.

Standing waves: minimization method

To explain our second, independent way of defining and computing standing-wave solutions, it is best to start with the standing-wave solution in the linear model problem. This is simply half the sum of the "outgoing at infinity" solution in Eq. (2.10), and the equivalent ingoing solution. The result is

$$\Psi_{\rm stnd} = \sum_\ell \sum_{m={\rm even}} 2m\Omega Y^*_{\ell m}(\pi/2, 0) Y_{\ell m}(\theta, \varphi) j_\ell(m\Omega r_<) n_\ell(m\Omega r_>) \, . \qquad (2.18)$$

In this solution each multipole has an equal amplitude for ingoing and outgoing amplitude waves, and one might suspect that this property suffices to define standing waves for a nonlinear model. This is not, in fact the case, since we could add a multiple of the homogeneous solution $j_\ell(m\Omega r) j_\ell(m\Omega a)$ to the ℓ, m mode without changing the balance between ingoing and outgoing. This degree of freedom is equivalent to the degree of freedom inherent in the phase between the outgoing and ingoing waves. This extra degree of freedom exists also (though not so transparently) in a nonlinear problem.

To resolve this degree of freedom we can use a generalization of a property that is unique, in the linear case, to the correct standing-wave solution Eq. (2.18): In each multipole, the solution is required to have the minimum wave amplitude of any solution with balanced ingoing and outgoing waves [26].

This method, while very interesting in principle, is difficult in practice to implement in a finite difference boundary value approach. One could imagine using a guess for the value of a multipole coefficient at some outer boundary, and then searching for the value that gives the minimum for

the amplitudes of the waves in that multipole. In a nonlinear problem, the values of each multipole will influence other multipoles, so the search for minimum waves will, in principle, be a search in a many dimensional space.

The real difficulty of this numerical approach is that it uses multipoles as part of the boundary condition. That means that multipole coefficients must be extracted. Even in spherical coordinates, the extraction of the multipole coefficients involves a weighted sum over all angular grid points. Most important, this sum would not be performed as a postprocessing step on a computed solution, but rather would have to be written as a set of equations that would form part of the *a priori* problem to be solved. The set of equations to be solved would then have, in addition to great complexity, a boundary-related subset connecting distant grid points. The matrix representation of these equations would not have banded structure. In addition to these technical difficulties, the use of spherical coordinates is very ill suited to the structure of our source objects, so coordinate patches for the sources would be required.

For these reasons, we have not attempted to use the minimization criterion in a finite difference code. We have, however, implemented this criterion with a spectral approach based on a specially adapted coordinate system. Results from this approach are extremely encouraging, but the approach poses new computational challenges, so we are continuing to explore two distinct paths: finite difference methods and the iterative definition of standing waves, and a spectral/adapted coordinate technique for the minimization criterion. Since the adapted coordinate system necessary for the second approach requires a separate development, and is not fundamental to the PSW approximation, we confine the present discussion to the first approach, finite difference boundary value problems, with the iterative criterion for standing waves.

2.3 Numerical implementation and results

Extraction of an outgoing approximation

Model problems allow us to test a key idea of the PSW approach, that a good approximation of the outgoing solution can be extracted from the computed standing-wave solution

$$\Psi_{\rm stndcomp} = \sum_{\text{even } \ell} \sum_{m=0,\pm 2,\pm 4..} \alpha_{\ell m}(r) Y_{\ell m}(\theta,\varphi)\,. \tag{2.19}$$

The coefficients $\alpha_{\ell m}(r)$ are computed from $\Psi_{\rm comp}$, by projection with $Y^*_{\ell m}$. From the reality of $\Psi_{\rm stndcomp}$, the coefficients will obey $\alpha^*_{\ell m} = \alpha_{\ell -m}$, and from the standing-wave symmetry ($\cos m\varphi$ only, no $\sin m\varphi$ terms) they will also obey $\alpha_{\ell m} = \alpha_{\ell -m}$.

This form of the computed standing-wave solution is compared with a general homogeneous

linear ($\lambda = 0$) standing-wave (equal magnitude in- and outgoing waves) solution of Eq. (2.5), with the symmetry of two equal and opposite sources:

$$\Psi_{\rm stndlin} = \sum_{\text{even } \ell} \sum_{m=0,\pm2,\pm4..} Y_{\ell m}(\theta,\varphi)\, \left[\tfrac{1}{2}\, C_{\ell m} h_\ell^{(1)}(m\Omega r) + \tfrac{1}{2}\, C^*_{\ell m} h_\ell^{(2)}(m\Omega r)\right] , \tag{2.20}$$

where $C_{\ell -m} = C^*_{\ell m}$, from the reality of $\Psi_{\rm stndlin}$. A fitting, in the weak-field zone, of this form of the standing-wave multipole to the computed function $\alpha_{\ell m}(r)$ gives the value of $C_{\ell m}$.

By viewing the linear solution as half-ingoing and half-outgoing we define the extracted outgoing solution to be

$$\Psi_{\rm exout} = \sum_{\text{even } \ell} \sum_{m=0,\pm2,\pm4..} Y_{\ell m}(\theta,\varphi)\, C_{\ell m} h_\ell^{(1)}(m\Omega r) \, . \tag{2.21}$$

Since this extracted solution was fitted to the computed solution assuming only that linearity applied, it will be a good approximation except in the strong-field region. In the problems of interest, the strong fields should be confined to a region near the sources. In those regions, small compared to a wavelength, the field will essentially be that of a static source, and will be insensitive to the distant radiative boundary conditions. As pointed out in Sec. 2.1, the solutions in this region will be essentially the same for the ingoing, outgoing, and standing-wave problem. In this inner region then, we take our extracted outgoing solution simply to be the computed standing-wave solution, so that

$$\Psi_{\rm exout} = \begin{cases} \sum Y_{\ell m} C_{\ell m} h_\ell^{(1)} & \text{weak field outer region} \\ \Psi_{\rm stndcomp} & \text{strong field inner region} \end{cases} . \tag{2.22}$$

The boundary between a strong field inner region and weak field outer region would ideally be a closed surface surrounding each of the source regions. This is easily implemented with the adapted coordinates to be introduced in a subsequent paper. Here, for simplicity, we take the boundary to be a spherical surface around the origin. In order for the extracted solution to be smooth at this boundary, we use a blending of the inner and outer solution in a transition region extending between radii $r_{\rm low}$ and $r_{\rm high}$ and, in this region, we take

$$\Psi_{\rm exout} = \beta(r) \, \sum Y_{\ell m} C_{\ell m} h_\ell^{(1)} + [1 - \beta(r)] \, \Psi_{\rm stndcomp} \, . \tag{2.23}$$

Here

$$\beta(r) \equiv 3 \left[\frac{r - r_{\rm low}}{r_{\rm high} - r_{\rm low}}\right]^2 - 2 \left[\frac{r - r_{\rm low}}{r_{\rm high} - r_{\rm low}}\right]^3 , \tag{2.24}$$

so that $\beta(r)$ goes from 0 at $r = r_{\rm low}$ to unity at $r = r_{\rm high}$ and has a vanishing r-derivative at both ends.

In the case of our typical choice $\Omega = 0.3$, the value of $r_{\rm low}$ is chosen to be $r = 1.3\, a$—the value at which the static and standing-wave solutions of the linear problem differ by 10%. This value

should decrease with increasing Ω, but it must be larger than the orbital radius $r = a$, so we choose it to be

$$r_{\rm low} = a[1 + 0.3(0.3/\Omega)]\,. \tag{2.25}$$

In order to have a moderately thin transition region we somewhat arbitrarily take

$$r_{\rm high} = a[1 + 0.6(0.3/\Omega)]\,. \tag{2.26}$$

For the numerical results reported below, the extraction details of Eqs. (2.19)–(2.26) are used, and extraction is carried out using the $\ell = 0, 2, 4$ multipoles.

Choice of model

To verify and demonstrate several innovative features (well-posed mixed boundary value problem, standing waves, effective linearity) of the PSW approximation, we use the nonlinear scalar model of Eq. (2.5), with the δ function sources given by Eq. (2.4). We make the simplifying assumption that the nonlinear function F in Eq. (2.5) depends only on Ψ, not on its derivatives. From this an obvious simplification follows for the iteration method of Eqs. (2.13)–(2.16). We replace Eq. (2.13) by

$$\mathcal{L}(\Psi) = \sigma_{\rm eff}[\Psi]\,. \tag{2.27}$$

with $\mathcal{L}$ taken to be

$$\mathcal{L} \equiv \frac{1}{r^2}\frac{\partial}{\partial r}\left(r^2\frac{\partial}{\partial r}\right) + \frac{1}{r^2\sin\theta}\frac{\partial}{\partial\theta}\left(\sin\theta\frac{\partial}{\partial\theta}\right) + \left[\frac{1}{r^2\sin^2\theta} - \Omega^2\right]\frac{\partial^2}{\partial\varphi^2}\,. \tag{2.28}$$

The effective source term includes both the true point source and the nonlinear term

$$\sigma_{\rm eff}[\Psi] = \frac{\delta(r-a)}{a^2}\delta(\theta - \pi/2)\left[\delta(\varphi) + \delta(\varphi - \pi)\right] - \lambda F\,. \tag{2.29}$$

Our choice of the nonlinearity function F is

$$F = \frac{\Psi^5}{\Psi_0^4 + \Psi^4}\,. \tag{2.30}$$

(We will comment below on the difference between this choice and that made in previous work, including previous versions of this paper.) Here Ψ_0 is a second nonlinearity parameter (λ being the first). We shall choose Ψ_0 to be less than unity; in the numerical results to be presented, Ψ_0 is taken to be 0.15.

To understand the effect of this nonlinearity, let R denote the distance from one of the point sources. Very near a source point, at very small R, where the field is strong, F has the limit $F \to \Psi$,

so that the solution of Eqs. (2.27)–(2.30) approximately has the Yukawa form

$$\Psi \approx \frac{e^{-\sqrt{-\lambda}\,R}}{4\pi R} \qquad \text{near source pt}\,. \tag{2.31}$$

At some distance from the source—call it $R_{\rm lin}$—the field Ψ becomes smaller than Ψ_0, and F can be approximated as Ψ^5. Since Ψ itself is less than Ψ_0, and hence less than unity, this Ψ^5 nonlinearity is small enough to be considered a perturbative correction.

If the transition at $R_{\rm lin}$ takes place well inside the near zone of the problem, then the effect of the nonlinearity can be understood as follows: Near a source point the solution has the form of a unit strength Yukawa potential. At distance $R_{\rm lin}$ the effect of the λF term is turned off and the solution becomes a simple Coulomb potential. The source strength for this Coulomb field, though, will be less than unity. Due to the $\exp\left(-\sqrt{-\lambda}R\right)$ Yukawa factor, the source strength decreases in the region from $R = 0$ to $R = R_{\rm lin}$, and the effect of the nonlinearity is to reduce the effective source strength by a factor of order $\exp\left(-\sqrt{-\lambda}R_{\rm lin}\right)$. Since this transition takes place well within the near zone, it should be this *reduced* source strength that is responsible for generating radiation. The effect of the nonlinearity on radiation, then, will be the same reduction factor $\exp\left(-\sqrt{-\lambda}R_{\rm lin}\right)$, and we can easily estimate the size of this nonlinear effect. One estimate can be found by solving

$$\Psi \approx \frac{e^{-\sqrt{-\lambda}\,R_{\rm lin}}}{4\pi R_{\rm lin}} = \Psi_0 \tag{2.32}$$

for $R_{\rm lin}$, and using this value of $R_{\rm lin}$ in the expression $\exp\left(-\sqrt{-\lambda}R_{\rm lin}\right)$ for the reduction factor. Another estimate follows by solving the spherically symmetric static nonlinear problem for a unit strength source

$$\frac{1}{r^2}\frac{\partial}{\partial r}\left(r^2\frac{\partial\Psi}{\partial r}\right) + \lambda\,\frac{\Psi^5}{\Psi_0^4 + \Psi^4} = \delta^3(\vec{r})\,. \tag{2.33}$$

(Here the right hand side is the unit δ function at the origin.) For this solution the ratio is found of the large-r monopole moment to the small-r monopole moment, and this ratio is taken as the reduction factor. Since these methods for the reduction factor ignore the nonlinear interaction between the two source points, and since they assume that all the wave generation occurs far outside $R_{\rm lin}$, they can only be considered an approximation for the nonlinear reduction effect on the wave amplitude. We shall see, however, that these estimates are accurate enough to be taken as a good heuristic explanation of the role of the nonlinearity.

In previous work, a form of the nonlinearity was used that was different from that in Eq. (2.30). To give that previous form we first defined the distance R_+ (R_-) from the source point on the x axis at $x = a$ ($x = -a$) to be given by

$$R_\pm^2 = (r\sin\theta\cos\varphi \mp a)^2 + r^2\sin^2\theta\cos^2\varphi + r^2\cos^2\theta\,. \tag{2.34}$$

We then introduced the distance variable

$$\chi \equiv \sqrt{R_+ R_-}\ . \tag{2.35}$$

At either of the source points $\chi \to 0$, and far from the sources $\chi \to r$. In terms of χ, the form of the nonlinearity previously used [27] is

$$F_{\rm prev} = \left(\frac{\chi}{na}\right)^n e^{(n-\chi/a)}\ \frac{\Psi^3}{1+\Psi^2}\,. \tag{2.36}$$

The χ-dependent prefactor $(\chi/na)^n e^{(n-\chi/a)}$ was included so that we could force the nonlinearity to be concentrated near $\chi = na$. By choosing n to be 5 or 10 we could, in this way, have strong nonlinearity in the wave zone, and we could numerically demonstrate the failure of effective nonlinearity. The χ-dependent prefactor, however, makes it difficult to find a numerical solution that is physically meaningful.

The prefactor is a difficulty because the solution near the source can have either the Yukawa form $\exp\left(-\sqrt{-\lambda}R\right)$, or the "anti-Yukawa" form $\exp\left(+\sqrt{-\lambda}R\right)$. If there is any of the latter included in the solution, then the field gets larger at larger distance from the sources, so the strong nonlinearity is never suppressed, the λF term continues to approximate $\lambda\Psi$, and the sum of the Yukawa and anti-Yukawa forms continues to be a valid solution. But if the anti-Yukawa part is present, the solution cannot meet the fall-off conditions at an outer boundary at large r. Without the prefactor, then, the outer boundary conditions act to suppress the anti-Yukawa part of a solution. With the prefactor present, however, the nonlinearity can be turned off by the fall off of $\exp\left(-\chi/a\right)$, even if the solution contains an anti-Yukawa part close to the sources. The prefactor, in effect, shields the inner region from the influence of the outer boundary conditions. When the prefactor is included in the nonlinearity, the solution in the inner region will be a somewhat unpredictable mixture of Yukawa and anti-Yukawa parts that is sensitive to grid spacing.

The choice made for the Ψ dependence in Eq. (2.30), rather than that in Eq. (2.36), is motivated by the fact that $F \sim \Psi^3$ falls off rather slowly in the weak wave zone. Changing the form of F to $\Psi^5/(1+\Psi^4)$ cures this slow fall off, but imposes a very sharp cutoff near the sources, one that is too sharp for our relatively coarse computational grid. By taking F proportional to $\Psi^5/(\Psi_0^4+\Psi^4)$, with a fairly small value of Ψ_0, the falloff of F is smoothed out and moved to a larger distances from the source.

Numerical methods

Since $\mathcal{L}$ is independent of Ψ we can (as in [15]) compute once and for all the inverses of $\mathcal{L}$, i.e., the Green functions corresponding to specific boundary conditions. In this way, we can compute

$\mathcal{L}_{\rm out}^{-1}$ and $\mathcal{L}_{\rm in}^{-1}$, the Green functions for outgoing and for ingoing boundary conditions. The direct iterative method of Eqs. (2.14)–(2.15), then amounts to

$$\Psi_{\rm out}^{n+1} = \mathcal{L}_{\rm out}^{-1}\left(\sigma_{\rm eff}[\Psi_{\rm out}^{n}]\right) \qquad\qquad \Psi_{\rm in}^{n+1} = \mathcal{L}_{\rm in}^{-1}\left(\sigma_{\rm eff}[\Psi_{\rm in}^{n}]\right) \tag{2.37}$$

$$\Psi_{\rm stnd}^{n+1} = \tfrac{1}{2}\left\{\mathcal{L}_{\rm out}^{-1} + \mathcal{L}_{\rm in}^{-1}\right\}\sigma_{\rm eff}[\Psi_{\rm stnd}^{n}]\,. \tag{2.38}$$

Since $\mathcal{L}$ has no Ψ dependence, the basic Newton-Raphson iteration simplifies to

$$\left\{\mathcal{L} - \left[\frac{\partial\sigma_{\rm eff}}{\partial\Psi}\right]_{\Psi=\Psi^n}\right\}\Psi = \sigma_{\rm eff}[\Psi^n] - \Psi^n\ \left[\frac{\partial\sigma_{\rm eff}}{\partial\Psi}\right]_{\Psi=\Psi^n}\,. \tag{2.39}$$

This Newton-Raphson approach can be applied to find outgoing, ingoing, and standing-wave solutions analogous to Eqs. (2.37) and (2.38).

Each iteration of Eqs. (2.37), (2.38), or (2.39) is equivalent to the solution of a large set of linear equations. Such systems are most typically encountered for elliptic boundary value problems, and are typically solved most efficiently with relaxation methods, or related methods (e.g., multigrid) based on the geometry of the problem. Such methods start with an approximate set of values for each of the unknowns at every point of the numerical grid. At each point the solution is then recalculated on the basis of the values at nearby grid points. This method sweeps through all the points of the grid and is iterated until an error criterion is met. Such a method must be compatible with the domain of dependence for the points of the grid. For an elliptic PDE, for example, the values of unknowns are updated at a central point of a set of grid points. For a hyperbolic PDE, on the other hand, the field computation, or updating, must be done only at a point in the "future" of those grid points being used. For a mixed boundary value problem a relaxation method has special difficulties, especially at the interface between elliptic and hyperbolic regions. Nevertheless, relaxation methods have been successfully applied to mixed PDEs in transonic aerodynamics, first by Murman and Cole [28]. The slow convergence of this method at the interface (the "sonic surface" in transonic aerodynamics) can be improved with special techniques that may need to be specific to the problem [29].

We are presently investigating relaxation and other numerical methods (e.g., decomposing the grid into regions and applying different techniques, preconditioners, etc.) for large grids and many variables. For our three-dimensional scalar problem illustrated here, however, we have been able to use a more-or-less straightforward method of inverting the matrix for the finite difference equations.

In one approach to finding an iterative solution, we use matrix inversion at each step of the direct iteration of Eqs. (2.37), (2.38), and we take advantage of the fact that $\mathcal{L}^{-1}$ is rotationally symmetric (i.e., it is translationally symmetric with respect to φ), and we work with the Fourier

components $\Psi^n_m(r,\theta)e^{im\varphi}$ of the iterative solution. At each step of iteration we project out the Fourier components of the effective source. Due to the nonlinearity in the effective source, the Fourier modes of $\Psi^n_m(r,\theta)e^{im\varphi}$ mix in this step, but $\mathcal{L}^{-1}$ is rotationally symmetric so the Fourier modes do not mix in the step of solving for Ψ^{n+1}. This method takes advantage of the efficiency of a fast Fourier transform (FFT) and reduces the RAM needed to little more than that for a two-dimensional r,θ grid. This method, therefore, allows a rather fine grid in r and θ.

We have used this efficient FFT method extensively, but direct iteration has the drawback already cited following Eq. (2.16): it is limited in the strength of the nonlinearity it can handle. Direct iteration will not converge for very strong nonlinearity. The iterative Newton-Raphson method of Eq. (2.39), on the other hand, does almost always converge once one has a solution sufficiently close to the correct solution. The operator on the left in Eq. (2.39), however, contains the previous iteration Ψ^n, which is not symmetric in φ, so that the FFT method cannot be used with Newton-Raphson iteration. This has meant that a relatively coarse grid, or large RAM, had to be used. We have not yet implemented a parallelizable method for solving the iteration steps, and have been restricting most runs to 8 GB.

It is worth mentioning an interesting hybrid method that we have explored. The problem in Eqs. (2.27)–(2.30), outside the point sources, can be written as

$$(\mathcal{L}+\lambda)\,\Psi = \lambda\Psi_0^5\,\frac{\Psi}{\Psi_0^4+\Psi^4}\,. \tag{2.40}$$

The nonlinearity on the right is never large; it is small both for $\Psi > \Psi_0$ near the sources, and for $\Psi < \Psi_0$ far from the sources. The weakness of the formal nonlinearity suggests that a solution may converge with direct iteration even for large nonlinear effects. The operator $(\mathcal{L}+\lambda)$, furthermore, is rotationally symmetric, so the FFT method can be used. The method, however, turns out to have a serious flaw. Where Ψ is small, the left-hand side of Eq. (2.40) is dominated by $\lambda\Psi$, which is very nearly equal to the right-hand side. In the analogy we gave, following Eq. (2.16), to the iterative solution for a root of $x = f(x)$, this is equivalent to f having a derivative very close to unity at the root. It would appear that this difficulty could be avoided by iterating Eq. (2.40) near the source, where the nonlinearity is strong, and iterating the standard form of the problem in the weak field region. Numerical experiments with this approach have been inconclusive. Since we do not intend to use a single-patch spherical coordinate sysem in the future, we have not examined this hybrid method exhaustively.

In practice we have used the following eclectic approach to find solutions: (i) For linear models, for which no iteration is required, we have taken advantage of the RAM-reduction of the FFT method. (ii) For strongly nonlinear models we have used Newton-Raphson iteration on a three-dimensional (non-FFT) grid, and have used continuation (i.e., "ramping up") both in λ and in Ω.

Despite RAM limitations, we have been able to confirm that the solutions are second-order convergent. (iii) For $-\lambda$ less than around 2, it has been been possible to find solutions with the direct-iteration, FFT method. These solutions have been compared with the corresponding solutions from the non-FFT, Newton-Raphson method, and have been found to agree within the numerical uncertainty in the solutions.

In applying the iteration methods, and looking for convergence, we have used two error measures. One, $\epsilon_{\rm iter} \equiv \Psi^n - \Psi^{n-1}$, is the difference at a grid point between the computed value at a grid point, and the value computed at the previous iteration. The second error measure, $\epsilon_{\rm soln}$ is the value of $(\mathcal{L}(\Psi^n) - \sigma_{\rm eff}[\Psi^n])$ at a grid point. In our FFT computations the criterion for convergence was to have the rms value of $\epsilon_{\rm iter}$ (averaged over the entire grid) fall below 1×10^{-6}. The value of $\epsilon_{\rm soln}$ was also monitored in the FFT computations and was found not to be larger than 1×10^{-6} at any grid point, and to have an rms value typically around 1×10^{-7}. A much more stringent requirement for convergence was used in the Newton-Raphson computations: the rms value of $\epsilon_{\rm soln}$ had to fall below 5×10^{-11} for the solution to be acceptable.

Numerical results

We first illustrate the fundamental concept of the PSW method with various solutions of Eq. (2.5), with the nonlinearity given in Eq. (2.30). Figure 2.3 shows solutions in the equatorial ($\theta = \pi/2$) plane; the amplitude of the field Ψ is plotted as a function of corotating Cartesian coordinates $x = r\cos\varphi$, and $y = r\sin\varphi$. The source points are on the x axis at $x = \pm a$, and the outer boundary is at $r = 30a$. For all four plots, $a\Omega = 0.3$, $\lambda = -1$, and $\Psi_0 = 0.15$. The results plotted are those from direct iteration with the FFT method, for a computational grid using 361 radial divisions, 16 divisions in θ, and 32 Fourier modes. For all models, the computed results are dominated by the monopole, so for clarity in the figures the φ-average of the solution has been subtracted at every radius. It is worth noting that this procedure not only removes the monopole (the $\ell = 0$ part of the solution), but also removes the $m = 0$ part of the quadrupole, etc.

The plot in part (a) of Fig. 2.3 shows the outgoing solution (solution for outgoing boundary conditions); the plot in part (b) shows the corresponding ingoing solution. The plot in part (c) is the computed standing-wave solution for the same problem parameters. (Note: this nonlinear standing-wave solution is *not* half the superposition of the outgoing and ingoing solutions. Rather, it is the nonlinear field equation solved with the standing-wave definition discussed in Sec. 2.2.) Part (d) shows the key idea of the PSW approximation, the outgoing solution extracted from the standing-wave solution, by the extraction method described in Eqs. (2.19)–(2.26). When the PSW method is used in general relativity, it will be possible only to compute the standing-wave solution; the extracted outgoing solution will represent the approximation to the physical, outgoing solution.

Table 2.1 gives quantitative results for strongly nonlinear outgoing waves. In that table, values

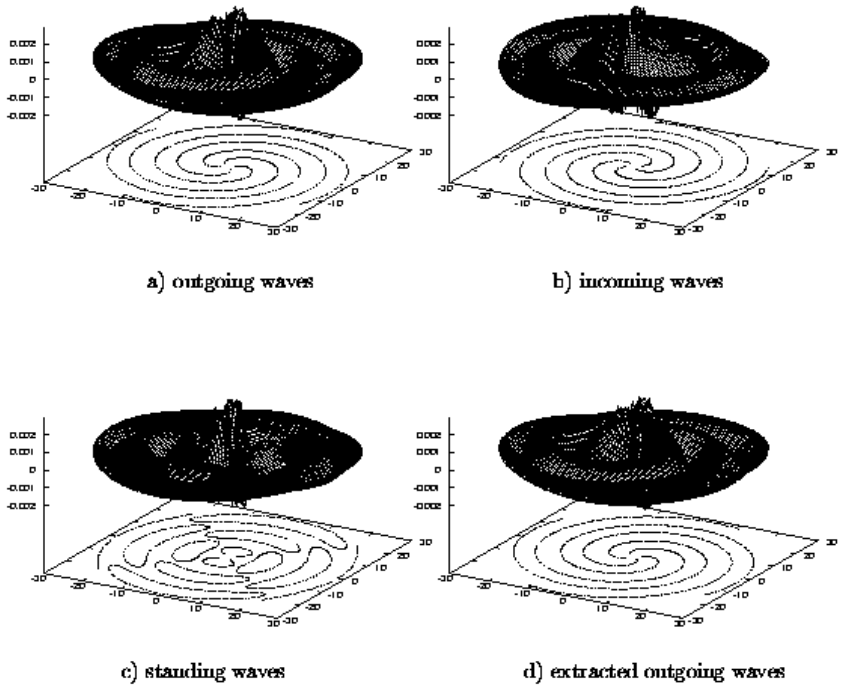

Figure 2.3: The Ψ field for two rotating point sources in the equatorial plane. The fields shown are nonlinear solutions of Eqs. (2.4), (2.5), and (2.30), with $a\Omega = 0.3$ and $\lambda = -1$. For clarity, the φ-average is removed at each radius. Parts (a) and (b) of the figure show, respectively, the nonlinear outgoing and ingoing solutions. Part (c) is the standing-wave solution, and part (d) is the outgoing solution extracted from it. The vertical scale gives field strength (arbitrary units) and the horizontal coordinates are co-rotating Cartesian coordinates in units of a, the distance of a source from the rotation axis.

are given for the reduction factor due to the nonlinearity. As explained following Eq. (2.31), this is the factor by which the nonlinearity decreases the amplitude of the waves. (For the same $a\Omega$ and source strength, the amplitude of outgoing waves for the linear problem $\lambda = 0$ is compared to the amplitude for a problem with $\lambda \neq 0$.) The fact that the reduction factors are significantly different from 100% shows that we are able to compute models in which nonlinear effects are strong. In the table the computed reduction is compared with estimates from heuristic models of Eqs. (2.31)–(2.33) in which Ψ is taken to have a Yukawa form very near the source, and a Coulomb form further out, but well within the near zone. The agreement of the computations with the estimates is strong evidence that the heuristic model captures much of the nature of the nonlinear effect.

Table 2.2 gives information on the numerical errors of the most computationally intensive so-

Table 2.1: The reduction factor for outgoing waves due to the nonlinearity. For all cases, $\Psi_0 = 0.15$. The second column refers to Eq. (2.32). This equation is solved for $R_{\rm lin}$. Estimate 1 uses this value of $R_{\rm lin}$ in $\exp(-\sqrt{-\lambda}R_{\rm lin})$. Estimate 2 is the reduction factor found from a numerical solution of Eq. (2.33). The last column gives the results from Newton-Raphson computation with $a\Omega = 0.3$, with the outer boundary at $r = 30a$, and with a r, θ, φ grid of $120 \times 20 \times 32$.

λ	Estimate 1	Estimate 2	Computation
-1	69%	87%	78%
-2	62%	73%	68%
-5	53%	65%	55%
-10	46%	54%	47%
-25	37%	41%	35%

Table 2.2: Convergence of finite difference computations. Nonlinear outgoing solutions are computed with five different grid resolutions for $\lambda = -10$, $\Psi_0 = 0.15$, $a\Omega = 0.3$, and outer boundary at $r = 30a$. An $L2$ norm is computed for the difference between the solution for grid k and grid $k+1$. This is reported as the "Error" for grid k.

k	$n_r \times n_r \times n_\varphi$	Error
1	90×10×16	2.71 E-5
2	120×14×22	1.60 E–5
3	150×16×26	8.68 E-6
4	180×20×32	5.22 E-6
5	210×24×38	

lution type: that for strongly nonlinear waves computed via Newton-Raphson iteration. A single physical model ($\lambda = -10$, $\Psi_0 = 0.15$, $a\Omega = 0.3$, outer boundary at $r = 30a$) is computed on five different grids. As a measure of the truncation error for grid k, the L2 difference (the square root of the average square difference) is found between the results for grid k and for grid $k + 1$. This is listed in Table 2.2 as the error in grid k. These results, especially for the finest three grids, suggest quadratic convergence of the numerical process.

The crux of the PSW method is that a good approximation to a nonlinear outgoing solution can be extracted from a standing wave nonlinear solution. Examples of this are given in the next two figures, the central numerical results in this paper.

Figure 2.4 shows results for computations of linear ($\lambda = 0$) and nonlinear ($\lambda = -2$ and -10) models for Ψ along the $\theta = \pi/2$, $\varphi = 0$ lines. All models used rotation rate $a\Omega = 0.3$ and nonlinearity parameter $\Psi_0 = 0.15$ and the $180 \times 20 \times 32$ grid with an outer boundary at $r = 30a$. The nonlinear models were solved through Newton-Raphson iteration with continuation in λ. The figure shows, as continuous lines, the computed solutions for outgoing waves with $\lambda = 0, -2, -10$. Included in the figure also are the $\lambda = -2, -10$ results for the approximate outgoing waves extracted from the nonlinear standing wave solutions by the method of Eq. (3.60). The difference between these outgoing approximations and the true outgoing waves is so small that the approximation results

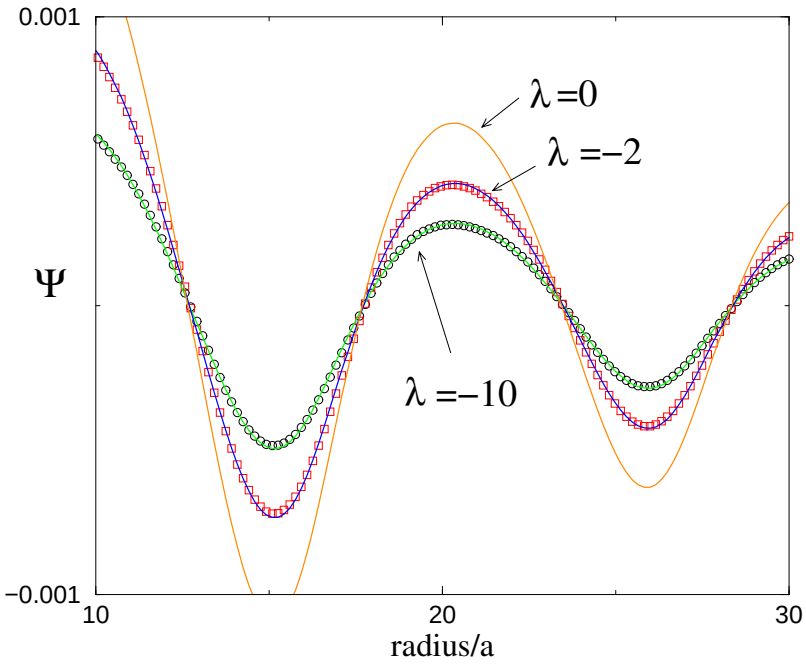

Figure 2.4: Extracted outgoing nonlinear waves vs. true outgoing nonlinear waves. For $\lambda = 0, -2, -10$, $\Psi_0 = 0.15$, $a\Omega = 0.3$, with a $180 \times 20 \times 32$ grid. The field Ψ is shown as a function of r along a radial line through the source point, i.e., along the $\theta = \pi/2$, $\varphi = 0$ line. Continuous curves show computational results for outgoing waves. Discrete points, for the nonlinear models, show the approximate outgoing waves extracted from standing wave solutions.

are given as discrete data points to aid in visualization.

Figure 2.5 shows the small-radius portions of the same models as those in Fig. 2.4. (The $\lambda = 0$ curve is nearly indistinguishable from that for $\lambda = -2$, and is omitted from the figure.) The radial $\theta = \pi/2, \varphi = 0$ line along which the results are presented, goes through the source point at $r = a$, so Fig. 2.5 shows the computed solution in the neighborhood of the source. The Yukawa-like effect of the nonlinearity near the source is evident in more rapid fall-off of the $\lambda = -10$ model away from the source point.

The results in Figs. 2.5 and 2.4 are graphical evidence for the accuracy of the PSW method; the outgoing waveforms extracted from the nonlinear standing wave solution are excellent approximations to the true outgoing waves both near the sources and in the wave zone. The agreement in the intermediate zone (not shown in the figures) is equally impressive. A quantitative measure of the agreement is the "L2" difference of the outgoing wave and the extracted outgoing approximation. This measure is the square root of the average (over all grid points) of the squared difference between the true and the extracted outgoing solutions. For $\lambda = -10$ this L2 difference is 8.7×10^{-6} and is of the same order as the error in Table 2.2 for the $180 \times 20 \times 32$ grid being used. Since the numerical uncertainties are of the same order as the difference between the true and the ex-

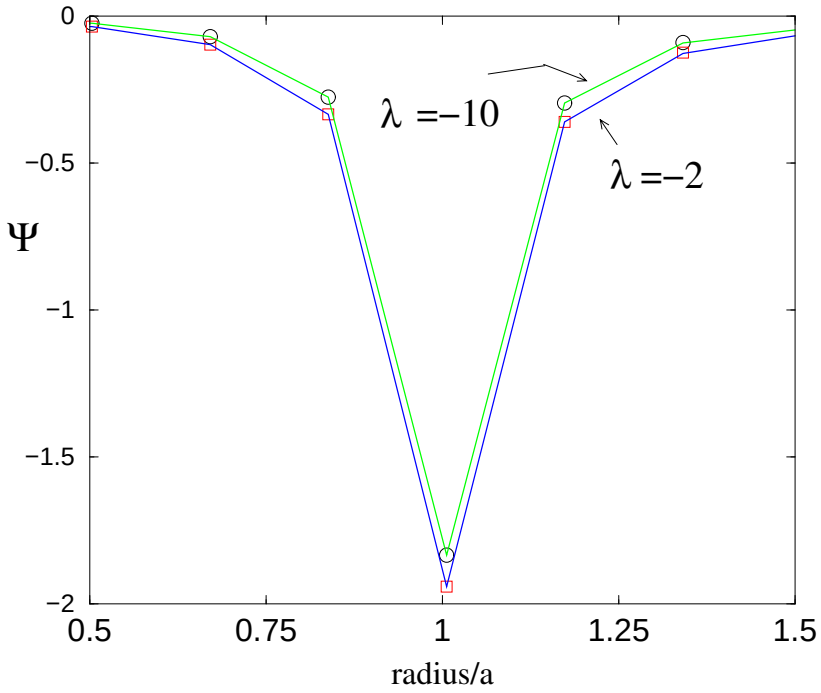

Figure 2.5: The same models as in Fig. 2.4, but in the region of the sources. As in Fig. 2.4 continuous curves show the computations of the true nonlinear outgoing waves, and discrete points show the outgoing wave approximation extracted from the nonlinear standing wave solution.

tracted outgoing waves we cannot claim to have computed *any* meaningful inaccuracy in the PSW approximation.

This is unfortunate. In presenting numerical results it would be useful to demonstrate that the PSW approximation is, after all, an approximation by showing a model in which the extracted outgoing solution is significantly different from the true outgoing solution. Our inability to do this is related to limitations on numerical solutions. Our arguments for effective linearity show that the PSW approximation should fail only if the region of significant nonlinearity overlaps the wave zone. For this reason we used the χ-dependent prefactor of Eq. (2.36) in an earlier version of the present paper to allow us to force the nonlinearity to be concentrated in the wave zone. Although that technique did allow us to induce significant errors in the PSW approximation, we have explained, following Eq. (2.36), why the solutions for the models with the prefactor have undesirable features. If no unnatural χ-dependence is explicitly injected in the source, the way in which effective nonlinearity can be made to fail is for $a\Omega$ to approach unity, i.e., for the source points to move very relativistically (a case in which the PSW would be expected to fail for binary inspiral). Unfortunately, we have not been able to find convergent solutions for large $a\Omega$. Presumably this is due to the fact that large $a\Omega$ means fields with sharp gradients, too sharp to be handled by our necessarily coarse grids.

2.4 Conclusions

We have given here the foundations of the PSW method based on the extraction of an outgoing solution from a computed standing-wave solution. We have also given the details of the extraction calculation.

The results provided for convergent nonlinear models are "proof" by example that there is no fundamental mathematical problem of well-posedness of the mixed PDE problem, with radiative boundary conditions on a sphere that is in both the elliptic and hyperbolic regions of the problem. We have, furthermore, presented limited numerical evidence for the validity of the PSW method, i.e., that the extracted outgoing solution is a good approximation to the true nonlinear outgoing solution. This evidence helps make the case for the application of the method to the general relativistic problem, in which only the standing-wave solution will be computable, and the extracted solution will be taken as the approximation to the physical problem.

The numerical studies have also taught a lesson about the limitations of the relatively straightforward numerical method used here, matrix inversion of the finite difference equations in spherical coordinates. We have found that this method is limited by the coarse grid that can be used for the finite-differencing. We could, in principle, use a software engineering approach to increase the range of nonlinearity and rotation rate that can be handled. But the methods used here, spherical coordinates and delta function sources, are meant only to provide a relatively simple context for establishing the foundations for more advanced approaches.

In a paper now in preparation [20], we will present an important step forward in dealing with PSW problems, a coordinate system that conforms to the geometry near the sources and far from the source asymptotically goes to spherical polar coordinates, the coordinates best suited to the description of the waves. One advantage of this method is that it allows us very simply to put in details of the sources as inner boundary conditions rather than point sources. In addition, the new coordinates turn out to be very well suited to a spectral method that has shown remarkable computational efficiency, but that poses new computational problems. Computations using an adapted coordinate system have already been carried out for the three-dimensional nonlinear scalar problem with both the finite difference and spectral formulation, and for linearized general relativity using the finite difference formulation. Since the details of adapted coordinates, especially with the unusual spectral method, are not directly related to the foundations of the PSW method, those details are appropriate to a separate paper.

A very different approach to better numerics is to use relaxation methods, already mentioned in Sec. 2.3. In view of the large number of uncertainties about their application, we have started on a basic study of relaxation methods in mixed PDE systems in PSW-type problems, but will continue to explore a number of different numerical approaches to the PSW problem.

2.5 Acknowledgements

We gratefully acknowledge the support of the National Science Foundation under grants PHY9734871 and PHY0244605. We also thank the University of Utah Research Foundation for support during this work. We thank Christopher Johnson and the Scientific Computing and Imaging Institute of the University of Utah for time on their supercomputers to produce the non-FFT results of Sec. 2.3. We have also made use of supercomputing facilities provided by funding from JPL Institutional Computing and Information Services and the NASA Offices of Earth Science, Aeronautics, and Space Science. We thank John Friedman and Kip Thorne for helpful discussions and suggestions about this work.

Bibliography

[1] G. Gonzalez. Gravitational wave detectors: A report from LIGO-land. In *Recent Developments in Gravity: Proceedings of the 10th Hellenic Relativity Conference*, K. D. Kokkotas and N. Stergioulas, Eds. World Scientific, Singapore, 2003; gr-qc/0303117

[2] F. Acernese et al., Class. Quant. Grav. **20**, 609, 2003.

[3] H. Lück et al., in *Gravitational Waves, Third Edoardo Amaldi Conference held in Pasadena, CA 12-16 July, 1999*, S. Meshkov, Ed., AIP Conference Proceedings, Vol. 523, AIP Press, New York, 2000, pp. 119–127.

[4] M. Ando. Current status of the TAMA300 interferometer, prepared for 2nd Workshop on Gravitational Wave Detection, Tokyo, Japan, 19-22 Oct 1999.

[5] E. Colbert and A. Ptak. Astrophys. J. Supp. **143**, 25, 2002.

[6] B. F. Schutz. In *Lighthouses of the Universe — The Most Luminous Celestial Objects and Their Use for Cosmology: Proceedings of the Mpa/Eso/Mpe/Usm Joint Astronomy Conference*, C. K. Chui, R. A. Siuniaev, and E. Churazov, Eds. Springer-Verlag, New York, 2002, pp. 207–224; gr-qc/0111095.

[7] See `http://lisa.jpl.nasa.gov`.

[8] M. A. Scheel et al., Phys. Rev. D **66**, 124005, 2002.

[9] H.-J. Yo, T. W. Baumgarte, and S. L. Shapiro. Phys. Rev. **D66**, 084026, 2002.

[10] J. Baker et al., Phys. Rev. D **65**, 124012, 2002.

[11] J. K. Blackburn and S. Detweiler. Phys. Rev. D **46**, 2318, 1992.

[12] S. Detweiler. Phys. Rev. D **50**, 4929, 1994.

[13] J. Friedman. private communication.

[14] C. W. Misner, K. S. Thorne and J. A. Wheeler. *Gravitation*. Freeman, San Francisco, 1973, Sec. 20.3.

[15] J. T. Whelan, W. Krivan, and R. H. Price. Class. Quant. Grav. **17**, 4895, 2000.

[16] R. H. Price. Class. Quant. Grav. **21**, S281-S293, 2004.

[17] A. Ashtekar et al., Phys. Rev. Lett. **85**, 3564, 2000.

[18] J. W. York, Jr.. Phys. Rev. Lett. **26**, 1656, 1971.

[19] J. W. York, Jr.. J. Math. Phys. **14**, 456, 1973.

[20] Z. Andrade et al., (in preparation).

[21] G. W. Gibbons and J. M. Stewart. In *Classical General Relativity*, W. B. Bonnor, J. N. Islam, and M. A. H. MacCallum, Eds. Cambridge University Press, Cambridge, 1983, pp. 77–94.

[22] J. L. Friedman, K. Uryu, and M. Shibata. Phys. Rev. D **65**, 064035, 2002.

[23] For $\lambda = 0$ the problem in Eq. (2.5) has been shown to be well posed for a range of source functions and boundary conditions; C. Torre. math-ph/0309008.

[24] C. Ferrari and F. G. Tricomi. *Transonic Aerodynamics*. Academic Press, New York, 1968; J. D. Cole and L. P. Cook. *Transonic Aerodynamics* North-Holland, Amsterdam, 1986.

[25] This is an expanded version of an argument given in the two-dimensional context in [15].

[26] J. T. Whelan, C. Beetle, W. Landry, and R. H. Price. Class. Quant. Grav. **19**, 1285, 2002.

[27] This form was used in early versions of the present paper, is described in [16], and is closely related to the nonlinearity used in [15].

[28] E. M. Murman and J. D. Cole, AIAA J. **9**, 114, 1971.

[29] D. Nixon. In *Computational methods and problems in aeronautical fluid dynamics*. B. L. Hewit, Ed. Academic Press, New York, 1976, pp. 290–326.

Chapter 3

The periodic standing-wave approximation: nonlinear scalar fields, adapted coordinates, and the eigenspectral method

Originally published as Phys.Rev. D71 (2005) 104017.

The periodic standing-wave (PSW) method for the binary inspiral of black holes and neutron stars computes exact numerical solutions for periodic standing wave spacetimes and then extracts approximate solutions of the physical problem, with outgoing waves. The method requires solution of a boundary value problem with a mixed (hyperbolic and elliptic) character. We present here a new numerical method for such problems, based on three innovations: (i) a coordinate system adapted to the geometry of the problem, (ii) an expansion in multipole moments of these coordinates and a filtering out of higher moments, and (iii) the replacement of the continuum multipole moments with their analogs for a discrete grid. We illustrate the efficiency and accuracy of this method with nonlinear scalar model problems. Finally, we take advantage of the ability of this method to handle highly nonlinear models to demonstrate that the outgoing approximations extracted from the standing wave solutions are highly accurate even in the presence of strong nonlinearities.

3.1 Introduction

3.1.1 Background

The detection and interpretation of gravitational wave signals from inspiralling black holes or neutron stars requires a solution of Einstein's equations for the late stages of the inspiral [1, 2, 3]. Much

effort is going into the development of computer codes that will evolve solutions forward in time. For recent progress see [4, 5, 6]. Such codes will eventually provide the needed answers about the strong field interaction and merger of the binary objects, but many technical challenges of such a computation slow the development of the needed codes. This has led us to propose, as a near-term alternative, the periodic standing-wave (PSW) approach. Elements of this approximation have been introduced elsewhere [7, 8, 9], but are most thoroughly presented in a recent paper [10] that we will hereafter refer to as "Paper I." In the PSW approach, a numerical solution is sought to Einstein's equations, not for a spacetime geometry evolved from initial data, but rather for sources and fields that rotate rigidly (i.e., with a helical Killing vector) and that are coupled to standing waves.

Paper I gives the details of how to extract from this solution an approximation to the problem of interest: a slowly inspiralling pair of objects coupled to outgoing waves. Paper I also describes the nature of the mathematical problem that must be solved numerically: a boundary-value problem with "standing wave boundary conditions" on a large sphere surrounding the sources. The differential equations of this boundary value problem are mixed, elliptical in one region (inside a "light cylinder") and hyperbolic in another (outside).

The method of solution in Paper I was straightforward. The differential equations and boundary conditions were implemented with a finite difference method (FDM) in a single patch of standard co-rotating spherical coordinates. The equations were solved with Newton-Raphson iteration of a sequence of linear approximations, and a straightforward inversion of each linear approximation. The relative simplicity of this approach was useful to demonstrate the basic well-posedness and solubility of the problem and to illustrate the important issues of the PSW method, especially the "effective linearity" that explains the accuracy of the PSW approximation for the physical solution. The method, however, has severe shortcomings. Multipole moments, and hence spherical coordinates are necessary in the wave zone for the imposition of outer boundary conditions and for the extraction of outgoing solutions from standing-wave solutions. Spherical, and other standard coordinates are, however, not well suited to resolving the relatively small sources of the binary. This is especially true if the sources are to be represented by boundary conditions on the outer surface of a source, rather than by explicit source terms. The usual technique for handling such problems is coordinate patches and interpolation. This would be particularly inconvenient for the PSW computations since standard iterative approaches are inapplicable to mixed equations.

In this paper we report on an alternative approach, one that has the disadvantage of adding some analytic complexity to the problem, and some worrisome features. But it is a method that gives both remarkably efficient results for model problems, and a potentially useful new approach to the coupling of moving sources to their radiation field. This new method is based on a coordinate system that is adapted to the local structure of the sources and to the large-scale structure of the distant waves. Though the PSW computations have been the proximate motivation for intro-

ducing an adapted coordinate system, the success with this system suggests that its utility may be more broadly applicable. Such coordinates, in fact, have already been exploited, even in numerical relativity. "Čadež coordinates" [11, 12], a carefully adapted coordinate system of this type, was used in much of the work on head-on collisions of black holes, and has more recently found to be useful [13, 14] for initial data and apparent horizon finding. Like the Čadež coordinates, our coordinate systems will reduce to source-centered spherical polar coordinates in the vicinity of the sources, and to rotation-centered spherical polar coordinates far from the sources.

The core of the usefulness of the adapted coordinates is that the field near the sources is well described by a few multipoles in these coordinates, primarily the monopole of the sources, and that the field far from the sources is well described only by a few multipoles in these coordinates. A spectral method (that is, a multipole decomposition), therefore, requires only a small number of multipoles. We will demonstrate, in fact, that for mildly relativistic sources (source velocity = 30% c), excellent results are found when we keep only monopole and quadrupole terms.

There is, of course, a price to be paid for this. For one thing, there is additional analytic complexity in the set of equations. Another difficulty is the unavoidable coordinate singularity that is a feature of coordinates adapted to the two different limiting regions. Still, the potential usefulness of the method, and the success reported here have led to us treating this approach as the main focus of our computations in the PSW work.

3.1.2 Nonlinear model problem

The innovative features of this method present enough new uncertainties that it is important to study this method in the context of the simplest problem possible. We use, therefore, the same model problem as in Paper I, a simple scalar field theory with an adjustable nonlinearity. We will find it quite useful to set the nonlinearity to zero for comparison with the known solution of the linear problem, since many features of our method are unusual even for a linear problem.

For the description of our model problem, we start with Euclidean space coordinatized by the usual spherical coordinates r, θ, ϕ, and we consider sources concentrated near the points $r = a$, $\theta = \pi/2$, in the equatorial plane, and moving symmetrically according to $\phi = \Omega t$ and $\phi = \Omega t + \pi$. As in Paper I, we seek a solution of the flat-spacetime scalar field equation

$$\Psi_{;\alpha;\beta} g^{\alpha\beta} + \lambda F = \nabla^2 \Psi - \partial_t^2 \Psi + \lambda F = \text{Source}\,, \tag{3.1}$$

where F depends nonlinearly on Ψ. The explicit form of F will be the same as that in Paper I. This will allow comparisons with the results of the very different numerical technique in Paper I, and, as in Paper I, allows a very useful comparison of the near-source nonlinear solution with an analytic limit.

We are looking for solutions to Eq. (3.1) with the same helical symmetry as that of the source motions, that is, solutions for which the Lie derivative $\mathcal{L}_\xi \Psi$ is zero for the Killing vector $\xi = \partial_t + \Omega\partial_\phi$. It is useful to introduce the auxiliary coordinate $\varphi \equiv \phi - \Omega t$. In terms of spacetime coordinates t, r, θ, φ the Killing vector is simply ∂_t and the symmetry condition becomes the requirement that the scalar field Ψ is a function only of the variables r, θ and φ. (We are assuming, of course, that the form of the nonlinear term is compatible with the helical symmetry.) It is useful to consider the symmetry to be equivalent to the rule

$$\partial_t \rightarrow \ -\Omega\partial_\varphi \tag{3.2}$$

for scalar functions. In terms of the r, θ, φ variables, Eq. (3.1) for $\Psi(r, \theta, \varphi)$ takes the explicit form

$$\frac{1}{r^2}\,\frac{\partial}{\partial r}\left(r^2\frac{\partial\Psi}{\partial r}\right) + \frac{1}{r^2\sin\theta}\frac{\partial}{\partial\theta}\left(\sin\theta\,\frac{\partial\Psi}{\partial\theta}\right) + \left(\frac{1}{r^2\sin^2\theta} - \Omega^2\right)\frac{\partial^2\Psi}{\partial\varphi^2} + \lambda F(\Psi, r, \theta, \varphi) = \text{Source}\,, \tag{3.3}$$

that was used in Paper I.

3.1.3 Outline and summary

The remainder of this paper has the following organization, and makes the following points. In Sec. 3.2 we introduce the concept of adapted coordinates, co-moving coordinates that conform to the source geometry near the source and that become spherical co-moving coordinates far from the source. A particular system of adapted coordinates, two center bispherical coordinates (TCBC), is introduced in this section. Though these coordinates are not optimal for computational accuracy, they have the advantage of analytic simplicity and are the only adapted coordinates explicitly used in the computations of this paper. Though the TCBC system is relatively simple it is still sufficiently complex that that many details of the use of this method are relegated to Appendix 3.8.

In Sec. 3.2 we also discuss the use of these adapted coordinates in a FDM calculation, and explain the computational difficulties we encountered in trying to find stable solutions with this approach. These difficulties led us to use a spectral type method with the adapted coordintes. In Sec. 3.3 we present the fundamental ideas of expanding the solution in spherical harmonics of the angular adapted coordinates. In this section we also explain why we are not, strictly speaking, using a spectral method since we do the angular differencing by FDM, not by relationships of the spherical harmonics. (For background on spectral methods, and an important recent use of spectral methods in numerical relativity, see [15].) Furthermore, we keep many fewer multipoles than would in principle be justified by the number of points in our angular grid. This "multipole filtering" is one of the most interesting and innovative aspects of our method. Because the adapted coordinates in some sense handle much of the computation analytically only a few multipoles need be kept. In most of the results, in fact, only monopole and quadrupole moments are kept.

To illustrate a more standard spectral method, we present in Appendix 3.9 a standard spectral approach to the linear PSW problem in two spatial dimensions described in TCBC coordinates. The appendix also uses severe multipole filtering and serves to demonstrate in a very different, and generally simpler, numerical context the fundamental correctness of multipole filtering.

For the problem in three spatial dimensions, we have found that a special technique must be used for multipole expansion and multipole filtering. A straightforward approach would use the continuum multipoles evaluated on the angular grid. We explain in Sec. 3.3 why this method involves unacceptably large numerical errors, and why we introduce a second innovative numerical technique, one that we call the "eigenspectral method." In place of the continuum spherical harmonics evaluated on the angular grid, we use eigenvectors of the angular FDM Laplacian. These eigenvectors approach the grid-evaluated continuum spherical harmonics as the grid becomes finer but, as we explain in this section, the small differences are very important in the multipole expansion/filtering method. Some of the details of the eigenspectral method are put into Appendix 3.10, in particular the way the FDM angular Laplacian can be treated as a self-adjoint operator.

Section 3.4 starts by presenting the details of the model scalar field problems to which we apply the eigenspectral method: the choice of the nonlinearity, and the justification for this choice; the manner in which we choose data on an inner boundary taken to be the outer surface of a source; the outer radiative boundary conditions; the Newton-Raphson procedure for finding solutions to nonlinear problems; and the method by which we extract approximate nonlinear outgoing solutions from computed nonlinear standing wave solutions.

This is followed, in Sec. 3.5, by a presentation of numerical results that demonstrate convergence of the method. These results show that the numerical methods are quite accurate despite the inclusion of only a very minimal number of multipoles. In addition, the power of the numerical method allows us to compute models with much stronger nonlinearity than could be handled with the straightforward FDM of Paper I. For these highly nonlinear models we confirm the "effective linearity" that was demonstrated in Paper I with less dramatic models: the outgoing solution extracted from a standing wave solution is an excellent approximation to the true outgoing solution, even for very strong nonlinearity. Conclusions are briefly summarized in Sec. 3.6.

Throughout this paper we follow the notation of Paper I [10]. (A few changes from the notation and choices of Paper I are made to correct minor errors of Paper I: (i) The point source delta function is now divided by a Lorentz γ factor, as explained following Eq. (3.47). (ii) The nonlinearity parameter λ was used with inconsistent dimensionality in Paper I. Here λ is consistently treated as a dimensionless parameter, requiring the insertion of a factor $1/a^2$ in the model nonlinearity of Eq. (3.48).

3.2 Adapted coordinates

3.2.1 General adapted coordinates

For the definition of the adapted coordinates it is useful to introduce several Cartesian coordinate systems. We shall use the notation x, y, z to denote inertial Cartesian systems related to r, θ, ϕ in the usual way (e.g., z is the rotation axis, one of the source points moves as $x = a\cos(\Omega t)$, $y = a\sin(\Omega t)$, and so forth). We now introduce a co-moving Cartesian system $\widetilde{x}, \widetilde{y}, \widetilde{z}$ by

$$\widetilde{z} = r\cos\theta \qquad \widetilde{x} = r\sin\theta\cos(\phi - \Omega t) \qquad \widetilde{y} = r\sin\theta\sin(\phi - \Omega t)\,. \tag{3.4}$$

In this system, as in the inertial x, y, z system, the $\widetilde{z}$ axis is the azimuthal axis. We next define the

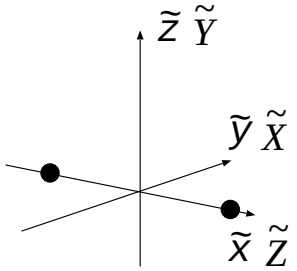

Figure 3.1: Two sets of co-moving Cartesian coordinates

comoving system

$$\widetilde{X} = \widetilde{y} \qquad \widetilde{Y} = \widetilde{z} \qquad \widetilde{Z} = \widetilde{x}\,, \tag{3.5}$$

in which the azimuthal $\widetilde{Z}$ axis is not the rotation axis, but rather is the line through the source points, as shown in Fig. 3.1.

Our goal now is to introduce new comoving coordinates $\chi(\widetilde{X}, \widetilde{Y}, \widetilde{Z})$, $\Theta(\widetilde{X}, \widetilde{Y}, \widetilde{Z})$, $\Phi(\widetilde{X}, \widetilde{Y}, \widetilde{Z})$ that are better suited to a description of the physical problem, and that allow for more efficient computation. We will assume that the coordinate transformation is invertible, except at a finite number of discrete points, so that we may write $\widetilde{X}, \widetilde{Y}, \widetilde{Z}$, or $\widetilde{x}, \widetilde{y}, \widetilde{z}$ as functions of χ, Θ, Φ.

In terms of the comoving Cartesian coordinates, the helical symmetry rule in Eq. (3.2) takes the form

$$\partial_t \to -\Omega\left(\widetilde{x}\frac{\partial}{\partial\widetilde{y}} - \widetilde{y}\frac{\partial}{\partial\widetilde{x}}\right) = -\Omega\left(\widetilde{Z}\frac{\partial}{\partial\widetilde{X}} - \widetilde{X}\frac{\partial}{\partial\widetilde{Z}}\right)\,. \tag{3.6}$$

Our nonlinear scalar field equation of Eq. (3.1) can then be written, for helical symmetry, as

$$\mathcal{L}\Psi + \lambda F = \frac{\partial^2\Psi}{\partial\widetilde{X}^2} + \frac{\partial^2\Psi}{\partial\widetilde{Y}^2} + \frac{\partial^2\Psi}{\partial\widetilde{Z}^2} - \Omega^2\left(\widetilde{Z}\frac{\partial}{\partial\widetilde{X}} - \widetilde{X}\frac{\partial}{\partial\widetilde{Z}}\right)^2\Psi + \lambda F = \text{Source}\,. \tag{3.7}$$

This field equation can be expressed completely in terms of adapted coordinates in the form

$$\mathcal{L}\Psi + \lambda F = A_{\chi\chi}\,\frac{\partial^2\Psi}{\partial\chi^2} + A_{\Theta\Theta}\,\frac{\partial^2\Psi}{\partial\Theta^2} + A_{\Phi\Phi}\,\frac{\partial^2\Psi}{\partial\Phi^2} + 2A_{\chi\Theta}\,\frac{\partial^2\Psi}{\partial\chi\partial\Theta} + 2A_{\chi\Phi}\,\frac{\partial^2\Psi}{\partial\chi\partial\Phi} + 2A_{\Theta\Phi}\,\frac{\partial^2\Psi}{\partial\Theta\partial\Phi}$$

$$+B_\chi\,\frac{\partial\Psi}{\partial\chi} + B_\Theta\,\frac{\partial\Psi}{\partial\Theta} + B_\Phi\,\frac{\partial\Psi}{\partial\Phi} + \lambda F = \text{Sources}\,. \tag{3.8}$$

It is straightforward to show that the A_{ij} and B_i coefficients here are given by

$$\begin{aligned}
A_{\chi\chi} &= \vec{\nabla}\chi\cdot\vec{\nabla}\chi - \Omega^2\bar{A}_{\chi\chi} && (3.9)\\
A_{\Theta\Theta} &= \vec{\nabla}\Theta\cdot\vec{\nabla}\Theta - \Omega^2\bar{A}_{\Theta\Theta} && (3.10)\\
A_{\Phi\Phi} &= \vec{\nabla}\Phi\cdot\vec{\nabla}\Phi - \Omega^2\bar{A}_{\Phi\Phi} && (3.11)\\
A_{\chi\Theta} &= \vec{\nabla}\chi\cdot\vec{\nabla}\Theta - \Omega^2\bar{A}_{\chi\Theta} && (3.12)\\
A_{\chi\Phi} &= \vec{\nabla}\chi\cdot\vec{\nabla}\Phi - \Omega^2\bar{A}_{\chi\Phi} && (3.13)\\
A_{\Theta\Phi} &= \vec{\nabla}\Theta\cdot\vec{\nabla}\Phi - \Omega^2\bar{A}_{\Theta\Phi} && (3.14)\\
B_\chi &= \nabla^2\chi - \Omega^2\bar{B}_\chi && (3.15)\\
B_\Theta &= \nabla^2\Theta - \Omega^2\bar{B}_\Theta && (3.16)\\
B_\Phi &= \nabla^2\Phi - \Omega^2\bar{B}_\Phi\,. && (3.17)
\end{aligned}$$

Here the gradients, Laplacians and dot products are to be taken treating the $\widetilde{X}$,$\widetilde{Y}$,$\widetilde{Z}$ as Cartesian coordinates, so that, for example,

$$\vec{\nabla}\chi\cdot\vec{\nabla}\Theta = \frac{\partial\chi}{\partial\widetilde{X}}\frac{\partial\Theta}{\partial\widetilde{X}} + \frac{\partial\chi}{\partial\widetilde{Y}}\frac{\partial\Theta}{\partial\widetilde{Y}} + \frac{\partial\chi}{\partial\widetilde{Z}}\frac{\partial\Theta}{\partial\widetilde{Z}}\,. \tag{3.18}$$

The form of the $\bar{A}_{ij}$ and $\bar{B}_j$ terms in Eqs. (3.9)–(3.17) are given, for general adapted coordinates, in Eqs. (3.82)–(3.92).

3.2.2 A specific adapted coordinate system: TCBC

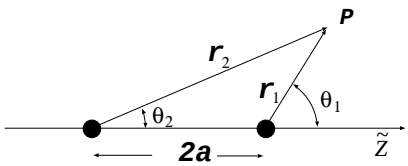

Figure 3.2: Geometric basis for the TCBC adapted coordinates

Before discussing general features of an adapted coordinate system, it will be useful to give a specific example. For that example, we choose a coordinate system χ, Θ, Φ that is particularly

simple in form, though (as we shall discuss below) not the choice that is numerically most efficient. The chosen coordinates are most easily understood by starting with the distances r_1 and r_2 from the source points, and with the angles θ_1, θ_2 shown in Fig. 3.2. The formal definitions of the adapted coordinates are

$$\chi \equiv \sqrt{r_1 r_2} = \left\{ \left[\left(\widetilde{Z} - a\right)^2 + \widetilde{X}^2 + \widetilde{Y}^2 \right] \left[\left(\widetilde{Z} + a\right)^2 + \widetilde{X}^2 + \widetilde{Y}^2 \right] \right\}^{1/4} \tag{3.19}$$

$$\Theta \equiv \frac{1}{2}\left(\theta_1 + \theta_2\right) = \frac{1}{2}\tan^{-1}\left(\frac{2\widetilde{Z}\sqrt{\widetilde{X}^2 + \widetilde{Y}^2}}{\widetilde{Z}^2 - a^2 - \widetilde{X}^2 - \widetilde{Y}^2} \right) \tag{3.20}$$

$$\Phi \equiv \tan^{-1}\left(\widetilde{X}/\widetilde{Y}\right). \tag{3.21}$$

This choice is sometimes called "two-center bipolar coordinates" [16], hereafter TCBC, and is equivalent to the zero-order coordinates used by Čadež [11, 12].

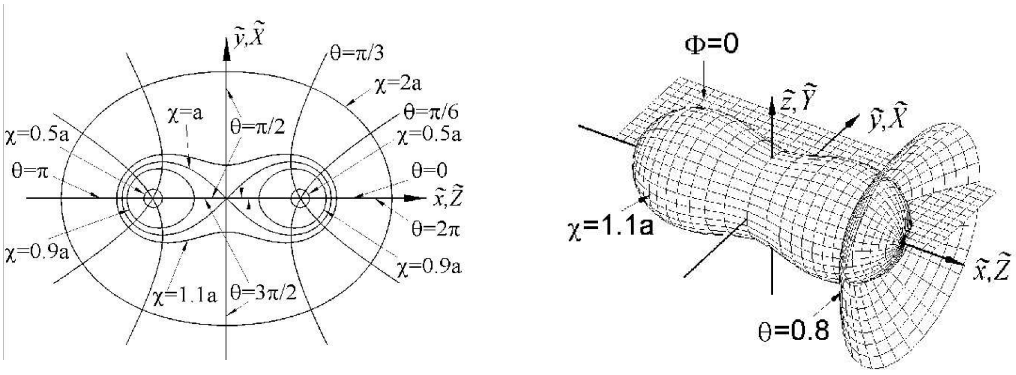

Figure 3.3: Adapted coordinates in the $\widetilde{x}, \widetilde{y}$ plane, and three-dimensional coordinate surfaces

An attractive feature of this particular choice of adapted coordinates is that the above relationships can be inverted in simple closed form to give

$$\widetilde{Z} = \sqrt{\frac{1}{2}\left[a^2 + \chi^2\cos 2\Theta + \sqrt{(a^4 + 2a^2\chi^2\cos 2\Theta + \chi^4)}\right]} \tag{3.22}$$

$$\widetilde{X} = \sqrt{\frac{1}{2}\left[-a^2 - \chi^2\cos 2\Theta + \sqrt{(a^4 + 2a^2\chi^2\cos 2\Theta + \chi^4)}\right]}\ \cos\Phi\,. \tag{3.23}$$

$$\widetilde{Y} = \sqrt{\frac{1}{2}\left[-a^2 - \chi^2\cos 2\Theta + \sqrt{(a^4 + 2a^2\chi^2\cos 2\Theta + \chi^4)}\right]}\ \sin\Phi\,. \tag{3.24}$$

The meaning of the χ, Θ coordinates in the $\widetilde{x}, \widetilde{y}$ plane (the $\widetilde{Z}, \widetilde{X}$ plane) is shown on the left in Fig. 3.3; a picture of three-dimensional χ, Θ, and Φ surfaces is shown on the right.

The geometrical definition inherent in Fig. 3.2 suggests that the adapted coordinate surfaces have the correct limit far from the sources. This is confirmed by the limiting forms Eqs. (3.22)–

(3.24) for $\chi \gg a$. Aside from fractional corrections of order a^2/χ^2 the relations are

$$\widetilde{Z} \to \chi \cos\Theta \qquad \widetilde{X} \to \chi \sin\Theta \cos\Phi \qquad \widetilde{Y} \to \chi \sin\Theta \sin\Phi \,. \tag{3.25}$$

Near the source point at $\widetilde{Z} = \pm a$, the limiting forms, aside from fractional corrections of order χ^2/a^2, are

$$\widetilde{Z} \to \pm a + \frac{\chi^2}{2a}\cos(2\Theta) \qquad \widetilde{X} \to \frac{\chi^2}{2a}\sin(2\Theta)\cos\Phi \qquad \widetilde{Y} \to \frac{\chi^2}{2a}\sin(2\Theta)\sin\Phi \,. \tag{3.26}$$

These limits, and Fig. 3.2, show that near the source point at $\widetilde{Z} = a$ the expression $\chi^2/2a$ plays the role of radial distance, and 2Θ plays the role of polar coordinate. (Near the source point at $\widetilde{Z} = -a$, the expression $\chi^2/2a$ again plays the role of radius, but the polar angle is $\pi - 2\Theta$.) Notice that both for the near and the far limit, the polar angle is defined with respect to the line through the sources, the $\widetilde{Z}$ axis, not with respect to the rotational $\widetilde{z}$ axis.

It is clear that our new system has a coordinate singularity at the origin. Indeed, there must be a coordinate singularity in any such adapted coordinate system. The switch from the small-χ coordinate surfaces, disjoint 2-spheres around the sources, to the large-χ single 2-sphere cannot avoid a singularity.

The remaining specification needed is the outer boundary conditions on some large approximately spherical surface $\chi = \chi_{\max}$. For the monopole moment of the field this condition is simply that the field dies off as $1/\chi$. For the radiative part of the field we use the usual Sommerfeld outgoing outer boundary condition $\partial_t\psi = -\partial_r\psi$, approximated as $\partial_t\psi = -\partial_\chi\psi$. The fractional error introduced by this substitution is of order a^2/χ^2. The Sommerfeld condition itself is accurate only up to order $(\text{wavelength}/r)$. Since the wavelength is larger than a, our substitution $r \to \chi$ in the outer boundary condition introduces negligibly small errors. To apply the helical symmetry we use the replacement rule in Eq. (3.6) and the outgoing boundary condition becomes

$$\frac{\partial\Psi}{\partial\chi} = \Omega\left(\widetilde{Z}\frac{\partial\Psi}{\partial\widetilde{X}} - \widetilde{X}\frac{\partial\Psi}{\partial\widetilde{Z}}\right) = \Omega\left(\Gamma^\Theta\frac{\partial\Psi}{\partial\Theta} + \Gamma^\Phi\frac{\partial\Psi}{\partial\Phi} + \Gamma^\chi\frac{\partial\Psi}{\partial\chi}\right), \tag{3.27}$$

where the Γs are given explicitly in Appendix 3.8. At large χ the outgoing condition can be written

$$\frac{\partial\Psi}{\partial\chi} = \Omega\left(\cos\Phi\frac{\partial\Psi}{\partial\Theta} - \frac{\cos\Theta}{\sin\Theta}\sin\Phi\frac{\partial\Psi}{\partial\Phi}\right)\left(1 + \mathcal{O}(a^2/\chi^2)\right). \tag{3.28}$$

The correction on the right is higher-order at the outer boundary $\chi = \chi_{\max}$ and can be ignored. The ingoing boundary condition follows by changing the sign of the right hand side of Eq. (3.27) or (3.28).

The problem of Eqs. (3.8) and (3.28) is a well-posed boundary-value problem analagous to that

in Paper I [10]. As in Paper I, this problem can be numerically implemented using the finite difference method (FDM) of discretizing derivatives. The difference between such a computation and that of Paper I is, in principle, only in the coordinate dependence of the coefficients ($A_{\chi\chi}$, $A_{\Theta\Theta}, \cdots$) that appear in the differential equation and ($\Gamma^{\Theta}, \cdots$) in the outer boundary condition.

3.2.3 Requirements for adapted coordinates

For the scalar problem, there are obvious advantages of the coordinate system pictured in Fig. 3.3. First, the surfaces of constant χ approximate the surfaces of constant Ψ near the sources, where field gradients are largest, and where numerical difficulties are therefore expected. Since the variation with respect to Θ and Φ is small on these surfaces, finite differencing of Θ and Φ derivatives should have small truncation error. The steep gradients in χ, furthermore, can be dealt with in principle by a reparameterization of χ to pack more grid zones near the source points. An additional, independent advantage to the way the coordinates are adapted to the source region is that these coordinates are well suited for the specification of inner boundary conditions on a constant χ surface. Because of these advantages we shall reserve the term "adapted" to a coordinate system for which constant χ surfaces near the source approximate spheres concentric with the source.

A second feature of the TCBC coordinates that we shall also require in general, is that in the region far from the sources, χ,Θ,Φ asymptotically approach spherical coordinates, the coordinates best suited for describing the radiation field. If the approach to spherical coordinates is second-order in a/r, then the outgoing boundary conditions will be that in Eq. (3.28).

There are practical considerations that also apply to the choice of adapted coordinates. The coefficients of the rotational terms in the equation (i.e. , those involving $\bar{A}_{ij}$ and $\bar{B}_i$ in Eqs. (3.9)–(3.17)) require computing second derivatives of the transformation from Cartesian to adapted coordinates. If those relationships are only known numerically, these second derivatives will tend to be noisy. For that reason, a desirable and perhaps necessary feature of the adapted coordinates is that closed form expressions exist for $\chi(\widetilde{x},\widetilde{y},\widetilde{z})$, and $\Theta(\widetilde{x},\widetilde{y},\widetilde{z})$. (The expression for Φ, the azimuthal angle about the line through the source points, is trivial.) It is possible in principle, of course, to have the adapted coordinates defined without respect to the Cartesians. In the scalar model problem, the coordinates could be defined by giving the form of the flat spacetime metric in these coordinates. The nature of the helical Killing symmetry, analogous to Eq. (3.6) would still have to be specified of course. The choice of adapted coordinates becomes a much richer subject in the case of the gauge-fixed general relativity problem that is the ultimate goal of the work; see [17].

The TCBC coordinates satisfy all the practical requirements of an adapted coordinate system. In particular, the functions $\chi(\widetilde{x},\widetilde{y},\widetilde{z})$, and $\Theta(\widetilde{x},\widetilde{y},\widetilde{z})$, as well as their inverses, are all explicitly known in terms of elementary functions. Though the TCBC coordinates are therefore convenient, in addition to being well suited to the problem in Eq. (3.1), they are not optimal. The perfect coordinates would

be those for which the constant χ surfaces agree exactly with the constant Ψ surfaces. This of course is impossible in practice (and, in addition, would not be compatible with the requirement that the coordinates go asymptotically to spherical coordinates). We should therefore modify the criterion for the "perfect coordinates" to that of having Ψ constant on constant χ surfaces for no rotation ($\Omega = 0$). The TCBC coordinate system, in fact, does satisfy that requirement for the version of the problem of Eq. (3.1) in two spatial dimensions with no nonlinearity, as detailed in Appendix 3.9. Due to this "near perfection" of the TCBC coordinates for the linear two-dimensional problem we found that we were able to achieve very good accuracy for that case with moderate rates of rotation.

These considerations suggest that we could achieve an improvement over the TCBC coordinates, by choosing χ to be proportional to solutions of the nonrotating case of Eq. (3.1) in three spatial dimensions. Since the nonlinear case would result in a solution that is known only numerically, we can follow the pattern of the two-dimensional case and choose χ simply to be proportional to the solution of the linear nonrotating three-dimensional problem. The Θ coordinate that is orthogonal to this χ would have to be found numerically, and would therefore be troublesome. But there is no need for Θ and χ to be orthogonal. We could, therefore, use the TCBC definition of Θ in Eq. (3.20). An improved set of adapted coordinates, then, would seem to be

$$\chi = \frac{1}{2}\left(\frac{1}{r_1} + \frac{1}{r_2}\right) \qquad \Theta = \frac{1}{2}\left(\theta_1 + \theta_2\right) , \tag{3.29}$$

where r_i, θ_i are the distances and angles shown Fig. 3.2.

In this paper, we shall report only numerical results from the simplest adapted coordinate system to implement, the TCBC coordinates. There are two reasons for this. The first is the obvious advantages of working with the simplicity of the TCBC case, and the advantage of having simple explicit expressions for all coefficients in Eq. (3.8). The second reason that we do not use the apparently superior adapted coordinate in Eq. (3.29), is that we do not expect there to be an equivalent for the general relativity problem. In that case there will be several different unknown fields to solve for, and there is no reason to think that the optimal coordinate system for one of the fields will be the same for the others.

3.3 Spectral methods with adapted coordinates

The wave equation in Eq. (3.8), along with the boundary conditions Eq. (3.28), can in principle be solved by imposing a χ, Θ, Φ grid and by using FDM. In practice, numerical problems hinder a straightforward finite difference computation. Evidence for this is shown in Fig. 3.4, in which the error (the difference between the computed solution and the analytic solution) for the linear outgoing problem is plotted for different locations of the outer boundary $\chi_{\max}$. As Fig. 3.4 shows, the

quality of our solutions was highly sensitive to small changes in grid parameters, such as the location of the outer boundary. We attribute these difficulties to the orientation of the finite difference grid at large distance from the source. Loosely speaking, the spherical polar grid is "aligned" with the solutions, and errors are distributed evenly on the grid. Adapted coordinates become spherical polar at large distances, but the polar axis is aligned with the sources, not with the rotation axis. The result may be a nonuniform distribution of errors, which effectively excites spurious modes analogous to modes excited inside a resonant cavity.

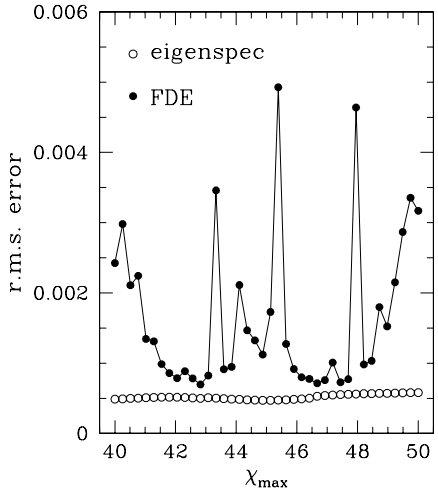

Figure 3.4: Error in the computed outgoing linear solution as a function of the location of the outer boundary. Results are shown both for straightforward FDM in adapted coordinates and for the eigenspectral method, explained in the text, with only monopole and quadrupole terms kept.

An attractive alternative to FDM is to expand Ψ in a complete set of functions of the angular coordinates Θ and Φ. Since one of our goals is to describe the radiation in the weak wave zone, and since Θ and Φ approach co-moving spherical coordinates in the weak wave zone, the natural set of basis functions is the spherical harmonics $Y_{\ell m}(\Theta, \Phi)$. In terms of these we would look for a solution of Eq. (3.8) in the form

$$\Psi = \sum_{\text{even } \ell} \sum_{m} a_{\ell m}(\chi) Y_{\ell m}(\Theta, \Phi)\,. \tag{3.30}$$

(The odd ℓs are omitted due to the symmetry of the problem.)

The possibility of such a spectral method has been introduced in Paper I as a potentially powerful way of dealing with radiation from moving sources. The reason for this is that near the source points the field is nearly spherically symmetric, and hence can be described with very few mul-

tipoles. Far from the source, the contribution from multipoles of order ℓ scale as $(a\Omega)^\ell$, so the radiation field is dominated by the monopole and quadrupole, and again can be described with very few multipoles. It is, therefore, plausible that with very few multipoles—perhaps only the monopole and quadrupole—the fields everywere can be described with reasonable accuracy.

In the multipole method, the expansion in Eq. (3.30) is substituted in Eq. (3.8) to give

$$\mathcal{L}\Psi = \sum_{\ell m} \frac{d^2 a_{\ell m}}{d\chi^2}\ [A_{\chi\chi} Y_{\ell m}] + a_{\ell m}(\chi)\ \left[A_{\Theta\Theta}\frac{\partial^2 Y_{\ell m}}{\partial\Theta^2} + A_{\Phi\Phi}\frac{\partial^2 Y_{\ell m}}{\partial\Phi^2} + 2A_{\Theta\Phi}\frac{\partial^2 Y_{\ell m}}{\partial\Theta\partial\Phi} + B_\Theta\frac{\partial Y_{\ell m}}{\partial\Theta} + B_\Phi\frac{\partial Y_{\ell m}}{\partial\Phi}\right]$$

$$+\frac{da_{\ell m}}{d\chi}\left[2A_{\chi\Theta}\frac{\partial Y_{\ell m}}{\partial\Theta} + 2A_{\chi\Phi}\frac{\partial Y_{\ell m}}{\partial\Phi} + B_\chi Y_{\ell m}\right]\ . \tag{3.31}$$

The next step is to project out ordinary differential equations. This is most naturally done by multiplying by some weight function $W(\chi,\Theta)$ and by $Y_{\ell' m'}$, and by integrating over all Θ and Φ. The result is our multipole equations

$$\sum_{\ell m} \alpha_{\ell' m' \ell m}\frac{d^2 a_{\ell m}(\chi)}{d\chi^2} + \beta_{\ell' m' \ell m} a_{\ell m}(\chi) + \gamma_{\ell' m' \ell m}\frac{da_{\ell m}(\chi)}{d\chi} = S_{\ell m}\ , \tag{3.32}$$

where $S_{\ell m}$ is the multipole of the source term, and where

$$\begin{aligned}
\alpha_{\ell' m' \ell m} &= \int_0^{2\pi} d\Phi \int_0^{\pi} d\Theta\ W(\chi,\Theta)\ Y^*_{\ell' m'}(\Theta,\Phi) A_{\chi\chi} Y_{\ell m}(\Theta,\Phi) \\
\beta_{\ell' m' \ell m} &= \int_0^{2\pi} d\Phi \int_0^{\pi} d\Theta\ W(\chi,\Theta)\ Y^*_{\ell' m'}(\Theta,\Phi) \times \\
&\quad \left[A_{\Theta\Theta}\frac{\partial^2 Y_{\ell m}}{\partial\Theta^2} + A_{\Phi\Phi}\frac{\partial^2 Y_{\ell m}}{\partial\Phi^2} + 2A_{\Theta\Phi}\frac{\partial^2 Y_{\ell m}}{\partial\Phi\partial\Theta} + B_\Theta\frac{\partial Y_{\ell m}}{\partial\Theta} + B_\Phi\frac{\partial Y_{\ell m}}{\partial\Phi}\right] \\
\gamma_{\ell' m' \ell m} &= \int_0^{2\pi} d\Phi \int_0^{\pi} d\Theta\ W(\chi,\Theta)\ Y^*_{\ell' m'}(\Theta,\Phi) \left[2A_{\chi\Theta}\frac{\partial Y_{\ell m}}{\partial\Theta} + 2A_{\chi\Phi}\frac{\partial Y_{\ell m}}{\partial\Phi} + B_\chi Y_{\ell m}\right].
\end{aligned} \tag{3.33}$$

The problem with this straightforward approach to multipole decomposition is that the angular integrals needed for the projection are very computationally intensive, and the solutions of the differential equations in χ are very sensitive to the values of the αs, βs, and γs, that are computed by these projection integrals. These shortcomings do not apply to the 2-dimensional version of the helically symmetric wave equation. In that case the projection integrals involve only a single integration variable, and it proves to be fairly easy to compute accurate angular integrals. We present the straightforward 2-dimensional multipole expansion in Appendix 3.9. This is meant to illustrate the multipole expansion in a particularly simple context, but more importantly it demonstrates a crucial point, that we can get excellent accuracy by keeping only two multipoles. This 2-dimensional computation also illustrates the alternative definiton of standing waves, that of minimum wave amplitude, as sketched in Paper I.

It turns out that for the 3-dimensional problem, even with only a small number of multipoles,

there are two classes of severe computational difficulties. First, the projection integrals in Eq. (3.33) are very computationally intensive, especially due to the singularity at $\Theta = \pi/2$ for $\chi/a \leq 1$, a singularity that must be canceled in the projection integrals by the choice of the weight function $W(\chi, \Theta)$. In trials with the linear problem, and in comparisons with the known exact answer, we have found that accuracy of the computed field is poor unless the integrals are done very precisely. A second, quite distinct, difficulty is related to the projection at the outer boundary. An outgoing boundary condition is applied to $a_{\ell m}$, for $\ell > 0$. The radiative moments, however, are much smaller than the monopole moment a_{00}. Projection of a $a_{\ell m}$ moment with $\ell > 0$ will be contaminated by the much larger monopole moment a_{00}, due to small numerical inaccuracies in the projection. We have found this to be a problem even in the simplest (static linear) models.

We have used an alternative approach to multipole decomposition and multipole filtering, an approach that gives excellent results for the nonlinear scalar models and promises to be similarly useful in gravitational models. Underlying this approach is the concept that the angular nature of the multipole components of the radiation field is determined by FDM operations, in particular by the FDM implementation of the Laplacian. The properties of the spherical harmonics that make them useful in the continuum description of radiation is taken over, in FDM computations, by the eigenvectors of the FDM Laplacian.

To implement this idea we start by viewing the grid values of the scalar field Ψ on a constant-χ surface as a vector $\mathbf{\Psi}$ whose components are most conveniently expressed with a double index

$$\Psi_{ij} = \Psi(\Theta_i, \Phi_j)\,. \tag{3.34}$$

Here Θ_i and Φ_j are the values on the Θ, Φ grid with spacings $\Delta\Theta$ and $\Delta\Phi$. It follows that $\mathbf{\Psi}$ is a vector in a space of dimension $N \equiv n_\Theta \times n_\Phi$.

In the Θ, Φ continuum, the angular part of the Laplacian at $\chi/a \gg 1$ is the operator

$$\nabla^2_{\rm ang} \equiv \frac{1}{\sin\Theta}\,\frac{\partial}{\partial\Theta}\left[\sin\Theta\,\frac{\partial}{\partial\Theta}\right] + \frac{1}{(\sin\Theta)^2}\,\frac{\partial^2}{\partial\Phi^2}\,. \tag{3.35}$$

In a FDM this is replaced by an operator in the N-dimensional space of angular grid values. Our eigenspectral method is based on finding the eigenvectors of this N-dimensional operator.

The i, j component of the eigenvector will have the form $Y^{(k)}_{ij}$ which should be a good approximation to some $Y_{\ell m}(\Theta_i, \Phi_j)$, i.e., to some continuum spherical harmonic evaluated at grid points. (In practice we work only with real eigenvectors that are approximations to normalized real and imaginary parts of the grid-evaluated spherical harmonics.) In Fig. 3.5 continuum spherical harmonics are compared to the eigenvectors found for a grid with $n_\Theta \times n_\Phi$=16 $\times$ 32 on an angular domain $0 \leq \Theta \leq \pi/2$, $0 \leq \Phi \leq \pi$. As might be expected, the agreement between eigenvector and continuum function is quite good when the scale for change of the continuum function is long

compared to the spacing betwen grid points.

The eigenvalues found for the discrete and continuum angular Laplacians are in good agreement for small eigenvalues. For the discrete problem we define an effective multipole index ℓ in the obvious way, by setting $-\ell(\ell+1)$ equal to the eigenvalue for each eigenvector. A comparison is given in Fig. 3.6 of the integer continuum values of ℓ and those found for a 16×32 grid on the region $0 \leq \Theta \leq \pi/2, 0 \leq \Phi \leq \pi$. (Unlike the spherical harmonics, the eigenvectors are not degenerate, so there is a small range of ℓ values of the eigenspectral method corresponding to each ℓ of the continuum problem.) For the discrete operator the eigenvectors) For our problem the other angular regions are related by symmetry. These symmetries also eliminate the odd values of ℓ omitted from Fig. 3.6. The figure shows that for small ℓ there is good agreement between the discrete and continuum eigenvalues. Because of this we can refer to monopole, quadrupole, hexadecapole, ... eigenvectors without ambiguity.

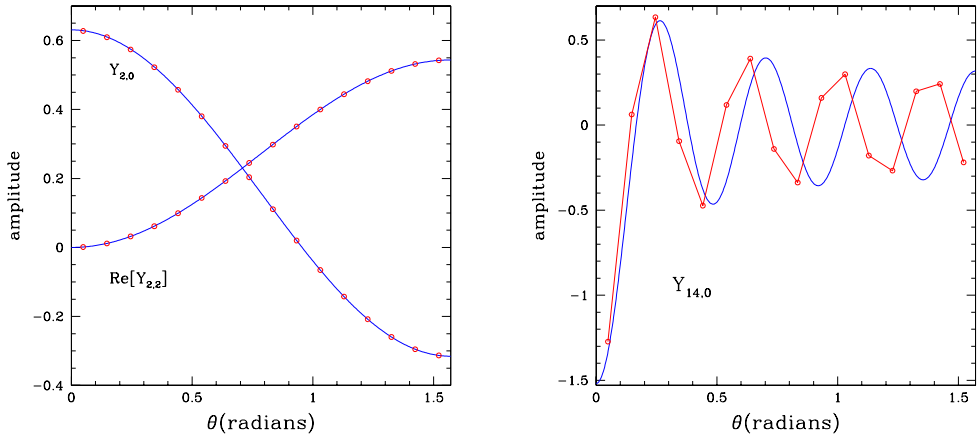

Figure 3.5: The eigenvectors for a 16×32 grid compared to the corresponding continuum eigenfunctions, the spherical harmonics. The continuous curves show the spherical harmonics; the data points are the components of the eigenvectors.

In the mathematics of the grid space, two vectors F_{ij} and G_{ij} are taken to have an inner product

$$F \cdot G \equiv \sum_{i=1}^{n_\Theta} \sum_{j=1}^{n_\Phi} F_{ij} G_{ij} \sin(\Theta_i) \Delta\Theta \, \Delta\Phi \, . \tag{3.36}$$

With some care, detailed in Appendix 3.10, we can construct the FDM angular Laplacian to be self-adjoint with respect to the inner product in Eq. (3.36). This guarantees that the eigenvectors can be chosen to be orthogonal. We complete the analogy to the spherical harmonics by choosing the

eigenvectors to be normalized, so that we have

$$\sum_{i=1}^{n_\Theta}\sum_{j=1}^{n_\Phi} Y_{ij}^{(k)} Y_{ij}^{(k')} \sin(\Theta_i)\Delta\Theta\,\Delta\Phi = \delta_{kk'}\,. \tag{3.37}$$

(This normalization has been used for the eigenvectors shown in Fig. 3.5.) With these definitions we can now write a multipole expansion as

$$\Psi(\chi,\Theta_i,\Phi_j) = \sum_k a^{(k)}(\chi) Y_{ij}^{(k)}\,, \tag{3.38}$$

with

$$a^{(k)}(\chi) = \sum_{i=1}^{n_\Theta}\sum_{j=1}^{n_\Phi} \Psi(\chi,\Theta_i,\Phi_j) Y_{ij}^{(k)} \sin(\Theta_i)\Delta\Theta\Delta\Phi. \tag{3.39}$$

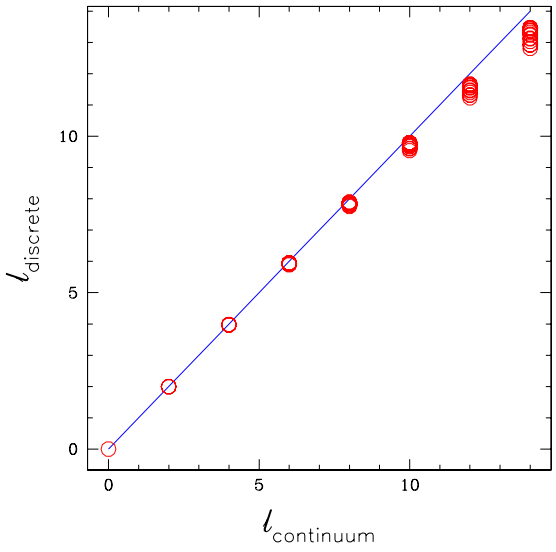

Figure 3.6: The ℓ values of the discrete angular Laplacian on a 16×32 grid compared with the integer ℓ values of the continuum angular Laplacian. The eigenvectors of the discrete angular Laplacian are not degenerate, so a cluster of several ℓ values of the eigenspectral method corresponds to a single ℓ value of the continuum problem.

The multipole filtering that was the motivation for the introduction of the spectral decomposition is implemented simply by limiting the terms included in the sum in Eq. (3.38). Rather than include all eigenvectors, only those with $\ell < \ell_{\max}$ are included. Since the discrete ℓs are never larger than the continuum ℓs, a choice $\ell_{\max} = 5$ means that the monopole, quadrupole, and octupole terms, with $\ell \approx 0, 2, 4$ are included. The effect of the eigenspectral method and multipole filtering are the suppression of the large FDM boundary-related errors, as illustrated in Fig. 3.4.

In this method the k summation in Eq. (3.38) stops at some maximum value governed by $\ell_{\max}$, and the equations to be solved are the following modifications of Eqs. (3.32):

$$\sum_k \alpha_{k'k} \frac{d^2 a^{(k)}(\chi)}{d\chi^2} + \beta_{k'k} a^{(k)}(\chi) + \gamma_{kk'} \frac{da^{(k)}(\chi)}{d\chi} = S_{k'} \, . \tag{3.40}$$

In place of Eq. (3.33) the coefficients in this sum are now evaluated from

$$\alpha_{k'k} = Y^{(k')} \cdot A_{\chi\chi} Y^{(k)} \tag{3.41}$$

$$\beta_{k'k} = Y^{(k')} \cdot \left[A_{\Theta\Theta} \frac{\partial^2 Y^{(k)}}{\partial \Theta^2} + A_{\Phi\Phi} \frac{\partial^2 Y^{(k)}}{\partial \Phi^2} + 2A_{\Theta\Phi} \frac{\partial^2 Y^{(k)}}{\partial \Phi \partial \Theta} + B_\Theta \frac{\partial Y^{(k)}}{\partial \Theta} + B_\Phi \frac{\partial Y^{(k)}}{\partial \Phi} \right] \tag{3.42}$$

$$\gamma_{k'k} = Y^{(k')} \cdot \left[2A_{\chi\Theta} \frac{\partial Y^{(k)}}{\partial \Theta} + 2A_{\chi\Phi} \frac{\partial Y^{(k)}}{\partial \Phi} + B_\chi Y_{\ell m} \right] , \tag{3.43}$$

where it is understood that the angular derivatives are computed by finite differencing. In the effective source term,

$$S_{k'} \equiv -\lambda Y^{(k')} \cdot F\left(\sum a^{(k)} Y^{(k)} \right) , \tag{3.44}$$

only the nonlinearity appears. There is no "true" source term since we solve only outside the source and introduce the properties of the source through boundary conditions.

Our method is clearly spectral in flavor, but it is worth pointing out explicitly that this method is not a spectral method according to the meaning usually given to that term in numerical analysis. If it were a spectral, or pseudospectral (collocation) method, then angular derivatives in the field equations and boundary conditions would be taken using properties of the spectral functions. (If the decomposition were done into continuum spherical harmonics, for example, a spectral method would evaluate $\partial\Psi/\partial\Theta$ by using relations among the spherical harmonics.) In our method, angular derivatives are taken by finite differencing, not by relations among the eigenvectors and their angular derivatives. We could, in principle, convert our method to one that meets the "spectral method" (actually pseudospectral) definition. We could use finite differencing to compute, once and for all, relations among the eigenvectors and their derivatives. These relations could then be used to replace any derivative by a linear combination of eigenvectors. We have, however, not explored this approach.

Some comment must be made about a subtle but fundamental point in our spectral method. For a given $\chi < a$, the angular specification $\Theta = \pi/2$ refers to a single point on the $\widetilde{Z}$ axis; the value of Φ is irrelevant. On the other hand, the function $Y_{\ell m}(\pi/2, \Phi)$, for even ℓ and $m \neq 0$ is, in general, not a single value. There are, then, terms in Eq. (3.30) that in principle are multivalued at $\chi < a$,$\Theta = \pi/2$. We can, of course, delete the value $\Theta = \pi/2$ from our grid. (And we, in fact, delete this value for several reasons, such as the requirement that the FDM Laplacian be self-adjoint; see Appendix 3.10.) We still have the problem that the variation of these awkward terms diverges as

$\Delta\Theta \to 0$ and the grid converges to the continuum. In principle, for any $\Delta\Theta$ the summation in Eq. (3.30) at any grid point will approach (in the mean) the correct answer if we include enough multipoles.

In practice, we include very few multipoles. We must therefore ask whether the summation will give a highly inaccurate answer in the region of the $\chi < a$ grid near $\Theta = \pi/2$. We avoid this problem by choosing source structures that are symmetric about the $\widetilde{Z}$ axis. This means that at some inner boundary $\chi_{\rm min}$ we set the nonaxisymmetric $a^{(k)}$ to zero. The radial equations, the FDM eigenspectral versions of Eq. (3.32), do mix the $a^{(k)}$, so the nonaxisymmetric $a^{(k)}$ will be generated. But the mixing of the multipoles is small until χ is on the order of a. As a consequence, the nonaxisymmetric $a^{(k)}$ can play their needed role in the wave region without generating large errors in the near-source region.

This behavior of the coefficients is illustrated in Fig. 3.7 for an outgoing linear wave. The solid curve shows, as a function of χ, the eigenspectral coefficient $a^{(k)}$ corresponding to the $\ell = 2$ mode that is symmetric about the source axis $\widetilde{Z}$, that is, the mode corresponding to $Y_{20}(\Theta, \Phi)$; the dashed curve shows the eigenspectral mode corresponding to the real part of $Y_{22}(\Theta, \Phi)$. In both cases, the value of the coefficient is divided by the value of the monopole coefficient to give a better idea of the relative importance of the mode in determining the overall angular behavior. The $Y_{20}(\Theta, \Phi)$ mode, which does not involve multivalued behavior on the $\widetilde{Z}$ axis has a nonnegligible coefficient at small χ. By contrast the $Y_{22}(\Theta, \Phi)$, which is multivalued, has a very small coefficient, one that is two orders of magnitude smaller than the monopole, up to $\chi \approx 1$. For larger χ this mode gets "turned on," as it must, since it is part of the radiation.

3.4 Models and methods

Nonlinear scalar models

The model problem of Paper I, in the original co-moving spherical coordinate system is

$$\mathcal{L}(\Psi) = \sigma_{\rm eff}[\Psi]\,, \tag{3.45}$$

with $\mathcal{L}$ taken to be

$$\mathcal{L} \equiv \frac{1}{r^2}\frac{\partial}{\partial r}\left(r^2\frac{\partial}{\partial r}\right) + \frac{1}{r^2\sin\theta}\frac{\partial}{\partial\theta}\left(\sin\theta\frac{\partial}{\partial\theta}\right) + \left[\frac{1}{r^2\sin^2\theta} - \Omega^2\right]\frac{\partial^2}{\partial\varphi^2}\,, \tag{3.46}$$

and with the effective source terms

$$\sigma_{\rm eff}[\Psi] = \text{point source} - \lambda F\,. \tag{3.47}$$

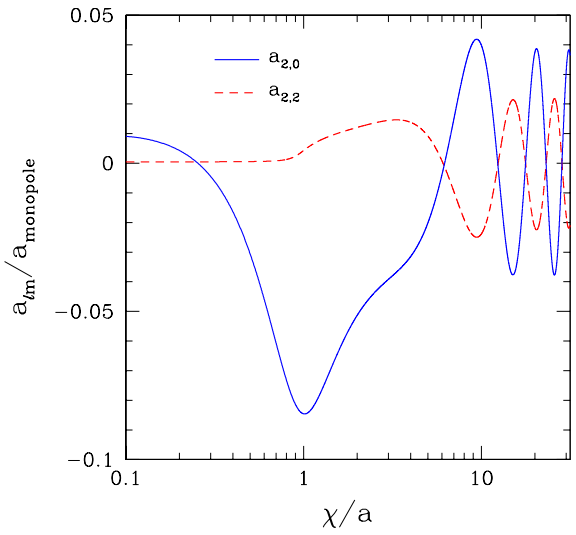

Figure 3.7: The χ dependence of the eigenspectral mode coefficients. The solid curve shows the coefficient of the mode Y_{20} that is symmetric about the $\widetilde{Z}$ axis; the dashed curve shows the real part of Y_{22}. In both cases the plot shows the coefficients divided by the monopole coefficient.

In Paper I an explicit delta function term was used in $\sigma_{\rm eff}$ to represent the point source. Here we compute only outside the source and include source effects by the inner boundary conditions described below.

Our choice of the nonlinearity function F is

$$F = \frac{1}{a^2}\frac{\Psi^5}{\Psi_0^4 + \Psi^4}\,, \tag{3.48}$$

in which Ψ_0 is an adjustable parameter that we set to 0.15 or 0.01 in the numerical results to be reported. As detailed in Paper I, this choice of F allows us to make useful estimates of the action of the nonlinearity. We briefly review this feature here.

We define R to mean distance from a source point, and we identify $R_{\rm lin}$ as the characteristic distance separating the $|\Psi| \gg |\Psi_0|$ near-source nonlinear region, and the $|\Psi| \ll |\Psi_0|$ distant region in which nonlinear effects are negligible. In the nonlinear region near a source of strength Q/a the solution approximately has the Yukawa form

$$\Psi \approx \frac{Q}{a}\,\frac{e^{-\sqrt{-\lambda}\,R/a}}{4\pi R/a} \qquad \text{near source pt}\,. \tag{3.49}$$

We can estimate $R_{\rm lin}$ by taking it to be the value of R at which the expression in Eq. (3.49) is equal

to Ψ_0:

$$\frac{Q}{a}\,\frac{e^{-\sqrt{-\lambda}\,R_{\rm lin}/a}}{4\pi R_{\rm lin}/a} = \Psi_0\,. \tag{3.50}$$

If $R_{\rm lin}$ is significantly less than a, which it is for most of the models we consider, then we can approximate Ψ as having the Yukawa form in Eq. (3.49) out to $R_{\rm lin}$. For $R > R_{\rm lin}$ the linear Coulombic form should apply. We can therefore view $\exp\left(-\sqrt{-\lambda}\,R_{\rm lin}/a\right)$ as a factor by which the strength of the source is reduced. Since the waves are generated at distances from the source much greater than $R_{\rm lin}$, the wave amplitude as well as the monopole moment of the source should be reduced by this factor. We saw in Paper I that these estimates were in reasonably good agreement with the results of computation, good enough to give confidence of the fundamental correctness of the picture on which the estimate is based. We therefore use this picture in the present paper in interpreting some of the computational results.

Boundary conditions

In Paper I the source was taken to be two unit point charges moving at radius a

$$S = \gamma^{-1}\frac{\delta(r-a)}{a^2}\,\delta(\theta-\pi/2)\left[\delta(\varphi)+\delta(\varphi-\pi)\right]\,. \tag{3.51}$$

Here γ is the Lorentz factor $1/\sqrt{1-a^2\Omega^2}$. This factor is necessary if the source is to correspond to points of unit strength as measured in a frame co-moving with the source points. (This factor was inadvertently omitted from the source in Paper I. In that paper only the case $a\Omega = 0.3$ was studied, so we may consider the point sources in Paper I not to have been unit scalar charges, but source points with charges $\gamma = 1.048$.) In the present paper we specify inner boundary conditions on some surface $\chi_{\rm min}$ rather than an explicit source term as in Paper I. Our standard choice for the inner boundary conditions will be those that correspond to the point sources of Eq. (3.51). For this choice of source and for $\chi_{\rm min} \ll a$ and $\ll (-\lambda)^{-1/4}a$, we can use an approximation for a single source point.

In notation appropriate to the 3D case we have

$$R^2 = \tilde{Z}^2 + \gamma^2(\tilde{X}-\beta t)^2 + \tilde{Y}^2 \tag{3.52}$$

Now we use the transformations of Eq. (3.22)–(3.24) to get

$$R^2 = \frac{\chi^4}{4} + \left(\gamma^2-1\right)\left(\tilde{X}-\beta t\right)^2 + \mathcal{O}(\chi^6) = \frac{\chi^4}{4}\left[1+\left(\gamma^2-1\right)\sin^2 2\Theta\cos^2\Phi\right] \tag{3.53}$$

For a unit strength source at position 1, the field near position 1, due to source 1, should be

$$\psi = \frac{1}{4\pi}\frac{1}{R} \approx \frac{1}{4\pi}\frac{2}{\chi^2}\frac{1}{\sqrt{1+(\gamma^2-1)\sin^2 2\Theta\cos^2\Phi}}. \tag{3.54}$$

The outer boundary condition in our computation is based on the the Sommerfeld condition in Eq. (3.28); the ingoing condition is identical except for a change of sign. These radiative boundary conditions should be applied only to the radiative part of the wave. This is done by applying the conditions to the sum on the right side of Eq. (3.38) with the monopole mode omitted. The multipole components of this outer boundary condition are then projected out. The monopole moment, of course, is nonradiative. Since it falls off at large distances as $1/\chi$, the outer boundary condition is taken to be

$$\left(\frac{da^{(0)}}{d\chi} + \frac{a^{(0)}}{\chi}\right)_{\chi_{\max}} = 0\,. \tag{3.55}$$

Extraction of an outgoing approximation

In Paper I, we explained how to extract a good approximation of the outgoing solution from the computed standing-wave solution. That explanation started with the solution of the linearized problem

$$\Psi_{\rm stndcomp} = \sum_{\text{even }\ell}\ \sum_{m=0,\pm2,\pm4..} \alpha_{\ell m}(r) Y_{\ell m}(\theta,\varphi)\,. \tag{3.56}$$

We keep that notation here, but understand that (i) the role of the continuum spherical harmonics is played by appropriate linear combinations of the eigenvectors, that (ii) the role of the coefficients $a_{\ell m}$ is played by appropriate linear combinations of the coefficients $a^{(k)}(\chi)$, and that (iii) the summations only extend up to $\ell_{\max}$.

As in Paper I, this form of the computed standing-wave solution is compared with a general homogeneous linear ($\lambda = 0$) standing-wave (equal magnitude in- and outgoing waves) solution of, with the symmetry of two equal and opposite sources,

$$\Psi_{\rm stndlin} = \sum_{\text{even }\ell,\,m} Y_{\ell m}(\theta,\varphi)\,\left[\tfrac{1}{2}\,C_{\ell m} h_\ell^{(1)}(m\Omega r) + \tfrac{1}{2}\,C^*_{\ell m} h_\ell^{(2)}(m\Omega r)\right]\,. \tag{3.57}$$

A fitting, in the weak-field zone, of this form of the standing-wave multipole to the computed function $\alpha_{\ell m}(r)$ gives the value of $C_{\ell m}$.

By viewing the linear solution as half-ingoing and half-outgoing we define the extracted outgoing solution to be

$$\Psi_{\rm exout} = \sum_{\text{even }\ell}\ \sum_{m=0,\pm2,\pm4..} Y_{\ell m}(\theta,\varphi)\, C_{\ell m} h_\ell^{(1)}(m\Omega r)\,. \tag{3.58}$$

Since this extracted solution was fitted to the computed solution assuming only that linearity ap-

plied, it will be a good approximation except in the strong-field region. In the problems of interest, the strong-fields should be confined to a region near the sources. In those regions, small compared to a wavelength, the field will essentially be that of a static source, and will be insensitive to the distant radiative boundary conditions. As explained in Paper I, the solutions in this region will be essentially the same for the ingoing, outgoing, and standing-wave problem. In this inner region then, we take our extracted outgoing solution simply to be the computed standing-wave solution, so that

$$\Psi_{\rm exout} = \begin{cases} \sum Y_{\ell m} C_{\ell m} h_\ell^{(1)} & \text{weak field outer region} \\ \Psi_{\rm stndcomp} & \text{strong field inner region} \end{cases} . \tag{3.59}$$

The transition between a strong field inner region and weak field outer region can be considered to occur in some range of χ. The maximum χ in this range must be small compared to the wavelength $1/\Omega$, and the minimum χ must correspond to a distance from the source larger than our estimate of $R_{\rm lin}$. [See Eq. (3.50).] For distances R from the source that are of order a or less, $\chi \approx \sqrt{2aR}$ so the the minimum χ in the transition region should be larger than $\chi \approx \sqrt{2aR_{\rm lin}}$.

In order for the extracted solution to be smooth at this boundary, we construct our extracted solution by using a blending of the strong-field inner solution and the weak-field outer solution over a range from $\chi_{\rm low}$ to $\chi_{\rm high}$. In this range we take

$$\Psi_{\rm exout} = \beta(\chi) \sum Y_{\ell m} C_{\ell m} h_\ell^{(1)} + [1 - \beta(\chi)] \, \Psi_{\rm stndcomp} \, . \tag{3.60}$$

Here

$$\beta(\chi) \equiv 3 \left[\frac{\chi - \chi_{\rm low}}{\chi_{\rm high} - \chi_{\rm low}} \right]^2 - 2 \left[\frac{\chi - \chi_{\rm low}}{\chi_{\rm high} - \chi_{\rm low}} \right]^3 , \tag{3.61}$$

so that $\beta(\chi)$ goes from 0 at $\chi = \chi_{\rm low}$ to unity at $\chi = \chi_{\rm high}$ and has a vanishing χ-derivative at both ends. In principle we should choose $\chi = \chi_{\rm high}$ to depend on the location of the wave zone, and hence on Ω, and in principle we should choose $\chi = \chi_{\rm low}$ to depend on the nature of the nonlinearity, and hence on λ and Ψ_0. In practice we have found it to be adequate to choose $\chi_{\rm high} = 2a$ and $\chi_{\rm high} = 3a$ for all models.

Nonlinear iteration

The computational problem of finding a solution Ψ consists of finding a set of coefficients $a^{(k)}(\chi)$ that satisfy the field equation Eqs. (3.40) along with the inner and outer boundary conditions. The operations on the left-hand side of Eqs. (3.40) are linear on the $a^{(k)}(\chi)$, as are the boundary conditions, so the problem of finding the $a^{(k)}(\chi)$ can be written as

$$\sum_k \mathcal{L}_{k'k} a^{(k)} = \mathcal{F}_{k'}(\{a^{(p)}\}) \, , \tag{3.62}$$

where $\mathcal{L}_{k'k}$ is a linear differential operator on the $a^{(k)}(\chi)$, and where $\mathcal{F}_{k'}(\{a^{(p)}\}$, containing the nonlinearity in the model, is nonlinear in the $a^{(k)}(\chi)$.

For different boundary conditions (outgoing or ingoing) the linear operator $\mathcal{L}_{k'k}$ has different forms, but in either form we can invert to get the outgoing or ingoing Green functions $\mathcal{L}^{-1,\mathrm{out}}_{k'k}$ and $\mathcal{L}^{-1,\mathrm{in}}_{k'k}$. In principle we can then find solutions by direct iteration

$$a^{(k')}_{n+1,\mathrm{out}} = \sum_k \mathcal{L}^{-1,\mathrm{out}}_{k'k}\left(\mathcal{F}_{k'}(\{a^{(p)}_{n,\mathrm{out}}\})\right) \qquad a^{(k')}_{n+1,\mathrm{in}} = \sum_k \mathcal{L}^{-1,\mathrm{in}}_{k'k}\left(\mathcal{F}_{k'}(\{a^{(p)}_{n,\mathrm{in}}\})\right)$$

$$a^{(k')}_{n+1,\mathrm{stnd}} = \sum_k \tfrac{1}{2}\left\{\mathcal{L}^{-1,\mathrm{out}}_{k'k} + \mathcal{L}^{-1,\mathrm{out}}_{k'k}\right\}\left(\mathcal{F}_{k'}(\{a^{(p)}_{n,\mathrm{stnd}}\})\right) \ . \tag{3.63}$$

In Paper I it was pointed out that this kind of direct iteration converges only for weak nonlinearity. More generally we use Newton-Raphson iteration and solve

$$\sum_k \left[\mathcal{L}_{k'k} - \left.\frac{\partial \mathcal{F}_{k'}}{\partial a^{(k)}}\right|_{a^{(p)}_n}\right] a^{(k')}_{n+1} = \mathcal{F}_{k'}\left(\{a^{(p)}_n\}\right) - \sum_k \left.\frac{\partial \mathcal{F}_{k'}}{\partial a^{(k)}}\right|_{a^{(p)}_n} a^{(k)}_{n+1}. \tag{3.64}$$

This Newton-Raphson approach can be applied to find outgoing, ingoing and standing-wave solutions analogous to those in Eqs. (3.63). It has been applied with an error measure

$$\epsilon \equiv \sqrt{\frac{1}{k_{\max} n_\chi}\sum_{k=1}^{k_{\max}}\sum_{i=1}^{n_\chi}\left(a^{(k)}_{n+1}(\chi_i) - a^{(k)}_{n+1}(\chi_i)\right)^2} \ . \tag{3.65}$$

Iteration was halted when this error measure fell below $\sim 10^{-6}$. Note that for strongly nonlinear models, convergence sometimes required that the iteration described in Eq. (3.64), had to be somewhat modified. The last term on the right in Eq. (3.64), had to be weighted by a factor less than unity, at least until the iteration got close to the true solution.

3.5 Numerical results

If numerical results are to be trusted they must converge, or at least be stable, as computational parameters (grid size, etc.) change, and there must be evidence that the result is the correct answer to the physical problem. A complication in demonstrating this is that at the same time we are making two different classes of approximations: (i) we use values on a grid in place of the continuum mathematics, (ii) we are keeping only low-order multipoles. In addition, to represent point sources we use approximations for inner boundary data that are exact only only for $\chi_{\min} \to 0$. Our outer boundary conditions in Eq. (3.55) also add an error, in principle one of order $(a/\chi_{\max})^2$, but we have found that this error is negligible compared to that of our other approximations. (Moving the boundary outward has no discernible effect on results.) Here we present results of varying the grid

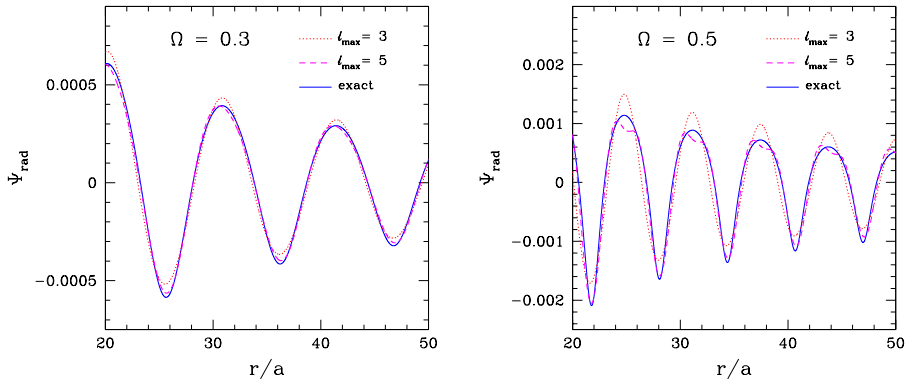

Figure 3.8: Comparison of exact and eigenspectral linear outgoing solutions. The solid curve shows the exact solution, in the wave region, computed from an infinite series. The other curves show the result of computation with a grid with $n_\chi \times n_\Theta \times n_\Phi$=$12001 \times 16 \times 32$ and $\chi_{\min}/a = 0.2$, $\chi_{\max}/a = 75$. Results are shown with $\ell_{\max} = 3$ (monopole and quadrupole modes kept) and $\ell_{\max} = 5$ (monopole, quadrupole, and hexadecapole). The results are shown at $\Theta = 0$ as a function of r, the distance from the center of the configuration.

resolution, the number of multipoles kept, and the inner surface $\chi_{\min}$ on which inner Dirichlet data is set.

Error is most easily measured for solutions to the linear problem since there exists an exact series solution for comparison. Figure 3.8 shows a comparison of this series solution with computed solutions for two different source speeds $a\Omega$. The qualitative features of these plots agree with what should be expected: the eigenspectral/multipole filtering technique is more accurate at lower source speed, and is more accurate when more multipoles are allowed to pass through the "filter." (Of course, there will be a point of diminishing returns. If we let too many modes through then we are no longer filtering, and we experience the difficulties that plagued the FDM method for adapted coordinates.)

An obvious unwelcome feature of the results with $\ell_{\max} = 5$ is the phase error in the hexadecapole mode. This error is especially noticeable in the $a\Omega = 0.5$ plot where it causes an artifact fine structure at the positive peak of the waves. We are investigating the source of this phase error which we suspect is a result of truncation error in angular differencing and/or in the computation of the eigenvectors. We have anecdotal evidence that the phase error decreases as the angular grid is refined.

The reliability of the eigenspectral method for a wider variety of linear models is presented in Table 3.1. In this table, the measure of error is the value of Q_{eff}, the monopole moment computed near the outer boundary for the "charge," i.e., the monopole moment of the two sources each with scalar charge $Q/a = 1$. Though the monopole moment would seem to be less interesting than

Table 3.1: Convergence for rotating linear models. All models have $a\Omega = 0.3$, $\lambda = 0$, and use outgoing boundary conditions at $\chi_{\max} = 50a$. The computed monopole to source strength index, $\gamma Q_{\rm eff}/Q$, is unity in the exact solution. The "two region" computation retains all multipoles for $\chi < 3a$.

n_χ	n_Θ	n_Φ	$\chi_{\min}/a$	$\ell_{\max}$	$\gamma Q_{\rm eff}/Q$	two region
1001	8	16	0.2	3	1.0116	-
2001	16	32	0.2	3	1.0246	-
4001	16	32	0.2	3	1.0275	-
8001	16	32	0.2	3	1.0282	-
16001	32	64	0.2	3	1.0284	-
8001	16	32	0.2	3	1.0282	-
8001	16	32	0.2	5	1.0036	1.0035
8001	16	32	0.2	7	0.9968	0.9966
8001	16	32	0.2	9	0.9934	0.9928
16001	16	32	0.2	5	1.0037	-
16001	16	32	0.1	5	1.0036	-
16001	16	32	0.05	5	1.0032	-
16001	16	32	0.025	5	1.0007	-

features of the radiation, we have found in essentially all computations that the largest error is in the monopole. For example, the majority of the error in the computed amplitude of radiation could be understood to be due to the error in the monopole. The error in the ratio of radiation amplitude to monopole was several times smaller than the raw errors in either quantity by itself. For simplicity we use this one measurement to characterize convergence and correctness.

To show that the computed solution is accurate it is convenient to consider first the linear outgoing problem for two unit point charges, since the solution for this case is known to be $Q_{\rm eff} = 1/\gamma$, where γ, the Lorentz factor, is $1/\sqrt{1 - a^2\Omega^2}$. (The complete solution for Ψ in this case is given as Eq. (10) of Paper I, though the series solution must be multiplied by $1/\gamma$ since we are now considering unit charges.)

Table 3.1 presents results for linear ($\lambda = 0$), rotating ($a\Omega = 0.3$) models, for scalar source points with unit charge. For all models the inner boundary conditions were those of the small-χ point approximation given in Eq. (3.54) at some $\chi_{\min}$. The number of multipoles kept is specified by the parameter $\ell_{\max}$. Choosing $\ell_{\max} = 3$ means that modes corresponding to monopole and quadrupole were kept; $\ell_{\max} = 5$ means that in addition the hexadecapole was kept; and so forth. The accuracy criterion used is the quantity $\gamma Q_{\rm eff}/Q$, the value of which is unity in the exact solution.

The results in the table are divided into three sections. In the first section the number of grid points n_χ, n_Θ, and n_Φ, was varied, while the values of $\chi_{\min}$ and $\ell_{\max}$ are kept fixed. The results show 3% accuracy, and demonstrate that, for the parameters of this computation there is no advantage to grid size larger than $8001 \times 16 \times 32$. Note that simple considerations of truncation error do not apply, since the angular grid is not used in a straightforward finite differencing, but rather to

Table 3.2: Convergence for rotating nonlinear models. All models have $a\Omega = 0.3$, $\lambda = -25$, $\Psi_0 = 0.15$, and all use outgoing boundary conditions at $\chi_{\max} = 50a$. The "two region" method retains all multipoles for $\chi < 3a$.

n_χ	n_Θ	n_Φ	$\chi_{\min}/a$	$\ell_{\max}$	$Q_{\rm eff}/Q$	two region
1001	8	16	0.2	3	0.3440	-
2001	16	32	0.2	3	0.3450	-
4001	16	32	0.2	3	0.3452	-
8001	16	32	0.2	3	0.3452	-
16001	32	64	0.2	3	0.3452	-
8001	16	32	0.2	3	0.3452	-
8001	16	32	0.2	5	0.3431	0.3424
8001	16	32	0.2	7	0.3421	0.3415
8001	16	32	0.2	9	0.3417	0.3410
16001	16	32	0.2	5	0.3230	-
16001	16	32	0.1	5	0.3213	-
16001	16	32	0.05	5	0.3198	-
16001	16	32	0.025	5	0.3192	-

establish the angular eigenvectors.

In the second section the results show that increasing $\ell_{\max}$, for an adequately large grid, improves accuracy, and results come within a fraction of a percent of the correct answer. Note that using *all* the eigenvectors is equivalent to no multipole filtering. In that case we would be simply doing finite differencing in the multipole basis, and we would be plagued by the problems described at the start of Sec. 3.3. Accuracy must, therefore, drop off when $\ell_{\max}$ is increased past some optimal value. The results in the table suggest that the optimal value for this model and this grid size may be $\ell_{\max} \approx 5$. Larger values of $\ell_{\max}$ are more difficult computationally, and appear to give no improvement in accuracy.

In the third section of the table the value of $\chi_{\min}$ is decreased and, for a fairly large grid and for $\ell_{\max} = 5$, the results show that the errors in the inner Dirichlet data were the dominant source of error. More important, the results show that very high accuracy can be achieved with the eigenspectral method using a small number of multipoles.

In the last column of Table 3.1 several results are given of a "two region" method of computation. The motivation for this method is that severe multipole truncation is really necessary only in the wave zone. Closer to the source more multipoles can be kept and more precise computation can be carried out. For the results in the last column, all multipoles up to $\ell_{\max}$ were kept for grid points with $\chi < 3a$; for $\chi > 3a$ only the monopole and quadrupole eigenmodes were used. The results show no increase in error compared with standard method, but the error in any case is dominated by the inner boundary data, not by truncation.

For nonlinear models, with $\lambda = -25$ and $\Psi_0 = 0.15$, Table 3.2 gives results roughly equivalent to the linear-model results in Table 3.1. Now there is no *a priori* correct answer known, so we look only

for convergence of the value of the monopole moment $Q_{\rm eff}$. (Due to the effects of the nonlinearity, this value can be reduced well below unity.) The computational results in the table show few differences from those in Table 3.1. Again, the answer is shown to be stable for moderate grid size, and there is no evidence of a strong dependence on $\ell_{\rm max}$. The two-region computations converged more quickly than those with a uniform multipole cutoff, and give results in good agreement with those of the uniform cutoff standard approach. This two-region technique, therefore, can be considered a computational tool that may prove useful in more difficult problems.

Though there is no *a priori* known general solution for the nonlinear problem, we do know one useful limit of the solution. As argued in Sec. 3.4, and in Paper I, Ψ should have an approximately Yukawa form for a range of small χ. Evidence of this in the results is presented in Fig. 3.9, which gives computed nonlinear outgoing solutions near the sources. The computations start with the boundary conditions of Eq. (3.54). The variable R in the figure is $\widetilde{Z} - a$ along a line through the sources, that is, the radial distance from a source. A straight line in the log-log plots of the figure indicate that Ψ is falling off approximately as $1/4\pi R$; the downward deviation from a straight line is a manifestation of the nonlinearity. According to the analysis following Eq. (3.49), the radius $R_{\rm lin}$ at which nonlinear effects become significant, decreases with increasing $|\lambda|$ and with decreasing Ψ_0. Results for our standard choice $\Psi_0 = 0.15$ are shown on the left. The nonlinear effects become important for R/a=$R_{\rm lin}/a$ on the order a few tenths. In this case Ψ is comparable to Ψ_0 when nonlinear effects become important, and the Yukawa form is not distinguishable from a $1/R$ fall off. For more convincing evidence of the working of the nonlinearity we change Ψ_0 to 0.01. The results, shown on the right in Fig. 3.9 for $\lambda = -25$ shows the excellent agreement of of the computed solution to the Yukawa form in the range R/a=0.1 to around 0.4.

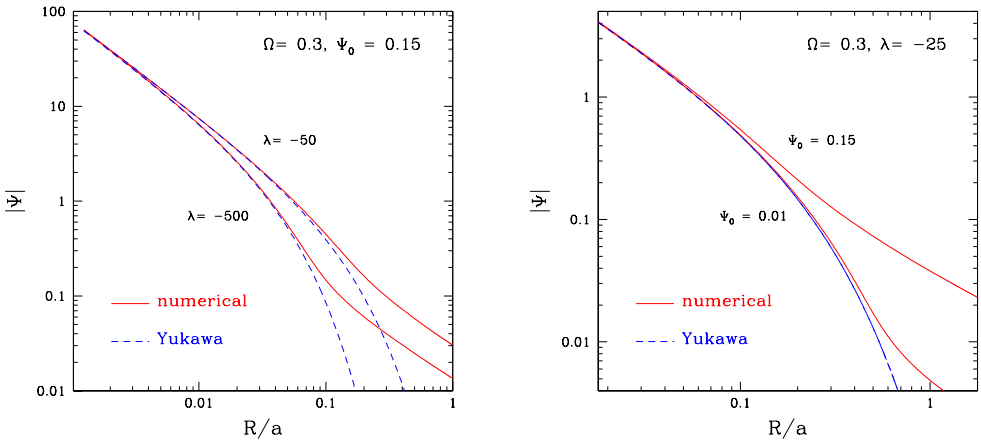

Figure 3.9: Near-source fields for nonlinear models

Table 3.3: The radiation reduction factor due to the nonlinearity. For all cases, $\Psi_0 = 0.15$, and $a\Omega = 0.3$. The second column refers to Eq. (3.50). The third column gives the reduction factors presented in Paper I. The last column gives the results of the eigenspectral computation with $\chi_{\min} = 0.3a$, with outgoing boundary conditions at $\chi_{\max} = 50a$, $\ell_{\max} = 3$, and a grid with $n_\chi = 8001$, $n_\Theta = 16$, $n_\Phi = 32$.

λ	Estimate	Paper I	Eigenspec
-1	69%	78%	77.0%
-2	62%	68%	68.1%
-5	53%	55%	55.7%
-10	46%	47%	46.4%
-25	37%	35%	35.5%
-50	25.6%	-	28.5%
-100	19.5%	-	22.7%

Paper I used Eq. (3.50) as the basis of an estimate of the nonlinear solution. That estimate was applied to the radiation "reduction factor," the factor by which the radiation amplitude is reduced for a nonlinear model as compared with a model with the same parameters, but with $\lambda = 0$. This provides us with a convenient comparison of the nonlinear results in Paper I and with the present eigenspectral method. In Table 3.3 we give those Paper I results again, along with eigenspectral computations of the same models. We present additional models, since the standard coordinate/finite differencing method of Paper I was limited in the size of λ for which Newton-Raphson runs converged; with the eigenspectral method we can give results for much larger values of $-\lambda$. The last column in Table 3.3 gives the computed reduction factor computed with the eigenspectral method keeping only the monopole and quadrupole terms. (Note: In Paper I the factor $1/\gamma$=1/1.048 was mistakenly omitted from the delta function source. Here we choose to treat that as a source of strength 1.048, rather than unity. Our eigenspectral computations therefore used this enhanced source. The estimates of $R_{\rm lin}$ were also slightly in error in Paper I since they assumed a unit source strength. They have been recomputed and are slightly different from the estimates presented in Paper I.)

The agreement of the computed results with the simple estimate is gratifying, as it was in Paper I. More important, the comparison of the second and third columns of Table 3.3 shows that the eigenspectral method with only two multipoles gives 1% agreement of the computed radiation with the very different and much more computationally intensive finite difference method.

We have argued that the details of the higher moments of the source are not important in determining the radiation. Some numerical justification for this is given in Fig. 3.10, which shows computed results for nonlinear models with the standard parameters. The solid curve uses the point source initial data of Eq. (3.54) as inner Dirichlet data at $\chi_{\min} = 0.2a$. For these inner boundary conditions the multipole moments at $\chi_{\min} = 0.2a$ are $a_0 = -13.90$, $a_{20} = 0.11045$. The coefficient

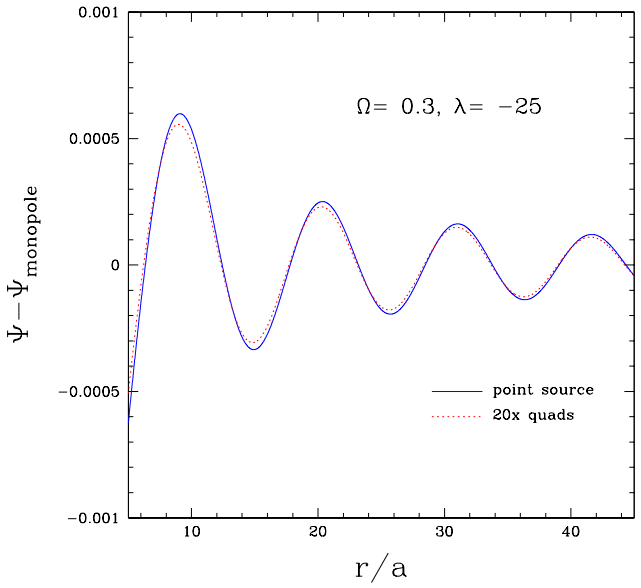

Figure 3.10: For outgoing nonlinear waves, the sensitivity of the radiation to details of source multipole structure

corresponding to the real part of Y_{22} is 0.1920; the coefficient corresponding to the imaginary part is zero. We first compute the outgoing linear solution for these inner Dirichlet data. Next we, somewhat arbitrarily, set all the quadrupole components to -2.209, which is 20 times the original value of a_{20}, and calculate the outgoing linear radiation. The results in Fig. 3.10 show that the effect on the radiation is of order 10%. Some interpretation is needed to connect this result to multipoles of sources, especially because the effect on the radiation of a physically plausible source quadrupole depends on the size of the source.

If we had a source with a surface at $\chi = 0.2a$ the computed result tells us that a rather large deformation, with $|a_{2k}/a_0| \sim 0.16$ will have a 10% effect on the radiation as compared with a source with a negligible quadrupole. With a simple argument, we can apply this 10% effect to sources of other size. Mathematically the conditions at $\chi_{\rm min} = 0.2a$ can be ascribed to a source with a surface at $\chi_{\rm surf} \neq 0.2a$. Quadrupole moments fall off as $1/R^3$, where R is the distance (small compared to a) from the source point, and monopole moments fall off as $1/R$. The quadrupole to monopole ratio, therefore, falls off as $1/R^2$, or $1/\chi^4$. Since the 10% effect corresponds to $|a_{2k}/a_0| \approx 0.16$ at $\chi_{\rm surf} = 0.2a$, it also applies, to $0.16 \times (1/2)^4 \approx 0.01$ at $\chi_{\rm surf} = 0.4a$, and to $0.16 \times (2)^4 \approx 2.6$ at $\chi_{\rm surf} = 0.1a$. This means that the radiation generated is reasonably sensitive to a mild quadrupole deformation of a source that is comparable to the size of the binary system, but for small sources unphysically large deformations are required to have any effect on the radiation. (See also the

related discussion of the two-dimensional case in Appendix 3.9.)

Figure 3.11 shows the central result of our method, the accuracy of the outgoing approximation, for a model with $\Omega = 0.3$ and $\lambda = -25$, one of the models presented in Paper I [10]. A measure of the strength of the nonlinearity is the fact that the nonlinearity reduces the amplitude of the waves to 35% of those for $\lambda = 0$ in the same model (i.e., the same Ω and inner boundary data and outgoing boundary conditions). The figure shows that the extracted solution is in remarkably good agreement with the computed nonlinear solution in the three regions of the extraction protocol described in Sec. 3.4: (i) the wave region in which the solution is treated as a half-outgoing and half-ingoing superposition, (ii) the inner region in which the outgoing solution is taken to be well approximated by the standing wave solution since the radiative boundary conditions are irrelevant close to the source, and (iii) the blending region described in Eqs. (3.60)–(3.61).

The excellent agreement between the computed outgoing solution and the extracted approximation should not be confused with agreement with the exact solution. As we have seen in the comparisons of exact and computed linear solutions, e.g. in Fig. 3.8, the multipole filtering does entail an inaccuracy of a percent or so. Figure 3.11, then, is not a demonstration of the accuracy of the eigenspectral method, but rather a powerful statement about effective linearity, the accuracy of the process of extracting an outgoing approximation from a standing wave solution.

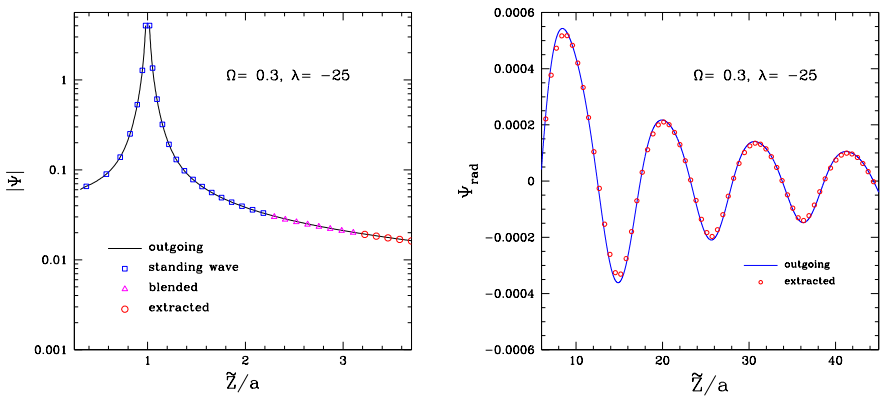

Figure 3.11: Comparison of a computed outgoing nonlinear solution (continuous curve), and an approximation to the outgoing solution extracted from the standing wave solution (data type points). Results are shown for a typical nonlinear scalar model, with parameters $\Omega = 0.3$, $\lambda = -25$, $\Psi_0 = 0.15$, $\chi_{\min}/a = 0.05$, $\chi_{\max}/a = 200$, for a grid with $n_\chi \times n_\Theta \times n_\Phi$=12001 $\times$ 16 $\times$ 32. Results are shown along the $\widetilde{Z}$ axis. The solution is plotted as a function of $\widetilde{Z}$, the distance from the origin along the axis through the source. The extracted points in the wave zone are a result of treating the waves as linear. The small-distance plot shows the blending region and the inner region in which the standing wave solution is used as an approximation for the outgoing solution.

In Table 3.4, we present a broad overview of the validity of effective linearity for a range of

Table 3.4: The reduction factors for nonlinear outgoing waves (the decrease in amplitude due to nonlinear effects). For $a\Omega = 0.3$ models, the factors are compared for the directly computed outgoing solutions and for outgoing solutions extracted from nonlinear standing waves solutions. The $\lambda = 0$ results indicate linear models in which the reduction factor is unity by definition. The value 1.0064 found for the extracted solution gives an indication of the numerical accuracy of the extraction procedure. All results were computed with $\ell_{\max} = 3$, $\chi_{\min} = 0.2a$, and $\chi_{\max} = 50a$ on a grid with $n_\chi \times n_\Theta \times n_\Phi = 8001 \times 16 \times 32$. The reduction factor was computed by taking the ratio of the quadrupole components. Also listed are the estimated values of $R_{\rm lin}$, the distance from the sources beyond which the nonlinear effects are suppressed, and estimates of the reduction factors based on the estimates of $R_{\rm lin}$. [See Eq. (3.50).] For consistency with Table 3.3 the source strength has been taken to be 1.048.

	$\Psi_0 = 0.15$				$\Psi_0 = 0.01$			
λ	$R_{\rm lin}/a$	estimate	true	extract	$R_{\rm lin}/a$	estimate	true	extract
0	-	-	1	1.0064	-	-	1	1.0064
-1	0.355	0.7012	0.7695	0.7740	1.574	0.2072	0.1745	0.1728
-2	0.321	0.6348	0.6813	0.6852	1.266	0.1668	0.1323	0.1315
-5	0.274	0.5417	0.5565	0.5597	0.936	0.1233	0.09121	0.09109
-10	0.238	0.4707	0.4643	0.4669	0.737	0.09711	0.06764	0.06771
-25	0.193	0.3811	0.3548	0.3569	0.532	0.0700	0.04453	0.04466
-50	0.162	0.3191	0.2849	0.2865	0.412	0.05427	0.03231	0.03244
-100	0.133	0.2635	0.2265	0.2278	0.317	0.0418	0.02368	0.02380

nonlinear strengths in $a\Omega = 0.3$ models. As in Table 3.3, we give the nonlinear "reduction factor," the reduction in wave amplitude due to nonlinear effects. Here we present a comparison of those factors for computed outgoing solutions and for the approximate outgoing solution extracted from the standing wave solution. It is clear that, judged by the criterion of reduction factor (and limited to $a\Omega = 0.3$ models), effective linearity is highly accurate, within a percent or so, for models with extremely strong nonlinear effects. In the $\Psi_0 = 0.01$, $\lambda = -100$ model, the nonlinearity reduces the wave amplitude by a factor of 40, but effective linearity appears to be accurate to better than 1%. It should be noted that the agreement of the computed outgoing solution and the extracted outgoing solution is excellent even for models (e.g., $\Psi_0 = 0.01$ and small λ) for which the strong nonlinear effects are not confined to a small region around the source points. This is evidence that effective linearity does not require such confinement; it only requires that the nonlinearity falls off before outer boundary effects are important, i.e., in the induction and wave zones.

3.6 Conclusions

The fundamental concepts of the PSW method were introduced in Paper I. In the current paper we concentrate on efficient numerical methods for solving the mixed PDEs of the PSW method. The innovative method we present here is a mixture of adapted coordinates, multipole filtering, and the use of eigenvectors in place of continuum multipoles. This method seems to meet the needs

of the problem remarkably well. The method requires relatively little machine memory, and runs very quickly on workstations. The power of the method has allowed us to run nonlinear scalar field models with larger velocity and much larger nonlinearity than was possible with the method of Paper I.

We have shown that the method is convergent and reliable in a number of senses: (i) For a linear problem, the computed solution converges to the known analytic solution as the computational grid becomes finer and the number of retained multipoles increases. (ii) For a nonlinear model the Newton-Raphson iteration stably and reliably gives a solution to outgoing or standing-wave problems. We have confirmed that our solutions agree, to the expected accuracy, with the results presented in Paper I.

In addition to the role they play in the efficient computation, the adapted coordinates are very well suited to the specifications of inner boundary conditions, rather than to the specification of actual source terms. We have confirmed that there is low sensitivity to the details of the inner boundary conditions. The solution in the wave zone has a sensitivity to these conditions that is compatible with physical intuition; there is no excess sensitivity that is an artifact of the numerical method.

Two major points are worth emphasizing. First, we have confirmed that excellent results can be obtained for moderate source velocities with computations that keep only the monopole and the quadrupole moments of the adapted coordinates. This allows an enormous decrease in the computational intensity of a solution. The cost is only a moderate increase in analytic complexity. A second and even more important point concerns "effective linearity," the approximate validity of superposing half-ingoing and half-outgoing nonlinear solutions. We have been able to verify effective linearity for a wider range of nonlinear models than in Paper I, including models with extremely strong nonlinearity.

3.7 Acknowledgements

We gratefully acknowledge the support of NSF grant PHY0244605 and NASA grant ATP03-0001-0027 to UTB, and of NSF grant PHY-0099568 and NASA grant NAG5-12834 to Caltech. We thank Chris Beetle and Lior Burko for useful discussions and suggestions. We also thank Alexey Blinov and Maria Cranor for help with figures, and with checking calculations.

3.8 Appendix: Coefficients for adapted coordinates

The inner products $\vec{\nabla}\chi \cdot \vec{\nabla}\Theta$, $\vec{\nabla}\chi \cdot \vec{\nabla}\Phi$, and $\vec{\nabla}\Theta \cdot \vec{\nabla}\Phi$, vanish since the adapted coordinates are orthogonal (with respect to a Cartesian metric on $\widetilde{X}$,$\widetilde{Y}$,$\widetilde{Z}$). The other inner products and Laplacians

are evaluated with the explicit transformations in Eqs. (3.19)–(3.24), from which we find

$$\nabla^2\chi = \frac{a^2+2Q}{\chi^3} \tag{3.66}$$

$$\nabla^2\Theta = \frac{\sqrt{Q+a^2+\chi^2\cos(2\,\Theta)}}{\sqrt{Q-a^2-\chi^2\cos(2\,\Theta)}}\,\frac{\left(Q-a^2\right)}{\chi^4} \tag{3.67}$$

$$\nabla^2\Phi = 0 \tag{3.68}$$

$$\vec{\nabla}\chi\cdot\vec{\nabla}\chi = \frac{Q}{\chi^2} \tag{3.69}$$

$$\vec{\nabla}\Theta\cdot\vec{\nabla}\Theta = \frac{Q}{\chi^4} \tag{3.70}$$

$$\vec{\nabla}\Phi\cdot\vec{\nabla}\Phi = 2\,\frac{Q+a^2+\chi^2\cos(2\,\Theta)}{\chi^4\sin^2(2\,\Theta)} \tag{3.71}$$

where Q is the function

$$Q \equiv \sqrt{a^4+2\,a^2\chi^2\cos(2\Theta)+\chi^4}\,. \tag{3.72}$$

In general, the $\bar{A}$ and $\bar{B}$ terms are computed from the following:

$$\bar{A}_{\chi\chi} = Z^2\left(\frac{\partial\chi}{\partial X}\right)^2 + X^2\left(\frac{\partial\chi}{\partial Z}\right)^2 - 2XZ\left(\frac{\partial\chi}{\partial X}\right)\left(\frac{\partial\chi}{\partial Z}\right) \tag{3.73}$$

$$\bar{A}_{\Theta\Theta} = Z^2\left(\frac{\partial\Theta}{\partial X}\right)^2 + X^2\left(\frac{\partial\Theta}{\partial Z}\right)^2 - 2XZ\left(\frac{\partial\Theta}{\partial X}\right)\left(\frac{\partial\Theta}{\partial Z}\right) \tag{3.74}$$

$$\bar{A}_{\Phi\Phi} = Z^2\left(\frac{\partial\Phi}{\partial X}\right)^2 + X^2\left(\frac{\partial\Phi}{\partial Z}\right)^2 - 2XZ\left(\frac{\partial\Phi}{\partial X}\right)\left(\frac{\partial\Phi}{\partial Z}\right) \tag{3.75}$$

$$\bar{A}_{\chi\Theta} = Z^2\left(\frac{\partial\chi}{\partial X}\right)\left(\frac{\partial\Theta}{\partial X}\right) + X^2\left(\frac{\partial\chi}{\partial Z}\right)\left(\frac{\partial\Theta}{\partial Z}\right) - XZ\left[\left(\frac{\partial\chi}{\partial Z}\right)\left(\frac{\partial\Theta}{\partial X}\right) + \left(\frac{\partial\chi}{\partial X}\right)\left(\frac{\partial\Theta}{\partial Z}\right)\right] \tag{3.76}$$

$$\bar{A}_{\chi\Phi} = Z^2\left(\frac{\partial\chi}{\partial X}\right)\left(\frac{\partial\Phi}{\partial X}\right) + X^2\left(\frac{\partial\chi}{\partial Z}\right)\left(\frac{\partial\Phi}{\partial Z}\right) - XZ\left[\left(\frac{\partial\chi}{\partial Z}\right)\left(\frac{\partial\Phi}{\partial X}\right) + \left(\frac{\partial\chi}{\partial X}\right)\left(\frac{\partial\Phi}{\partial Z}\right)\right] \tag{3.77}$$

$$\bar{A}_{\Theta\Phi} = Z^2\left(\frac{\partial\Theta}{\partial X}\right)\left(\frac{\partial\Phi}{\partial X}\right) + X^2\left(\frac{\partial\Theta}{\partial Z}\right)\left(\frac{\partial\Phi}{\partial Z}\right) - XZ\left[\left(\frac{\partial\Theta}{\partial Z}\right)\left(\frac{\partial\Phi}{\partial X}\right) + \left(\frac{\partial\Theta}{\partial X}\right)\left(\frac{\partial\Phi}{\partial Z}\right)\right] \tag{3.78}$$

$$\bar{B}_{\chi} = Z^2\left(\frac{\partial^2\chi}{\partial X^2}\right) + X^2\left(\frac{\partial^2\chi}{\partial Z^2}\right) - 2XZ\left(\frac{\partial^2\chi}{\partial X\partial Z}\right) - X\left(\frac{\partial\chi}{\partial X}\right) - Z\left(\frac{\partial\chi}{\partial Z}\right) \tag{3.79}$$

$$\bar{B}_{\Theta} = Z^2\left(\frac{\partial^2\Theta}{\partial X^2}\right) + X^2\left(\frac{\partial^2\Theta}{\partial Z^2}\right) - 2XZ\left(\frac{\partial^2\Theta}{\partial X\partial Z}\right) - X\left(\frac{\partial\Theta}{\partial X}\right) - Z\left(\frac{\partial\Theta}{\partial Z}\right) \tag{3.80}$$

$$\bar{B}_{\Phi} = Z^2\left(\frac{\partial^2\Phi}{\partial X^2}\right) + X^2\left(\frac{\partial^2\Phi}{\partial Z^2}\right) - 2XZ\left(\frac{\partial^2\Phi}{\partial X\partial Z}\right) - X\left(\frac{\partial\Phi}{\partial X}\right) - Z\left(\frac{\partial\Phi}{\partial Z}\right)\,. \tag{3.81}$$

In the case of the TCBC coordinates defined in Eqs. (3.19) – (3.24), the explicit forms of the coefficients are

$$\bar{A}_{\chi\chi} = \frac{a^4\sin^2(2\Theta)\,\cos^2\Phi}{\chi^2} \tag{3.82}$$

$$\bar{A}_{\Theta\Theta} = \frac{\cos^2\Phi\ \left[\chi^2 + a^2\cos(2\Theta)\right]^2}{\chi^4} \tag{3.83}$$

$$\bar{A}_{\Phi\Phi} = \sin^2\Phi\ \frac{Q + a^2 + \chi^2\cos(2\Theta)}{Q - a^2 - \chi^2\cos(2\Theta)} \tag{3.84}$$

$$\bar{A}_{\chi\Theta} = \frac{a^2\ \left[\chi^2 + a^2\cos(2\Theta)\right]\ \sin(2\Theta)\cos^2\Phi}{\chi^3} \tag{3.85}$$

$$\bar{A}_{\chi\Phi} = -\frac{a^2\ \left[Q + a^2 + \chi^2\cos(2\Theta)\right]\ \sin\Phi\cos\Phi}{\chi^3} \tag{3.86}$$

$$\bar{A}_{\Theta\Phi} = -\frac{\sin(\Phi)\cos(\Phi)\left[a^2 + \chi^2\cos(2\,\Theta) + Q\right]\left[\chi^2 + a^2\cos(2\,\Theta)\right]}{\chi^4\sin(2\,\Theta)} \tag{3.87}$$

$$\bar{B}_{\chi} = \frac{a^2\left[\cos^2(\Phi)\left\{3a^2\cos^2(2\Theta) - Q - 2a^2 + \chi^2\cos(2\Theta)\right\} + Q + a^2 + \chi^2\cos(2\Theta)\right]}{\chi^3} \tag{3.88}$$

$$\bar{B}_{\Phi} = \frac{\left(3Q + a^2 + \chi^2\cos 2\Theta\right)\sin(\Phi)\cos(\Phi)}{Q - a^2 - \chi^2\cos 2\Theta} \tag{3.89}$$

$$\bar{B}_{\Theta} = \frac{\sqrt{Q + a^2 + \chi^2\cos(2\Theta)}}{\chi^6\sqrt{Q - a^2 - \chi^2\cos(2\Theta)}}\ (c\cos^2\Phi + d) \tag{3.90}$$

where

$$c \equiv a^2\chi^4\cos(2\,\Theta) + 2\,a^4\chi^2 + 4\,a^6\cos(2\,\Theta) + 4\,a^4\chi^2\left(\cos(2\,\Theta)\right)^2 - 4\,a^4 Q\cos(2\,\Theta) - 2\,a^2 Q\chi^2 - \chi^6 \tag{3.91}$$

$$d \equiv \chi^4\left(a^2\cos(2\,\Theta) + \chi^2\right)\ . \tag{3.92}$$

The coefficients needed in the Sommerfeld boundary condition Eq. (3.27) are

$$\Gamma^{\Theta} = \frac{\chi^2 + a^2\cos 2\Theta}{\chi^2}\ \cos\Phi = \cos\Phi\left(1 + \mathcal{O}(a^2/\chi^2)\right) \tag{3.93}$$

$$\Gamma^{\Phi} = -\sqrt{\frac{Q + a^2 + \chi^2\cos(2\Theta)}{Q - a^2 - \chi^2\cos(2\Theta)}}\ \sin\Phi = -\cot\Theta\sin\Phi\left(1 + \mathcal{O}(a^2/\chi^2)\right) \tag{3.94}$$

$$\Gamma^{\chi} = \frac{1}{\chi^3}\ \sqrt{\left[Q + a^2 + \chi^2\cos(2\Theta)\right]\left[Q - a^2 - \chi^2\cos(2\Theta)\right]} = \frac{2\sin 2\Theta}{\chi}\left(1 + \mathcal{O}(a^2/\chi^2)\right)\ . \tag{3.95}$$

3.9 Appendix: The standard spectral method for the 2+1 dimensional linear scalar field

Here we consider the 2+1 dimensional version of our helical problem, one equivalent to the 3+1 problem with line sources that are infinitely long in the $\widetilde{z}$ (equivalently $\widetilde{Y}$) direction. We choose to set $\lambda = 0$, i.e. , to make the problem linear, since that will turn out to allow a very efficient method of multipole projection. The 2+1 dimensional version of Eqs. (3.3) and (3.51) is

$$\frac{1}{r}\frac{\partial}{\partial r}\left(r\,\frac{\partial \Psi}{\partial r}\right) + \left(\frac{1}{r^2} - \Omega^2\right)\frac{\partial^2 \Psi}{\partial \varphi^2} = \gamma^{-1}\frac{\delta(r-a)}{a}\left[\delta(\varphi) + \delta(\varphi - \pi)\right] . \tag{3.96}$$

Here $\varphi \equiv \phi - \Omega t$ where ϕ is the usual polar angle $\tan^{-1}(\widetilde{y}/\widetilde{x})$ in the $\widetilde{x}, \widetilde{y}$ plane.

The 2+1 dimensional forms of the adapted coordinates of Sec. 3.2 are

$$\chi \equiv \sqrt{r_1 r_2} = \left\{\left[(\widetilde{x}-a)^2 + \widetilde{y}^2\right]\left[(\widetilde{x}+a)^2 + \widetilde{y}^2\right]\right\}^{1/4} \tag{3.97}$$

$$\Theta \equiv \frac{1}{2}\left(\theta_1 + \theta_2\right) = \frac{1}{2}\tan^{-1}\left(\frac{2\widetilde{x}\widetilde{y}}{\widetilde{x}^2 - a^2 - \widetilde{y}^2}\right) . \tag{3.98}$$

With these coordinates the 2+1 dimensional version of Eq. (3.1) takes a form like that of Eq. (3.8). As in the 3-dimensional case we use only the homogeneous form of Eq. (3.96), since the effect of the source will be introduced through inner boundary conditions.

In working with the sourceless linear 2+1 dimensional problem, it turns out to be convenient to divide the original wave equation by Q/χ^2, where

$$Q \equiv \sqrt{a^4 + 2\,a^2\chi^2\cos(2\Theta) + \chi^4} . \tag{3.99}$$

The result is

$$\mathcal{L}\Psi \equiv \chi^2 Q^{-1}\left(\nabla^2 - \Omega^2\partial_\varphi^2\right)\Psi = A\,\frac{\partial^2\Psi}{\partial\chi^2} + B\,\frac{\partial^2\Psi}{\partial\Theta^2} + 2C\,\frac{\partial^2\Psi}{\partial\chi\partial\Theta} + D\,\frac{\partial\Psi}{\partial\chi} + E\,\frac{\partial\Psi}{\partial\Theta} , \tag{3.100}$$

where

$$A = 1 - \Omega^2\,\frac{a^4\sin^2(2\Theta)}{Q} \tag{3.101}$$

$$B = \frac{1}{\chi^2}\left[1 - \Omega^2\,\frac{\left(a^2\cos(2\Theta) + \chi^2\right)^2}{Q}\right] \tag{3.102}$$

$$C = -\Omega^2\,\frac{a^2\sin(2\Theta)\left(a^2\cos(2\Theta) + \chi^2\right)}{Q\,\chi} \tag{3.103}$$

$$D = \frac{1}{\chi}\left[1 - \Omega^2\,\frac{a^2\left(-a^2 + 3\,a^2\cos^2(2\,\Theta) + 2\,\chi^2\cos\left(2\,\Theta\right)\right)}{Q}\right] \tag{3.104}$$

$$E \;=\; +\Omega^2\,\frac{2a^2\left(2\,a^2\cos(2\,\Theta)+\chi^2\right)\sin(2\,\Theta)}{Q\,\chi^2}\,. \tag{3.105}$$

By dividing through by Q we have put the wave equation in a form in which the coefficients are Θ-independent in the $\Omega \to 0$ limit. With the standard method, used below, for projecting out multipole components of the wave equation, this property of the coefficients means that the mixing of the multipoles can be directly ascribed to the rotation.

We now expand the standing wave solution $\Psi(\chi,\Theta)$ as

$$\Psi(\chi,\Theta) = \sum_{n=0,2,4\ldots}^{N} a_n(\chi)\cos n\Theta\,, \tag{3.106}$$

and our equation becomes

$$\sum_{n=0,2,4\ldots}^{N}\left[A\,\frac{d^2a_n(\chi)}{d\chi^2} - n^2B\;a_n(\chi) + D\,\frac{da_n(\chi)}{d\chi}\;\right]\cos n\Theta$$

$$-\left[2nC\,\frac{da_n(\chi)}{d\chi}\;+nEa_n(\chi)\right]\sin n\Theta\,. \tag{3.107}$$

Projecting with $\int_0^{2\pi}\sin m\Theta\cdots d\Theta$, gives zero by symmetry; projecting with $\int_0^{2\pi}\cos m\Theta\cdots d\Theta$, gives

$$\sum_{n=0,2,4\ldots}^{N}\alpha_{mn}\,\frac{d^2a_n(\chi)}{d\chi^2} + \beta_{mn}a_n(\chi) + \gamma_{mn}\,\frac{da_n(\chi)}{d\chi} = 0 \qquad m = 0,2,4\ldots. \tag{3.108}$$

where

$$\alpha_{mn} \;\equiv\; \frac{4}{\pi}\int_0^{\pi/2}\cos m\Theta\cos n\Theta\,[A(\chi,\Theta)]\;d\Theta \tag{3.109}$$

$$\begin{aligned}\beta_{mn} \;\equiv\; & -n^2\,\frac{4}{\pi}\int_0^{\pi/2}\cos m\Theta\cos n\Theta\,[B(\chi,\Theta)]\;d\Theta \\ & -n\frac{4}{\pi}\int_0^{\pi/2}\cos m\Theta\sin n\Theta\,[E(\chi,\Theta)]\;d\Theta\end{aligned} \tag{3.110}$$

$$\begin{aligned}\gamma_{mn} \;\equiv\; & \frac{4}{\pi}\int_0^{\pi/2}\cos m\Theta\cos n\Theta\,[D(\chi,\Theta)]\;d\Theta \\ & -2n\frac{4}{\pi}\int_0^{\pi/2}\cos m\Theta\sin n\Theta\,[C(\chi,\Theta)]\;d\Theta\,.\end{aligned} \tag{3.111}$$

When the explicit expressions for A–E, in Eqs. (3.101)–(3.105), are used in Eqs. (3.109)–(3.111), the results are

$$\alpha_{mn} = \epsilon_{mn} - \Omega^2\;a^4\;\frac{4}{\pi}\int_0^{\pi/2}\cos m\Theta\cos n\Theta\;\frac{\sin^2(2\Theta)}{Q}\;d\Theta \tag{3.112}$$

$$\beta_{mn} = -\frac{n^2}{\chi^2}\epsilon_{mn} + \frac{4}{\pi}\frac{\Omega^2}{\chi^2}\left[n^2\int_0^{\pi/2}\cos m\Theta\cos n\Theta\;\frac{\left(a^2\cos(2\Theta)+\chi^2\right)^2}{Q}\;d\Theta\right.$$

$$-n\int_0^{\pi/2}\cos m\Theta\sin n\Theta\;\frac{2a^2\left(2\,a^2\cos(2\,\Theta)+\chi^2\right)\sin(2\,\Theta)}{Q}\Bigg] \tag{3.113}$$

$$\gamma_{mn}=\frac{1}{\chi}\epsilon_{mn}+\frac{4}{\pi}\frac{a^2\Omega^2}{\chi}\left[-\int_0^{\pi/2}\cos m\Theta\cos n\Theta\frac{\left(-a^2+3\,a^2\cos^2(2\,\Theta)+2\,\chi^2\cos\left(2\,\Theta\right)\right)}{Q}\,d\Theta\right.$$

$$\left.+2n\int_0^{\pi/2}\cos m\Theta\sin n\Theta\frac{\sin(2\Theta)\;\left(a^2\cos(2\Theta)+\chi^2\right)}{Q}\,d\Theta\right] \tag{3.114}$$

where

$$\epsilon_{mn}\equiv\delta_{m+n,0}+\delta_{m,n}=\begin{cases}2\text{ if }m=n=0\\1\text{ if }m=n\neq 0\\0\text{ if }m\neq n\end{cases}\quad. \tag{3.115}$$

The integrals needed in Eqs. (3.112)–(3.114) are all of the form

$$\mathcal{I}=\int_0^{\pi/2}\frac{\cos\left(2P\Theta\right)\sin\left(2J\Theta\right)}{Q(\chi,\Theta)}\,d\Theta \tag{3.116}$$

where P and J are integers. With trigonometric identities, and with the substitution $x=\sin\Theta$, such integrals can all be expressed in terms of integrals of the form

$$\mathcal{K}_N(k)\equiv\int_0^1\frac{x^N}{\sqrt{1-k^2x^2}\sqrt{1-x^2}}\,dx\,, \tag{3.117}$$

where

$$k\equiv\frac{2a\chi}{a^2+\chi^2}\,. \tag{3.118}$$

For the integrals in Eq. (3.116) only even values of N are needed for $\mathcal{K}_N$. All such integrals can be evaluated in terms of the complete elliptic integrals [18],

$$K(k)\equiv\int_0^1\frac{1}{\sqrt{1-k^2x^2}\sqrt{1-x^2}}\,dx\qquad E(k)\equiv\int_0^1\frac{\sqrt{1-k^2x^2}}{\sqrt{1-x^2}}\,dx\,. \tag{3.119}$$

To use the elliptic integrals to evaluate the $\mathcal{K}_N(k)$, for even N, we start with the relationship (for $M\geq 0$)

$$0=\int_0^1(d/dx)\left[x^{2M+1}\sqrt{1-k^2x^2}\sqrt{1-x^2}\right]\,dx$$

$$=\int_0^1\frac{x^{2M}\left[(2M+1)-(2M+2)(1+k^2)x^2+(2M+3)k^2x^4\right]}{\sqrt{1-k^2x^2}\sqrt{1-x^2}}\,dx\,. \tag{3.120}$$

This gives us the recursion relation

$$(2M+1)\mathcal{K}_{2M}(k)-(2M+2)(1+k^2)\mathcal{K}_{2M+2}(k)+(2M+3)k^2\mathcal{K}_{2M+4}(k)=0\,. \tag{3.121}$$

We know that

$$\mathcal{K}_0(k) = K(k) \ ,$$

and we can easily show that

$$\mathcal{K}_2(k) = \frac{1}{k^2}\left[K(k) - E(k)\right] \ ,$$

so all values of $\mathcal{K}_{2M}(k)$ follow from the recursion relation.

Very efficient computation follows from the results above. At a given value of χ, only two integral evaluations must be done, those for $K(k)$ and $E(k)$. All values of $\mathcal{K}_{2M}(k)$ then follow from the recursion relation, and hence all values of α_{mn}, β_{mn}, γ_{mn}, can be found at negligible computational expense.

Here we use this method only to illustrate important general issues. To make this illustration as clear as possible, we take the simplest nontrivial case of the multipole expansion: we keep only the $n = 0$ and $n = 2$ terms [19], so that

$$\Psi(\chi, \Theta) = a_0(\chi) + a_2(\chi)\cos 2\Theta \ . \tag{3.122}$$

The equations in Eq. (3.108), then describe the interaction of the monopole $a_0(\chi)$ and quadrupole $a_2(\chi)$ terms. For $\chi/a \ll 1$ and $\chi/a \gg 1$ the terms that mix the multipoles die off; it is only in the transaction region, $\chi/a \sim 1$ that there is strong mixing of the multipoles, a mixing that for our problem is quadratic in the source velocity $a\Omega$. The process of the generation of radiation can be viewed as the growth of a_2 from the small-χ near-source region to the large-χ radiation region.

In principle, the linear standing wave problem could be solved by including a term $a_s \sin(2\Theta)$, leading to an additional second-order differential equation. At some inner boundary $\chi_{\rm min} \ll a$ the values could be specified for all multipoles, and at some outer boundary $\chi_{\rm min} \gg a$, a fall off condition could be specified for a_0. Ingoing or outgoing conditions could be used to relate a_2 and a_s.

It is easier, and more instructive, to use another approach to finding the standing-wave solution, the minimum amplitude method presented in Paper I. For the linear problem it is straightforward to show [8] that of all solutions that (i) have the form of Eq. (3.106), and (ii) correctly couple to the source, the solution with the minimum wave amplitude in each multipole is the standing-wave solution, i.e., the solution that is half-ingoing and half-outgoing. In principle, the minimum-amplitude criterion can be used as a definition of standing waves in a nonlinear problem. Here we are dealing with a linear problem, so we are simply exploiting a known property of the solutions.

In this minimum-amplitude method we specify a_0, $da_0/d\chi$, a_2 and $da_2/d\chi$ at $\chi_{\rm min}$, then shoot outward. The choice of a_0, and $da_0/d\chi$, at $\chi_{\rm min}$ are those for unit point charges. The value of a_0 at $\chi_{\rm min}$ sets the scale of the linear solution. The value of $da_0/d\chi$ can be approximated as $1/\pi\chi_{\rm min}$.

In principle this starting value can be adjusted so that at large χ the results for a_0 satisfy the fall-off condition $da_0/d\chi = a_0/\chi\log\chi$. In practice, the overall result (after the minimization described below) is very insensitive to the choice of $da_0/d\chi$ at $\chi_{\min}$.

The choices for a_0 and $da_0/d\chi$ at $\chi_{\min}$ are determined by the form of Ψ very close to one of the unit point charges. Some care is necessary in taking this limit. In the x, y frame co-moving with one of the unit point charges the value of Ψ due only to that charge is $\log\left[(x^2+y^2)/a^2\right]/4\pi$. We must now transform this result to the "lab" frame of our calculation in which we use coordinates $\widetilde{x}, \widetilde{y}, t$. The Lorentz transformation is

$$x = \widetilde{x} \qquad y = \gamma\widetilde{y}\,. \tag{3.123}$$

(The last relation follows since $\widetilde{y}$ is in a coordinate frame that comoves with the point source, but which is related to the lab frame by a simple translation by vt.) Since Ψ is a Lorentz invariant we have $\Psi = \log(r^2/a^2)/4\pi$ where $r^2 = \widetilde{x}^2 + \gamma^2\widetilde{y}^2$, expressed in adopted coordinates, is

$$r^2 = \frac{1}{4}\frac{\chi^4}{a^2}\left[1 - \frac{1}{2}\frac{\chi^2}{a^2}\cos(2\Theta)\right] + \left(\gamma^2-1\right)\frac{1}{4}\sin^2(2\Theta)\frac{\chi^4}{a^2}\left[1 - \frac{\chi^2}{a^2}\cos 2\Theta\right]\,, \tag{3.124}$$

and Ψ is therefore

$$\begin{aligned}\psi &= \frac{1}{4\pi}\left(\log\left[\frac{\chi^4}{4a^4}\right] + \log\left[1 + \left(\gamma^2-1\right)\sin^2(2\Theta)\right]\right) + \mathcal{O}(\chi/a)^2 \\ &= \frac{1}{4\pi}\left(\log\left[\frac{\chi^4}{4a^4}\right] + 2\log\left[\frac{\gamma+1}{2}\right]\right) + \mathcal{O}(\cos(4\Theta)) + \mathcal{O}(\chi/a)^2\,.\end{aligned} \tag{3.125}$$

The last relationship is meant to emphasize that in the $\chi \to 0$ limit Ψ has no $\cos(2\Theta)$ component. This comes from the fact that the Lorentzian pancaking of the source field has the nature of a local quadrupole deformation, while the $\cos(2\Theta)$ term represents a local dipole. (As defined in Eq. (3.98), $\Theta \approx \theta/2$ or $(\theta+\pi)/2$ near the source points, so the $\cos(2\Theta)$ dependence near the source point corresponds to the dipole field of the source.)

The contribution, near $\chi = 0$, due to the distant point can be approximated with $r = 2a$ so that at $\chi = \chi_{\min}$ the appropriate starting conditions for unit point charges are

$$a_0 = \frac{1}{4\pi}\left(\log\left[\frac{\chi^4}{4a^4}\right] + 2\log\left[\frac{\gamma+1}{2}\right] + \log 4\right) \quad \frac{da_0}{d\chi} = \frac{1}{\pi\chi} \quad a_2 = 0 \quad \frac{da_2}{d\chi} = 0. \tag{3.126}$$

While $da_2/d\chi$ at $\chi \to 0$ vanishes in principle, in the numerical computation, $da_2/d\chi$ plays a more delicate role. It is chosen to minimize the wave amplitude at large χ. It is actually the values of a_2 and $da_2/d\chi$, at $\chi_{\min}$ that determine the radiation field at large χ, and determine whether there is any a_2 radiation except the radiation coupled to the source. To minimize that radiation (and suppress radiation that is not coupled to the source) we fix a_2 and vary $da_2/d\chi$. (We could just as

well fix $da_2/d\chi$ and vary a_2.) Minimization is taken to mean the minimum value of the amplitude defined by

$$\text{Amp} \equiv \left\langle (\chi/a)^{1/2} \sqrt{a_2^2 + \frac{1}{4\Omega^2}\left(\frac{da_2}{d\chi} + \frac{a_2}{2\chi}\right)^2} \right\rangle . \tag{3.127}$$

For the expected large distance form of the waves $r^{-1/2}\cos(2\Omega r + \delta)$, the quantity inside the angle brackets is expected to be nearly χ-independent; this is confirmed by the numerical results. The angle brackets denote an average over a wavelength, resulting in a quantity that is χ independent to high accuracy at large χ. In our minimization procedure we vary $da_2/d\chi$ at $\chi_{\min}$ to minimize Amp. The meaningfulness of this minimization procedure, of course, depends on its insensitivity to the details of how a_2 and $da_2/d\chi$ are chosen at $\chi_{\min}$. This is discussed below.

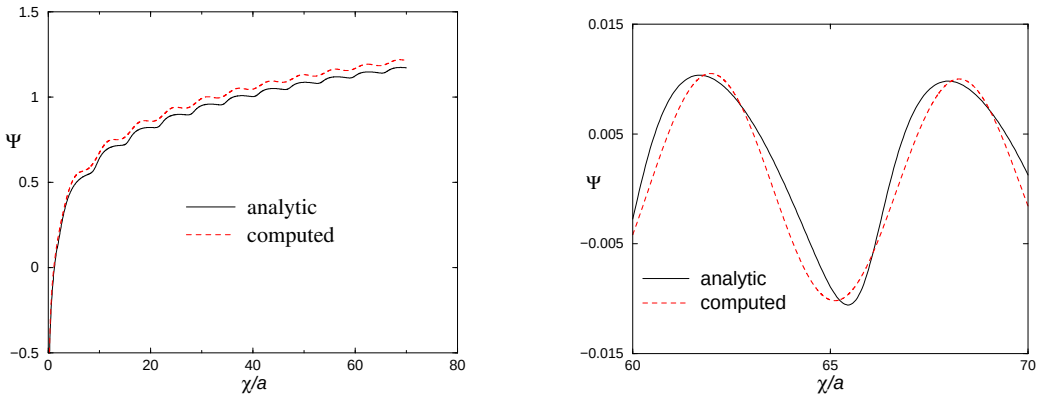

Figure 3.12: Comparison of the analytic waves and the computed waves for $a\Omega = 0.5$, $\chi_{\min} = 0.05a$ and $\chi_{\max} = 70a$, and $a_2 = 0$ at $\chi_{\min} = 0$. The monopole is subtracted in the figure on the right to allow for a comparison of computed and analytic wave amplitudes. .

For the source speed $a\Omega = 0.5$, results, for $\Theta = 0$, of our computation are shown in Fig. 3.12, and are compared with the analytic solution for two point sources each of unit strength

$$\Psi = \sqrt{1-a^2\Omega^2}\left[\left\{\begin{array}{ll} \frac{1}{\pi}\ln(r/a) & \text{for } r > a \\ 0 & \text{for } r < a \end{array}\right\} + \sum_{m=2,4,6\ldots} J_m(m\Omega r_<)N_m(m\Omega r_>)\cos(m\Theta)\right], \tag{3.128}$$

(where $r_>, r_<$ indicate, respectively, the greater and lesser of r, a). For our more typical choice $a\Omega = 0.3$, the difference of the computed and analytic solution are too small to show up well in a plot. The plot on the left shows the comparison for the whole range of the computation. Dividing the analytic solution by 1.039 brings it into nearly perfect alignment with the computed solution; we therefore characterize the overall error in the computed solution as 3.9%. Overall errors for several values of $a\Omega$ are listed in Table 3.5.

The plot on the right in Fig. 3.12 focuses on the oscillations in the far zone by removing effective monopole terms. For the analytic result this is done by subtracting the asymptotic monopole solu-

Table 3.5: The errors (differences from analytic solution) of the monopole+quadrupole approximation for different values of the source speed $a\Omega$. The overall error is the difference of the computational and analytic solution at $\chi_{\max} = 70a$; the wave error is the difference of the computational and analytic peak-to-peak amplitudes.

$a\Omega$	Overall Error	Wave Error
0.1	0.08%	0.14%
0.3	1.0%	0.1%
0.5	3.9%	1.2%
0.7	13%	3%

tion $\sqrt{1-a^2\Omega^2}\,\log(\chi^2/2a^2)/\pi$. For the computed solution this is done by plotting only $a_2(\chi)$. The comparison shows two effects. First, there is a 1.2% difference in peak-to-peak amplitude. Errors of this type are tabulated for different values of $a\Omega$ in Table 3.5. A second and more interesting effect, apparent in the waves of Fig. 3.12, is the difference in shapes. Since the computed wave contains only the quadrupole component it has a nearly perfect sinusoidal form. The analytic solution, on the other hand, shows a rapid rise and a slow fall off due to the contribution of the hexadecapole and higher modes. For small $a\Omega$ the amplitude of a $\cos(m\Theta)$ component depends on $a\Omega$ approximately according to $(a\Omega)^{m-0.5}$, so the contributions from $m = 4, 6, 8\ldots$ decrease quickly with Ω.

We now want to use the accuracy of the linear 2+1 dimensional model to make an important point about the role played by the source structure in generating radiation. To do this in our monopole+quadrupole computational models we depart from considering "point" sources and we vary the choice of $a_2(\chi_{\min})$. In each case the specification of $da_2/d\chi$ at $(\chi_{\min})$ is fine-tuned to get a minimum wave amplitude at $\chi_{\max}$. For this investigation to have physical relevance we need to ask what a "reasonable" value is for $a_2(\chi_{\min})$.

If $\chi_{\rm surf}$ specified the (approximately spherical) location of the outer surface of the source, then we can write

$$a_2(\chi_{\rm surf}) = \kappa\, a_0(\chi_{\rm surf})\,, \tag{3.129}$$

where κ indicates the relative quadrupole strength of the source. We expect κ to be small for realistic sources and of order unity only for highly distorted sources.

In our computational models we take $\chi_{\min}/a$ to be very small, typically 0.05. It is useful, however, to consider the computed results applying to larger sources, sources with $\chi_{\rm surf}$ significantly larger than $\chi_{\min}$. To do this we can use the fact that outside, but very close to a source, a_0 varies as $\log\chi$ and a_2 falls off as $1/\chi^2$. From this we conclude that for small χ

$$\frac{a_2(\chi_{\min})}{a_0(\chi_{\min})} = \kappa\,\frac{\chi^2_{\rm surf}\log\chi_{\rm surf}}{\chi^2_{\min}\log\chi_{\min}}\,. \tag{3.130}$$

We can now fix $\kappa = \pm 1$, its maximum reasonable value, and we can choose a value of $\chi_{\rm surf}$, the value at which the quadrupole and monopole have equal strength. These choices determine $a_2(\chi_{\rm min})/a_0(\chi_{\rm min})$, and therefore the computational model.

Results are presented in Table 3.6. For the choices $\chi_{\rm surf}/a = 0.1$, 0.2 and 0.3, and for κ =1 and -1, the amplitude of the quadrupole waves is computed for $\chi_{\rm min}/a = 0.05$ and $\chi_{\rm max}/a = 70$. For each choice of $a_2(\chi_{\rm min})$, the starting value of $da_2/d\chi$ is fine tuned for minimum wave amplitude. Since $a_2(\chi)$ should have the form const./χ^2, the value of $da_2/d\chi$ should be very nearly equal to $-2a_2/\chi$. The values for $da_2/d\chi$ in table 3.6 are very close to this prediction. The table presents the "relative amplitude," the ratio of the radiation amplitude to the radiation amplitude for the case $a_2(\chi_{\rm min}) = 0$. It is clear from the results that the structure of the source has little influence on the radiation unless the source is large and has an extreme nonspherical deformation.

In the case of gravitational sources, an even stronger statement can be made. As already pointed out, the "quadrupole" mode $a_2(\chi)\cos(2\Theta)$ near the source point is actually a local dipole $a_2(\chi)\cos(\theta_1)$. This dipole moment can be viewed as a displacement of the center of scalar charge, and hence a change in the radius at which the source points move. The change in the radiation amplitude can be ascribed to this change in radius. This explanation of the change can be made quantitative. We let r represent the distance from source point 1 at which inner boundary data is being specified and we let δ be the radial distance by which the center of scalar charge is being moved outward. The solution for the scalar field is

$$\Psi = \frac{1}{4\pi}\log\left(r^2 - 2r\delta\cos\theta_1 + \delta^2\right) \approx \frac{1}{4\pi}\left[\log r^2 - 2(\delta/r)\cos\theta_1\right] . \tag{3.131}$$

From this we infer that

$$a_2 = -\frac{\delta}{2\pi r} . \tag{3.132}$$

This means that the radius of orbital motion is changed from a according to

$$a \to a + \delta = a - 2\pi r a_2 . \tag{3.133}$$

From Eq. (3.128) we see that for quadrupole radiation (that is, $m = 2$) the amplitude of the waves scales $\propto a^2$. It follows that the amplitude of the waves should depend on a_2 according to

$$\text{amplitude} \propto 1 - 4\pi r a_2/a . \tag{3.134}$$

For the computations presented in Table 3.6, a_2 is evaluated at $\chi_{\rm min} = 0.05a$, so $r \approx 0.05^2 a$. The numerical results following from this simple explanation of the shift of the center of charge, presented as the last column in Table 3.6, are convincingly accurate.

Table 3.6: The effect on the wave amplitude of the conditions on a_2 and $da_2/d\chi$ at $\chi_{\rm min} = 0.3a$. The role of the a_2 term can be understood as an effective shift of the center of scalar charge. See text for details.

κ	$\chi_{\rm surf}$	$a_2(\chi_{\rm min})$	$da_2/d\chi$ at $\chi_{\rm min}$	Rel. Amp.	$1 - 4\pi r a_2/a$
1	0.1	-2.92007	116.999652	1.045	1.046
-1	0.1	2.92007	-117.011864	0.955	0.954
1	0.2	-8.16416	327.127955	1.125	1.128
-1	0.2	8.16416	-327.140167	0.875	0.872
1	0.3	-13.7416	550.612310	1.211	1.216
1	0.3	13.7416	-550.6245521	0.789	0.784

This explanation for the role of the $m = 2$ mode is of considerable significance for gravitational problems. The equivalence principle implies that there is no local dipole for the gravitational sources. Thus the starting value of a_2 which, at large distances gives the quadrupole radiation, is not a parameter of the structure of the source; if we know the location of the effective center of the source, the structure is fixed.

3.10 Appendix: Details of the eigenspectral method

In this appendix we explain how the continuum angular Laplacian of Eq. (3.35) is implemented as a linear operator in the $N = n_\Theta \times n_\Phi$ dimensional space. That linear operator must represent the angular Laplacian evaluated at a grid point Θ_a, Φ_b. That is, the linear operator $L_{ab,ij}$ must satisfy

$$\left[\sin\Theta\nabla^2_{\rm ang}\Psi\right]_{ab} \approx \sum_{ij} L_{ab,ij}\Psi_{ij}\,, \tag{3.135}$$

where the approximation is due to FDM truncation error. It will be convenient below to write the linear operator as a sum $L = L^{(1)} + L^{(2)}$ with $L^{(1)}$ containing Θ derivatives and $L^{(2)}$ containing Φ derivatives.

By exploiting the symmetries of the PSW configuration we can limit the range of angular coordinates to one quarter of the complete 2-sphere. The indices a, i range from 1 to n_Θ , representing, respectively $\Theta = \Delta\Theta/2$ to $\Theta = \pi/2 - \Delta\Theta/2$. The indices b, j range from 1 to n_Φ, representing, respectively $\Phi = \Delta\Phi/2$ to $\Phi = \pi - \Delta\Phi/2$. Our goal here will be to show that with this choice of the grid, the linear operator can be chosen to have the symmetry

$$L_{ab,ij} = L_{ij,ab}\,. \tag{3.136}$$

The elements of $L_{ab,ij}$ have a different form for the boundaries at $\Theta = \Delta\Theta/2, \pi/2 - \Delta\Theta/2$ and at $\Phi = \Delta\Phi/2, \pi - \Delta\Phi/2$, and in the interior of the angular grid. We consider each case separately.

Case I: Interior points, $1 < a < n_\Theta$**,** $1 < b < n_\Phi$

The first contribution is

$$L^{(1)}_{ab,ij} = \frac{\delta_{bj}}{(\Delta\Theta)^2}\left[\sin\Theta_{a-1/2}\delta_{a-1,i} - \left(\sin\Theta_{a+1/2} + \sin\Theta_{a-1/2}\right)\,\delta_{ia} + \sin\Theta_{a+1/2}\delta_{a+1,i}\right] \tag{3.137}$$

and the second is

$$L^{(2)}_{ab,ij} = \frac{1}{(\Delta\Phi)^2}\frac{\delta_{ai}}{\sin\Theta_a}\left(\delta_{b-1,j} - 2\delta_{b,j} + \delta_{b+1,j}\right)\,. \tag{3.138}$$

Here $\delta_{j,c}$ is the Kronecker delta, and $\sin\Theta_{a\pm1/2}$ is defined to mean $\sin\left(\Theta_a \pm \Delta\Theta/2\right)$. It can be seen that both contributions to $L_{ab,ij}$ are symmetric with respect to the interchange of the pair ab with the pair ij, and hence Eq. (3.136) is satisfied.

Case II: Boundary at $a = 1$**,** $1 < b < n_\Phi$

The Θ derivative part of the operator formally takes the form

$$L^{(1)}_{1b,ij} = \frac{\delta_{bj}}{(\Delta\Theta)^2}\left[\sin 0\,\delta_{0,i} - \left(\sin 0 + \sin\Delta\Theta\right)\,\delta_{i1} + \sin\Delta\Theta\delta_{2,i}\right]\,. \tag{3.139}$$

In the sum in Eq. (3.135) the $\delta_{0,i}$ term respresents $\Psi(\Theta = -\Delta\Theta/2, \Phi)$, which is not a value available on the angular grid. This term however, is multiplied by $\sin 0 = 0$ and can be ignored, so $L^{(1)}_{ab,ij}$ satisfies the symmetry condition in Eq. (3.136). The form of $L^{(2)}_{ab,ij}$ also applies without change to $a = 1$, and hence Eq. (3.136) is satisfied for the index range $a = 1$, $1 < b < n_\Phi$.

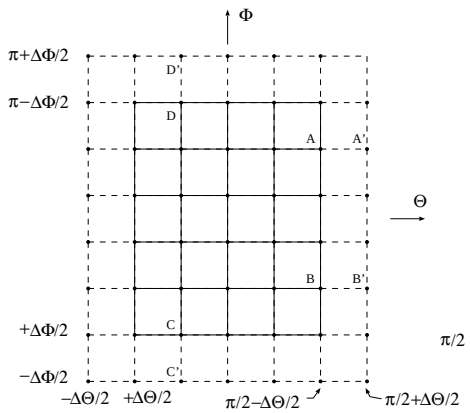

Figure 3.13: An angular grid with $n_\Theta = 5$ and $n_\Phi = 6$. Grid points, points at which a value for Ψ is computed, are connected by solid lines. The dashed lines extend the grid to "phantom" points needed for the computation. For the FDM implementation of the Laplacian at point A the value of Ψ at point A' is needed. By the symmetry of the physical problem, this value can be replaced by the value at point B, which *is* on the grid. Similarly the value at B', when needed, can be replaced by that at point A; the value at C' can be replaced by that at C; the value at D' can be replaced by that at D; and so forth.

Case III: Boundary at $a = n_\Theta$, $1 < b < n_\Phi$

In this case the Θ derivative part of the operator formally takes the form

$$L^{(1)}_{n_\Theta b,ij} = \frac{\delta_{bj}}{(\Delta\Theta)^2}\left[\sin(\pi/2-\Delta\Theta)\delta_{n_\theta-1,i} - \left(\sin(\pi/2-\Delta\Theta)+\sin(\pi/2)\right)\delta_{n_\Theta,i} + \sin(\pi/2)\delta_{n_\theta+1,i}\right] . \tag{3.140}$$

The $\delta_{n_\theta+1,i}$ represents $\Psi(\Theta_{n_\Theta+1},\Phi_b) = \Psi(\Theta = \pi/2+\Delta\Theta/2,\Phi)$. This value is not directly available on the grid, but we can get an equivalent value that is on the grid by using the symmetry

$$\Psi(\Theta,\Phi) = \Psi(\pi-\Theta,\pi-\Phi) . \tag{3.141}$$

This is equivalent to the statement that Ψ is invariant with respect to inversion through the origin and reflection in the orbital plane (or equivalently $\widetilde{Z}\to-\widetilde{Z}$, $\widetilde{X}\to-\widetilde{X}$, $\widetilde{Y}\to\widetilde{Z}$ in Fig. 3.3.) As shown in Fig. 3.13, we can, therefore, replace $\Psi(\Theta=\pi/2+\Delta\Theta/2,\Phi)$ with $\Psi(\Theta=\pi/2-\Delta\Theta/2,\pi-\Phi)$, or can replace $\Psi(\Theta_{n_\Theta+1},\Phi_b)$ with $\Psi(\Theta_{n_\Theta},\Phi_{\bar{b}})$ where $\bar{b}\equiv N_\Phi - b$. Equivalently, we can rewrite Eq (3.140) as

$$L^{(1)}_{n_\Theta b,ij} = \frac{\delta_{bj}}{(\Delta\Theta)^2}\left[\sin(\pi/2-\Delta\Theta)\delta_{n_\theta-1,i} - \left(\sin(\pi/2-\Delta\Theta)+\sin(\pi/2)\right)\delta_{n_\Theta,i}\right] + \frac{\delta_{\bar{b}j}}{(\Delta\Theta)^2}\sin(\pi/2)\delta_{n_\theta,i} . \tag{3.142}$$

The term that has been introduced is

$$L^{(1)}_{n_\Theta b,n_\Theta\bar{b}} = \frac{1}{(\Delta\Theta)^2} . \tag{3.143}$$

Since $\bar{\bar{b}} = b$, we have $L^{(1)}_{n_\Theta b,n_\Theta\bar{b}} = L^{(1)}_{n_\Theta\bar{b},n_\Theta b}$ which satisfies the symmetry in Eq. (3.136). All other terms in $L^{(1)}_{n_\Theta b,ij}$ remain the same as in Case I, and hence Eq. (3.136) is satisfied for the index range $a = n_\Theta$, $1 < b < n_\Phi$.

Case IV: Boundaries at $1 \le a < n_\Theta$, $b = 1$ and $b = n_\Phi$

For these boundary points Case I considerations apply to $L^{(1)}_{ab,ij}$. For $b = 1$, however, $L^{(2)}_{ab,ij}$ takes the form

$$L^{(2)}_{a1,ij} = \frac{1}{(\Delta\Phi)^2}\frac{\delta_{ai}}{\sin\Theta_a}\left(\delta_{0,j} - 2\delta_{1,j} + \delta_{2,j}\right) . \tag{3.144}$$

The $\delta_{0,j}$ refers to an angular location ($\Phi = -\Delta\Phi/2$) that is not on the grid. Here we can use the symmetry $\Psi(\Theta,-\Phi)$=$\Psi(\Theta,\Phi)$, and hence $\Psi(\Theta,-\Delta\Phi/2)$=$\Psi(\Theta,\Delta\Phi/2)$, to replace $\delta_{0,j}$ with $\delta_{1,j}$. The resulting $L_{ab,ij}$ satisfies the symmetry of Eq. (3.136).

For $b = n_\Phi$, the considerations are very similar. The $\Psi(\Theta,-\Phi)$=$\Psi(\Theta,\Phi)$ symmetry is used to replace $\delta_{n_\Phi+1,j}$ by $\delta_{n_\Phi,j}$.

Case V: Boundaries at $a = n_\Theta$, $b = 1$ and $b = n_\Phi$

Here the forms of $L^{(1)}_{n_\Theta 1,ij}$ and $L^{(1)}_{n_\Theta n_\Phi,ij}$ are taken from Case III with $b = 1, n_\Phi$, and the forms of $L^{(2)}_{n_\Theta 1,ij}$ and $L^{(2)}_{n_\Theta n_\Phi,ij}$ are taken from Case IV with $a = n_\Theta$. From the considerations of Case III and Case IV it follows that the results here also satisfy Eq. (3.136).

To clarify the results derived above, we list here all nonzero elements of $L^{(1)}_{ab,ij}$ and $L^{(2)}_{ab,ij}$:

$$L^{(1)}_{ab,ab} = -\frac{\sin\Theta_{a+1/2} + \sin\Theta_{a-1/2}}{(\Delta\Theta)^2} \quad \text{all } a, b \tag{3.145}$$

$$L^{(1)}_{ab,(a-1)b} = L^{(1)}_{(a-1)b,ab} = \frac{\sin\Theta_{a-1/2}}{(\Delta\Theta)^2} \quad \text{for } 1 < a \tag{3.146}$$

$$L^{(1)}_{ab,(a+1)b} = L^{(1)}_{(a+1)b,ab} = \frac{\sin\Theta_{a+1/2}}{(\Delta\Theta)^2} \quad \text{for } a < n_\Theta \tag{3.147}$$

$$L^{(1)}_{n_\Theta b,n_\Theta \bar{b}} = L^{(1)}_{n_\Theta \bar{b},n_\Theta b} = \frac{1}{(\Delta\Theta)^2} \quad \text{where } \bar{b} = n_\Phi - b \tag{3.148}$$

$$L^{(2)}_{ab,ab} = -\frac{2}{\sin\Theta_a(\Delta\Theta)^2} \quad \text{all } 1 < b < n_\Phi \tag{3.149}$$

$$L^{(2)}_{a1,a1} = L^{(2)}_{an_\Phi,an_\Phi} = -\frac{1}{\sin\Theta_a(\Delta\Theta)^2} \tag{3.150}$$

$$L^{(2)}_{ab,a(b+1)} = L^{(2)}_{a(b+1),ab} = \frac{1}{\sin\Theta_a(\Delta\Theta)^2} \quad \text{all } b < n_\Phi \tag{3.151}$$

$$L^{(2)}_{ab,a(b-1)} = L^{(2)}_{a(b-1),ab} = \frac{1}{\sin\Theta_a(\Delta\Theta)^2} \quad \text{all } 1 < b\,. \tag{3.152}$$

This completes the proof that for the full range of its indices $L_{ab,ij}$ satisfies Eq. (3.136). With this result in hand we can go on to the computation that is central to our eigenspectral method: finding the eigenvectors of

$$\sum_{ij} L_{ab,ij}\, Y^{(k)}_{ij} = -\Lambda^{(k)}\, \sin\Theta_a Y^{(k)}_{ab}\,, \tag{3.153}$$

where the k index indicates that the solution is the kth eigensolution. Aside from the $\sin\Theta_a$ factor on the right, this is a standard eigenproblem for a symmetric real matrix, and we conclude that the eigenvalues are real and the eigenvectors form a complete basis. It is easy to show that the factors of $\sin\Theta_a$ do not change these conclusions.

The finite difference problem in Eq. (3.153), along with Eq. (3.135), can be seen to be the finite difference equivalent of the continuum eigenproblem

$$\nabla^2_{\text{ang}} Y(\Theta,\Phi) = -\Lambda Y(\Theta,\Phi)\,. \tag{3.154}$$

With the usual boundary conditions, the solutions of Eq. (3.154) can be taken to be the spherical harmonics, and Λ to have values $\ell(\ell+1)$ where ℓ is an integer. The solutions of Eq. (3.153) should then

be approximately proportional to the real and imaginary parts of $Y_{\ell m}(\Theta_i, \Phi_j)$, the approximation becoming perfect as the grid goes to the continuum limit.

We next define the inner product in the grid vector space by the expression in Eq. (3.36). It is simple to show, following the usual pattern with eigenproblems, that with respect to this inner product, two nondegenerate eigenvectors $Y_{ij}^{(k)}$. and $Y_{ij}^{(k')}$ are orthogonal as a consequence of the symmetry in Eq. (3.136). Since we find the grid multipoles to have no degeneracies it follows that the solutions to Eq. (3.153) constitute a complete, orthogonal basis, and can be normalized to satisfy Eq. (3.37). It should be clear that this is the finite difference equivalent of well-known continuum relations. In the continuum limit, Eq. (3.36) is the inner product on the two sphere. The orthogonality of our grid multipoles is therefore just the finite difference form of the orthogonality of spherical harmonics.

Bibliography

[1] É. É. Flanagan and S. A. Hughes. Phys. Rev. D **57**, 4566, 1998.

[2] T. Damour, B. R. Iyer, and B. S. Sathyaprakash. Phys. Rev. D **63**, 044023, 2001.

[3] S. A. Hughes, S. Marka, P. L. Bender, and C. J. Hogan. eConf **C010630**, P402, 2001.

[4] B. Bruegmann, W. Tichy, and N. Jansen. Phys. Rev. Lett. **92**, 211101, 2004.

[5] T. W. Baumgarte and S. L. Shapiro. Phys. Rept. **376**, 41, 2003.

[6] M. Campanelli. Proceedings of the 5th LISA Symposium. preprint astro-ph/0411744, 2004.

[7] J. T. Whelan, W. Krivan, and R. H. Price. Class. Quant. Grav. **17**, 4895, 2000.

[8] J. T. Whelan, C. Beetle, W. Landry, and R. H. Price. Class. Quant. Grav. **19**, 1285, 2002.

[9] R. H. Price. Class. Quant. Grav. **21**, S281, 2004.

[10] Z. Andrade et al., Phys. Rev. D **70**, 064001, 2004.

[11] A. Čadež. Ph.D. thesis. University of North Carolina at Chapel Hill, Chapel Hill, North Carolina, 1971.

[12] A. Čadež. Ann. Phys. **91**, 58, 1975.

[13] G. B. Cook. Phys. Rev. D **44**, 2983, 1991.

[14] G. B. Cook et al., Phys. Rev. D **47**, 1471, 1993.

[15] H. P. Pfeiffer, L. E. Kidder, M. A. Scheel, and S. A. Teukolsky. Comput. Phys. Commun. **152**, 253, 2003.

[16] E. H. Lockwood. *A book of curves.* Cambridge University Press, Cambridge, 1967, Chap. 25, pages 186–190.

[17] C. Beetle. (in preparation).

[18] M. Abramowitz and I. A. Stegun. *Handbook of mathematical functions with formulas, graphs, and mathematical tables*. Dover, New York, 1970.

[19] The explicit $\alpha_{mn}, \beta_{mn}, \gamma_{mn}$ coefficients for $n = 0, 2, 4$ can be found at `http://www.physics.utah.edu/~rprice/AREA51DOCS/spectral.pdf`.

Chapter 4

Optimal constraint projection for hyperbolic evolution systems

Originally published as Phys.Rev. D70 (2004) 084017.

Techniques are developed for projecting the solutions of symmetric hyperbolic evolution systems onto the constraint submanifold (the constraint-satisfying subset of the dynamical field space). These optimal projections map a field configuration to the "nearest" configuration in the constraint submanifold, where distances between configurations are measured with the natural metric on the space of dynamical fields. The construction and use of these projections is illustrated for a new representation of the scalar field equation that exhibits both bulk and boundary generated constraint violations. Numerical simulations on a black-hole background show that bulk constraint violations cannot be controlled by constraint-preserving boundary conditions alone, but are effectively controlled by constraint projection. Simulations also show that constraint violations entering through boundaries cannot be controlled by constraint projection alone, but are controlled by constraint-preserving boundary conditions. Numerical solutions to the pathological scalar field system are shown to converge to solutions of a standard representation of the scalar field equation when constraint projection and constraint-preserving boundary conditions are used together.

4.1 Introduction

The exponential growth of constraint violations in the evolutions of black-hole spacetimes is probably the most critical problem facing the numerical relativity community today. The evolution equations of any self-consistent evolution system with constraints (including Einstein's) ensure that if the constraints are satisfied identically on an initial spacelike surface, they will remain satisfied within the domain of dependence of that surface. This does not mean that small initial violations

of the constraints will remain small, or that constraint violations will not flow into the computational domain through timelike boundaries. On the contrary, experience has shown that constraint violations seeded by roundoff or truncation level errors in the initial data tend to grow exponentially in the numerical evolutions of black-hole spacetimes (see, e.g., [25, 31, 36]). At present these constraint-violating instabilities are the limiting factor preventing these numerical simulations from running for the desired length of time. Finding ways to control the growth of these constraints is therefore our most urgent priority.

Recent work has demonstrated numerically that constraint violations that flow into the computational domain through timelike boundaries can be controlled effectively by the use of special constraint-preserving boundary conditions [23, 40, 10, 41, 32]. A number of groups have constructed such boundary conditions for various representations of the Einstein evolution system [39, 16, 10, 40, 11, 41, 17, 18, 12, 19, 4]. However, constraint violations in many evolution systems (including Einstein's) are driven by bulk terms in addition to boundary terms in the constraint evolution equations. In this paper we demonstrate that such bulk generated constraint violations cannot be controlled effectively through the use of boundary conditions alone. Alternative methods of controlling the growth of constraints are still required in such systems.

The most widely used method of controlling the growth of constraints in the Einstein evolution system is called fully constrained evolution. In this method, which is often applied to spherical or axisymmetric problems, symmetry considerations are used to separate the dynamical fields into those that are determined by solving evolution equations and those that are determined by enforcing the constraints at each time step [38, 2, 13, 3, 1, 14, 15]. In 3D problems without symmetry there is no obvious way to perform such a separation in a general coordinate system; however, fully constrained 3D methods based on spherical coordinates have yielded promising results [8]. Various groups have studied a closely related method, constraint projection, which can be used for general 3D evolutions in any coordinate system. The idea is to use the evolution system to advance all of the dynamical fields in time, and then at each time step (or whenever the constraints become too large) to force the solution back onto the constraint submanifold by solving the constraint equations (for the conformal factor and the longitudinal part of the extrinsic curvature in the case of the Einstein system). The first preliminary results obtained with this constraint projection technique have been moderately successful [5, 8, 37]. Constraint projection has not gained widespread use in 3D simulations, however, due in part to the traditionally high cost of solving the elliptic constraint equations. Difficult questions also remain unanswered about the proper boundary conditions to impose on the constraint equations, for example at black hole excision boundaries. Moreover, little attention has been given to the question of whether these projections correctly map a field configuration onto (or near) the correct point of the constraint submanifold, i.e., the point through which the exact evolution of the system would pass at that time. In particular, it is not clear whether the

overall time evolution scheme—including the projections—remains consistent, stable, and convergent.

The need to enforce constraints is a common feature of many problems in mathematical physics besides numerical relativity, and for many problems successful techniques have been developed to ensure that numerical solutions satisfy the needed constraints. Under mild assumptions on the constraints, the subset of the field space satisfying the constraint equations defines a formal differentiable manifold (a classical result due to Ljusternik [45]), and the evolution of a dynamical system of ordinary (ODE) or partial differential equations (PDE) subject to constraints may be viewed as evolution on this submanifold. Constraint control methods for such systems are generally based on ideas from variational mechanics, where the Lagrangian (whose stationary points describe the physical states of the system) is augmented with a sum of terms consisting of products of Lagrange multipliers and the constraints [27, 6, 33]. A necessary condition for a configuration point to be a solution of both the field equations and the constraint equations is that the augmented Lagrangian be stationary with respect to variations in both the fundamental fields and the Lagrange multipliers [45]. The additional terms in the augmented Lagrangian involving Lagrange multipliers can be viewed as forcing the dynamics to remain on the constraint submanifold.

These augmented Lagrangian techniques are the basis of well-studied numerical methods for controlling constraint violations in ODE systems. Many ODE systems are subject to algebraic constraints which must be preserved as the solution evolves. For such systems there exist numerical integration techniques that enforce these algebraic constraints exactly, and that also conserve various important properties of the ODE solution (e.g., time-reversibility and symplectic structure). These numerical techniques are derived by adding to the ODEs terms chosen to make a suitable augmented Lagrangian for the system stationary [20, 29, 30, 28, 22]. The resulting numerical schemes, referred to as "step-and-project" methods, can be thought of as standard time integration steps followed by projections. First a preliminary step is taken forward in time using a standard numerical scheme, after which the solution will generally not satisfy the constraint equations. Then the solution from the preliminary step is corrected using a formal (optimal, or nearest point) projection back onto the constraint submanifold. This projection step typically involves solving algebraic equations. Unlike the simple constraint projection methods used so far in numerical relativity, "step-and-project" numerical methods for constrained systems are well studied and well understood. It has been shown that they retain the consistency and stability properties of the original one-step method on which they are based, and they generally have the same convergence properties [22]. These techniques are immediately applicable to constrained PDE systems that are discretized in space to produce constrained ODE systems (as we do, see Sec. 4.4); and numerical methods based on augmented Lagrangians for PDE systems have also been developed [44, 9].

In this paper we apply these augmented variational techniques to obtain equations that project

solutions of constrained hyperbolic evolution systems onto the constraint submanifold of the appropriate dynamical field space. We construct projections that are optimal, in the sense that they map a given field configuration to the "nearest" point on the constraint submanifold. We use the natural metric, the symmetrizer, that exists in any symmetric hyperbolic evolution system to define distances on the space of fields. Hence this optimal projection is the one that minimizes this symmetrizer distance (typically called the energy) between a given field configuration and its projection. The general formalism for constructing such optimal projections for constrained hyperbolic evolution systems is described in Sec. 4.2.

We illustrate these optimal constraint projection ideas in Sec. 4.3 by deriving the optimal projection for a new symmetric-hyperbolic representation of the scalar field equation on a fixed background spacetime. This scalar field system has the interesting property that it suffers from constraint violations driven both by bulk terms as well as boundary flux terms in the equations. (And so this system serves as a good model of the pathologies present in the Einstein system.) The optimal projection for this scalar field system is determined by solving a certain elliptic PDE. In Sec. 4.4 we test these optimal projection techniques by studying numerical solutions to this scalar field system on a fixed black-hole background spacetime. In particular we demonstrate that constraint-preserving boundary conditions are necessary, but not sufficient, to control the growth of constraints in this pathological scalar field system. We demonstrate that constraint projection succeeds in producing convergent constraint-satisfying solutions, but only if constraint-preserving boundary conditions are used as well. These tests also illustrate that the projections are best performed at fixed time intervals ($\Delta T \approx 2M$ for this problem) rather than after each time step. And we show that the computational cost of solving the constraint projection equations for this system (using our spectral elliptic solver [34]) is a very small fraction (below 1% for the resolution needed to achieve roundoff level accuracy) of the total computational cost of evolving this system. The symmetrizer metric for this model scalar field system (like many hyperbolic evolution systems) is not unique; so the projections defined in terms of the symmetrizer are not unique. Nevertheless, we demonstrate for the model scalar field system that numerical evolutions based on these different projections all converge to the same solution. The rate of this convergence is not the same for all projections, however, and we find an "optimal" projection for this system that maximizes this convergence rate.

4.2 Optimal constraint projection

Our objective is to construct a projection operator that maps a given field configuration to the nearest constraint-satisfying configuration (the nearest point on the constraint submanifold). That is, we wish to map an initial point $\bar{u}^\alpha$ in the field configuration space to a new point u^α that satisfies

a set of constraint equations:

$$c^A(u^\alpha) = 0. \tag{4.1}$$

(We use Greek indices to label individual components of the dynamical fields, and upper case Latin indices to label the individual components of the constraints.) To find the optimal projection we also need to have a distance measure between field points. We define the needed measure in terms of a symmetric positive-definite metric, $S_{\alpha\beta}$, on the dynamical field space. The distance between field points is then defined as

$$|| \, \delta u \, ||^2 = \int S_{\alpha\beta}(u^\alpha - \bar{u}^\alpha)(u^\beta - \bar{u}^\beta) d^3x. \tag{4.2}$$

Building on the augmented variational techniques commonly used to construct step-and-project constraint control schemes in other areas of numerical analysis [20, 30, 22], we are now prepared to construct the optimal projection map. We introduce a Lagrangian density $\mathcal{L}$ that consists of the distance between the given field configuration $\bar{u}^\alpha$ and its projection u^α, plus the products of the constraints with Lagrange multipliers. Thus we introduce the Lagrangian density,

$$\mathcal{L} = S_{\alpha\beta}(u^\alpha - \bar{u}^\alpha)(u^\beta - \bar{u}^\beta) + \lambda_A c^A. \tag{4.3}$$

The stationarity of the Lagrangian (the volume integral of this Lagrangian density) with respect to variations of the Lagrange multipliers λ_A enforces the constraints, while stationarity with respect to variations of the fields u^α are necessary conditions for the projection to minimize the distance to the constraint submanifold.

The optimal projection procedure outlined above could be carried out using any definition of the distance between field points, e.g., using any positive definite metric $S_{\alpha\beta}$ on the space of fields. For a particular problem this distance measure should be chosen to be the natural measure associated with that problem. Our primary interest here is the construction of projections for constrained hyperbolic evolution systems. So we will focus our attention on fields u^α that satisfy a first-order evolution equation of the form

$$\partial_t u^\alpha + A^{k\alpha}{}_\beta \partial_k u^\beta = F^\alpha. \tag{4.4}$$

We use lower case Latin indices to label spatial coordinates x^k, $\partial_t = \partial/\partial t$ to denote time derivatives, and $\partial_k = \partial/\partial x^k$ to denote spatial derivatives. Such systems are called symmetric hyperbolic if they have a positive definite metric $S_{\alpha\beta}$ on the space of fields (typically called the symmetrizer) that

symmetrizes the characteristic matrices:

$$S_{\alpha\gamma}A^{k\gamma}{}_{\beta} \equiv A^{k}_{\alpha\beta} = A^{k}_{\beta\alpha}. \tag{4.5}$$

The well-posedness of the initial value problem for linear symmetric-hyperbolic evolution systems is demonstrated by establishing bounds on the square-integral norm of the dynamical fields defined with this symmetrizer metric [42, 21]. This metric defines the meaningful measure on the dynamical field space for symmetric-hyperbolic systems, so this is the appropriate measure to use for constructing optimal constraint projections for these systems. Most hyperbolic evolution systems of interest in mathematical physics (including many representations of the Einstein system) are symmetric hyperbolic, and so we limit our consideration here to systems of this type.

In Sec. 4.3 we use the procedure outlined above to construct explicitly the optimal projection for the relatively simple case of the scalar wave equation on a curved background spacetime. But before we focus on that special case, we take a few (rather more abstract) steps in the construction of this projection for the general case. To do this we assume that the constraints c^A are linear in the derivatives of the dynamical fields:

$$c^A = K^{Ak}{}_{\beta}\partial_k u^\beta + L^A, \tag{4.6}$$

where $K^{Ak}{}_{\beta}$ and L^A may depend on u^α but not its derivatives. The constraints have this general form in many evolution systems of interest (e.g., the Einstein system, the Maxwell system, the incompressible fluid system). In this case we can explicitly compute the variations of the Lagrangian density defined in Eq. (4.3):

$$\begin{aligned}
\tfrac{\delta\mathcal{L}}{\delta u^\alpha}\delta u^\alpha &= \delta u^\alpha\Big\{2S_{\alpha\beta}(u^\beta - \bar{u}^\beta) - \partial_k(\lambda_A K^{kA}{}_{\alpha}) \\
&\quad +\lambda_A\big(\partial_\alpha K^{Ak}{}_{\beta}\partial_k u^\beta + \partial_\alpha L^A\big)\Big\} \\
&\quad +\partial_k\big(\lambda_A K^{Ak}{}_{\alpha}\delta u^\alpha\big), \qquad (4.7) \\
\tfrac{\delta\mathcal{L}}{\delta\lambda_A}\delta\lambda_A &= c^A\delta\lambda_A. \qquad (4.8)
\end{aligned}$$

Here we use the notation $\partial_\alpha \equiv \partial/\partial u^\alpha$ to denote derivatives with respect to the fields. We have also assumed that the symmetrizer $S_{\alpha\beta}$ may depend on $\bar{u}^\alpha$ but not u^α. We wish to find the stationary points of this Lagrangian with respect to arbitrary variations in the fields u^α and the Lagrange multipliers λ_A. Stationarity with respect to the variations of these quantities (that vanish on the boundaries) implies that

$$0 \;=\; u^\alpha - \bar{u}^\alpha - \tfrac{1}{2}S^{\alpha\beta}\partial_k(\lambda_A K^{kA}{}_{\beta})$$

$$+\tfrac{1}{2}\lambda_A S^{\alpha\beta}\big(\partial_\beta K^{Ak}{}_\gamma \partial_k u^\gamma + \partial_\beta L^A\big), \tag{4.9}$$

$$0 \quad = \quad c^A = K^{Ak}{}_\beta \partial_k u^\beta + L^A \tag{4.10}$$

at each interior point, and stationarity with respect to boundary variations implies that

$$0 = n_k \lambda_A K^{Ak}{}_\beta \tag{4.11}$$

at each boundary point, where n_k is the outward directed unit normal to the surface. We use the notation $S^{\alpha\beta}$ to denote the inverse of $S_{\alpha\beta}$. The general idea is to use Eqs. (4.9) and (4.10), with appropriate boundary conditions (such as those provided by Eq. [4.11]), to determine the field configuration u^β and the Lagrange multipliers λ_A for any given field point $\bar{u}^\alpha$. If u^α and λ_A satisfying these equations can be found, then we are guaranteed that the field u^α is the constraint-satisfying solution nearest the point $\bar{u}^\alpha$ as desired. We do not know whether these equations always admit solutions in the general case. So in Sec. 4.3 we study in detail this optimal projection for the simple case of the scalar field equations on a fixed background spacetime. We show that solutions to the optimal projection equations always exist and are relatively easy to compute numerically in this simple case. And in Sec. 4.4 we show that this optimal projection is very effective in controlling the growth of constraints for the scalar field system.

4.3 Scalar fields in curved spacetime

In this section we examine in some detail the scalar wave system on a fixed background spacetime. In Sec. 4.3.1 we review the standard treatment of this system, and then modify it so that it exhibits bulk generated constraint violations in addition to the boundary generated violations present in the standard system. This new, more pathological, symmetric-hyperbolic scalar field system now serves as a good model of the constraint violating problems inherent in the Einstein system. We construct constraint-preserving boundary conditions for this system in Sec. 4.3.2, and the optimal projection map for this system in Sec. 4.3.3 following the procedure outlined in Sec. 4.2.

4.3.1 Modified scalar wave system

The standard scalar field equation on a fixed background spacetime is

$$\nabla^\mu \nabla_\mu \psi = 0, \tag{4.12}$$

where ψ represents the scalar field and ∇_μ the covariant derivative associated with the background spacetime metric. We represent the background spacetime metric in terms of the usual $3+1$ split-

ting:

$$ds^2 = -N^2 dt^2 + g_{ij}(dx^i + N^i dt)(dx^j + N^j dt), \tag{4.13}$$

where the lapse N and the spatial metric g_{ij} are assumed to be positive definite, while the shift N^i is arbitrary. The equation for the scalar field ψ, Eq. (4.12), can be re-expressed as a first-order evolution system in the standard way (see, e.g., [35]):

$$\partial_t \psi - N^k \partial_k \psi = -N\Pi, \tag{4.14}$$

$$\partial_t \Pi - N^k \partial_k \Pi + N g^{ki} \partial_k \Phi_i = N J^i \Phi_i + NK\Pi, \tag{4.15}$$

$$\partial_t \Phi_i - N^k \partial_k \Phi_i + N \partial_i \Pi = -\Pi \partial_i N + \Phi_j \partial_i N^j. \tag{4.16}$$

The field Φ_i represents the spatial gradient $\partial_i \psi$, and Π represents the time derivative of ψ (and is defined precisely by Eq. [4.14]). The auxiliary quantities K (the trace of the extrinsic curvature) and J^i depend only on the background spacetime geometry, and are defined by

$$J^i = -N^{-1} g^{-\frac{1}{2}} \partial_j (N g^{\frac{1}{2}} g^{ij}), \tag{4.17}$$

$$K = -N^{-1} g^{-\frac{1}{2}} \left[\partial_t g^{\frac{1}{2}} - \partial_j (g^{\frac{1}{2}} N^j) \right]. \tag{4.18}$$

Solutions to the first-order system, Eqs. (4.14)–(4.16), are also solutions to Eq. (4.12) only if the constraints are satisfied: $0 = c^A \equiv \{\mathcal{C}_i, \mathcal{C}_{ij}\}$, where

$$\mathcal{C}_i = \partial_i \psi - \Phi_i, \tag{4.19}$$

$$\mathcal{C}_{ij} = \partial_{[i} \Phi_{j]}. \tag{4.20}$$

Although the second constraint, $C_{ij} = 0$, follows from the first, $C_i = 0$, the converse is not true. Hence we include both constraints in the analysis here. Note that both constraints are necessary to construct a first-order hyperbolic evolution system for the constraint quantities (discussed below, Eqs. (4.29) and (4.30)). Note also that the analogues of both constraints play essential roles in first-order hyperbolic formulations of Einstein's equations.

We now generalize the evolution system, Eqs. (4.14)–(4.16), somewhat by adding multiples of the constraint $\mathcal{C}_i$ to Eqs. (4.14) and (4.16):

$$\partial_t \psi - N^k \partial_k \psi = -N\Pi + \gamma_1 N^k \mathcal{C}_k, \tag{4.21}$$

$$\partial_t \Phi_i - N^k \partial_k \Phi_i + N \partial_i \Pi = -\Pi \partial_i N + \Phi_j \partial_i N^j + \gamma_2 N \mathcal{C}_i, \tag{4.22}$$

where γ_1 and γ_2 are arbitrary constants. The constraint-satisfying solutions to these equations are

the same as those of the original system; but as we shall see, the constraint violating properties of the new system are significantly different from those of the original. Substituting the definition of $\mathcal{C}_i$ in Eqs. (4.21) and (4.22) gives us new evolution equations for ψ and Φ_i:

$$\partial_t \psi \qquad -(1+\gamma_1) N^k \partial_k \psi = -N\Pi - \gamma_1 N^k \Phi_k, \tag{4.23}$$

$$\partial_t \Phi_i \qquad -N^k \partial_k \Phi_i + N \partial_i \Pi - \gamma_2 N \partial_i \psi = -\Pi \partial_i N + \Phi_j \partial_i N^j - \gamma_2 N \Phi_i. \tag{4.24}$$

The first-order system that represents the scalar wave equation, Eqs. (4.15), (4.23), and (4.24), has the standard first-order form,

$$\partial_t u^\alpha + A^{k\alpha}{}_\beta \partial_k u^\beta \quad = \quad F^\alpha, \tag{4.25}$$

where $u^\alpha = \{\psi, \Pi, \Phi_i\}$. Systems of this type are called symmetric hyperbolic if there exists a symmetric positive-definite tensor $S_{\alpha\beta}$ on the space of fields that symmetrizes the characteristic matrices $A^{k\alpha}{}_\beta$:

$$S_{\alpha\gamma} A^{k\gamma}{}_\beta \equiv A^k_{\alpha\beta} = A^k_{\beta\alpha}. \tag{4.26}$$

The most general symmetrizer for our new scalar wave system is (up to an overall factor),

$$\begin{aligned} ds^2 &= S_{\alpha\beta} du^\alpha du^\beta, \\ &= \Lambda^2 d\psi^2 - 2\gamma_2 d\psi\, d\Pi + d\Pi^2 + g^{ij} d\Phi_i d\Phi_j, \end{aligned} \tag{4.27}$$

where Λ is an arbitrary non-vanishing function. This $S_{\alpha\beta}$ symmetrizes the characteristic matrices $A^k_{\alpha\beta}$ so long as $\gamma_1\gamma_2 = 0$. Thus we must take at least one of these parameters to be zero for our new system to be symmetric hyperbolic. This symmetrizer is positive definite whenever

$$\Lambda^2 > \gamma_2^2. \tag{4.28}$$

In this case $S_{\alpha\beta}$ provides a dynamically meaningful measure of the distance between field configurations, which we use to define our optimal constraint projection operator in Sec. 4.3.3.

The evolution of the constraints follows from the principal evolution system, Eqs. (4.15), (4.23), and (4.24):

$$\partial_t \mathcal{C}_i - (1+\gamma_1) \mathcal{L}_{\vec{N}} \mathcal{C}_i \quad = 2\gamma_1 N^j \mathcal{C}_{ji} - \gamma_2 N \mathcal{C}_i, \tag{4.29}$$

$$\partial_t \mathcal{C}_{ij} - \mathcal{L}_{\vec{N}} \mathcal{C}_{ij} \qquad = -\gamma_2 N \mathcal{C}_{ij} - \gamma_2 \mathcal{C}_{[i} \partial_{j]} N, \tag{4.30}$$

where $\mathcal{L}_{\vec{N}}$ represents the Lie derivative along the shift vector N^i. If the constraints are satisfied at some initial time, then these equations guarantee (at least at the analytical level) that the constraints remain satisfied in the domain of dependence of the initial data. These equations also show that any constraint violations in this system will be advected along a congruence of timelike curves. Constraint violations can therefore flow into the computational domain if these curves intersect the boundaries. And like the Einstein evolution system, these equations also contain bulk terms that amplify any existing constraint violations. When $\gamma_1 = 0$ we see that Eq. (4.29) implies that the constraint $\mathcal{C}_i$ has the simple time dependence $\mathcal{C}_i(\tau) = \mathcal{C}_i(0)e^{-\gamma_2 \tau}$, where τ measures proper time as seen by a hypersurface orthogonal observer. Whenever $\gamma_2 < 0$ this constraint grows exponentially, and in this case the modified scalar wave system serves as a good model of the constraint violations in the Einstein system. (Constraint violations of all wavelengths grow exponentially in this system, and so it may be even more pathological than the Einstein system where constraint violating instabilities are typically dominated by long wavelength modes [31, 36].) Conversely, if $\gamma_2 > 0$ then this modified scalar wave system exponentially suppresses any residual constraint violations that may be present in the initial data. This latter property suggests that analogous terms could be introduced to control some of the bulk constraint-violating terms in the Einstein system.

4.3.2 Constraint preserving boundary conditions

Boundary conditions for hyperbolic evolution systems are defined in terms of the characteristic fields of these systems, so we must construct these fields for our modified scalar wave system. The characteristic fields are defined with respect to a spatial direction at each point, represented here by a unit normal co-vector field n_k. For the purposes of imposing boundary conditions, the appropriate n_k is the outward-pointing normal to the boundary. Given a direction field n_k we define the left eigenvectors ${e^{\hat{\alpha}}}_{\alpha}$ of the characteristic matrix $n_k {A^{k\,\alpha}}_{\beta}$ by

$$ {e^{\hat{\alpha}}}_{\alpha} n_k {A^{k\,\alpha}}_{\beta} = v_{(\hat{\alpha})} {e^{\hat{\alpha}}}_{\beta}, \tag{4.31} $$

where $v_{(\hat{\alpha})}$ denotes the eigenvalue (also called the characteristic speed). The index $\hat{\alpha}$ labels the various eigenvectors and eigenvalues, and there is no summation over $\hat{\alpha}$ in Eq. (4.31). Since we are interested in hyperbolic evolution systems, the space of eigenvectors has the same dimension as the space of dynamical fields, and the matrix ${e^{\hat{\alpha}}}_{\beta}$ is invertible. The projections of the dynamical fields u^{α} onto these left eigenvectors are called the characteristic fields $u^{\hat{\alpha}}$:

$$ u^{\hat{\alpha}} = {e^{\hat{\alpha}}}_{\beta} u^{\beta}. \tag{4.32} $$

At each boundary point, boundary conditions must be imposed on any characteristic field having negative characteristic speed, $v_{(\hat{\alpha})} < 0$, at that point [24, 43]. We refer to fields with $v_{(\hat{\alpha})} < 0$ as the incoming characteristic fields at that point. Conversely, those characteristic fields having non-negative characteristic speeds (the outgoing fields) must not have boundary conditions imposed on them there.

The characteristic fields for the symmetric hyperbolic representations ($\gamma_1\gamma_2 = 0$) of the scalar wave system are the quantities $u^{\hat{\alpha}} = \{Z^1, Z^2_i, U^{1\pm}\}$:

$$Z^1 = \psi, \tag{4.33}$$

$$Z^2_i = P^k{}_i\Phi_k, \tag{4.34}$$

$$U^{1\pm} = \Pi \pm n^k\Phi_k - \gamma_2\psi, \tag{4.35}$$

where $P^k{}_i = \delta^k{}_i - n^k n_i$, $n^k = g^{kj}n_j$, and $n^k n_k = 1$. The fundamental fields u^α can be reconstructed from the characteristic fields $u^{\hat{\alpha}}$ by inverting Eq. (4.32):

$$\psi = Z^1, \tag{4.36}$$

$$\Pi = \tfrac{1}{2}(U^{1+} + U^{1-}) + \gamma_2 Z^1, \tag{4.37}$$

$$\Phi_i = \tfrac{1}{2}(U^{1+} - U^{1-})n_i + Z^2_i. \tag{4.38}$$

The characteristic field Z^1 propagates with speed $-\gamma_1 n_k N^k/N$, the field Z^2_i with speed 0, and the fields $U^{1\pm}$ with speeds ± 1 relative to the hypersurface orthogonal observers. The coordinate characteristic speeds of these fields are $-(1+\gamma_1)n_k N^k$, $-n_k N^k$, and $-n_k N^k \pm N$ respectively.

At each boundary point, boundary conditions are required on each characteristic field whose coordinate characteristic speed is negative at that point. The field U^{1-}, in particular, requires a boundary condition on all timelike boundaries. For the standard representation of the scalar field system, Eqs. (4.14)–(4.16), the boundary condition $U^{1-} = \Pi - n^k\Phi_k = 0$ is used to ensure (approximately) that no scalar waves enter the computational domain. We wish to enforce this condition on our generalized scalar field system, Eqs. (4.15), (4.23), and (4.24), in such a way that the physical (constraint satisfying) solutions are the same for all values of the parameters γ_1 and γ_2. Since U^{1-} depends on γ_2, Eq. (4.35), the proper boundary condition must also depend on γ_2: $U^{1-} + \gamma_2\psi = \Pi - n^k\Phi_k = 0$. Thus the appropriate boundary condition to impose on U^{1-} is $U^{1-} = -\gamma_2\psi$. The freezing form of this boundary condition (as used in our code) is,

$$\partial_t U^{1-} = -\gamma_2\partial_t\psi. \tag{4.39}$$

For boundary conditions on the fields Z^1 and Z^2_i (when necessary), we explore two choices:

One is the freezing boundary condition $\partial_t Z^i = \partial_t Z^2_i = 0$. In Sec. 4.4 we show that this boundary condition allows constraint violations to enter the computational domain through the boundaries. Therefore, we also explore conditions that prevent this influx of constraint violations: When the fields Z^1 and/or Z^2_i require boundary conditions, we set

$$\partial_t Z^1 = N^k \Phi_k - N\Pi, \tag{4.40}$$

$$\partial_t Z^2_i = P^k{}_i \partial_k \partial_t \psi. \tag{4.41}$$

Equation (4.40) is based on Eq. (4.14) combined with Eq. (4.19), while Eq. (4.41) is derived from the time-derivative of Eq. (4.19). We note that with the choice $\gamma_1 = -1$, the field Z^1 never requires a boundary condition. We also note that the term $\partial_t \psi$ that appears on right side of Eqs. (4.39) and (4.41) must be evaluated using the appropriate expression for $\partial_t \psi = \partial_t Z^1$ on this boundary: Eq. (4.40) when Z^1 requires a boundary condition, or Eq. (4.23) when no boundary condition is required. In Sec. 4.4 we compare numerically the results of using these constraint-preserving boundary conditions with the use of the freezing boundary conditions $\partial_t Z^1 = \partial_t Z^2_i = 0$ on these fields.

4.3.3 Optimal constraint projection

The idea is to use the full evolution system, Eqs. (4.15), (4.23), and (4.24), to evolve initial data forward in time an amount ΔT and then (when the constraint violations become too large) to project this solution back onto the constraint submanifold in some optimal way. Let $\bar{u}^\alpha = \{\bar{\psi}, \bar{\Pi}, \bar{\Phi}_i\}$ denote the solution obtained directly from this free evolution step. This solution $\bar{u}^\alpha$ may not satisfy the constraints because roundoff or truncation level constraint violations have been amplified, or constraint violations have flowed through the boundaries. Thus we wish to project $\bar{u}^\alpha$ in an optimal way back onto the constraint submanifold. Following the procedure outlined in Sec. 4.2 we construct a Lagrangian density,

$$\begin{aligned}
\mathcal{L} &= g^{\frac{1}{2}} \left[S_{\alpha\beta} (u^\alpha - \bar{u}^\alpha)(u^\beta - \bar{u}^\beta) + \lambda_A c^A \right] \\
&= g^{\frac{1}{2}} \Big[\Lambda^2 (\psi - \bar{\psi})^2 - 2\gamma_2 (\psi - \bar{\psi})(\Pi - \bar{\Pi}) \\
&\quad + (\Pi - \bar{\Pi})^2 + g^{ij} (\Phi_i - \bar{\Phi}_i)(\Phi_j - \bar{\Phi}_j) \\
&\quad + \lambda^i (\partial_i \psi - \Phi_i) + \lambda^{ij} \partial_{[i} \Phi_{j]} \Big],
\end{aligned} \tag{4.42}$$

using the symmetrizer $S_{\alpha\beta}$ of the hyperbolic evolution system, Eq. (4.27), and the Lagrange multipliers $\lambda_A = \{\lambda^i, \lambda^{ij}\}$. The stationary points of the Lagrangian,

$$L = \int \mathcal{L}\, d^3x, \tag{4.43}$$

with respect to variations in u^α and λ_A define the optimally projected field configuration u^α. We have included the multiplicative factor $g^{\frac{1}{2}} = (\det g_{ij})^{\frac{1}{2}}$ in Eq. (4.42) to ensure that L is coordinate invariant.

The scalar field constraint Lagrangian density, Eq. (4.42), has the following variations:

$$\begin{aligned}
\tfrac{\delta\mathcal{L}}{\delta\psi}\delta\psi &= 2g^{\frac{1}{2}}\big[\Lambda^2(\psi-\bar\psi) - \gamma_2(\Pi-\bar\Pi)\big]\delta\psi \\
&\quad -\partial_i(g^{\frac{1}{2}}\lambda^i)\delta\psi + \partial_i(g^{\frac{1}{2}}\lambda^i\delta\psi), && (4.44)\\
\tfrac{\delta\mathcal{L}}{\delta\Pi}\delta\Pi &= 2g^{\frac{1}{2}}\big[\Pi-\bar\Pi - \gamma_2(\psi-\bar\psi)\big]\delta\Pi, && (4.45)\\
\tfrac{\delta\mathcal{L}}{\delta\Phi_i}\delta\Phi_i &= \big[2g^{\frac{1}{2}}g^{ij}(\Phi_i-\bar\Phi_i) - g^{\frac{1}{2}}\lambda^j - \partial_i(g^{\frac{1}{2}}\lambda^{ij})\big]\delta\Phi_j \\
&\quad +\partial_i(g^{\frac{1}{2}}\lambda^{ij}\delta\Phi_j), && (4.46)\\
\tfrac{\delta\mathcal{L}}{\delta\lambda^i}\delta\lambda^i &= g^{\frac{1}{2}}(\partial_i\psi - \Phi_i)\delta\lambda^i, && (4.47)\\
\tfrac{\delta\mathcal{L}}{\delta\lambda^{ij}}\delta\lambda^{ij} &= g^{\frac{1}{2}}\partial_{[i}\Phi_{j]}\delta\lambda^{ij}. && (4.48)
\end{aligned}$$

We require that the Lagrangian L from Eq. (4.43) be stationary with respect to *all* variations in the dynamical fields $\delta u^\alpha = \{\delta\psi, \delta\Pi, \delta\Phi_i\}$ (including those that do not vanish on the boundaries) as well as all variations in the Lagrange multipliers $\delta\lambda_A = \{\delta\lambda^i, \delta\lambda^{ij}\}$. From Eqs. (4.44)–(4.46), it follows that

$$\begin{aligned}
\psi &= \bar\psi + \gamma_2\Lambda^{-2}(\Pi-\bar\Pi) + \tfrac{1}{2}\Lambda^{-2}g^{-\frac{1}{2}}\partial_i(g^{\frac{1}{2}}\lambda^i), && (4.49)\\
\Pi &= \bar\Pi + \gamma_2(\psi-\bar\psi), && (4.50)\\
\Phi_i &= \bar\Phi_i + \tfrac{1}{2}g_{ij}\lambda^j + \tfrac{1}{2}g^{-\frac{1}{2}}g_{ij}\partial_k(g^{\frac{1}{2}}\lambda^{kj}), && (4.51)
\end{aligned}$$

and Eqs. (4.47) and (4.48) imply that the projected solution satisfies the constraints. We now solve Eq. (4.51) for λ^i, substitute it into Eq. (4.49), and use Eqs. (4.47) and (4.50), to obtain the following equation for ψ,

$$\nabla^i\nabla_i\psi - (\Lambda^2-\gamma_2^2)\psi = \nabla^i\bar\Phi_i - (\Lambda^2-\gamma_2^2)\bar\psi, \tag{4.52}$$

where ∇_i represents the spatial covariant derivative that is compatible with g_{ij}. In deriving this equation we have also used the fact that the term $\partial_i\partial_k(g^{\frac{1}{2}}\lambda^{ki})$ vanishes identically because λ^{ij} is antisymmetric. Equation (4.52) is just the covariant inhomogeneous Helmholtz equation. We note

that the parameters must satisfy the condition $\Lambda^2 - \gamma_2^2 > 0$ for the evolution system to be symmetric hyperbolic. Solving Eq. (4.52) determines the optimal projection ψ; the optimal Π is determined from Eq. (4.50),

$$\Pi = \bar{\Pi} + \gamma_2(\psi - \bar{\psi}); \tag{4.53}$$

and the optimal Φ_i is obtained by enforcing the constraint,

$$\Phi_i = \partial_i \psi. \tag{4.54}$$

We note that the Lagrange multiplier λ^{ij} does not play any essential role in this analysis: we could just as well have set $\lambda^{ij} = 0$ and still obtained the same projection. This makes sense, because the constraint $\mathcal{C}_{ij}$ is really a consequence of the constraint $\mathcal{C}_i$ in this case.

The evolution equations for Π and Φ_i, Eqs. (4.15) and (4.16), decouple from the larger scalar field evolution system, Eqs. (4.15), (4.23), and (4.24), when $\gamma_2 = 0$. It is sometimes of interest to consider the properties of this smaller system, Eqs. (4.15) and (4.16), subject to the single constraint, Eq. (4.20). The optimal constraint projection for this reduced system consists of Eqs. (4.50) and (4.51) (with $\lambda^i = \gamma_2 = 0$), together with the single constraint equation $\partial_{[i}\Phi_{j]} = 0$. This constraint equation implies that $\Phi_i = \partial_i \psi$ for some scalar function ψ. Inserting this expression for Φ_i in Eq. (4.51), multiplying by $g^{\frac{1}{2}} g^{ij}$, and taking the divergence, we obtain the following equation for ψ,

$$\nabla^i \nabla_i \psi \quad = \quad \nabla^i \bar{\Phi}_i. \tag{4.55}$$

In deriving this equation we have used the fact that the term $\partial_i \partial_k (g^{\frac{1}{2}} \lambda^{ki})$ vanishes identically because λ^{ij} is antisymmetric. The optimal projection in this reduced system then sets $\Pi = \bar{\Pi}$ and $\Phi_i = \partial_i \psi$, where ψ is the solution to Eq. (4.55). We note that Eq. (4.55) is just the $\Lambda^2 - \gamma_2^2 = 0$ limit of the original projection Eq. (4.52).

Unfortunately the optimal constraint projection for the scalar field system is not unique, because the parameter Λ in the symmetrizer metric is not unique. We have seen that taking the limit $\Lambda^2 \to \gamma_2^2$ is equivalent to ignoring the evolution of the scalar field $\bar{\psi}$ in constructing the optimal projection. Alternatively, the limit $\Lambda \to \infty$ corresponds to the simple projection $\psi = \bar{\psi}$, $\Pi = \bar{\Pi}$, and $\Phi_i = \partial_i \bar{\psi}$. In this limit, no elliptic equation has to be solved, and the evolution of the field $\bar{\Phi}_i$ is effectively ignored when constructing the projection. We expect that the optimal choice of Λ will be one for which $1/\Lambda$ corresponds to some characteristic length or timescale associated with the particular problem. We explore in Sec. 4.4.3 the properties of these projection operators for a range of Λ, and show that an optimal value does exist. When $\gamma_2 \neq 0$ the optimal choice seems to be $\Lambda^2 = 2\gamma_2^2$, where $1/|\gamma_2|$ is the timescale on which the constraints are amplified.

Finally, we must consider the boundary conditions for the projection equations that determine

ψ, i.e. Eq. (4.52) or (4.55). In general, boundary conditions for the projection equations must satisfy two criteria: First, they must be consistent with boundary conditions imposed on the evolution equations, and second, the projection equations plus boundary conditions must not modify solutions that already satisfy the constraints. Typically, we enforce approximate outgoing wave boundary conditions on the evolution equations. For the case of the scalar wave equation, the approximate outgoing wave boundary condition, Eq. (4.39), sets $U^{1-} = -\gamma_2\psi$ or equivalently $n^k\Phi_k = \Pi$ on the boundaries (where n^k is the outward directed unit normal). Since $\Phi_i = \partial_i\psi$ in these projected solutions, the appropriate boundary condition to impose on ψ in Eq. (4.52) or (4.55) in this case would be

$$n^k\partial_k\psi = \Pi = \bar{\Pi} + \gamma_2(\psi - \bar{\psi}). \tag{4.56}$$

Alternatively we can derive boundary conditions for ψ from the requirement that the boundary variations of the Lagrangian vanish. The divergence terms in Eqs. (4.44) and (4.46) imply that

$$0 = n_k\lambda^k = n_k\lambda^{ki}, \tag{4.57}$$

on the boundaries for the scalar field system. A short calculation (using the fact that n_k is proportional to a gradient, and λ^{ki} is antisymmetric) shows that $n_i\partial_k(g^{\frac{1}{2}}\lambda^{ki}) = 0$, so we see from Eq. (4.51) that the natural boundary condition is

$$n^k\partial_k\psi = n^k\bar{\Phi}_k. \tag{4.58}$$

If the approximate outgoing wave boundary condition, $n^k\bar{\Phi}_k = \bar{\Pi}$, was used in the free evolution step, then the natural boundary condition Eq. (4.58) differs from Eq. (4.56) by the term $\gamma_2(\psi - \bar{\psi})$. For the constraint projections described in Section 4.4, we impose the Robin boundary condition Eq. (4.56) on the solutions of Eq. (4.52) at the boundaries where U^{1-} requires a boundary condition in the evolution step, and Eq. (4.58) on the solutions at all other boundaries (e.g., inside an event horizon). We note that the discrepancy between the natural and the physical outgoing boundary condition could be eliminated by adding an appropriate boundary term to the constraint projection Lagrangian.

4.4 Numerical results

We have studied the effectiveness of the optimal constraint projection methods developed in Secs. 4.2 and 4.3 for the case of a scalar field propagating on a fixed black-hole spacetime. For these simula-

tions we use the Kerr-Schild form of the Schwarzschild metric as our background geometry:

$$ds^2 = -dt^2 + \frac{2M}{r}(dt + dr)^2 + dr^2 + r^2 d\Omega^2. \tag{4.59}$$

We express all lengths and times associated with these simulations in units of the mass, M, of this black hole. Our computational domain consists of a spherical shell extending from $r_{\min} = 1.9\,M$ (just inside the black-hole event horizon) to $r_{\max} = 11.9\,M$. For initial data we use a constraint satisfying Gaussian shaped pulse with dipolar angular structure,

$$\psi = 0, \tag{4.60}$$

$$\Pi = Y_{10}(\theta, \varphi) e^{-(r-r_0)^2/w^2}, \tag{4.61}$$

$$\Phi_i = 0, \tag{4.62}$$

with $r_0 = 5M$ and $w = 1M$. The value of Π is about 2×10^{-21} at the outer boundary of our computational domain, below the level of double precision roundoff error.

For the remainder of this section we describe briefly the numerical methods used to solve this problem. Then in Sec. 4.4.1 we describe three numerical simulations designed to explore the effects of boundary conditions on the evolution of the constraints in these solutions. In Sec. 4.4.2 we describe two additional numerical simulations that illustrate the effectiveness of constraint projection in controlling the growth of constraints. And finally in Sec. 4.4.3 we explore ways to optimize the use of the constraint projection method and measure its computational cost.

All numerical computations presented here are performed using a pseudospectral collocation method. Our numerical methods are essentially the same as those we have applied to evolution problems with the Einstein system [26, 25, 31, 36], with scalar fields [35], and with the Maxwell system [32]. Given a system of partial differential equations

$$\partial_t u^\alpha(\mathbf{x}, t) = \mathcal{F}^\alpha[u(\mathbf{x}, t), \partial_i u(\mathbf{x}, t)], \tag{4.63}$$

where u^α is a collection of dynamical fields, the solution $u^\alpha(\mathbf{x}, t)$ is expressed as a time-dependent linear combination of N spatial basis functions $\phi_k(\mathbf{x})$:

$$u^\alpha_N(\mathbf{x}, t) = \sum_{k=0}^{N-1} \tilde{u}^\alpha_k(t) \phi_k(\mathbf{x}). \tag{4.64}$$

We expand each scalar function (ψ and Π) and the Cartesian components of each vector (Φ_x, Φ_y, and Φ_z) in terms of the basis functions $T_n(\rho)Y_{lm}(\theta, \varphi)$, where Y_{lm} are spherical harmonics and $T_n(\rho)$

are Chebyshev polynomials with

$$\rho = \frac{2r - r_{\max} - r_{\min}}{r_{\max} - r_{min}}. \tag{4.65}$$

We use spherical harmonics with $\ell \leq \ell_{\max} = 5$ and a varying number of Chebyshev polynomials with degrees $N_r \leq 81$. Spatial derivatives are evaluated analytically using the known derivatives of the basis functions:

$$\partial_i u_N^\alpha(\mathbf{x}, t) = \sum_{k=0}^{N-1} \tilde{u}_k^\alpha(t) \partial_i \phi_k(\mathbf{x}). \tag{4.66}$$

Associated with the basis functions is a set of N_c collocation points $\mathbf{x}_i$. Given spectral coefficients $\tilde{u}_k^\alpha(t)$, the function values at the collocation points $u^\alpha(\mathbf{x}_i, t)$ are computed by Eq. (4.64). Conversely, the spectral coefficients are obtained by the inverse transform

$$\tilde{u}_k^\alpha(t) = \sum_{i=0}^{N_c-1} w_i u_N^\alpha(\mathbf{x}_i, t) \phi_k(\mathbf{x}_i), \tag{4.67}$$

where w_i are weights specific to the choice of basis functions and collocation points; thus it is straightforward to transform between the spectral coefficients $\tilde{u}_k^\alpha(t)$ and the function values at the collocation points $u_N^\alpha(\mathbf{x}_i, t)$. The partial differential equation, Eq. (4.63), is now rewritten using Eqs. (4.64)–(4.67) as a set of *ordinary* differential equations for the function values at the collocation points,

$$\partial_t u_N^\alpha(\mathbf{x}_i, t) = \mathcal{G}_i^\alpha[u_N(\mathbf{x}_j, t)], \tag{4.68}$$

where $\mathcal{G}_i^\alpha$ depends on $u_N^\alpha(\mathbf{x}_j, t)$ for all j. This system of ordinary differential equations, Eq. (4.68), is integrated in time using a fourth-order Runge-Kutta algorithm. Boundary conditions are incorporated into the right side of Eq. (4.68) using the technique of Bjørhus [7]. The time step is typically chosen to be about one fifth the distance between the closest collocation points, which ensures that the Courant condition is well satisfied. This small time step is needed to reduce the time discretization error to the same order of magnitude as the spatial discretization error at radial resolution $N_r = 61$.

Elliptic partial differential equations, Eq. (4.52) or (4.55), are solved using similar pseudospectral collocation methods. As detailed in [34], we consider a mixed real/spectral expansion of the desired solution $\psi(\mathbf{x})$:

$$\psi(\rho_n, \theta, \phi) = \sum_{l=0}^{l_{\max}} \sum_{m=-l}^{l} \hat{\psi}_{lmn} Y_{lm}(\theta, \phi), \tag{4.69}$$

where ρ_n (for $n = 0, \ldots, N_r - 1$) are the collocation points of the Chebyshev expansion in (rescaled) radius ρ. Given a set of coefficients $\hat{\psi}_{lmn}$, we can evaluate the residual of the elliptic equation and the residual of the boundary conditions using expressions like Eq. (4.66); the requirement that each Y_{lm} component (for $l \leq l_{\max}$) of this residual vanishes at the radial collocation points results in a

system of algebraic equations for the coefficients $\hat{\psi}_{lmn}$. For the problem considered here these algebraic equations are linear, and with suitable preconditioning are solved using standard numerical methods like GMRES. The elliptic solver is described in detail in [34].

We use no filtering on the radial basis functions, but apply a rather complicated filtering rule for the angular functions. When evaluating the right side of Eq. (4.68), we set to zero the coefficients of the terms with $\ell = \ell_{\max}$ in the expansions of the scalars, $\partial_t \psi$ and $\partial_t \Pi$. The vector $\partial_t \Phi_i$ is filtered by transforming its components to a vector spherical harmonic basis, setting to zero the coefficients of the terms with $\ell = \ell_{\max}$ in this basis, and then transforming back to Cartesian components. The result ψ of each elliptic solve and the projected Π (cf. Eq. (4.53)) are filtered similarly. The projected Φ_i is computed via Eq. (4.54) from the filtered ψ. We find no angular instability, such as the one reported in [32], when we use this filtering method. And we find no significant change in our results for this problem by increasing the value of $\ell_{\max}$ beyond the value $\ell_{\max} = 5$.

4.4.1 Testing boundary conditions

In this section we describe the results of three numerical simulations that explore the effects of boundary conditions on the evolution of the constraints in the scalar field system. First we evolve the initial data in Eqs. (4.60)–(4.62) using the standard representation of the scalar field system ($\gamma_1 = \gamma_2 = 0$), and using the standard freezing boundary conditions on the incoming fields. We use no constraint projection in this initial simulation. At the inner boundary of the computational domain, $r = r_{\min} = 1.9\,M$, all of the fields are outgoing and so no boundary condition is needed there on any of the fields. At the outer boundary, $r = r_{\max} = 11.9\,M$, the fields Z^1, Z^2_i and U^{1-} are all incoming since the shift points out of the computational domain there: $n_k N^k = 2M/r$. So we impose the freezing boundary conditions $0 = \partial_t Z^1 = \partial_t Z^2_i = \partial_t U^{1-}$ on these fields. The results of this first numerical simulation are depicted in Figs. 4.1 and 4.2.

Figure 4.1 illustrates the evolution of the constraints, which we measure using the quantity $||C(t)||$,

$$||C(t)||^2 = \int \left(C_i C^i + C_{ij} C^{ij}\right) g^{\frac{1}{2}}\, d^3x, \tag{4.70}$$

divided by a suitable normalization. The constraints in this system are combinations of the derivatives of the dynamical fields. So we normalize the curves in this figure by the quantity $||\nabla u(t)||$, which is the natural coordinate-invariant L^2 measure of the derivatives of the dynamical fields:

$$||\nabla u(t)||^2 = \int g^{ij} \nabla_i u^\alpha \nabla_j u^\beta S_{\alpha\beta}\, g^{\frac{1}{2}}\, d^3x. \tag{4.71}$$

The ratio of these quantities, $||C(t)||/||\nabla u(t)||$, is therefore a meaningful dimensionless measure

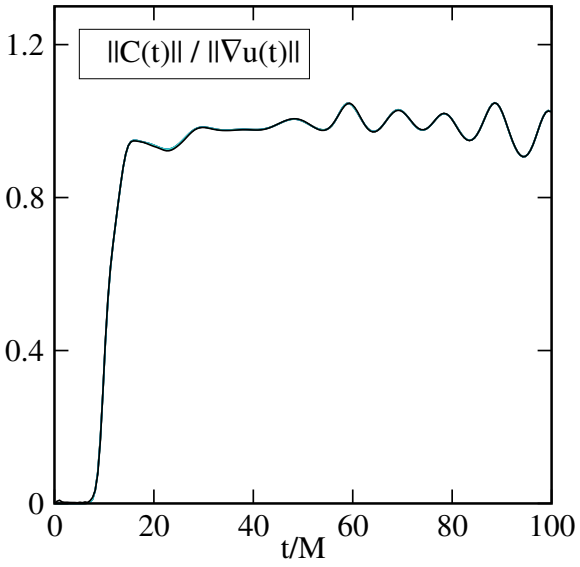

Figure 4.1: Constraint violations for evolutions with $\gamma_1 = \gamma_2 = 0$, freezing boundary conditions, and no constraint projections. Plotted are radial resolutions $N_r = 21, 31, \ldots, 61$; all curves lie on top of each other.

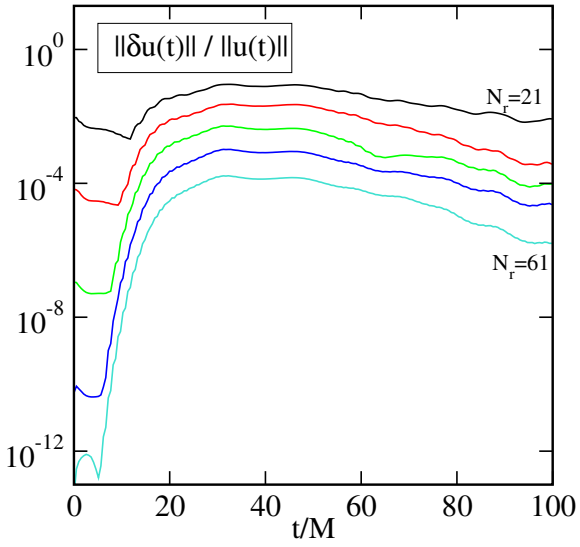

Figure 4.2: Convergence plot for the evolution presented in Fig. 4.1. Plotted are differences from the solution with radial resolution $N_r = 81$.

of the magnitude of constraint violations. When the value of this ratio becomes of order unity, the dynamical fields do not satisfy the constraints at all. As we can see in Fig. 4.1, the constraint-satisfying initial data quickly evolve to a state in which this constraint measure is of order unity. A large increase in constraint violation occurs as the outgoing scalar wave pulse passes through the outer boundary of the computational domain. After this time the numerical solution to the first-order scalar wave system no longer represents a solution to the original scalar field equation.

In Fig. 4.2 we demonstrate that these numerical solutions are nevertheless numerically convergent. We measure the convergence of these solutions by depicting the quantity

$$||\delta u(t)||^2 = \int S_{\alpha\beta} \left(u^\alpha_{N_r} - u^\alpha_R\right) \left(u^\beta_{N_r} - u^\beta_R\right) g^{\frac{1}{2}}\, d^3x, \tag{4.72}$$

divided by a suitable normalization. This quantity measures the difference between the solution $u^\alpha_{N_r}$ obtained with radial resolution N_r, compared to a reference solution u^α_R. In Fig. 4.2 we use the numerical solution computed with the largest number of radial basis functions ($N_r = 81$ in this case) as the reference solution. In order to make these difference measures meaningful, we normalize them by dividing by an analogous measure of the solution itself:

$$||u(t)||^2 = \int S_{\alpha\beta} u^\alpha_{N_r} u^\beta_{N_r}\, g^{\frac{1}{2}}\, d^3x. \tag{4.73}$$

Figure 4.2 shows that our computational methods are numerically convergent, even if the solutions are constraint violating and are therefore unphysical. The rate of convergence of these solutions changes at about $t = 10M$ because a short wavelength reflected pulse enters the computational domain at about this time. The convergence of these solutions shows that these constraint violations are a feature of the evolution system and the boundary conditions, rather than being artifacts of a poor numerical technique.

Next we evolve the same initial data, Eqs. (4.60)–(4.62), using the same standard scalar wave evolution equations ($\gamma_1 = \gamma_2 = 0$), but this time we use constraint-preserving boundary conditions on the fields Z^1 and Z^2_i, Eqs. (4.40) and (4.41). We use no constraint projection in these evolutions. Figure 4.3 shows that the constraints are in fact satisfied by these solutions to truncation level errors. The solid curves in Fig. 4.3 show the ratio $||C(t)||/||\nabla u(t)||$ while the dashed curves show $||C(t)||/||\nabla u(0)||$. The only difference is that the denominator used for the dashed curves is time independent. The solid curves show that the relative constraint error is approximately constant in time until about $t = 40$, at which time a truncation error level constraint-violating pulse from the outer boundary has advected inward across the grid and fallen into the black hole. After $t = 40$ the relative constraint error decreases with time. The highest-resolution solid curves behave differently: they increase exponentially with time. However, this growth occurs only because the normalization factor in the denominator (which measures the size of the derivatives of the fields)

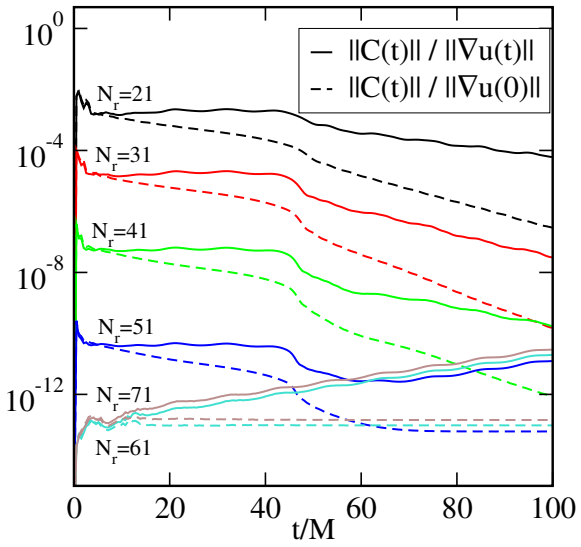

Figure 4.3: Constraint violations for evolutions with $\gamma_1 = \gamma_2 = 0$, constraint-preserving boundary conditions, and no constraint projection. Solid curves are normalized by the quantity $||\nabla u(t)||$ while the dashed curves are normalized by $||\nabla u(0)||$. Decay of the normalization factor $||\nabla u(t)||$ rather than growth of the constraints causes the growth in the highest-resolution solid curves, which have constant round-off-level constraint violations.

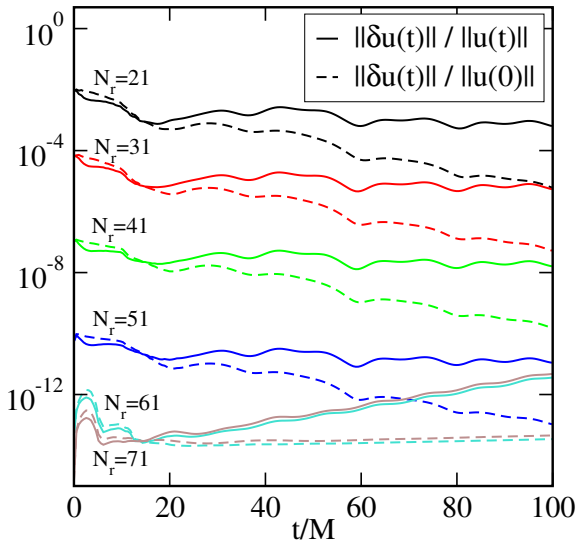

Figure 4.4: Convergence of evolutions shown in Fig. 4.3. Plotted are differences from the evolution with $N = 81$, which is henceforth the reference solution u_R. Solid curves are normalized by $||u(t)||$ while the dashed curves are normalized by $||u(0)||$. Decay of the normalization factor $||u(t)||$ causes the growth in the highest-resolution solid curves, for which $||\delta u(t)||$ is constant at roundoff level.

goes to zero as the scalar wave pulse leaves the computational domain. The highest resolution dashed curves show that the absolute constraint error for these resolutions is constant at round-off level.

Figure 4.4 illustrates the numerical convergence of these evolutions. Plotted are the ratios of the differences $||\delta u(t)||$ to a measure of the size of the fields. The solid curves in Fig. 4.4 show the ratio $||\delta u(t)||/||u(t)||$ while the dashed curves show $||\delta u(t)||/||u(0)||$. Again, the only difference is that the denominator used for the dashed curves is time independent. Figures 4.3 and 4.4 show that these scalar field evolutions are stable, constraint preserving and numerically convergent. These solutions therefore represent what we expect to be the correct physical solution to this problem. Were this our only objective, this paper would end here. However our primary interest here is to study the use of projection methods to control the growth of constraints. So we will use the solution found here as a reference to which our later evolutions using constraint projection can be compared.

Our last simulation to study the effects of boundary conditions on the growth of the constraints uses a non-standard scalar field evolution system with $\gamma_1 = 0$ and $\gamma_2 = -1/M$. In other respects, however, this simulation is identical to the one depicted in Figs. 4.3 and 4.4: It uses the same initial data, Eqs. (4.60)–(4.62), the same constraint-preserving boundary conditions, and no constraint projection. Because we use Eq. (4.39) as a boundary condition on U^{1-}, the *constraint-preserving* solutions of the equations are the same as those obtained with $\gamma_1 = \gamma_2 = 0$. However, using an evolution system with $\gamma_2 = -1/M$ introduces unstable bulk terms into the constraint evolution equations, Eqs. (4.29) and (4.30), so the *constraint-violating* solutions of the equations will be different. Consequently this system is much more pathological than the standard scalar field system, and provides a much more difficult challenge for the constraint control methods studied here. Fig. 4.5 shows the evolution of the constraints in this system. Truncation level constraint violations in the initial data grow exponentially with an e-folding time of approximately $1.1\,M$ in these evolutions. The ratio $||C(t)||/||\nabla u(t)||$ approaches a constant of order unity at late times once the constraint-violating portion of the solution dominates and the denominator begins to grow exponentially as well. The small inset graph in Fig. 4.5 illustrates that the divergence of these solutions from the reference solution of Fig. 4.4 grows at the same rate for all spatial resolutions. This suggests that the growth is caused by a constraint-violating solution to the evolution equations rather than a numerical instability.

These evolutions with $\gamma_2 = -1/M$ demonstrate that constraint preserving boundary conditions alone are insufficient to control the growth of constraints in this system. Since the Einstein evolution system is also believed to contain bulk generated constraint violations [31], this example suggests that constraint preserving boundary conditions alone will not be sufficient to control the growth of the constraints in the Einstein system.

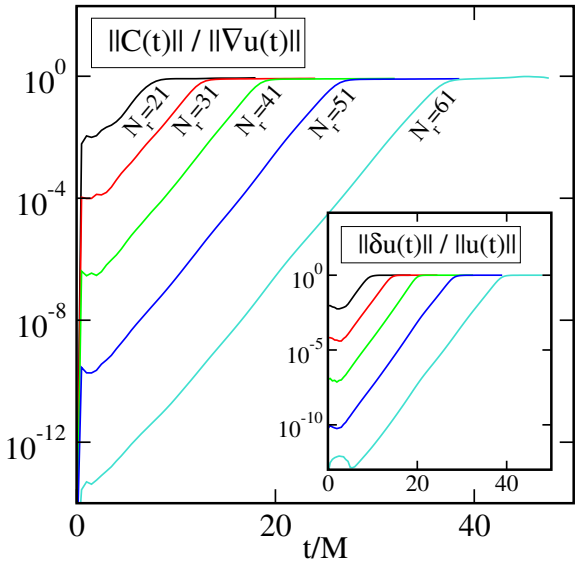

Figure 4.5: Constraint violations for evolutions with $\gamma_2 = -1/M$, constraint preserving boundary conditions, and without constraint projection. The inset shows differences $||\delta u(t)||/||u(t)||$ from the reference solution of Fig. 4.4. The curves level off at late times because both numerator and denominator grow exponentially at the same rates.

4.4.2 Testing constraint projection

In this section we discuss two numerical evolutions that explore the use of the constraint projection methods developed in Secs. 4.2 and 4.3.3. The first evolution uses the standard scalar wave evolution system with $\gamma_1 = \gamma_2 = 0$, and freezing boundary conditions. We have already seen in Figs. 4.1 and 4.2 that such evolutions exhibit significant constraint violations once the scalar wave pulse passes through the outer boundary of the computational domain. In this numerical experiment we freely evolve the scalar field to the time $t = 20M$, and then perform a single constraint projection on the solution using Eqs. (4.52)–(4.54) with $\Lambda = 2/M$. We then evolve the system freely again to $t = 40M$. Figure 4.6 shows how the constraints respond to a single constraint projection. We use a very fine timescale in Fig. 4.6, showing in detail the times around $t = 20M$ when the constraint projection is performed. Individual points in Fig. 4.6 show the amount of constraint violation after each individual time step. The value of the constraints drops sharply at the time step where the constraint projection is performed, and as we expect, the value of the constraints after this projection step is smaller for higher resolutions. So the constraint projection step is successful in significantly reducing the size of the constraints. But something rather unexpected happens next: the constraints increase by orders of magnitude on the very next free evolution time step after the constraint projection. The small inset in Fig. 4.6 shows the same data plotted on a linear rather than a logarithmic scale. This shows that the constraints grow linearly in time after the constraint projection step on a very short timescale.

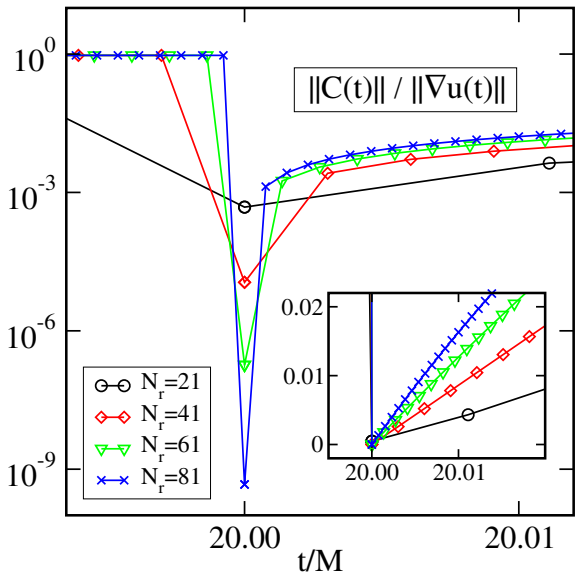

Figure 4.6: Constraint violations for evolutions with $\gamma_1 = \gamma_2 = 0$, freezing boundary conditions, and a single constraint projection at $t = 20M$ (with $\Lambda = 2/M$). Points show $||C(t)||/||\nabla u(t)||$ after each time step. The inset plots the same data on a linear scale.

Figure 4.7 provides some information about the reason for this strange behavior by showing the convergence of these numerical solutions. For times before the constraint projection step at $t = 20M$, the solutions show good numerical convergence as the number of radial collocation points is increased. But there is a sharp breakdown of numerical convergence (or at least a sharp drop in the rate of numerical convergence) after the constraint projection step.

Figure 4.8 provides some deeper insight into the reason for this lack of convergence. Plotted in Fig. 4.8 are a sequence of curves showing the radial dependences of the dipole part of the scalar field $\langle\psi\rangle_{10}$ and the monopole part of the constraints $\langle\mathcal{C}_i\mathcal{C}^i\rangle_{00}$ at a sequence of times including the constraint projection step. The spherical harmonic components of a function Q are defined by

$$\langle Q\rangle_{lm} = \int Y^*_{lm}(\theta,\varphi)Q(r,\theta,\varphi)\sin\theta\, d\theta d\varphi. \tag{4.74}$$

The dashed lines at the bottom of Fig. 4.8 show the radial profiles at $t = 20\,M$ immediately before the constraint projection, while the lowest solid lines show these profiles at the same time $t = 20\,M$ just after the projection. We see that the constraints essentially vanish after the constraint projection step. The next profile at $t = 21\,M$ shows that the scalar field develops some non-smooth radial structure immediately after the projection step, which subsequently propagates into the computational domain. This non-smoothness in ψ causes a sharp spike in the constraints, seen clearly in Fig. 4.8. Spectral methods do not converge well for non-smooth functions, so the emergence of this structure in ψ explains the breakdown in the numerical convergence and thence the breakdown in

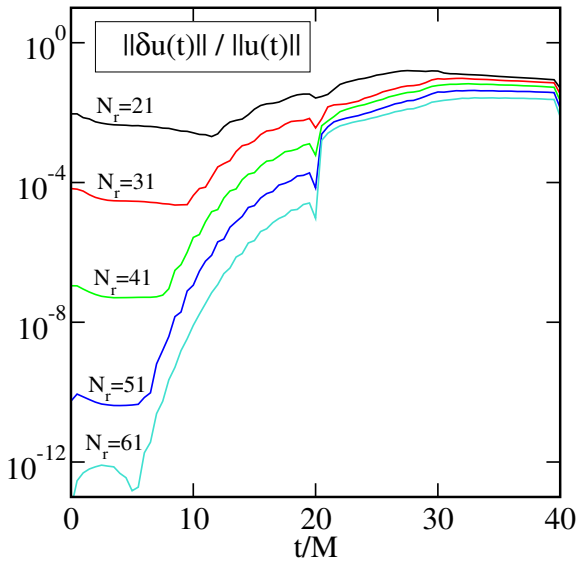

Figure 4.7: Convergence of evolutions shown in Fig. 4.6. Plotted are differences from the evolution with $N_r = 81$.

our constraint projection method. The emergence of the non-smoothness in ψ seems to be caused by the constraint projection step in the following way: The projection produces a ψ that is non-vanishing at the boundary, and the freezing boundary condition then forces $\psi = Z^1$ (and Z_i^2) to develop kinks (see [32]) which propagate into the computational domain during the free evolution steps following the projection.

Figures 4.6–4.8 demonstrate that constraint projection is not successful in removing large constraint violations when used in conjunction with freezing boundary conditions. One might hope that this failure could be corrected by projecting out the constraints before they are allowed to grow too large. Figure 4.9 shows the convergence of solutions in which a constraint projection is performed after each evolution time step, for a variety of different time steps Δt. Like the evolutions shown in Figures 4.6–4.8, these evolutions use the standard scalar field system ($\gamma_1 = \gamma_2 = 0$), freezing boundary conditions, and constraint projection with $\Lambda = 2/M$. The three curves in Fig. 4.9 measure the convergence of the solution (relative to the highest resolution reference solution depicted in Fig. 4.4) at three different times in this evolution, $t_0 = 10.24\,M$, $20.48\,M$, and $30.72\,M$. All of these evolutions use the same spatial resolution, $N_r = 51$. These graphs show that the convergence towards the reference solution is only first order in the time step Δt. This convergence is significantly worse than that expected for the fourth-order Runge-Kutta time step integrator that we use. In contrast the free evolutions with constraint-preserving boundary conditions shown in Fig. 4.4 achieve $||\delta u(t_0)||/||u(t_0)|| \lesssim 10^{-10}$ with a time step similar to the largest Δt shown in Fig. 4.9. We conclude that constraint projection produces only first order in time convergent numerical solutions when used in conjunction with standard freezing boundary conditions, and is

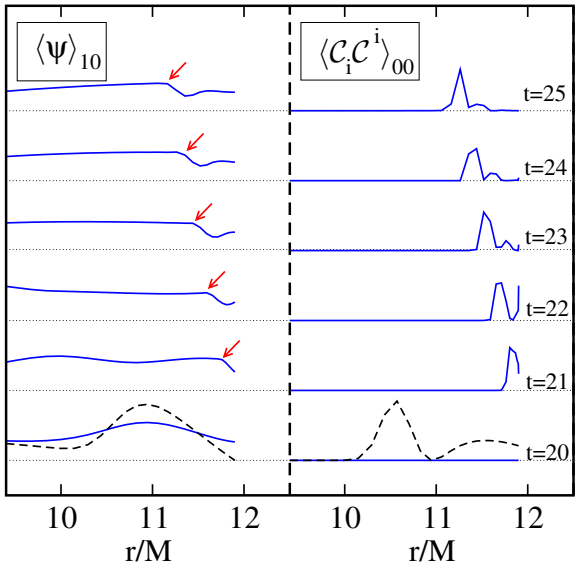

Figure 4.8: Radial profiles of $\langle\psi\rangle_{10}$ and $\langle C_i C^i\rangle_{00}$ for the evolution of Fig. 4.6. The solid lines represent times $t/M = 20, \ldots, 25$. The dashed line represents the state just before the constraint projection at $t/M = 20$. The arrows indicate the location of the non-smoothness in ψ.

therefore an ineffective substitute for constraint-preserving boundary conditions.

Finally we apply constraint projection to the pathological scalar wave evolution system ($\gamma_1 = 0$ and $\gamma_2 = -1/M$), which we failed to control with constraint preserving boundary conditions alone. We project every $\Delta T = 2M$ using $\Lambda = \sqrt{2}/M$, and we continue to use constraint preserving boundary conditions. Except for constraint projection, this is the same as the evolution shown in Fig. 4.5. Figure 4.10 shows that the constraints are reduced to truncation error levels in these evolutions. The small inset graph shows these same curves with a finer time resolution, so the saw-tooth shaped evolution of the constraints can be seen more clearly. We note that constraint projection does not occur at every evolution time step in these simulations, but rather at fixed times separated by $\Delta T = 2M$. The evolutions with the finest spatial resolution take more than one thousand time steps between projections. Figure 4.11 shows the convergence between these evolutions and the highest resolution reference solution depicted in Fig. 4.4. This figure demonstrates that the constraint projection method combined with constraint preserving boundary conditions succeeds in producing the same numerical solution as our reference solution—even for this pathological scalar field system.

4.4.3 Optimizing constraint projection

In this section we explore ways to optimize the use of the constraint projection methods developed in Secs. 4.2 and 4.3.3. In particular we investigate how important the choice of the parameter Λ is

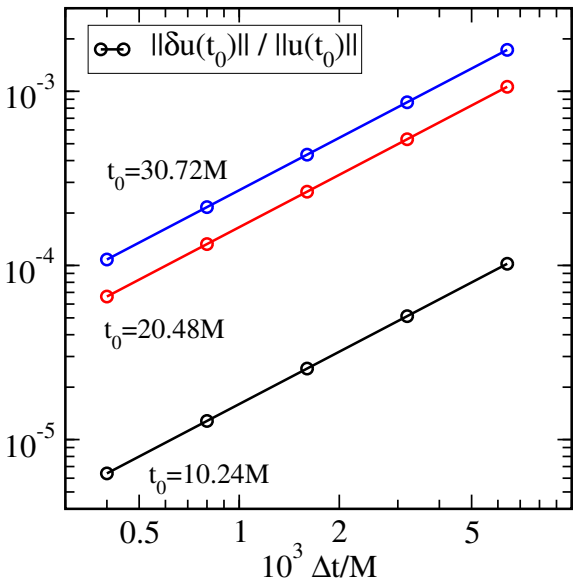

Figure 4.9: Differences between evolutions with time step Δt and the reference solution u_R (of Fig. 4.4) at fixed evolution times t_0. Evolutions use $\gamma_1 = \gamma_2 = 0$, freezing boundary conditions, and constraint projection with $\Lambda = 2/M$ after each time step, $\Delta T = \Delta t$.

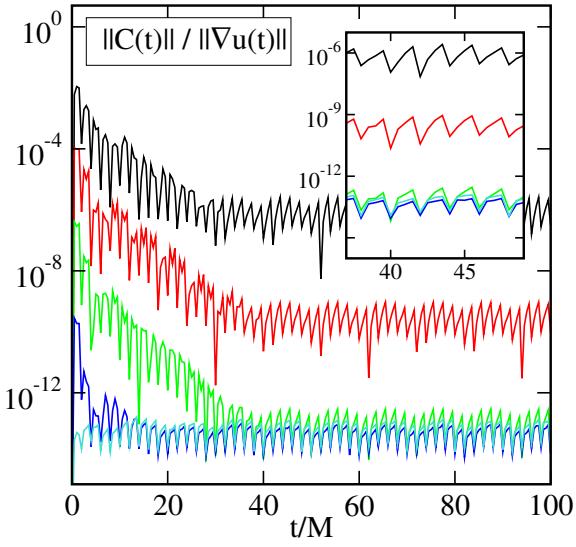

Figure 4.10: Constraint violations $||C(t)||/||\nabla u(t)||$ for evolutions with $\gamma_1 = 0$ and $\gamma_2 = -1/M$, constraint preserving boundary conditions, and constraint projection with $\Lambda = \sqrt{2}/M$ every $\Delta T = 2M$. Inset shows the same data with finer time resolution.

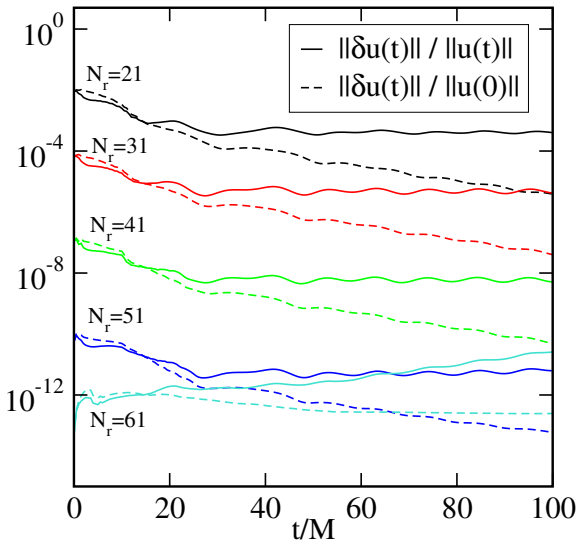

Figure 4.11: Differences from the reference solution u_R (of Fig. 4.4) for the evolutions shown in Fig. 4.10.

to the effectiveness of the projection, and we determine its optimal value. We also vary the time between projection steps, ΔT, and determine the optimal rate at which to perform these projections. Finally we measure the computational cost of performing a scalar field evolution with constraint projection, compared to the cost of doing a free evolution.

Figure 4.12 shows convergence plots for evolutions of the pathological scalar field system with $\gamma_1 = 0$ and $\gamma_2 = -1/M$, constraint-preserving boundary conditions, and constraint projection every $\Delta T = 2M$. All evolutions use the same radial resolution, $N_r = 41$. Each of the solid curves in Fig. 4.12 represents an evolution using a different choice of the parameter Λ. We see that the evolutions using projections with $\Lambda = \sqrt{2}/M$ are somewhat closer to the reference solution than the others, but the size of the differences are not very sensitive to the value of Λ. The only projected solution having significantly worse accuracy than the others is the one with $\Lambda = \infty$, which corresponds to the simple projection with $\psi = \bar{\psi}$, $\Pi = \bar{\Pi}$ and $\Phi_i = \partial_i \psi$. For all choices of Λ, including $\Lambda = \infty$, these evolutions are exponentially convergent with increasing N_r.

We have some understanding of why there is an optimal choice for the parameter Λ: It is possible to analyze the projection process completely and analytically for scalar field evolutions with a flat background metric on a computational domain with three-torus (T^3) topology. By performing a Fourier transform of the fields in this case it is easy to show that the fields break up into modes that propagate with the usual dispersion relation $\omega^2 = \vec{k} \cdot \vec{k}$, plus others that grow exponentially in time with dispersion relation $\omega = i\gamma_2$. The projection step becomes a simple algebraic transformation on the Fourier components of the field in this case. So it is straightforward to show that the projection step completely removes the modes that grow exponentially with time only when the

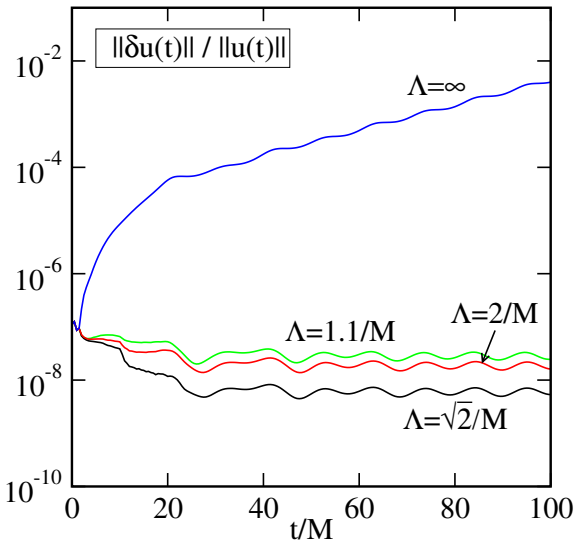

Figure 4.12: Differences $||\delta u(t)||/||u(t)||$ from the reference solution u_R of Fig. 4.4 are plotted for different choices of Λ. Evolutions with $\gamma_1 = 0$ and $\gamma_2 = -1/M$, constraint-preserving boundary conditions, constraint projection every $\Delta T = 2M$.

parameters satisfy $\Lambda^2 = 2\gamma_2^2$. For evolutions on computational domains with different topologies, and different background metrics, it is not possible to determine the optimal choice of Λ using such a simple argument. However it is not surprising that the optimal choice is not too different from $\Lambda^2 = 2\gamma_2^2$.

Next we consider the effect of varying the times between constraint projections. Figure 4.13 shows the convergence measure $||\delta u(t_0)||/||u(t_0)||$ for evolutions of the pathological scalar field system with $\gamma_1 = 0$ and $\gamma_2 = -1/M$, constraint preserving boundary conditions, and constraint projections with various values of Λ and ΔT. These evolutions are all carried out with the same radial resolution $N_r = 41$, and are compared with the reference solution of Fig. 4.4 at the time $t_0 = 100M$. Each curve in Fig. 4.13 represents a set of evolutions with the same value of Λ but varying ΔT. The smallest ΔT for each curve corresponds to projecting at each evolution time step. We see that all of these curves show a minimum difference with the reference solution, and this minimum occurs at about $\Delta T \approx 1M$ in all of these curves. This coincides with the e-folding time of the bulk constraint violations, $-1/\gamma_2$; hence we expect that constraint projection should generally be applied on a time-scale comparable to that of the constraint growth. Figure 4.13 also reveals that projections performed with $\Lambda^2 = 2\gamma_2^2$ are the optimal ones over a fairly broad range of projection times ΔT. The evolutions with simple constraint projection ($\Lambda = \infty$) crash for very small values of ΔT, as well as for $\Delta T = 10M$.

Finally, we have made some measurements to evaluate the computational cost of doing scalar field evolutions with constraint projection, compared to the cost of free evolution. Figure 4.14

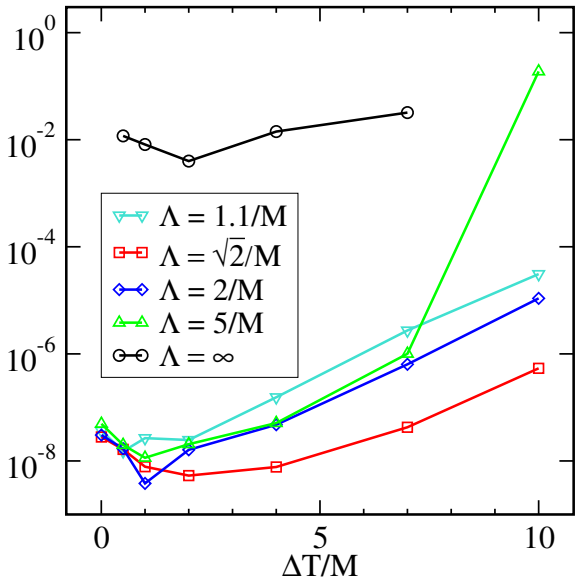

Figure 4.13: Evolutions with $\gamma_1 = 0$ and $\gamma_2 = -1/M$, constraint preserving boundary conditions and constraint projection every ΔT. Differences from the reference solution u_R (of Fig. 4.4) at $t_0 = 100M$ for different choices of ΔT and Λ.

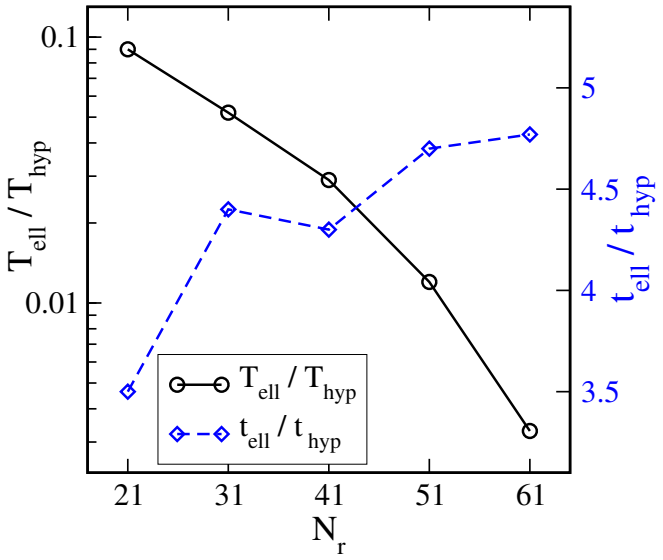

Figure 4.14: Solid curve (left axis) shows the ratio of time spent in elliptic solves to time spent in the hyperbolic evolution code. Dashed curve (right axis) shows the ratio of time required for one elliptic solve to the time for one evolution time step.

contains two curves that measure the computational cost of doing optimal projection with $\Delta T = 2M$. The solid curve shows the ratio of the time the code spends doing the constraint projection step (i.e., doing the elliptic solve) $T_{\rm ell}$ with the time the code spends doing evolution steps $T_{\rm hyp}$. This ratio decreases from about 0.1 using a very coarse spatial resolution to about 0.003 using a very fine spatial resolution. The ratio $T_{\rm ell}/T_{\rm hyp}$ decreases when the spatial resolution is increased because the code must take many more free evolution time steps in the time ΔT between projection steps in this case. The dashed curve in Fig. 4.14 measures the ratio of the time needed to perform one constraint projection, $t_{\rm ell}$, with the time needed to take one free evolution step, $t_{\rm hyp}$. We see that this ratio is fairly independent of resolution using our spectral elliptic solver, and ranges from about 3.5 at low spatial resolution to about 5 at high resolution. These tests show that the computational cost of performing constraint projection is only a small fraction of the total computational cost of performing these scalar field evolutions. We conclude that computational cost should not be used as an argument against the use of constraint projection methods.

4.5 Discussion

We have developed general methods in Sec. 4.2 for constructing optimal projection operators that map the dynamical fields of hyperbolic evolution systems onto the constraint submanifold associated with these systems. These methods are worked out explicitly in Sec. 4.3 for the case of a new evolution system that describes the propagation of a scalar field on a fixed background spacetime. The constraint projection map for this system requires the solution of one elliptic partial differential equation each time a projection is performed. The new scalar field system introduced in Sec. 4.3 has the interesting property that it suffers from constraint violations that flow into the domain through timelike boundaries and also from violations generated by bulk terms in the equations. So this system exhibits both types of constraint violating pathologies that can occur in the Einstein evolution system. To test our constraint projection methods, we perform a number of numerical evolutions of this scalar field system propagating on a black-hole spacetime. We show that constraint-preserving boundary conditions alone are not capable of controlling the growth of constraints in this scalar field system. Constraint projection is also shown to be ineffective when used in conjunction with traditional boundary conditions that do not prevent the influx of constraint violations through the boundary. However we show that the combination of constraint projection and constraint-preserving boundary conditions is a very effective method for controlling the growth of the constraints. We measure the computational cost of performing these constraint projections and show that at the highest numerical resolutions, the projections account for only a fraction of a percent of the total computational cost of the evolution. Thus high computational cost can no longer be cited as a reason to avoid constraint projection techniques.

4.6 Acknowledgements

We thank Saul Teukolsky and Manuel Tiglio for helpful comments. Some of the computations for this project were performed with the Tungsten cluster at NCSA. This work was supported in part by NSF grants PHY-0099568, PHY-0244906 and NASA grants NAG5-10707, NAG5-12834 at Caltech, NSF grants DMS-9875856, DMS-0208449, DMS-0112413 at UCSD, and NSF grants PHY-9900672, PHY-0312072 at Cornell.

Bibliography

[1] A. M. Abrahams, G. B. Cook, S. L. Shapiro, and S. A. Teukolsky. Solving Einstein's equations for rotating spacetimes: Evolution of relativistic star clusters. *Phys. Rev. D*, 49:5153–5164, 1994.

[2] A. M. Abrahams and C. R. Evans. Trapping a geon: Black hole formation by an imploding gravitational wave. *Phys. Rev. D*, 46:R4117–R4121, 1992.

[3] A. M. Abrahams and C. R. Evans. Critical behavior and scaling in vacuum axisymmetric gravitational collapse. *Phys. Rev. Lett.*, 70:2980–2983, 1993.

[4] Alexander M. Alekseenko. Constraint preserving boundary conditions for the linearized bssn formulation. 2004. gr-qc/0405080.

[5] M. Anderson and R. A. Matzner. Extended lifetime in computational evolution of isolated black holes. *Found. Phys.*, 35:1477–1495, 2005. gr-qc/0307055.

[6] V. I. Arnold. *Mathematical Methods of Classical Mechanics*. Springer-Verlag, New York, NY, 1989.

[7] Morten Bjørhus. The ode formulation of hyperbolic pdes discretized by the spectral collocation method. *SIAM J. Sci. Comput.*, 16(3):542–557, May 1995.

[8] S. Bonazzola, E. Gourgoulhon, P. Grandclement, and J. Novak. A constrained scheme for Einstein equations based on Dirac gauge and spherical coordinates. *Phys. Rev. D*, 70:104007, 2004.

[9] F. Brezzi and M. Fortin. *Mixed and Hybrid Finite Element Methods*. Springer-Verlag, New York, NY, 1991.

[10] Gioel Calabrese, Luis Lehner, and Manuel Tiglio. Constraint-preserving boundary conditions in numerical relativity. *Phys. Rev. D*, 65:104031, 2002.

[11] Gioel Calabrese, Jorge Pullin, Olivier Sarbach, Manuel Tiglio, and Oscar Reula. Well posed constraint-preserving boundary conditions for the linearized Einstein equations. *Commun. Math. Phys.*, 240:377–395, 2003.

[12] Gioel Calabrese and Olivier Sarbach. Detecting ill posed boundary conditions in general relativity. *J. Math. Phys.*, 44:3888–3899, 2003.

[13] Matthew W. Choptuik. Universality and scaling in gravitational collapse of a massless scalar field. *Phys. Rev. Lett.*, 70(1):9, January 1993.

[14] Matthew W. Choptuik, Eric W. Hirschmann, Steven L. Liebling, and Frans Pretorius. An axisymmetric gravitational collapse code. *Class. Quantum Grav.*, 20:1857–1878, 2003.

[15] Matthew W. Choptuik, Eric W. Hirschmann, Steven L. Liebling, and Frans Pretorius. Critical collapse of the massless scalar field in axisymmetry. *Phys. Rev. D*, 68:044007, 2003.

[16] Helmut Friedrich and Gabriel Nagy. The initial boundary value problem for Einstein's vacuum field equation. *Comm. Math. Phys.*, 201(3):619–655, 1999.

[17] Simonetta Frittelli and Roberto Gomez. Boundary conditions for hyperbolic formulations of the Einstein equations. *Class. Quantum Grav.*, 20:2379–2392, 2003.

[18] Simonetta Frittelli and Roberto Gomez. Einstein boundary conditions for the 3+1 Einstein equations. *Phys. Rev. D*, 68:044014, 2003.

[19] Simonetta Frittelli and Roberto Gomez. Einstein boundary conditions in relation to constraint propagation for the initial-boundary value problem of the Einstein equations. *Phys. Rev. D*, 69:124020, 2004.

[20] C. W. Gear. The simultaneous numerical solution of differential-algebraic equations. *IEEE Trans. Circuit Theory*, CT-18:89–95, 1971.

[21] Bertil Gustafsson, Heinz-Otto Kreiss, and Joseph Oliger. *Time Dependent Problems and Difference Methods. Pure and Applied Mathematics*. Wiley, New York, 1995.

[22] E. Hairer, C. Lubich, and G. Wanner. *Geometric Numerical Integration*. Springer-Verlag, Berlin, Germany, 2001.

[23] Mirta S. Iriondo and Oscar A. Reula. On free evolution of self gravitating, spherically symmetric waves. *Phys. Rev. D*, 65:044024, 2002.

[24] J. Kevorkian. *Partial Differential Equations*. Wadsworth & Brooks/Cole Advanced Books & Software, Pacific Grove, CA, 1990.

[25] L. E. Kidder, M. A. Scheel, and S. A. Teukolsky. Extending the lifetime of 3d black hole computations with a new hyperbolic system of evolution equations. *Phys. Rev. D*, 64(6):064017, Sep 2001.

[26] L. E. Kidder, M. A. Scheel, S. A. Teukolsky, Eric D. Carlson, and G. B. Cook. Black hole evolution by spectral methods. *Phys. Rev. D*, 62:084032, Oct 2000.

[27] C. Lanczos. *The Variational Principles of Mechanics.* Dover Publications, Inc., New York, NY, 1949.

[28] B. Leimkuhler. Comparison of geometric integrators for rigid body simulation. *Lect. Notes Comput. Sci. Eng.*, 4, 1999.

[29] B. Leimkuhler and S. Reich. Symplectic integration of constrained Hamiltonian systems. *Math. Comp.*, 63(208):589–605, 1994.

[30] B. Leimkuhler and R. D. Skeel. Symplectic numerical integrators in constrained Hamiltonian systems. *J. Comput. Phys.*, 112(1):117–125, 1994.

[31] Lee Lindblom and Mark A. Scheel. *Phys. Rev. D*, 66:084014, 2002.

[32] Lee Lindblom, Mark A. Scheel, Lawrence E. Kidder, Harald P. Pfeiffer, Deirdre Shoemaker, and Saul A. Teukolsky. Controlling the growth of constraints in hyperbolic evolution systems. *Phys. Rev. D*, 69:124025, 2004.

[33] J. E. Marsden and T. J. R. Hughes. *Mathematical Foundations of Elasticity*. Dover Publications, New York, NY, 1994.

[34] Harald P. Pfeiffer, Lawrence E. Kidder, Mark A. Scheel, and Saul A. Teukolsky. A multidomain spectral method for solving elliptic equations. *Comput. Phys. Commun.*, 152:253–273, 2003.

[35] Mark A. Scheel, Adrienne L. Erickcek, Lior M. Burko, Lawrence E. Kidder, Harald P. Pfeiffer, and Saul A. Teukolsky. 3d simulations of linearized scalar fields in Kerr spacetime. *Phys. Rev. D*, 69(10):104006, May 2004.

[36] Mark A. Scheel, Lawrence E. Kidder, Lee Lindblom, Harald P. Pfeiffer, and Saul A. Teukolsky. Toward stable 3d numerical evolutions of black-hole spacetimes. *Phys. Rev. D*, 66:124005, Dec 2002.

[37] Erik Schnetter. *Gauge Fixing for the Simulation of Black Hole Spacetimes.* PhD thesis, Universität Tübingen, 2003. gr-qc/0411002.

[38] R. F. Stark and T. Piran. Gravitational-wave emission from rotating gravitational collapse. *Phys. Rev. Lett.*, 55:891–894, 1985.

[39] John M. Stewart. The cauchy problem and the initial boundary value problem in numerical relativity. *Class. Quantum Grav.*, 15:2865–2889, 1998.

[40] Béla Szilágyi, Bernd Schmidt, and Jeffrey Winicour. Boundary conditions in linearized harmonic gravity. *Phys. Rev. D*, 65:064015, 2002.

[41] Béla Szilágyi and Jeffrey Winicour. Well-posed initial-boundary evolution in general relativity. *Phys. Rev. D*, 68:041501(R), 2003.

[42] M. E. Taylor. *Partial Differential Equations*, volume III. Springer-Verlag, New York, NY, 1996.

[43] M. E. Taylor. *Partial Differential Equations*, volume I. Springer-Verlag, New York, NY, 1996.

[44] R. Temam. *Navier-Stokes Equations: Theory and Numerical Analysis*. North-Holland, New York, NY, 1977.

[45] E. Zeidler. *Nonlinear Functional Analysis and its Applications*, volume III: Variational Methods and Optimization. Springer-Verlag, New York, NY, 1991.

Chapter 5

A first-order generalized harmonic evolution system

Originally published as Class.Quant.Grav. 23 (2006) S447-S462.

A new representation of the Einstein evolution equations is presented that is first order, linearly degenerate, and symmetric hyperbolic. This new system uses the generalized harmonic method to specify the coordinates, and exponentially suppresses all small short-wavelength constraint violations. Physical and constraint-preserving boundary conditions are derived for this system, and numerical tests that demonstrate the effectiveness of the constraint suppression properties and the constraint-preserving boundary conditions are presented.

5.1 Introduction

Harmonic and generalized harmonic (GH) coordinates have played important roles in general relativity theory from the very beginning. Einstein used harmonic (then called isothermal) coordinates in his analysis of candidate theories of gravitation (as recorded in his Zurich notebook of 1912) before general relativity even existed [24], DeDonder used them to analyze the characteristic structure of general relativity in 1921 [8, 9], and Fock used them to analyze gravitational waves in 1955 [11]. Harmonic coordinates played an important role in the proofs of the well-posedness of the Cauchy problem for the Einstein equations by Choquet-Bruhat in 1952 [12, 4] and by Fischer and Marsden in 1972 [10]. Harmonic coordinates have also been used to obtain numerical solutions of Einstein's equations by Garfinkle [15] and by Winicour and collaborators [30, 31, 2]. The idea of specifying *arbitrary* coordinate systems using a generalization of harmonic coordinates was introduced by Friedrich in 1985 [13]. And quite recently the GH approach to specifying coordinates played an important, perhaps seminal, role in the state-of-the-art numerical simulations of the final inspiral and merger of binary black-hole systems by Pretorius [22, 21] using a form of the equations suggested

by Gundlach et al. [16].

We think there are two important properties that have made harmonic or GH coordinates such an important tool throughout the history of general relativity theory. The first property is well known: this method of specifying the coordinates transforms the principal parts of the Einstein equations into a manifestly hyperbolic form, in which each component of the metric is acted on by the standard second-order wave operator. The second property is not as widely appreciated: this method of specifying coordinates fundamentally transforms the constraints of the theory. This new form of the constraints makes it possible to modify the evolution equations in a way that prevents small constraint violations from growing during numerical evolutions—without changing the physical solutions of the system and without changing the fundamental hyperbolic structure of the equations. The purpose of this paper is to explore and understand these important properties and to extend the GH evolution system in a way that makes it even more useful for numerical computations. In Sec. 5.2 we review the modified form of the GH evolution system of Gundlach et al. and Pretorius. We convert and extend this system in Sec. 5.3 into a symmetric-hyperbolic first-order evolution system that has constraint suppression properties comparable to those of the second-order system. We derive and analyze the well-posedness of constraint-preserving and physical boundary conditions for this new first-order system in Sec. 5.4, and in Sec. 5.5 we present numerical tests that demonstrate the effectiveness of its constraint suppression properties and the new constraint-preserving boundary conditions.

5.2 Generalized harmonic evolution system

Harmonic (sometimes called wave) coordinates are functions x^a that satisfy the covariant scalar wave equation. These coordinates are very useful because they significantly simplify the second-derivative terms in the Ricci curvature tensor. To see this explicitly, consider a spacetime with metric tensor ψ_{ab}:

$$ds^2 \quad = \quad \psi_{ab} dx^a dx^b. \tag{5.1}$$

(We use Latin indices from the first part of the alphabet $a, b, c, ...$ to denote 4-dimensional spacetime quantities.) A coordinate x^b is called harmonic if it satisfies the scalar wave equation,

$$0 = \psi_{ab} \nabla^c \nabla_c x^b = -\Gamma_a, \tag{5.2}$$

where ∇_c denotes the covariant derivative compatible with ψ_{ab}, and $\Gamma_a \equiv \psi^{bc}\Gamma_{abc}$ is the trace of the standard Christoffel symbol Γ_{abc}:

$$\Gamma_{abc} \quad = \quad \tfrac{1}{2}(\partial_b\psi_{ac} + \partial_c\psi_{ab} - \partial_a\psi_{bc}). \tag{5.3}$$

The right side of Eq. (5.2) is just the expression for this covariant wave operator acting on x^b in terms of partial derivatives and Christoffel symbols.

The Ricci curvature tensor can be written as

$$R_{ab} \quad = \quad -\tfrac{1}{2}\psi^{cd}\partial_c\partial_d\psi_{ab} + \nabla_{(a}\Gamma_{b)} + \psi^{cd}\psi^{ef}\left(\partial_e\psi_{ca}\partial_f\psi_{db} - \Gamma_{ace}\Gamma_{bdf}\right), \tag{5.4}$$

in any coordinate system, where $\nabla_a\Gamma_b \equiv \partial_a\Gamma_b - \psi^{cd}\Gamma_{cab}\Gamma_d$. In harmonic coordinates, $\Gamma_a = 0$, so the only second-derivative term remaining in the Ricci tensor is $\psi^{cd}\partial_c\partial_d\psi_{ab}$. Therefore in harmonic coordinates the vacuum Einstein equations, $R_{ab} = 0$, form a manifestly hyperbolic system [12],

$$\psi^{cd}\partial_c\partial_d\psi_{ab} \quad = \quad 2\,\psi^{cd}\psi^{ef}\left(\partial_e\psi_{ca}\partial_f\psi_{db} - \Gamma_{ace}\Gamma_{bdf}\right). \tag{5.5}$$

Friedrich [13] (and independently Garfinkle [15]) realized that the manifestly hyperbolic form of the Einstein system, Eq. (5.5), can also be achieved for *arbitrary* coordinates, if the choice of coordinates is fixed in a certain (but non-standard) way. This alternate method of specifying the choice of coordinates, which we call the generalized harmonic (GH) method, is implemented by assuming that the coordinates satisfy the inhomogeneous wave equation,

$$H_a(x,\psi) = \psi_{ab}\nabla_c\nabla^c x^b = -\Gamma_a, \tag{5.6}$$

where $H_a(x,\psi)$ is an arbitrary but fixed algebraic function of the coordinates x^a and the metric ψ_{ab} (but not its derivatives). In these GH coordinates $H_a = -\Gamma_a$, so the vacuum Einstein equations are again manifestly hyperbolic:

$$\psi^{cd}\partial_c\partial_d\psi_{ab} \quad = \quad -2\nabla_{(a}H_{b)} + 2\,\psi^{cd}\psi^{ef}\left(\partial_e\psi_{ca}\partial_f\psi_{db} - \Gamma_{ace}\Gamma_{bdf}\right). \tag{5.7}$$

The term containing H_b on the right side of Eq. (5.7) is a pre-specified algebraic function (of x^a and ψ_{ab}) that operates as a source term, rather than one of the principal terms containing second derivatives of ψ_{ab}. The principal (i.e., second-derivative) parts of this GH evolution system, Eq. (5.7), are therefore identical to those of the harmonic evolution system, Eq. (5.5).

To understand the GH method of specifying coordinates more clearly, it is helpful to compare

it to the more traditional way of specifying coordinates with the lapse and the shift. To do this we introduce a foliation of the spacetime by spacelike hypersurfaces, and adopt a coordinate system, $\{t, x^k\}$, with the $t =$ constant surfaces being the leaves of this foliation. The traditional lapse N, shift N^k, and 3-dimensional spatial metric g_{ij} associated with this coordinate system are then defined by

$$ds^2 \quad = \quad \psi_{ab} dx^a dx^b = -N^2 dt^2 + g_{ij}(dx^i + N^i dt)(dx^j + N^j dt). \tag{5.8}$$

(We use Latin indices $i, j, k, ...$ to denote 3-dimensional spatial quantities; while Latin indices from the first part of the alphabet $a, b, c, ...$ will continue to denote 4-dimensional quantities.) Expressing the GH coordinate condition, Eq. (5.6), in this 3+1 language implies evolution equations for the lapse and shift:

$$\partial_t N - N^k \partial_k N \quad = \quad -N\big(H_t - N^i H_i + NK\big), \tag{5.9}$$

$$\partial_t N^i - N^k \partial_k N^i \quad = \quad N g^{ij}\Big[N\big(H_j + g^{kl}\Gamma_{jkl}\big) - \partial_j N\Big], \tag{5.10}$$

where K is the trace of the extrinsic curvature. Specifying the GH gauge function $H_a(x, \psi)$ therefore determines the time derivatives of the lapse N and shift N^k, and hence the evolution of the gauge degrees of freedom of the system. Some gauge conditions (e.g., $N = 1$, $N^k = 0$) may not be simple conditions on H_a, just as some gauge conditions (e.g., $H_a = 0$) are not simple conditions on N and N^k. In this paper we restrict attention to the cases where $H_a(x, \psi)$ is a specified algebraic function. Any chosen coordinates can clearly be described (*ex post facto*) by an H_a of this form. But H_a may also be specified in more general ways, e.g., by giving evolution equations for H_a [22]. We expect (but have not proven) that any coordinates can be obtained by specifying *a priori* suitable (possibly complicated) conditions on H_a.

5.2.1 Constraint evolution

Our experience in solving the Einstein equations numerically is that small constraint violations typically grow into large constraint violations that quickly make the solutions unphysical. We think it is essential therefore to understand the constraints and how violations of those constraints evolve with time. To this end it is helpful to consider the following representation of the GH system, Eq. (5.7):

$$0 = R_{ab} - \nabla_{(a} C_{b)}, \tag{5.11}$$

where R_{ab} is the Ricci tensor defined in Eq. (5.4), and $\mathcal{C}_a$ is defined as

$$\mathcal{C}_a = H_a + \Gamma_a. \tag{5.12}$$

From this perspective the condition $\mathcal{C}_a = 0$ serves as the constraint that ensures the coordinates satisfy the GH coordinate condition, Eq. (5.6). It is straightforward to verify that Eq. (5.11) is equivalent to the GH evolution equations, Eq. (5.7). This form of the GH system, Eq. (5.11), is also formally equivalent to the Z4 system [3] (in the sense that there is a one-to-one correspondence between solutions of the two systems), where the constraint $\mathcal{C}_a$ plays the role of the Z4 vector field [16]. The systems differ however in the way the fields are evolved: in the Z4 system the field $\mathcal{C}_a$ is evolved as a separate dynamical field, while in the GH representation $\mathcal{C}_a$ is treated as a constraint which is not evolved separately.

The evolution equation for the constraints is easily deduced from the GH evolution system, Eq. (5.11): take the divergence of the trace-reversed Eq. (5.11), use the contracted Bianchi identity $\nabla^a R_{ab} - \frac{1}{2}\nabla_b R = 0$, and exchange the order of covariant derivatives with the Ricci identity, yielding

$$0 = \nabla^b \nabla_b \mathcal{C}_a + R_{ab}\,\mathcal{C}^{\,b}. \tag{5.13}$$

Finally the Ricci tensor can be eliminated using Eq. (5.11) to produce the following equation for the evolution of the constraints [14]:

$$0 = \nabla^b \nabla_b \mathcal{C}_a + \mathcal{C}^{\,b} \nabla_{(a} \mathcal{C}_{b)}. \tag{5.14}$$

This equation guarantees that the constraints $\mathcal{C}_a$ will remain zero within the domain of dependence of an initial surface on which $\mathcal{C}_a = \partial_t \mathcal{C}_a = 0$. Thus the GH evolution system is self-consistent.

The standard Hamiltonian and momentum constraints of general relativity are encoded in the constraints of the GH system in an interesting way. Let t^a denote the unit timelike normal to the $t =$ constant surfaces of the foliation used in Eq. (5.8). The standard Hamiltonian and momentum constraints are combined here into the single 4-dimensional momentum constraint $\mathcal{M}_a$, which is given by the contraction of t^a with the Einstein curvature tensor:

$$\mathcal{M}_a \equiv \big(R_{ab} - \tfrac{1}{2}\psi_{ab} R\big) t^b. \tag{5.15}$$

Using Eq. (5.11) for a spacetime that satisfies the GH evolution system, we see that

$$t^b \nabla_b \mathcal{C}_a = 2\mathcal{M}_a + (g^{bc} t_a - t^c g^b{}_a) \nabla_b \mathcal{C}_c, \tag{5.16}$$

where $g_{ab} = \psi_{ab} + t_a t_b$ is the intrinsic metric to the $t =$ constant hypersurfaces. Specifying the initial

data needed to determine the evolution of the constraints, $\{\mathcal{C}_a, \partial_t \mathcal{C}_a\}$, via Eq. (5.14) is equivalent therefore to specifying the more usual representation of the constraints, $\{\mathcal{C}_a, \mathcal{M}_a\}$, on that surface.

5.2.2 Constraint damping

The impressive numerical simulations of binary black-hole spacetimes performed recently by Pretorius [22, 21] are based on a modified form of the GH evolution system suggested by Gundlach et al. [16]. This modified system has the remarkable property that it causes constraint violations to be damped out as the system evolves. The modified system is given by

$$0 = R_{ab} - \nabla_{(a}\mathcal{C}_{b)} + \gamma_0 \big[t_{(a}\mathcal{C}_{\,b)} - \tfrac{1}{2}\psi_{ab}\, t^c \mathcal{C}_c \big], \tag{5.17}$$

where t^a (as before) is the future directed timelike unit normal to the $t =$ constant surfaces, and γ_0 is a constant that determines the timescale on which the constraints are damped. This system can also be written more explicitly as

$$\begin{aligned} \psi^{cd}\partial_c\partial_d\psi_{ab} \;\; &= \;\; -2\nabla_{(a}H_{b)} + 2\,\psi^{cd}\psi^{ef}\big(\partial_e\psi_{ca}\partial_f\psi_{db} - \Gamma_{ace}\Gamma_{bdf}\big) \\ &\quad + \gamma_0\big[2\delta^c{}_{(a}t_{b)} - \psi_{ab}\,t^c\big](H_c + \Gamma_c). \end{aligned} \tag{5.18}$$

This system is manifestly hyperbolic since the additional constraint damping terms (i.e., those proportional to γ_0) do not modify the principal parts of the standard GH evolution system. It is also clear that the constraint-satisfying solutions of this system are identical to those of the standard Einstein system.

In order to understand how this modification affects the constraints, we must analyze the associated constraint evolution system. This can be done by following the same steps that lead to Eq. (5.13), but in this case we obtain

$$0 = \nabla^b\nabla_b\mathcal{C}_a + R_{ab}\,\mathcal{C}^{\,b} - 2\gamma_0\nabla^b[\,t_{(b}\mathcal{C}_{a)}], \tag{5.19}$$

or using Eq. (5.17),

$$0 \;\; = \;\; \nabla^c\nabla_c\mathcal{C}_a - 2\gamma_0\nabla^b[\,t_{(b}\mathcal{C}_{a)}] + \mathcal{C}^{\,b}\nabla_{(a}\mathcal{C}_{b)} - \tfrac{1}{2}\gamma_0\, t_a\mathcal{C}^{\,b}\mathcal{C}_b. \tag{5.20}$$

This constraint evolution system has the same principal part as the unmodified system, Eq. (5.14). Therefore the same arguments about the self-consistency of the system and the preservation of the constraints within the domain of dependence apply. Similarly the relationship between the $\mathcal{C}_a$ constraint and the standard 4-dimensional momentum constraint is not changed in any essential way: setting $\mathcal{C}_a = \partial_t\mathcal{C}_a = 0$ on a $t =$constant surface is still equivalent to setting $\mathcal{C}_a = \mathcal{M}_a = 0$ there.

Consider the properties of the constraint evolution system for states that are very close to the constraint-satisfying submanifold $\mathcal{C}_a = \partial_t \mathcal{C}_a = 0$. We can ignore the terms in Eq. (5.20) that are quadratic in $\mathcal{C}_a$ in this case, so the constraint evolution system reduces to

$$0 \quad = \quad \nabla^b \nabla_b \mathcal{C}_a - 2\gamma_0 \nabla^b [\, t_{(b} \mathcal{C}_{a)}]. \tag{5.21}$$

Gundlach et al. [16] have shown that all the "short wavelength" solutions to this constraint evolution system are damped at either the rate $e^{-\gamma_0 t}$ or $e^{-\gamma_0 t/2}$. This explains how the addition of the terms proportional to γ_0 in the modified GH system, Eq. (5.17), tend to damp out small constraint violations. This also explains (in part) why the numerical evolutions of this system by Pretorius were so successful. A complete understanding of how the long wavelength constraints are damped (or not) in generic spacetimes would also be quite interesting, but this is not yet fully understood.

5.3 New first-order generalized harmonic evolution system

In this section we present a new first-order representation of the modified GH evolution system, which will (we think) be a useful counterpart to the second-order system described in Sec. 5.2.2 above. There is an extensive mathematical literature on first-order evolution systems that clarifies numerous issues of great importance in numerical relativity, e.g., how to formulate well-posed boundary conditions [23, 27, 28], which systems form shocks [20], etc. We have also been more successful implementing first-order systems in our spectral evolution code.

The principal part of each component of the modified GH system, $\psi^{cd}\partial_c\partial_d\psi_{ab}$, is the same as the principal part of the covariant scalar-field system. So a first-order representation of the GH system can be constructed simply by adopting the methods used for scalar fields [26, 18]. Using this method and the usual 3+1 coordinates, Eq. (5.8), a first-order representation of the GH system can be written down, and indeed was written down (in essentially this form) by Alvi [1]:

$$\partial_t \psi_{ab} - N^k \partial_k \psi_{ab} \quad \simeq \quad 0, \tag{5.22}$$

$$\partial_t \Pi_{ab} - N^k \partial_k \Pi_{ab} + N g^{ki} \partial_k \Phi_{iab} \quad \simeq \quad 0, \tag{5.23}$$

$$\partial_t \Phi_{iab} - N^k \partial_k \Phi_{iab} + N \partial_i \Pi_{ab} \quad \simeq \quad 0, \tag{5.24}$$

where $\Phi_{iab} = \partial_i \psi_{ab}$ and $\Pi_{ab} = -t^c \partial_c \psi_{ab}$ are new fields introduced to represent the first derivatives of ψ_{ab}. The notation $\simeq$ indicates that only the principal parts of the equations (i.e., the parts containing derivatives of the fields) are displayed.

In the discussion that follows, it will be helpful to discuss first-order evolution systems like this using a more compact and more abstract notation. Thus, we let $u^\alpha = \{\psi_{ab}, \Pi_{ab}, \Phi_{iab}\}$ denote the

collection of dynamical fields; and the evolution system for these fields can be written as

$$\partial_t u^\alpha + A^{k\,\alpha}{}_\beta \partial_k u^\beta = F^\alpha, \tag{5.25}$$

where $A^{k\,\alpha}{}_\beta$ and F^α may depend on u^α but not its derivatives. We use Greek indices throughout this paper to label the collection of dynamical fields. The principal part of this system is written abstractly as $\partial_t u^\alpha + A^{k\,\alpha}{}_\beta \partial_k u^\beta \simeq 0$, so Eqs. (5.22)–(5.24) determine the matrix $A^{k\,\alpha}{}_\beta$ but not F^α for this system. First-order evolution systems of this form are called *symmetric hyperbolic* if there exists a symmetric positive definite matrix $S_{\alpha\beta}$ (the symmetrizer) on the space of fields that satisfies the condition $S_{\alpha\mu}A^{k\,\mu}{}_\beta \equiv A^k_{\alpha\beta} = A^k_{\beta\alpha}$. The mathematical literature on symmetric hyperbolic systems is extensive, and includes, for example, strong existence and uniqueness theorems [10, 23, 27, 28]. Alvi's representation of the GH system [1] is symmetric hyperbolic, as was a similar representation of the Einstein system (for the case of harmonic coordinates) given earlier by Fischer and Marsden [10].

Alvi's first-order representation of the GH system has two serious problems: First, the use of the field Φ_{iab} introduces a new constraint,

$$\mathcal{C}_{iab} = \partial_i \psi_{ab} - \Phi_{iab}, \tag{5.26}$$

which can (and does) tend to grow exponentially during numerical evolutions. Second, this system does not satisfy the mathematical condition (linear degeneracy) that prevents the formation of shocks from smooth initial data [20]. The principal part of the ψ_{ti} component of Eq. (5.22), for example, can be written as $\partial_t N^i - N^k \partial_k N^i \simeq 0$; and these terms have the same form as those responsible for shock formation in the standard hydrodynamic equations.

We had previously developed ways to modify systems of this type to eliminate either of these problems [18]. However, these methods produce systems that are not symmetric hyperbolic when both problems are corrected simultaneously. Here we present new modifications that solve both problems without destroying symmetric hyperbolicity. We do this by adding appropriate multiples of the constraint $\mathcal{C}_{iab}$ to each of the equations: $\gamma_1 N^i \mathcal{C}_{iab}$ to Eq. (5.22), $\gamma_3 N^i \mathcal{C}_{iab}$ to Eq. (5.23), and $\gamma_2 N \mathcal{C}_{iab}$ to Eq. (5.24). These terms modify the principal parts of the equations:

$$\partial_t \psi_{ab} - (1+\gamma_1) N^k \partial_k \psi_{ab} \simeq 0, \tag{5.27}$$

$$\partial_t \Pi_{ab} - N^k \partial_k \Pi_{ab} + N g^{ki} \partial_k \Phi_{iab} - \gamma_3 N^k \partial_k \psi_{ab} \simeq 0, \tag{5.28}$$

$$\partial_t \Phi_{iab} - N^k \partial_k \Phi_{iab} + N \partial_i \Pi_{ab} - \gamma_2 N \partial_i \psi_{ab} \simeq 0. \tag{5.29}$$

Choosing $\gamma_3 = \gamma_1 \gamma_2$ makes this new system symmetric hyperbolic for any values of the parameters γ_1 and γ_2. The symmetrizer metric (which defines the energy norm) for this new system can be

written as

$$\begin{aligned} S_{\alpha\beta}du^\alpha du^\beta &= m^{ab}m^{cd}\big(\quad \Lambda^2 d\psi_{ac}d\psi_{bd} + d\Pi_{ac}d\Pi_{bd} \\ &\qquad -2\gamma_2 d\psi_{ac}d\Pi_{bd} + g^{ij}d\Phi_{iac}d\Phi_{jbd}\big), \end{aligned} \tag{5.30}$$

where m^{ab} is any positive definite metric (e.g., $m^{ab} = g^{ab} + t^a t^b$ or even $m^{ab} = \delta^{ab}$) and Λ is a constant with dimension length^{-1}. This symmetrizer is positive definite so long as $\Lambda^2 > \gamma_2^2$.

The eigenvectors of the characteristic matrix, $n_k A^{k\,\alpha}{}_\beta$ (where n_k is the outward directed unit normal to the boundary of the computational domain), play an important role in setting boundary conditions for first-order evolution systems. Let $e^{\hat{\alpha}}{}_\beta$ denote the left eigenvectors with eigenvalues $v_{(\hat{\alpha})}$, defined by

$$e^{\hat{\alpha}}{}_\mu n_k A^{k\,\mu}{}_\beta = v_{(\hat{\alpha})} e^{\hat{\alpha}}{}_\beta. \tag{5.31}$$

We use indices with hats (e.g., $\hat{\alpha}$) to label the characteristic eigenvectors and eigenvalues, and $\hat{\alpha}$ is not summed over in Eq. (5.31). The eigenvalues $v_{(\hat{\alpha})}$ are also called the characteristic speeds. The characteristic matrices of symmetric hyperbolic systems have complete sets of eigenvectors, so the matrix $e^{\hat{\alpha}}{}_\beta$ is invertible in this case. The characteristic fields, $u^{\hat{\alpha}}$, are defined as the projections of the dynamical fields onto the characteristic eigenvectors: $u^{\hat{\alpha}} \equiv e^{\hat{\alpha}}{}_\beta u^\beta$. Boundary conditions must be imposed on each incoming characteristic field, i.e., each $u^{\hat{\alpha}}$ with negative characteristic speed, $v_{(\hat{\alpha})} < 0$ [23, 27, 28]. The characteristic fields for the new GH evolution system, Eqs. (5.27)–(5.29), are given by

$$u^{\hat{0}}_{ab} = \psi_{ab}, \tag{5.32}$$

$$u^{\hat{1}\pm}_{ab} = \Pi_{ab} \pm n^i \Phi_{iab} - \gamma_2 \psi_{ab}, \tag{5.33}$$

$$u^{\hat{2}}_{iab} = P_i{}^k \Phi_{kab}, \tag{5.34}$$

where $P_i{}^k = \delta_i{}^k - n_i n^k$. The characteristic fields $u^{\hat{0}}_{ab}$ have coordinate characteristic speed $-(1+\gamma_1)n_k N^k$, the fields $u^{\hat{1}\pm}_{ab}$ have speed $-n_k N^k \pm N$, and the fields $u^{\hat{2}}_{iab}$ have speed $-n_k N^k$.

The complete equations for our new first-order representation of the GH evolution system (including all the non-principal parts) are

$$\partial_t \psi_{ab} - (1+\gamma_1) N^k \partial_k \psi_{ab} = -N\Pi_{ab} - \gamma_1 N^i \Phi_{iab}, \tag{5.35}$$

$$\begin{aligned} \partial_t \Pi_{ab} &- N^k \partial_k \Pi_{ab} + N g^{ki} \partial_k \Phi_{iab} - \gamma_1\gamma_2 N^k \partial_k \psi_{ab} \\ &= 2N\psi^{cd}\big(g^{ij}\Phi_{ica}\Phi_{jdb} - \Pi_{ca}\Pi_{db} - \psi^{ef}\Gamma_{ace}\Gamma_{bdf}\big) \\ &\quad -2N\nabla_{(a}H_{b)} - \tfrac{1}{2}Nt^c t^d \Pi_{cd}\Pi_{ab} - Nt^c \Pi_{ci} g^{ij}\Phi_{jab} \end{aligned}$$

$$+N\gamma_0\left[2\delta^c{}_{(a}t_{b)} - \psi_{ab}t^c\right](H_c + \Gamma_c) - \gamma_1\gamma_2 N^i\Phi_{iab}, \tag{5.36}$$

$$\begin{aligned}\partial_t\Phi_{iab} &= N^k\partial_k\Phi_{iab} + N\partial_i\Pi_{ab} - N\gamma_2\partial_i\psi_{ab} \\ &= \tfrac{1}{2}Nt^ct^d\Phi_{icd}\Pi_{ab} + Ng^{jk}t^c\Phi_{ijc}\Phi_{kab} - N\gamma_2\Phi_{iab}.\end{aligned} \tag{5.37}$$

The terms on the right sides of Eqs. (5.35)–(5.37) are algebraic functions of the dynamical fields. The connection terms Γ_{cab} appearing on the right side of Eq. (5.36) are computed using Eqs. (5.3), where it is understood that the partial derivatives are to determined from the dynamical fields by

$$\partial_t\psi_{ab} = -N\Pi_{ab} + N^i\Phi_{iab}, \tag{5.38}$$

$$\partial_i\psi_{ab} = \Phi_{iab}. \tag{5.39}$$

Choosing the parameter $\gamma_2 > 0$ in this new system causes the constraint $\mathcal{C}_{iab}$ to be exponentially suppressed [18], because the modified Eq. (5.37) implies an evolution equation for $\mathcal{C}_{iab}$ having the form, $\partial_t\mathcal{C}_{iab} - N^k\partial_k\mathcal{C}_{iab} \simeq -\gamma_2 N\mathcal{C}_{iab}$. Choosing $\gamma_1 = -1$ makes the system Eqs. (5.35)–(5.37) linearly degenerate, which implies that shocks do not form from smooth initial data [20]. And choosing the parameter $\gamma_0 > 0$ causes the constraint $\mathcal{C}_a$ to be exponentially suppressed, as discussed in Sec. 5.2.2.

5.4 Boundary conditions

The modifications of the GH evolution system discussed in Secs. 5.2.2 and 5.3 are designed to damp out small constraint violations that may arise from inexact initial data, numerical errors, etc. These modifications will do nothing, however, to prevent the influx of constraint violations through the boundaries of the computational domain. Constraint-preserving boundary conditions are needed to prevent this [29, 5, 6, 19, 25]. Such boundary conditions can be formulated once the propagation equations for the constraints are understood. So we derive a first-order system of evolution equations for the constraints in Sec. 5.4.1, use them to derive constraint-preserving boundary conditions in Sec. 5.4.2, present boundary conditions for the physical gravitational-wave degrees of freedom of the system in Sec. 5.4.3, and finally analyze the well-posedness of the combined set of new boundary conditions in Sec. 5.4.4.

5.4.1 First-order constraint evolution system

The primary constraint of the GH system is the gauge constraint, $\mathcal{C}_a$, which we re-write here in terms of the first-order dynamical fields:

$$\mathcal{C}_a = H_a + g^{ij}\Phi_{ija} + t^b\Pi_{ba} - \tfrac{1}{2}g^i_a\psi^{bc}\Phi_{ibc} - \tfrac{1}{2}t_a\psi^{bc}\Pi_{bc}. \tag{5.40}$$

This expression differs from Eq. (5.12) only by multiples of the constraint $\mathcal{C}_{iab}$. In the following we use this definition, Eq. (5.40), rather than Eq. (5.12), because it simplifies the form of the constraint evolution system. The evolution equation for $\mathcal{C}_a$, Eq. (5.14), is second order. Thus, we must define new constraint fields that represent the first derivatives of $\mathcal{C}_a$ in order to reduce the constraint evolution system to first-order form. Thus we define new constraint fields $\mathcal{F}_a$ and $\mathcal{C}_{ia}$ that satisfy

$$\mathcal{F}_a \approx t^c \partial_c \mathcal{C}_a = N^{-1}(\partial_t \mathcal{C}_a - N^i \partial_i \mathcal{C}_a), \tag{5.41}$$

$$\mathcal{C}_{ia} \approx \partial_i \mathcal{C}_a, \tag{5.42}$$

up to terms proportional to the constraints $\mathcal{C}_a$ and $\mathcal{C}_{iab}$. The following definitions of $\mathcal{F}_a$ and $\mathcal{C}_{ia}$ accomplish this in a way that keeps the form of the constraint evolution system as simple as possible:

$$\begin{aligned}
\mathcal{F}_a \equiv\ & \tfrac{1}{2} g_a^i \psi^{bc} \partial_i \Pi_{bc} - g^{ij} \partial_i \Pi_{ja} - g^{ij} t^b \partial_i \Phi_{jba} + \tfrac{1}{2} t_a \psi^{bc} g^{ij} \partial_i \Phi_{jbc} \\
& + t_a g^{ij} \partial_i H_j + g_a^i \Phi_{ijb} g^{jk} \Phi_{kcd} \psi^{bd} t^c - \tfrac{1}{2} g_a^i \Phi_{ijb} g^{jk} \Phi_{kcd} \psi^{cd} t^b \\
& - g_a^i t^b \partial_i H_b + g^{ij} \Phi_{icd} \Phi_{jba} \psi^{bc} t^d - \tfrac{1}{2} t_a g^{ij} g^{mn} \Phi_{imc} \Phi_{njd} \psi^{cd} \\
& - \tfrac{1}{4} t_a g^{ij} \Phi_{icd} \Phi_{jbe} \psi^{cb} \psi^{de} + \tfrac{1}{4} t_a \Pi_{cd} \Pi_{be} \psi^{cb} \psi^{de} - g^{ij} H_i \Pi_{ja} \\
& - t^b g^{ij} \Pi_{bi} \Pi_{ja} - \tfrac{1}{4} g_a^i \Phi_{icd} t^c t^d \Pi_{be} \psi^{be} + \tfrac{1}{2} t_a \Pi_{cd} \Pi_{be} \psi^{ce} t^d t^b \\
& + g_a^i \Phi_{icd} \Pi_{be} t^c t^b \psi^{de} - g^{ij} \Phi_{iba} t^b \Pi_{je} t^e - \tfrac{1}{2} g^{ij} \Phi_{icd} t^c t^d \Pi_{ja} \\
& - g^{ij} H_i \Phi_{jba} t^b + g_a^i \Phi_{icd} H_b \psi^{bc} t^d + \gamma_2 \left(g^{id} \mathcal{C}_{ida} - \tfrac{1}{2} g_a^i \psi^{cd} \mathcal{C}_{icd} \right) \\
& + \tfrac{1}{2} t_a \Pi_{cd} \psi^{cd} H_b t^b - t_a g^{ij} \Phi_{ijc} H_d \psi^{cd} + \tfrac{1}{2} t_a g^{ij} H_i \Phi_{jcd} \psi^{cd},
\end{aligned} \tag{5.43}$$

$$\begin{aligned}
\mathcal{C}_{ia} \equiv\ & g^{jk} \partial_j \Phi_{ika} - \tfrac{1}{2} g_a^j \psi^{cd} \partial_j \Phi_{icd} + t^b \partial_i \Pi_{ba} - \tfrac{1}{2} t_a \psi^{cd} \partial_i \Pi_{cd} \\
& + \partial_i H_a + \tfrac{1}{2} g_a^j \Phi_{jcd} \Phi_{ief} \psi^{ce} \psi^{df} + \tfrac{1}{2} g^{jk} \Phi_{jcd} \Phi_{ike} \psi^{cd} t^e t_a \\
& - g^{jk} g^{mn} \Phi_{jma} \Phi_{ikn} + \tfrac{1}{2} \Phi_{icd} \Pi_{be} t_a \left(\psi^{cb} \psi^{de} + \tfrac{1}{2} \psi^{be} t^c t^d \right) \\
& - \Phi_{icd} \Pi_{ba} t^c \left(\psi^{bd} + \tfrac{1}{2} t^b t^d \right) + \tfrac{1}{2} \gamma_2 \left(t_a \psi^{cd} - 2 \delta_a^c t^d \right) \mathcal{C}_{icd}.
\end{aligned} \tag{5.44}$$

The remaining constraints needed to complete the GH constraint evolution system are $\mathcal{C}_{iab}$ defined in Eq. (5.26), and the closely related $\mathcal{C}_{ijab}$, defined by

$$\mathcal{C}_{ijab} = 2 \partial_{[i} \Phi_{j]ab} = 2 \partial_{[j} \mathcal{C}_{i]ab}. \tag{5.45}$$

The complete collection of constraints for the GH evolution system is therefore the set $c^A \equiv \{\mathcal{C}_a, \mathcal{F}_a, \mathcal{C}_{ia}, \mathcal{C}_{iab}, \mathcal{C}_{ijab}\}$ defined in Eqs. (5.40), (5.43), (5.44), (5.26), and (5.45). (We use upper case Latin indices to label the constraints.) The constraints c^A depend on the dynamical fields $u^\alpha =$

$\{\psi_{ab}, \Pi_{ab}, \Phi_{iab}\}$ and their spatial derivatives $\partial_k u^\alpha$. Thus the evolution of the constraint fields c^A is completely determined by the evolution of the dynamical fields through Eqs. (5.35)–(5.37). We have evaluated these constraint evolution equations and have verified that they can be written in the abstract form

$$\partial_t c^A + A^{kA}{}_B(u)\partial_k c^B = F^A{}_B(u, \partial u)\, c^B, \tag{5.46}$$

where $A^{kA}{}_B$ and $F^A{}_B$ may depend on the dynamical fields u^α and their spatial derivatives $\partial_k u^\alpha$. Thus the constraint evolution system closes: the time derivatives of the constraints vanish initially when the constraints themselves vanish at an initial time. The principal part of the first-order constraint evolution system turns out to be remarkably simple (given the complexity of the expressions for the constraints themselves):

$$\begin{aligned}
\partial_t \mathcal{C}_a &\simeq 0, && (5.47)\\
\partial_t \mathcal{F}_a &\simeq N^i \partial_i \mathcal{F}_a + N g^{ij} \partial_i \mathcal{C}_{ja}, && (5.48)\\
\partial_t \mathcal{C}_{ia} &\simeq N^j \partial_j \mathcal{C}_{ia} + N \partial_i \mathcal{F}_a, && (5.49)\\
\partial_t \mathcal{C}_{iab} &\simeq (1+\gamma_1) N^k \partial_k \mathcal{C}_{iab}, && (5.50)\\
\partial_t \mathcal{C}_{ijab} &\simeq N^k \partial_k \mathcal{C}_{ijab}. && (5.51)
\end{aligned}$$

This constraint evolution system is symmetric hyperbolic with symmetrizer

$$\begin{aligned}
S_{AB} dc^A dc^B &= m^{ab}\Big[d\mathcal{F}_a d\mathcal{F}_b + g^{ij}\big(d\mathcal{C}_{ia} d\mathcal{C}_{jb} + g^{kl} m^{cd} d\mathcal{C}_{ikac} d\mathcal{C}_{jlbd}\big) \\
&\qquad + \Lambda^2 \big(d\mathcal{C}_a d\mathcal{C}_b + g^{ij} m^{cd} d\mathcal{C}_{iac} d\mathcal{C}_{jbd}\big)\Big], \qquad (5.52)
\end{aligned}$$

where Λ^2 is a positive constant and m^{ab} is an arbitrary positive definite metric. The constraint energy for this system is defined as

$$\mathcal{E}_c = \int S_{AB} c^A c^B \sqrt{g} d^3x. \tag{5.53}$$

Since the constraint evolution system is hyperbolic, it follows (at the continuum level) that the constraints will remain satisfied within the domain of dependence of the initial data, if they are satisfied initially.

We have analyzed the solutions to this constraint evolution system for the case of small constraint violations of solutions near flat space. We find that all of the short-wavelength constraint violations are damped at the rate $e^{-\gamma_0 t}$, $e^{-\gamma_0 t/2}$, or $e^{-\gamma_2 t}$. So choosing $\gamma_0 > 0$ and $\gamma_2 > 0$ is sufficient to guarantee that all of these constraints are suppressed. This new first-order GH system therefore

has the same constraint suppression properties as the second-order system of Gundlach et al. [16] and Pretorius [21].

The constraint evolution system, Eq. (5.46), is symmetric hyperbolic and it will be useful to determine the characteristic constraint fields. Thus, we evaluate the matrix of left eigenvectors of the constraint evolution system ${e^{\hat{A}}}_B$ and their corresponding eigenvalues $v_{(\hat{A})}$ (or characteristic speeds). The characteristic constraint fields are defined (in analogy with the principal evolution system) as the projections of the constraint fields onto these eigenvectors: $c^{\hat{A}} \equiv {e^{\hat{A}}}_B c^B$. The resulting characteristic fields for this constraint evolution system are

$$c_a^{\hat{0}\pm} = \mathcal{F}_a \mp n^k \mathcal{C}_{ka}, \tag{5.54}$$

$$c_a^{\hat{1}} = \mathcal{C}_a, \tag{5.55}$$

$$c_{ia}^{\hat{2}} = {P^k}_i \mathcal{C}_{ka}, \tag{5.56}$$

$$c_{iab}^{\hat{3}} = \mathcal{C}_{iab}, \tag{5.57}$$

$$c_{ijab}^{\hat{4}} = \mathcal{C}_{ijab}. \tag{5.58}$$

The characteristic constraint fields $c_a^{\hat{0}\pm}$ have coordinate characteristic speeds $-n_l N^l \pm N$, the fields $c_a^{\hat{1}}$ have speed 0, the fields $c_{ia}^{\hat{2}}$ and $c_{ijab}^{\hat{4}}$ have speed $-n_l N^l$, and the fields $c_{iab}^{\hat{3}}$ have speed $-(1+\gamma_1) n_l N^l$.

5.4.2 Constraint-preserving boundary conditions

Boundary conditions must be imposed on all the incoming characteristic fields $u^{\hat{\alpha}}$, i.e., all those with $v_{(\hat{\alpha})} < 0$ on a particular boundary. Thus, boundary conditions will typically be needed for the characteristic field $u_{ab}^{\hat{1}-}$, and (depending on the value of the parameter γ_1 and the orientation of the shift N^k at the boundary) may also be needed for $u_{ab}^{\hat{0}}$ and/or $u_{iab}^{\hat{2}}$. Some of these boundary conditions must be set by physical considerations, i.e., by specifying what physical gravitational waves enter the computational domain. Some of the boundary conditions can be used, however, to prevent the influx of constraint violations. This can be done by specifying the incoming $u^{\hat{\alpha}}$ at the boundary in a way that ensures the incoming characteristic constraint fields $c^{\hat{A}}$ also vanish there. The incoming constraint fields for this system include $c_a^{\hat{0}-}$, and perhaps $c_{iab}^{\hat{3}}$ and/or $c_{ikab}^{\hat{4}}$ depending on γ_1 and N^k at the boundary. We find that these incoming $c^{\hat{A}}$ are related to the incoming $u^{\hat{\alpha}}$ by the following expressions:

$$c_a^{\hat{0}-} \approx \sqrt{2}\left[k^{(c}{\psi^{d)}}_a - \tfrac{1}{2} k_a \psi^{cd}\right] d_\perp u_{cd}^{\hat{1}-}, \tag{5.59}$$

$$n^i c_{iab}^{\hat{3}} \approx d_\perp u_{ab}^{\hat{0}}, \tag{5.60}$$

$$n^i c_{ikab}^{\hat{4}} \approx d_\perp u_{kab}^{\hat{2}}. \tag{5.61}$$

Here the notation $d_\perp u^{\hat{\alpha}}$ denotes the characteristic projection of the normal derivatives of $u^{\hat{\alpha}}$ (i.e., $d_\perp u^{\hat{\alpha}} \equiv e^{\hat{\alpha}}{}_\beta n^k \partial_k u^\beta$), and $\approx$ implies that algebraic terms and terms involving tangential derivatives of the fields (i.e., $P^k{}_i \partial_k u^\alpha$) have not been displayed. The inward directed null vector k^c used here is defined as $k^c = (t^c - n^c)/\sqrt{2}$. The idea is to set the left sides of Eqs. (5.59)–(5.61) to zero to get Neumann-like boundary conditions for the indicated components of $d_\perp u^{\hat{\alpha}}$. By imposing these conditions on $d_\perp u^{\hat{\alpha}}$, we ensure that these incoming components of $c^{\hat{A}}$ vanish.

We have found that a convenient way to impose boundary conditions of this type is to set the incoming projections of the time derivatives of u^α, $d_t u^{\hat{\alpha}} \equiv e^{\hat{\alpha}}{}_\beta \partial_t u^\beta$, in the following way:

$$d_t u^{\hat{\alpha}} = D_t u^{\hat{\alpha}} + v_{(\hat{\alpha})} \big(d_\perp u^{\hat{\alpha}} - d_\perp u^{\hat{\alpha}} \big|_{BC} \big). \tag{5.62}$$

In this expression the terms $D_t u^{\hat{\alpha}}$ represent the projections of the right sides of the evolution system, Eqs. (5.35)–(5.37); so the equations at non-boundary points would simply be $d_t u^{\hat{\alpha}} = D_t u^{\hat{\alpha}}$. The term $d_\perp u^{\hat{\alpha}} \big|_{BC}$ is the value to which $d_\perp u^{\hat{\alpha}}$ is to be fixed on the boundary. This form of the boundary condition replaces all of the $d_\perp u^{\hat{\alpha}}$ that appears in $D_t u^{\hat{\alpha}}$ with $d_\perp u^{\hat{\alpha}} \big|_{BC}$. Applying this method to the constraint-preserving boundary conditions in Eqs. (5.59)–(5.61), we obtain the following rather simple conditions

$$\begin{aligned}
d_t u^{\hat{0}}_{ab} &= D_t u^{\hat{0}}_{ab} - (1+\gamma_1) n_j N^j n^k c^{\hat{3}}_{kab}, && (5.63)\\
d_t u^{\hat{1}-}_{ab} &= \big[\tfrac{1}{2} P_{ab} P^{cd} - 2 l_{(a} P_{b)}{}^{(c} k^{d)} + l_a l_b k^c k^d \big] D_t u^{\hat{1}-}_{cd} \\
&\quad + \sqrt{2} (N + n_j N^j) \big[l_{(a} P_{b)}{}^c - \tfrac{1}{2} P_{ab} l^c - \tfrac{1}{2} l_a l_b k^c \big] c^{\hat{0}-}_c, && (5.64)\\
d_t u^{\hat{2}}_{kab} &= D_t u^{\hat{2}}_{kab} - n_l N^l n^i P^j{}_k c^{\hat{4}}_{ijab}. && (5.65)
\end{aligned}$$

The quantity P_{ab} in these expressions is the projection tensor, $P_{ab} = \psi_{ab} + t_a t_b - n_a n_b$, and the outgoing null vector l^a is defined by $l^a = (t^a + n^a)/\sqrt{2}$.

5.4.3 Physical boundary conditions

The constraint-preserving boundary conditions presented in Eqs. (5.63)–(5.65) restrict only four degrees of freedom of $u^{\hat{1}-}_{ab}$. Two of the remaining degrees of freedom represent the physical gravitational waves, and the final four represent gauge freedom. We choose to characterize and control this gravitational wave freedom in terms of the incoming parts of the Weyl curvature. The propagating components of the Weyl tensor can be written as

$$w^{\pm}_{ab} = \big(P_a{}^c P_b{}^d - \tfrac{1}{2} P_{ab} P^{cd} \big) \big(t^e \mp n^e \big) \big(t^f \mp n^f \big) C_{cedf}. \tag{5.66}$$

We showed in [19] that these components of the Weyl tensor are the incoming and outgoing (respectively) characteristic fields of the curvature evolution system that follows from the Bianchi identities. The $w^{\pm}_{ab}$ are proportional to the Newman-Penrose curvature spinor components Ψ_4 (outgoing) and Ψ_0 (ingoing), respectively. We also note that the spatial components of $w^{\pm}_{ij}$ are equal to the components of the Weyl tensor characteristic fields $2U^{8\pm}_{ij}$ defined in our paper on constraint-preserving boundary conditions for the KST system [19]. The expression for the Weyl tensor in terms of our first-order variables is unique only up to terms proportional to constraints; it is possible to choose these constraint terms so that the $w^{\pm}_{ij}$ depend on the normal derivatives of $u^{\hat{\alpha}}$ in the following way:

$$w^{\pm}_{ab} \approx \left(P_a{}^c P_b{}^d - \tfrac{1}{2} P_{ab} P^{cd}\right)\left(d_\perp u^{\hat{1}\pm}_{cd} + \gamma_2 d_\perp u^{\hat{0}}_{cd}\right). \tag{5.67}$$

Thus a physical boundary condition can be placed on the relevant components of $u^{\hat{1}-}_{ab}$ using the method of Eq. (5.62) by setting

$$\begin{aligned} d_t u^{\hat{1}-}_{ab} &= \left(P_a{}^c P_b{}^d - \tfrac{1}{2} P_{ab} P^{cd}\right) \times \\ &\qquad \left[D_t u^{\hat{1}-}_{cd} - (N + n_j N^j)(w^-_{cd} - \gamma_2 n^i c^{\hat{3}}_{icd})\right]. \end{aligned} \tag{5.68}$$

We can also inject incoming physical gravitational waves with a predetermined waveform $\dot{h}_{ab}(t,x)$ through the boundary of the computational domain by setting

$$d_t u^{\hat{1}-}_{ab} = \left(P_a{}^c P_b{}^d - \tfrac{1}{2} P_{ab} P^{cd}\right)\dot{h}_{cd}(t,x). \tag{5.69}$$

The case $\dot{h}_{ab} = 0$ corresponds to an isolated system with no incoming gravitational waves.

More generally we can combine the constraint-preserving, physical no-incoming radiation, and the injected gravitational wave boundary conditions by setting $d_t u^{\hat{1}-}_{ab}$ equal to the sum of the right sides of Eqs. (5.64), (5.68), and (5.69), and setting the time derivatives of the other incoming fields according to Eqs. (5.63) and (5.65). Note that this set of combined boundary conditions holds the *pure gauge* components of $u^{\hat{1}-}_{ab}$ constant in time; other boundary conditions on the gauge degrees of freedom are of course possible but are not considered here.

5.4.4 Well-posedness

The well-posedness of the initial-boundary value problem can be analyzed using the Fourier-Laplace technique [17]. We have applied this method to the GH system with the combined set of boundary conditions presented here: we treat the case of high-frequency perturbations of flat spacetime in a slicing with flat spatial metric, unit lapse, and a constant shift that is tangent to the

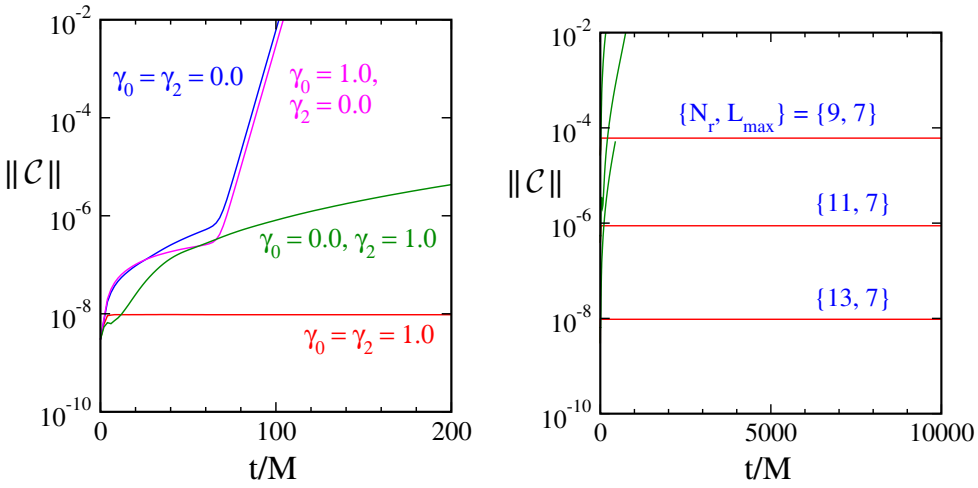

Figure 5.1: Evolution of constraint violations for Schwarzschild initial data. Left figure shows evolutions using various values of the constraint damping parameters γ_0 and γ_2 using numerical resolution $\{N_r, L_{max}\} = \{13, 7\}$. Right figure shows the long timescale evolution of the same data for three different numerical resolutions.

boundary. Applying the Fourier-Laplace technique to this case yields a necessary (but not sufficient) condition for well-posedness, the so-called determinant condition [17]; failure to satisfy this condition would mean the system admits exponentially growing solutions with arbitrarily large growth rates. We have verified that this determinant condition is satisfied for the GH system using the combined set of boundary conditions presented here.

5.5 Numerical results

In this section we describe several numerical tests of the new first-order GH evolution system. First we test the effectiveness of the two constraint damping terms included in Eqs. (5.35)–(5.37) by evolving Schwarzschild initial data (in Kerr-Schild coordinates). These tests are performed on a computational domain consisting of a spherical shell that extends from $r_{\rm min} = 1.8\,M$ (just inside the event horizon) to $r_{max} = 11.8\,M$, where M is the mass of the black hole. In these evolutions we "freeze" the values of the incoming characteristic fields to their initial values by setting $d_t u^{\hat{\alpha}} = 0$ on the boundaries for all incoming fields (i.e., all $u^{\hat{\alpha}}$ with $v_{(\hat{\alpha})} < 0$). We performed these numerical evolutions using spectral methods as described for example in [19] for a range of numerical resolutions specified by the parameters N_r (the highest radial spectral basis function) and L_{max} (the highest spherical-harmonic basis function). Fig. 5.1 illustrates the results of these tests for several values of the constraint damping parameters γ_0 and γ_2. These tests show that without constraint damping the extended GH evolution system is extremely unstable, but with constraint damping the evolutions of the Schwarzschild spacetime are completely stable up to $t = 10,000\,M$ (and for-

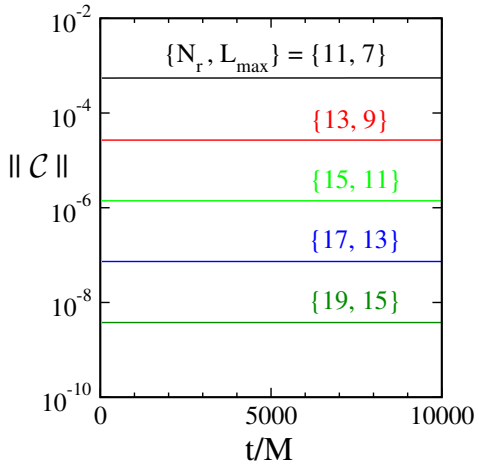

Figure 5.2: Evolution of constraint violations for Kerr initial data with spin parameter $\vec{a} = (0.1, 0.2, 0.3)$ for several numerical resolutions.

ever, we presume). These tests also illustrate that both the γ_0 and the γ_2 constraint damping terms are essential for stable evolutions.

Constraint violations in Fig. 5.1 (and in the rest of this paper) are measured with the constraint energy $\mathcal{E}_c$ defined in Eq. (5.53). Since $\mathcal{E}_c$ is not dimensionless, its magnitude has no absolute meaning. We construct an appropriate scale with which to compare $\mathcal{E}_c$ by evaluating the L^2 norm of the spatial gradients of the dynamical fields,

$$||\partial u||^2 = \int g^{ij} m^{ab} m^{cd} \Big(\Lambda^2 \partial_i \psi_{ac} \partial_j \psi_{bd} + \partial_i \Pi_{ac} \partial_j \Pi_{bd} + g^{kl} \partial_i \Phi_{kac} \partial_j \Phi_{lbd} \Big) \sqrt{g} d^3x. \tag{5.70}$$

The dimensionless constraint norm $||\mathcal{C}||$ shown in these figures is defined as

$$||\mathcal{C}|| = \frac{\sqrt{\mathcal{E}_c}}{||\partial u||}, \tag{5.71}$$

which is a meaningful measure of the relative size of constraint violations in a particular solution. In the figures shown here we evaluate $||\mathcal{C}||$ with $m^{ab} = \delta^{ab}$ and the dimensional constant $\Lambda = 1/M$.

Our second numerical test evolves the somewhat more challenging initial data for a Kerr black hole (in Kerr-Schild coordinates) on a computational domain consisting of a spherical shell that extends from $r_{min} = 1.8\,M$ (just inside the event horizon) to $r_{max} = 21.8\,M$. We use two subdomains, each having numerical resolution $\{N_r, L_{max}\}$, to cover this region. The spin of the Kerr spacetime used here is $\vec{a} = (0.1, 0.2, 0.3)M$, where the magnitude of this vector determines the Kerr spin parameter $a = |\vec{a}| \approx 0.374\,M$, and the direction determines the orientation of the Kerr rotation axis relative to the quasi-Cartesian coordinate system used in our code. For this test we

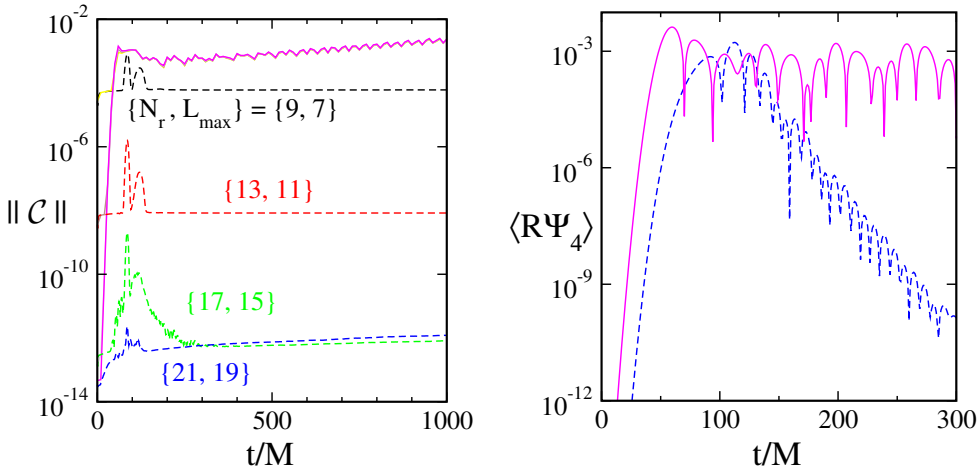

Figure 5.3: Evolution of Schwarzschild initial data perturbed by a gravitational wave pulse with amplitude 10^{-3}. Left figure depicts constraint violations at various numerical resolutions, and the right figure shows Ψ_4 averaged over the outer boundary of the computational domain at a single numerical resolution. Solid curves use freezing boundary conditions and dashed curves use constraint-preserving and physical boundary conditions.

use the combined set of physical and constraint-preserving boundary conditions discussed at the end of Sec. 5.4.3. Figure 5.2 shows that numerical evolutions of this Kerr spacetime are stable and numerically convergent to $t = 10,000M$ (and forever, we presume) using a range of numerical resolutions.

Our third numerical test is designed to demonstrate the effectiveness of our new constraint-preserving boundary conditions. This test consists of evolving a black-hole spacetime perturbed by an incoming gravitational wave pulse. We start with Schwarzschild initial data, and perturb it via the incoming gravitational wave boundary condition described in Eq. (5.69) with $\dot{h}_{ab} = \dot{f}(t)(\hat{x}^a\hat{x}^b + \hat{y}^a\hat{y}^b - 2\hat{z}^a\hat{z}^b)$ where $\hat{x}^a$, $\hat{y}^a$, and $\hat{z}^a$ are the components of the coordinate basis vectors, $\hat{x}^a\partial_a = \partial_x$, etc. For these evolutions we use an incoming gravitational wave pulse whose time profile is $f(t) = \mathcal{A}\, e^{-(t-t_p)^2/w^2}$ with $\mathcal{A} = 10^{-3}$, $t_p = 60\,M$, and $w = 10\,M$. This test is performed on the same computational domain described above for the second numerical test. Figure 5.3 illustrates the results of these tests using two types of boundary conditions: frozen-incoming-field (i.e., $d_t u^{\hat{\alpha}} = 0$ for $v_{(\hat{\alpha})} < 0$) boundary conditions (solid curves) and the new combined set of constraint-preserving and physical boundary conditions discussed at the end of Sec. 5.4.3 (dashed curves). The graph on the left in Fig. 5.3 shows that constraint violations converge toward zero as the numerical resolution is increased when the new boundary conditions are used, but not when frozen-incoming-field boundary conditions are used.

The graph on the right in Fig. 5.3 shows the outgoing physical gravitational wave flux (measured on the outer boundary of the computational domain) computed using frozen-incoming-fields

(sold curve) and the new constraint-preserving and physical (dashed curve) boundary conditions. These evolutions were computed with numerical resolution $\{N_r, L_{\max}\} = \{21, 19\}$. We measure the outgoing gravitational wave flux with the quantity $\langle R\Psi_4 \rangle$, which is the Weyl curvature component Ψ_4 averaged over the outer boundary of our computational domain:

$$4\pi \langle R\Psi_4 \rangle^2 \quad = \quad \int |\Psi_4|^2 d^2V. \tag{5.72}$$

Here $4\pi R^2$ is the proper surface area of the boundary, and d^2V represents the proper area element on this boundary. Since Ψ_4 falls off like $1/R$, this quantity should be independent of R (asymptotically). The dashed curve on the right in Fig. 5.3 clearly shows quasi-normal oscillations with frequency $\omega M = 0.376 - 0.089\,i$ (determined by a numerical fit to these data). This is in good agreement with the frequency of the most slowly damped quasi-normal mode of the black hole: $\omega M = 0.37367 - 0.08896\,i$ [7]. It is interesting to note that the solid curve—using frozen-incoming-fields boundary conditions—gives qualitatively incorrect results for the physical gravitational waveform, even though the level of constraint violations is fairly small numerically in this case. This is not surprising because the magnitude of constraint violations in this case is comparable to the size of the injected gravitational wave pulse.

5.6 Acknowledgements

We thank Steven Detweiler, Yvonne Choquet-Bruhat, Harald Pfeiffer, Frans Pretorius, Olivier Sarbach, Tilman Sauer, Saul Teukolsky, and James York for helpful discussions concerning this work. L.L. thanks the Isaac Newton Institute for Mathematical Sciences for their hospitality during a visit in which a portion of this work was completed. This work was supported in part by a grant from the Sherman Fairchild Foundation to Caltech and Cornell, by NSF grants PHY-0099568, PHY-0244906 and NASA grants NAG5-10707, NAG5-12834 at Caltech, and by NSF grants PHY-0312072, PHY-0354631, and NASA grant NNG05GG51G at Cornell. Some of the computations for this project were performed with the Tungsten cluster at the National Center for Supercomputing Applications.

Bibliography

[1] Kashif Alvi. First-order symmetrizable hyperbolic formulations of Einstein's equations including lapse and shift as dynamical fields. *Class. Quantum Grav.*, 19:5153–5162, 2002.

[2] Maria C. Babiuc, Béla Szilágyi, and Jeffrey Winicour. Testing numerical evolution with the shifted gauge wave. *Class. Quantum Grav.*, 2006. (submitted).

[3] C. Bona, T. Ledvinka, C. Palenzuela, and M. Žáček. General-covariant evolution formalism for numerical relativity. *Phys. Rev. D*, 67:104005, 2003.

[4] Y. Bruhat. Cauchy problem. In *Gravitation: An Introduction to Current Research*, L. Witten, Ed., John Wiley, New York, 1967, pages 130–168.

[5] Gioel Calabrese, Luis Lehner, and Manuel Tiglio. Constraint-preserving boundary conditions in numerical relativity. *Phys. Rev. D*, 65:104031, 2002.

[6] Gioel Calabrese, Jorge Pullin, Olivier Sarbach, Manuel Tiglio, and Oscar Reula. Well posed constraint-preserving boundary conditions for the linearized Einstein equations. *Commun. Math. Phys.*, 240:377–395, 2003.

[7] S. Chandrasekhar and S. Detweiler. The quasi-normal modes of the Schwarzschild black hole. *Proc. R. Soc. London A*, 344:441–452, 1975.

[8] T. DeDonder. *La Gravifique Einsteinienne*. Gunthier-Villars, Paris, 1921.

[9] T. DeDonder. *The Mathematical Theory of Relativity*. Massachusetts Institute of Technology, Cambridge, MA, 1927.

[10] A. E. Fischer and J. E. Marsden. The Einstein evolution equations as a first-order quasi-linear symmetric hyperbolic system. *Commun. Math. Phys.*, 28:1–38, 1972.

[11] V. Fock. *The Theory of Space Time and Gravitation*. Pergamon Press, New York, 1959.

[12] Y. Fourès-Bruhat. Théorème d'existence pour certains systèmes d'équations aux dérivées partielles non linéaires. *Acta Math.*, 88:141–225, 1952.

[13] Helmut Friedrich. On the hyperbolicity of Einstein's and other gauge field equations. *Commun. Math. Phys.*, 100:525–543, 1985.

[14] Helmut Friedrich. On the nonlinearity of the subsidiary systems. *Class. Quantum Grav.*, 22:L77, 2005.

[15] David Garfinkle. Harmonic coordinate method for simulating generic singularities. *Phys. Rev. D*, 65:044029, 2002.

[16] Carsten Gundlach, Gioel Calabrese, Ian Hinder, and Jose M. Martin-Garcia. Constraint damping in the Z4 formulation and harmonic gauge. *Class. Quantum Grav.*, 22:3767–3774, 2005.

[17] Bertil Gustafsson, Heinz-Otto Kreiss, and Joseph Oliger. *Time Dependent Problems and Difference Methods. Pure and Applied Mathematics*. Wiley, New York, 1995.

[18] Michael Holst, Lee Lindblom, Robert Owen, Harald P. Pfeiffer, Mark A. Scheel, and Lawrence E. Kidder. Optimal constraint projection for hyperbolic evolution systems. *Phys. Rev. D*, 70:084017, 2004.

[19] Lawrence E. Kidder, Lee Lindblom, Mark A. Scheel, Luisa T. Buchman, and Harald P. Pfeiffer. Boundary conditions for the Einstein evolution system. *Phys. Rev. D*, 71:064020, 2005.

[20] T. P. Liu. Development of singularities in the nonlinear waves for quasilinear hyperbolic partial differential equations. *J. Diff. Equations*, 33(1):92–111, 1979.

[21] Frans Pretorius. Evolution of binary black hole spacetimes. *Phys. Rev. Lett.*, 95:121101, 2005.

[22] Frans Pretorius. Numerical relativity using a generalized harmonic decomposition. *Class. Quantum Grav.*, 22:425–452, 2005.

[23] J. Rauch. Symmetric positive systems with boundary characteristics of constant multiplicity. *Trans. Am. Math. Soc.*, 291:167–187, 1985.

[24] Jürgen Renn and Tilman Sauer. Heuristics and mathematical representation in Einstein's search for a gravitational field equation. In *History of General Relativity, volume 7* of *Einstein Studies*, Hubert Goenner, Jürgen Renn, and Jim Ritter, Eds., Birkhäuser, Cambridge, MA, 1998, pages 87–125.

[25] Olivier Sarbach and Manuel Tiglio. Boundary conditions for einstein's field equations: Analytical and numerical analysis. *J. Hyperbolic Diff. Eq.*, 2:839–883, 2005.

[26] Mark A. Scheel, Adrienne L. Erickcek, Lior M. Burko, Lawrence E. Kidder, Harald P. Pfeiffer, and Saul A. Teukolsky. 3d simulations of linearized scalar fields in Kerr spacetime. *Phys. Rev. D*, 69(10):104006, May 2004.

[27] P. Secchi. The initial boundary value problem for linear symmetric hyperbolic systems with characteristic boundary of constant multiplicity. *Diff. Int. Eq.*, 9:671–700, 1996.

[28] P. Secchi. Well-posedness of characteristic symmetric hyperbolic systems. *Arch. Rat. Mech. Anal.*, 134:155–197, 1996.

[29] John M. Stewart. The cauchy problem and the initial boundary value problem in numerical relativity. *Class. Quantum Grav.*, 15:2865–2889, 1998.

[30] Béla Szilágyi, Bernd Schmidt, and Jeffrey Winicour. Boundary conditions in linearized harmonic gravity. *Phys. Rev. D*, 65:064015, 2002.

[31] Béla Szilágyi and Jeffrey Winicour. Well-posed initial-boundary evolution in general relativity. *Phys. Rev. D*, 68:041501(R), 2003.

Chapter 6

Constraint damping in the KST evolution systems

Submitted to Phys. Rev. D.

A new constraint-suppressing formulation of the Einstein evolution equations is presented, generalizing the five-parameter first-order system due to Kidder, Scheel, and Teukolsky (KST). The auxiliary fields, introduced to make the KST system first-order, are given modified evolution equations designed to drive constraint violations toward zero. The algebraic structure of the new system is investigated, showing that the modifications preserve the hyperbolicity of the fundamental and constraint evolution equations. The evolution of the constraints for pertubations of flat spacetime is completely analyzed, and all finite-wavelength constraint modes are shown to decay exponentially when certain adjustable parameters satisfy appropriate inequalities. Numerical simulations of a single Schwarzschild black hole are presented, demonstrating the effectiveness of the new constraint-damping modifications.

6.1 Introduction

Numerical relativity has recently undergone a revolution. Multiple research groups, using a variety of mathematical and computational formalisms, have produced consistent pictures of the late inspiral and coalescence of binary black hole systems [28, 13, 14, 15, 7, 8, 32, 11], a goal that until recently seemed remote. The community is opening a theoretical window on issues fundamental to gravitational wave astrophysics, but much work still remains to be done.

State of the art simulations have provided gravitational waveforms due to the last several orbits, coalescence and ringdown. This is an extraordinary achievement, but numerical relativity may need to handle well over a dozen orbits accurately before a seamless transition can be made from post-Newtonian analysis. When simulating so many orbits, the efficiency of the code becomes

nearly as important as its stability.

Numerical simulations can become unstable for a variety of reasons, some purely numerical (such as a poor choice of algorithm), some purely mathematical (such as ill-posedness of the continuum mathematical problem), and some a combination of the two. The subject of this paper is an instability of this last type: the exponential growth of the constraint fields under free evolution — an instability of the continuum evolution equations, seeded by numerical errors.

A variety of methods exist to deal with such instabilities. One very well-established method is known as constrained evolution [34, 2, 17, 3, 1, 18, 19, 30], in which some subset of the dynamical fields are integrated in time using the evolution equations, and others are obtained by solving the constraints after each time step. This separation of the fields into an "evolved" family and a "constrained" family is normally guided by some sort of symmetry. A related method, known as constraint projection [5, 22], places all fields on an equal footing, freely integrating everything using the evolution equations, then periodically "projecting" the fields down to the constraint-satisfying subset of the solution space. It appears that this method can be quite robust in practice, but it can also be technically demanding, requiring the repeated solution of nonlinear elliptic equations.

A preferable approach for dealing with these instabilities, whenever possible, is to remove them from the evolution system at the continuum level, before they reach the numerical code. This type of effort is often referred to as "constraint damping." It is possible to change the evolution equations without changing the physics they represent. For instance, coordinates can be chosen freely on the simulated spacetime, and indeed, careful choices of gauge have been shown to have a strong effect on the stability of simulations, particularly in the BSSN system [4, 37, 21, 36]. Another, perhaps more drastic, method to stabilize constraints involves extending the family of evolved fields. It is possible, with some care, to introduce fields whose evolution will naturally lead to the presence of friction terms in the implied constraint evolution system. Systems of this form have come to be referred to as "λ systems" in the relativity literature, after the pioneering work of Brodbeck et al. [10, 33].

The constraint damping of [10] utilizes the freedom to substitute constraint equations into the evolution equations. In the physical situation where the constraints are all satisfied, the equations are unchanged. However in the numerical situation where the constraint satisfaction is at best approximate, these substitutions can have a profound effect on the structure of the evolution system and the stability of its constraints. In [23], Kidder, Scheel and Teukolsky added terms, proportional to the constraints, to a first-order representation of the Arnowitt-Deser-Misner (ADM) equations [6] (in a form advocated by York [38]). With these modifications, they were able to change the principal part of the evolution system. When the free parameters satisfy certain inequalities, the evolution system becomes strongly, or symmetric, hyperbolic [23, 25, 26, 24]. The purpose of this paper is to generalize the KST systems even further, to add more terms proportional to constraints into the

evolution equations, but now with the goal of damping the constraints while preserving hyperbolicity. It will be shown that this goal can largely be achieved, stabilizing all the constraints of the KST systems, without the need to introduce extra fields as in the "λ system" approach.

The possibility of constraint damping along these lines is now widely seen as a major advantage of the generalized harmonic formalism. Pretorius [29, 28], building on Gundlach et al. [20], introduced such a modification in his generalized harmonic evolution code, leading to the first-ever simulation of a full orbit and merger of binary black holes. In [27] (chapter 5 of this thesis), this system was converted into an explicitly first-order, linearly degenerate, symmetric-hyperbolic form. An extensive body of mathematical literature exists on systems of this form, and they are also very well suited to highly accurate multidomain pseudospectral collocation methods. While this first-order generalized harmonic system is perfectly acceptable for numerical relativity, and indeed is now used for nearly all simulations currently being done by the Caltech and Cornell numerical relativity groups, there would be considerable value in implementing a KST system of comparable stability. For one thing, the KST system involves just over half as many fields as the first-order generalized harmonic system, so it could provide a considerable improvement in code runtime. The KST systems are also closer to the evolution systems used historically in numerical relativity. Gauge is specified again in terms of (densitized) lapse and shift. So a large body of research on gauge conditions can be more easily implemented.

As the standard KST systems already have adjustable parameters, it is an interesting question whether any of them can have constraint-damping properties. Even without calculations, it is clear that the answer must be "no." With the generalized-harmonic system presented in [27], two parameters are available, γ_0 and γ_2, which tune the stability of small constraint-violating perturbations of flat spacetime. The inverses of these parameters (up to factors of order unity) define timescales on which short-wavelength constraint modes will decay exponentially. All of the free parameters of the standard KST systems are dimensionless, so they cannot fix any preferred timescale for the damping of perturbations of flat spacetime. Of course in the full nonlinear phase space, the dimensions necessary for such a timescale can be provided by nontrivial features of a particular solution, for instance the mass of a black hole. Indeed, in [31], it was demonstrated that careful fine-tuning of the parameters can considerably extend the lifetime of a black hole simulation. This effect cannot really be considered constraint damping, though, as the optimum choice of parameters depends strongly on the details of the initial data, and in fact it must fail for small features in asymptotic regions, where the above flat-space arguments begin to apply.

In the present paper, the KST systems will be generalized even further, introducing one new free parameter with dimensions of inverse-time, that can be considered a mechanism for constraint damping. This generalization is directly analogous to methods used in the past [22, 27] (chapters 4 and 5 of this thesis) for controlling the stability of the constraints that appear when an evolution

system that is second-order in spatial derivatives is reduced to first-order form by the introduction of auxiliary fields. Such a constraint exists in the KST systems, and while our methods are only designed to control this particular constraint, the intricate coupling of the constraints, in their evolution, extends the constraint damping effect to all (finite wavelength) constraint modes, including the Hamiltonian and momentum constraints.

The format of this paper is as follows. In Sec. 6.2 the intuitive mechanism behind the new constraint damping terms is sketched out in the context of a simple toy model. In Sec. 6.3, analogous modifications are applied to the five-parameter KST evolution systems, and conditions on these modifications are noted to keep the resulting system hyperbolic. In Sec. 6.4, the hyperbolicity of the constraint evolution is investigated. In Sec. 6.5 the effectiveness of these modifications on constraint-violating perturbations of flat spacetime is seen in detail. In Sec. 6.6, the available parameter freedom is summarized, and in Sec. 6.7, results are presented of a few simple numerical simulations using this new evolution system.

6.2 Illustration of a simple model system

Before jumping into the full equations of general relativity, it would be instructive to outline the constraint damping idea in the context of the simplest hyperbolic system, the scalar wave equation:

$$\eta^{\mu\nu}\partial_\mu\partial_\nu\psi = 0, \tag{6.1}$$

for a real scalar field ψ, where $\eta_{\mu\nu}$ is the Minkowski metric in Cartesian coordinates. This equation involves only one field, and no constraints, but it is second-order in both space and time. The second-order derivatives are removed by promoting the first derivatives of ψ to independent fields. The first time derivative (up to a conventional minus sign) will be denoted with the symbol π. The wave equation now becomes the system:

$$\partial_t\psi = -\pi, \tag{6.2}$$

$$\partial_t\pi = -\delta^{ij}\partial_i\partial_j\psi, \tag{6.3}$$

where Latin indices refer to the spatial coordinates of the chosen inertial frame. The one-form ϕ_i, defined by a new constraint $\mathcal{C}_i$, can be used to remove second spatial derivatives from the system:

$$\partial_t\psi = -\pi, \tag{6.4}$$

$$\partial_t\pi = -\delta^{ij}\partial_i\phi_j, \tag{6.5}$$

$$\mathcal{C}_i := \partial_i\psi - \phi_i = 0. \tag{6.6}$$

Before this can be useful for free evolution, an equation is needed for evolving ϕ_i. This equation is commonly derived by equating the spatial coordinate derivatives of both sides of Eq. (6.4), commuting partial derivatives on the left, and substituting the constraint to find:

$$\partial_t \phi_i = -\partial_i \pi. \tag{6.7}$$

This equation closes the evolution system, and leaves us with a nice first-order symmetric-hyperbolic representation of the scalar wave equation. However the newly defined constraint field is only marginally stable. As is easily verified by direct substitution of the constraint definition and the evolution equations, the constraint is now conserved:

$$\partial_t \mathcal{C}_i = 0. \tag{6.8}$$

This shows that exact constraint satisfaction should be preserved within the domain of dependence of the initial data, but also that any violations that may arise will be preserved as well.

Because the constraint is linear in undifferentiated ϕ_i, anything added to the right side of Eq. (6.7) will transfer directly to the evolution equation implied for the constraint. For instance, if the equation is changed to:

$$\begin{aligned} \partial_t \phi_i &= -\partial_i \pi + \gamma \mathcal{C}_i & (6.9) \\ &= -\partial_i \pi + \gamma(\partial_i \psi - \phi_i), & (6.10) \end{aligned}$$

for some constant γ, then the constraint-satisfying solution space is unchanged, but the evolution of the constraint becomes

$$\partial_t \mathcal{C}_i = -\gamma \mathcal{C}_i. \tag{6.11}$$

Thus, with this method, the constraint can be damped (assuming hyperbolicity is preserved) exponentially on an arbitrary fixed timescale γ^{-1}. As we will see when we discuss the KST system, the constraint damping effect can extend even farther than the constraint that appears in the reduction. Even those constraints that exist before the reduction to first-order form can be damped.

The question of whether this modification preserves the clear symmetric hyperbolicity of the standard reduction is important, and a very simple argument shows that hyperbolicity is not affected. If a linear change of variables is made (in other words, a change of basis on the vector bundle of dynamical fields), defining $\bar{\pi} := \pi - \gamma\psi$, then all modifications of the principal part of the fundamental evolution system disappear:

$$\partial_t \psi \simeq 0, \tag{6.12}$$

$$\partial_t \bar{\pi} \simeq -\delta^{ij}\partial_i \phi_j, \tag{6.13}$$

$$\partial_t \phi_i \simeq -\partial_i \bar{\pi} \tag{6.14}$$

(the symbol "$\simeq$" means that all nonprincipal—in this case, algebraic—terms have been omitted). This transformed system is exactly the same as the unmodified system at principal order, and is clearly symmetric-hyperbolic. The existence of a positive-definite symmetrizing inner product is independent of the basis of dynamical fields. Indeed, the obvious symmetrizer for the transformed system,

$$dS^2 = \Lambda d\psi^2 + d\bar{\pi}^2 + \delta^{ij} d\phi_i d\phi_j, \tag{6.15}$$

$$= \Lambda d\psi^2 + (d\pi - \gamma d\psi)^2 + \delta^{ij} d\phi_i d\phi_j, \tag{6.16}$$

when expressed in terms of π, is positive-definite (for positive Λ) and symmetrizes the untransformed system. Therefore, this constraint-damped form of the scalar wave system is symmetric-hyperbolic for any fixed choice of the damping timescale.

6.3 The modified KST evolution system

The Kidder-Scheel-Teukolsky [23] evolution equations are a five-parameter[1] generalization of the standard first-order representation of the classic ADM [6] equations, in the form advocated by York [38]:

$$\partial_t g_{ij} - \mathcal{L}_{\vec{N}} g_{ij} = -2NK_{ij} \tag{6.17}$$

$$\partial_t K_{ij} - \mathcal{L}_{\vec{N}} K_{ij} = NR_{ij} + N(KK_{ij} - 2K_i{}^k K_{kj}) - \nabla_i \nabla_j N. \tag{6.18}$$

The dynamical fields are $\{g_{ij}, K_{ij}\}$, the metric intrinsic to the slice of constant t, and the extrinsic curvature of its embedding in spacetime. The gauge fields $\{N, N^i\}$, lapse and shift, determine the evolution of the coordinates.

The Ricci tensor R_{ij} written above is that of the spatial metric g_{ij}, so it implicitly involves second spatial derivatives of g_{ij}. The evolution system can be reduced to first-order form by promoting the partial derivatives of the spatial metric functions to an independent (nontensorial) three-index field:

$$D_{kij} := \frac{1}{2}\partial_k g_{ij}. \tag{6.19}$$

[1] A twelve-parameter system also exists, employing redefinitions of the fundamental dynamical fields and associated constraint substitutions. Here we will ignore this extra freedom.

As long as D_{kij}, under its own evolution, properly represents $\partial_k g_{ij}/2$, it can be substituted for any derivatives of g_{ij}. This renders the ADM system first-order.

This evolution system, like that for the scalar field, describes physics only when certain constraint fields vanish:

$$\mathcal{C} := \frac{1}{2}(R - K_{ij}K^{ij} + K^2), \tag{6.20}$$

$$\mathcal{C}_i := \nabla^j(K_{ij} - Kg_{ij}), \tag{6.21}$$

$$\mathcal{C}_{kij} := \partial_k g_{ij} - 2D_{kij}. \tag{6.22}$$

The *Hamiltonian* and *momentum* constraints, $\mathcal{C}$ and $\mathcal{C}_i$, must vanish (in vacuum) throughout each spatial slice, according to the four Einstein equations not represented in Eq. (6.18). The three-index constraint $\mathcal{C}_{kij}$ vanishes when D_{kij} properly represents $\partial_k g_{ij}/2$, in analogy with the constraint of the scalar field system.

The new field, D_{kij}, is to be considered independent in free evolution. An evolution equation must be defined for this field, one that is consistent with the satisfaction of the three-index constraint above. The equation analogous to Eq. (6.7) is

$$\hat{\partial}_0 D_{kij} = \frac{1}{2}\partial_k(\hat{\partial}_0 g_{ij}), \tag{6.23}$$

$$= -\partial_k(NK_{ij}), \tag{6.24}$$

where the shorthand $\hat{\partial}_0$ refers to the derivative, $\partial_t - \mathcal{L}_{\vec{N}}$, along the normal to the spatial slice[2].

The evolution system has now been written in first-order form, and we can begin to ask about its hyperbolicity. Kidder, Scheel, and Teukolsky [23] have shown that the above system can be rendered strongly hyperbolic with a few simple modifications. The first of these is commonly referred to as *densitization of the lapse*. Rather than fixing N directly, we fix a related field Q defined by

$$N = g^{\gamma_0}\exp(Q), \tag{6.25}$$

where g is the determinant of g_{ij} and γ_0 is a constant nonzero parameter. The occurences of $\partial_k g_{ij}$ that then arise arise from the $\nabla_i\nabla_j N$ term in Eq. (6.18) are replaced by $2D_{kij}$. The second modification required for hyperbolicity is the addition of terms to the evolution equations for K_{ij} and D_{kij} that are proportional to the constraints:

$$\hat{\partial}_0 K_{ij} = ... + \gamma_1 N g_{ij}\mathcal{C} + \gamma_2 N g^{ab}\mathcal{C}_{a(ij)b}, \tag{6.26}$$

$$\hat{\partial}_0 D_{kij} = ... + \frac{1}{2}\gamma_3 N g_{k(i}\mathcal{C}_{j)} + \frac{1}{2}\gamma_4 N g_{ij}\mathcal{C}_k, \tag{6.27}$$

[2]Note that $\hat{\partial}_0$, involving a Lie derivative, commutes with the partial derivative ∂_k. It is this commutation that defines the action of the Lie derivative on the nontensorial field D_{kij}.

where the ellipses refer to the right sides of Eqs. (6.18) and (6.24). The four-index object $\mathcal{C}_{klij} := 2\partial_{[k}D_{l]ij}$ used here can be thought of as another constraint, but it vanishes automatically whenever the three-index constraint vanishes. The parameters $\{\gamma_0, ..., \gamma_4\}$ do not affect the physical solution space of the equations in any way, but they directly affect the principal part of the evolution system. In Ref. [23], Kidder, Scheel and Teukolsky determined sufficient conditions for these parameters that render the evolution system strongly hyperbolic. In Ref. [26] and an appendix of Ref. [24], these arguments were extended, and it was also made clear on what subset of the parameter space the equations satisfied the stronger condition of symmetric hyperbolicity.

The focus of this paper is a further modification of Eq. (6.27) along the same lines as that described in Sec. 6.2. Here the goal is to modify the evolution of the three-index constraint, which in the ordinary KST system is implied to evolve as

$$\hat{\partial}_0 \mathcal{C}_{kij} = -\gamma_3 N g_{k(i}\mathcal{C}_{j)} - \gamma_4 N g_{ij}\mathcal{C}_k. \tag{6.28}$$

Note that the need for damping here is more dire than in the scalar field case. Hyperbolicity requires γ_3 and γ_4 to be nonzero, so any violation of the momentum constraint will feed directly into the three-index constraint. This is countered as in the previous section by including terms proportional to the three-index constraint in the evolution equation for D_{kij}. As we will see in a moment, multiples of the traces, denoted $\mathcal{C}^1_k := g^{ij}\mathcal{C}_{kij}$ and $\mathcal{C}^2_j := g^{ki}\mathcal{C}_{kij}$, must be added in separately, so the resulting evolution equation is:

$$\begin{aligned}
\hat{\partial}_0 D_{kij} &= ... + \frac{1}{2}\gamma_3 N g_{k(i}\mathcal{C}_{j)} + \frac{1}{2}\gamma_4 N g_{ij}\mathcal{C}_k \\
&\quad + \frac{1}{2}N\gamma_5 \mathcal{C}_{kij} + \frac{1}{2}N\gamma_6 \mathcal{C}^1_k g_{ij} \\
&\quad + \frac{1}{2}N\gamma_7 \mathcal{C}^2_{(i}g_{j)k} + \frac{1}{2}N\gamma_8 \mathcal{C}^1_{(i}g_{j)k} \\
&\quad + \frac{1}{2}N\gamma_9 \mathcal{C}^2_k g_{ij}.
\end{aligned} \tag{6.29}$$

The term proportional to γ_5 is analogous to the term proportional to γ in Eq. (6.9). The terms proportional to γ_6, γ_7, γ_8, and γ_9 are necessitated by the hyperbolicity conditions, which we now consider.

The principal part of this system is:

$$\hat{\partial}_0 g_{ij} \simeq 0, \tag{6.30}$$

$$\begin{aligned}
\hat{\partial}_0 K_{ij} &\simeq N[g^{ab}\delta^c_i\delta^d_j - (1+\gamma_2)g^{ad}\delta^b_{(i}\delta^c_{j)} \\
&\quad -(1-\gamma_2)g^{bc}\delta^a_{(i}\delta^d_{j)} + (1+2\gamma_0)g^{cd}\delta^a_{(i}\delta^b_{j)} \\
&\quad -\gamma_1 g^{ad}g^{bc}g_{ij} + \gamma_1 g^{ab}g^{cd}g_{ij}]\partial_a D_{bcd},
\end{aligned} \tag{6.31}$$

$$\begin{aligned}\hat{\partial}_0 D_{kij} \simeq & -N[\delta^c_k\delta^a_i\delta^b_j - \frac{1}{2}\gamma_3 g^{ca}g_{k(i}\delta^b_{j)} \\ & -\frac{1}{2}\gamma_4 g^{ca}g_{ij}\delta^b_k + \frac{1}{2}\gamma_3 g^{ab}g_{k(i}\delta^c_{j)} \\ & +\frac{1}{2}\gamma_4 g^{ab}g_{ij}\delta^c_k]\partial_c K_{ab} \\ & +N[\frac{1}{2}\gamma_5\delta^c_k\delta^a_i\delta^b_j + \frac{1}{2}\gamma_6\delta^c_k g^{ab}g_{ij} \\ & +\frac{1}{2}\gamma_7 g^{ca}\delta^b_{(i}g_{j)k} + \frac{1}{2}\gamma_8 g^{ab}\delta^c_{(i}g_{j)k} \\ & +\frac{1}{2}\gamma_9 g^{ca}\delta^b_k g_{ij}]\partial_c g_{ab}. \end{aligned} \tag{6.32}$$

Hyperbolicity is well established for the standard KST system, $\gamma_5 = \gamma_6 = ... = \gamma_9 = 0$, so as in Sec. 6.2, it is best to seek a linear change of variables to reduce the constraint-damped system to the standard system. Continuing the analogy with the scalar field, define

$$\bar{K}_{ij} := K_{ij} - \frac{1}{2}\gamma_5 g_{ij}. \tag{6.33}$$

Then the equation for $\hat{\partial}_0\bar{K}_{ij}$ has the same principal part as that for $\hat{\partial}_0 K_{ij}$. The equation for $\hat{\partial}_0 D_{kij}$ becomes

$$\begin{aligned}\hat{\partial}_0 D_{kij} \simeq & -N[\delta^c_k\delta^a_i\delta^b_j - \frac{1}{2}\gamma_3 g^{ca}g_{k(i}\delta^b_{j)} \\ & -\frac{1}{2}\gamma_4 g^{ca}g_{ij}\delta^b_k + \frac{1}{2}\gamma_3 g^{ab}g_{k(i}\delta^c_{j)} \\ & +\frac{1}{2}\gamma_4 g^{ab}g_{ij}\delta^c_k]\partial_c \bar{K}_{ab} \\ & +N[\frac{1}{2}(\gamma_6 - \frac{1}{2}\gamma_4\gamma_5)\delta^c_k g^{ab}g_{ij} \\ & +\frac{1}{2}(\gamma_7 + \frac{1}{2}\gamma_3\gamma_5)g^{ca}\delta^b_{(i}g_{j)k} \\ & +\frac{1}{2}(\gamma_8 - \frac{1}{2}\gamma_3\gamma_5)g^{ab}\delta^c_{(i}g_{j)k} \\ & +\frac{1}{2}(\gamma_9 + \frac{1}{2}\gamma_4\gamma_5)g^{ca}\delta^b_k g_{ij}]\partial_c g_{ab}. \end{aligned} \tag{6.34}$$

If, for arbitrary γ_5, the further parameters are fixed as

$$\gamma_6 = \frac{1}{2}\gamma_4\gamma_5 \tag{6.35}$$

$$\gamma_7 = -\frac{1}{2}\gamma_3\gamma_5 \tag{6.36}$$

$$\gamma_8 = \frac{1}{2}\gamma_3\gamma_5 \tag{6.37}$$

$$\gamma_9 = -\frac{1}{2}\gamma_4\gamma_5, \tag{6.38}$$

then the principal system, in the transformed variables, loses any reference to $\gamma_5, ..., \gamma_9$.

$$\begin{aligned}
\hat{\partial}_0 g_{ij} &\simeq 0, && (6.39)\\
\hat{\partial}_0 \bar{K}_{ij} &\simeq N[g^{ab}\delta^c_i\delta^d_j - (1+\gamma_2)g^{ad}\delta^b_{(i}\delta^c_{j)} \\
&\quad -(1-\gamma_2)g^{bc}\delta^a_{(i}\delta^d_{j)} + (1+2\gamma_0)g^{cd}\delta^a_{(i}\delta^b_{j)} \\
&\quad -\gamma_1 g^{ad}g^{bc}g_{ij} + \gamma_1 g^{ab}g^{cd}g_{ij}]\partial_a D_{bcd}, && (6.40)\\
\hat{\partial}_0 D_{kij} &\simeq -N[\delta^c_k\delta^a_i\delta^b_j - \frac{1}{2}\gamma_3 g^{ca}g_{k(i}\delta^b_{j)} \\
&\quad -\frac{1}{2}\gamma_4 g^{ca}g_{ij}\delta^b_k + \frac{1}{2}\gamma_3 g^{ab}g_{k(i}\delta^c_{j)} \\
&\quad +\frac{1}{2}\gamma_4 g^{ab}g_{ij}\delta^c_k]\partial_c \bar{K}_{ab}. && (6.41)
\end{aligned}$$

This is the principal part of the standard KST system. So for any value of the parameter γ_5, with $\gamma_6, ..., \gamma_9$ fixed by Eqs. (6.35) – (6.38)[3], the hyperbolicity of our modified system is the same as that of the corresponding standard KST system.

6.4 Hyperbolicity of the constraint evolution

Let us now turn our attention to the evolution of the constraint fields in our modified KST evolution system. Given the definitions of the constraints in terms of the fundamental dynamical fields, an evolution system for the constraints follows from our fundamental evolution equations. It is important, for the construction of constraint-preserving boundary conditions, that this system also be symmetric-hyperbolic [24, 35, 12]. The principal part of this evolution system can be expressed as,

$$\begin{aligned}
\hat{\partial}_0 \mathcal{C} &\simeq -\frac{1}{2}(2-\gamma_3+2\gamma_4)Ng^{ij}\partial_i \mathcal{C}_j \\
&\quad +\frac{1}{2}(\gamma_8 - 2\gamma_6 - \gamma_5)Ng^{ij}\partial_i \mathcal{C}^1_j \\
&\quad +\frac{1}{2}(\gamma_7 - 2\gamma_9 + \gamma_5)Ng^{ij}\partial_i \mathcal{C}^2_j, && (6.42)\\
\hat{\partial}_0 \mathcal{C}_i &\simeq -(1+2\gamma_1)N\partial_i \mathcal{C} \\
&\quad +\frac{1}{2}Ng^{kl}g^{ab}\big[(1-\gamma_2)\partial_k \mathcal{C}_{labi} + (1+\gamma_2)\partial_k \mathcal{C}_{ailb} \\
&\qquad -(1+2\gamma_0)\partial_k \mathcal{C}_{liab}\big], && (6.43)\\
\hat{\partial}_0 \mathcal{C}_{kij} &\simeq 0, && (6.44)\\
\hat{\partial}_0 \mathcal{C}_{abij} &\simeq -\frac{1}{2}N\gamma_3 g_{i[a}\partial_{b]}\mathcal{C}_j - \frac{1}{2}N\gamma_3 g_{j[a}\partial_{b]}\mathcal{C}_i
\end{aligned}$$

[3] This requirement can be weakened somewhat. There is one further degree of freedom, shared between γ_6 and γ_8, which will still preserve hyperbolicity. However when this degree of freedom is utilized, the simple argument used here must be replaced either by a somewhat more subtle argument, or a significantly more laborious one. We have not yet found a use for this further degree of freedom, so here we restrict attention to the simpler case.

$$
\begin{aligned}
&-N\gamma_4 g_{ij}\partial_{[b}\mathcal{C}_{a]} - N\gamma_6 g_{ij}\partial_{[b}\mathcal{C}^1_{a]} \\
&-\frac{1}{2}N\gamma_7 g_{i[a}\partial_{b]}\mathcal{C}^2_j - \frac{1}{2}N\gamma_7 g_{j[a}\partial_{b]}\mathcal{C}^2_i \\
&-\frac{1}{2}N\gamma_8 g_{i[a}\partial_{b]}\mathcal{C}^1_j - \frac{1}{2}N\gamma_8 g_{j[a}\partial_{b]}\mathcal{C}^1_i \\
&-N\gamma_9 g_{ij}\partial_{[b}\mathcal{C}^2_{a]},
\end{aligned} \tag{6.45}
$$

where the four-index object $\mathcal{C}_{klij} := 2\partial_{[k}D_{l]ij}$ is considered an independent constraint, so that the constraint evolution system is first-order.

The inclusion of the terms proportional to $\gamma_5, ..., \gamma_9$ in Eqs. (6.42) – (6.45) has seriously complicated this system. Let us consider, however, the case considered above, where γ_5 is arbitrary, and the other parameters are fixed by Eqs. (6.35) – (6.38). In this case, a number of remarkable simplifications occur and the above system can be written as

$$
\hat{\partial}_0\mathcal{C} \simeq -\frac{1}{2}(2-\gamma_3+2\gamma_4)Ng^{ij}\partial_i\bar{\mathcal{C}}_j, \tag{6.46}
$$

$$
\begin{aligned}
\hat{\partial}_0\bar{\mathcal{C}}_i \simeq\ & -(1+2\gamma_1)N\partial_i\mathcal{C} \\
& +\frac{1}{2}Ng^{kl}g^{ab}\big[(1-\gamma_2)\partial_k\mathcal{C}_{labi} + (1+\gamma_2)\partial_k\mathcal{C}_{ailb} \\
& \qquad -(1+2\gamma_0)\partial_k\mathcal{C}_{liab}\big],
\end{aligned} \tag{6.47}
$$

$$
\hat{\partial}_0\mathcal{C}_{kij} \simeq 0, \tag{6.48}
$$

$$
\begin{aligned}
\hat{\partial}_0\mathcal{C}_{abij} \simeq\ & -\frac{1}{2}N\gamma_3 g_{i[a}\partial_{b]}\bar{\mathcal{C}}_j - \frac{1}{2}N\gamma_3 g_{j[a}\partial_{b]}\bar{\mathcal{C}}_i \\
& -N\gamma_4 g_{ij}\partial_{[b}\bar{\mathcal{C}}_{a]},
\end{aligned} \tag{6.49}
$$

defining the new combination $\bar{\mathcal{C}}_k := \mathcal{C}_k + \frac{1}{2}\gamma_5\mathcal{C}^1_k - \frac{1}{2}\gamma_5\mathcal{C}^2_k$.

This constraint evolution system has the same principal part as the standard KST constraint system. Thus, when the parameters are chosen by Eqs. (6.35) – (6.38), the hyperbolicity of the fundamental and constraint evolution systems are independent of the parameter γ_5, so our modifications do not alter the hyperbolicity of these systems.

6.5 Stability of constraint fields under free evolution

Analyzing the stability of the constraint evolution system in generic simulations is essentially no different than the full numerical relativity problem itself. In order to get some handle, at the analytical level, on the effect of our modifications, we consider constraint-violating perturbations of Minkowski spacetime. Obviously these estimates will not be completely relevant in simulations of interest, but at least in the limit of short-wavelength perturbations, the dependence on the spacetime background should be minimal. In this sense, stability of short-wavelength constraint-

violating perturbations of Minkowski spacetime is a necessary condition for constraint damping in general. And while our Minkowski-spacetime analysis of long-wavelength modes may not be directly relevant for evolutions of curved spacetime, unstable long-wavelength modes should at least be disconcerting, as a signal that instabilities are likely in general simulations.

This analysis involves the full (not just principal) constraint evolution system, linearized about the limit that $g_{ij} = \delta_{ij}$, $K_{ij} = D_{kij} = 0$, $N = 1$, $N^i = 0$. In this context, the full constraint evolution system becomes:

$$\begin{aligned}
\partial_t \mathcal{C} &= -\frac{1}{2}(2 - \gamma_3 + 2\gamma_4)\delta^{ij}[\partial_i \mathcal{C}_j + \frac{1}{2}\gamma_5 \partial_i \mathcal{C}^1_j \\
&\qquad -\frac{1}{2}\gamma_5 \partial_i \mathcal{C}^2_j], \qquad (6.50)\\
\partial_t \mathcal{C}_i &= -(1 + 2\gamma_1)\partial_i \mathcal{C} \\
&\quad +\frac{1}{2}\delta^{kl}\delta^{ab}\big[(1 - \gamma_2)\partial_k \partial_{[a}\mathcal{C}_{l]bi} + (1 + \gamma_2)\partial_k \partial_{[i}\mathcal{C}_{a]lb} \\
&\qquad -(1 + 2\gamma_0)\partial_k \partial_{[i}\mathcal{C}_{l]ab}\big], \qquad (6.51)\\
\partial_t \mathcal{C}_{kij} &= -\gamma_5 \mathcal{C}_{kij} \\
&\quad -\gamma_3 \delta_{k(i}\mathcal{C}_{j)} - \gamma_4 \delta_{ij}\mathcal{C}_k \\
&\quad -\frac{1}{2}\gamma_3\gamma_5 \delta_{k(i}\mathcal{C}^1_{j)} - \frac{1}{2}\gamma_4\gamma_5 \delta_{ij}\mathcal{C}^1_k \\
&\quad +\frac{1}{2}\gamma_3\gamma_5 \delta_{k(i}\mathcal{C}^2_{j)} + \frac{1}{2}\gamma_4\gamma_5 \delta_{ij}\mathcal{C}^2_k. \qquad (6.52)
\end{aligned}$$

Notice that we are no longer considering $\mathcal{C}_{klij}$ an independent constraint field. In actual evolutions, where the fundamental fields are evolved, not the constraints, the three- and four-index constraints satisfy the identity

$$\mathcal{C}_{klij} = \partial_{[l}\mathcal{C}_{k]ij}. \qquad (6.53)$$

Violations of this identity will not appear in evolutions.

Now the above system is simplified by resolving all constraint fields into Fourier modes. This has the formal effect of replacing all spatial derivatives ∂_j with $-ik_j$, an imaginary unit times a propagation vector k_j. The result is a system of coupled ODEs for the various constraint modes $c^A(k_i, t)$:

$$\partial_t c^A = M^A_B c^B. \qquad (6.54)$$

Each eigenvector of $M^A_B(k_i)$ evolves as $\exp(st)$ for some $s(k_i)$. The real part of s is the rate of exponential growth (or damping, if negative) for the corresponding mode. Due to the rotational invariance of the problem, these eigenvalues should depend only on the magnitude of k_i, so the propagation vector is decomposed as $k_i = kn_i$ where n_i is a unit vector.

This eigenvalue problem naturally reduces into subspaces according to various possible spin weights about the propagation direction n_i. There is a five-dimensional space of longitudinal

modes: $\{\mathcal{C}, \mathcal{C}_n, \mathcal{C}^1_n, \mathcal{C}^2_n, \mathcal{C}_{nnn}\}$, where $\mathcal{C}_n := n^i \mathcal{C}_i$, etc. There is also a five-dimensional space of transverse vector modes: $\{\mathcal{C}_I, \mathcal{C}^1_I, \mathcal{C}^2_I, \mathcal{C}_{Inn}, \mathcal{C}_{nnI}\}$, where capital Latin indices now refer to a two-dimensional vector basis orthogonal to n^i. The remaining constraint fields, with higher spin weight, are represented among the various projections of the totally tracefree part of $\mathcal{C}_{kij}$. A glance at Eq. (6.52) shows that all of these high spin-weight fields propagate trivially with $s = -\gamma_5$ independent of wavelength. They are therefore damped exponentially on the timescale γ_5^{-1} for positive γ_5. The longitudinal and transverse constraint modes require more careful consideration.

6.5.1 Transverse vector constraint modes

The growth rates of the transverse vector modes are related to the eigenvalues of a five-by-five matrix. Three of these eigenvalues simply equal $-\gamma_5$. The remaining two are solutions of a quadratic equation, and depend on wavelength as:

$$s(k) = -\frac{1}{2}\gamma_5\Gamma \pm \sqrt{\frac{1}{4}\gamma_5^2\Gamma^2 - v_2^2 k^2}, \tag{6.55}$$

where we define the convenient shorthand

$$\Gamma := \frac{1}{2}(2 - \gamma_3 + 2\gamma_4), \tag{6.56}$$

and v_2 is one of the characteristic speeds of the KST system (relative to hypersurface-normal observers),

$$v_2^2 := \frac{1}{8}\gamma_3(1 - 3\gamma_2 - 4\gamma_0) - \frac{1}{4}\gamma_4(1 + 6\gamma_0). \tag{6.57}$$

Notice that one mode is undamped in the long-wavelength ($k \to 0$) limit, where one root in Eq. (6.55) becomes zero. This is not surprising: other constraint-damped representations of the Einstein system have the same property [10, 20, 27]. In practice, long wavelength constraint modes should be killed off by proper constraint-preserving boundary conditions.

In the short wavelength ($k \to \infty$) limit, the dispersion relation becomes

$$s(k) \to -\frac{1}{2}\gamma_5\Gamma \pm i v_2 k. \tag{6.58}$$

These represent propagating modes of the constraint system, damped at short wavelength on the timescale $(\frac{1}{2}\gamma_5\Gamma)^{-1}$. Notice the significance of the constant Γ. Most of the modes require $\gamma_5 > 0$ for damping, so the damping of the modes referred to in Eq. (6.58) requires $\Gamma > 0$ as well. Thus, the damping condition places a new condition on the standard KST parameters $\{\gamma_0, ..., \gamma_4\}$, beyond the conditions they must satisfy for the system to be hyperbolic.

6.5.2 Longitudinal constraint modes

The longitudinal modes again involve the eigenvalues of a five-by-five matrix. In this case two of the eigenvalues are simply $-\gamma_5$. The rest are the roots of the cubic polynomial

$$s^3 + \gamma_5\Gamma s^2 + k^2 v_3^2 s + k^2\gamma_5\Gamma(1+2\gamma_1) = 0, \tag{6.59}$$

where v_3 is another characteristic speed, given by

$$v_3^2 := \frac{1}{2}(1+2\gamma_1)(2-\gamma_3+2\gamma_4) - \frac{1}{2}\gamma_2\gamma_3. \tag{6.60}$$

Rather than giving complicated analytic expressions for the roots of this polynomial, we simply consider asymptotic limits in k. First, in the long-wavelength ($k = 0$) limit, two roots vanish and the third is $-\gamma_5\Gamma$. This is very similar to the long-wavelength behavior of the vector modes.

In the short-wavelength limit, the polynomial becomes singular. The terms proportional to k^2 dominate the polynomial, leaving a linear equation. The root of this linear equation, $s = -v_3^{-2}\gamma_5\Gamma(1+2\gamma_1)$, is the *regular root* of the polynomial in this limit. The two remaining roots disappear from the above polynomial in the limit $k \to \infty$. These singular roots correspond to traveling modes, with imaginary part linear in k in this limit. They can be found by substituting for s a power series in k, $s = s_1 k + s_0 + s_{-1}k^{-1} + ...$ in the above polynomial and solving the resulting polynomial order-by-order in k for the coefficients s_i. The result is

$$s(k) = -\frac{1}{2}\gamma_5\Gamma\left(1 - \frac{1+2\gamma_1}{v_3^2}\right) \pm i v_3 k + \mathcal{O}(k^{-1}). \tag{6.61}$$

So the damping of the traveling longitudinal modes requires that $v_3^2 > (1+2\gamma_1)$ when the transverse modes are damped as well.

In summary, the damping of short-wavelength constraint-violating modes requires that the rates

$$r_0 := \gamma_5 \tag{6.62}$$

$$r_1 := \frac{1}{2}\gamma_5\Gamma \tag{6.63}$$

$$r_2 := v_3^{-2}\gamma_5\Gamma(1+2\gamma_1) \tag{6.64}$$

$$r_3 := \frac{1}{2}v_3^{-2}\gamma_5\Gamma(v_3^2 - 1 - 2\gamma_1) \tag{6.65}$$

be positive, where Γ is defined by Eq. (6.56) and v_3 by Eq. (6.60).

6.6 Choosing parameters

Before proceeding with numerical tests, values must be fixed for the free parameters. The parameters associated with the constraint damping terms are reasonably well set. The overall damping timescale is set by $1/\gamma_5$, and this can be chosen to be any positive number. The other new parameters are determined by Eqs. (6.35) – (6.38). The original KST parameters should be chosen in accord with hyperbolicity conditions for the fundamental and constraint evolution systems, as well as the conditions that the damping rates of Eqs. (6.62) – (6.65) be positive.

The hyperbolicity conditions are quite complicated when considered in full generality. To make the situation more tractable, here we restrict attention to the subset of parameter space in which all characteristic speeds are equal to zero or unity, relative to hypersurface-normal observers. The hyperbolicity conditions in this subset of the parameter space are spelled out in Appendix B of [24], following work in [26]. The parameters γ_0, γ_3, and γ_4 are fixed in terms of γ_1 and γ_2 by the the conditions on the characteristic speeds:

$$\gamma_0 = \frac{1}{2} \tag{6.66}$$

$$\gamma_3 = \frac{-8}{4\gamma_2 + (5+3\gamma_2)(1+2\gamma_1)} \tag{6.67}$$

$$\gamma_4 = \frac{1-\gamma_2-(1+2\gamma_1)(5+3\gamma_2)}{4\gamma_2+(5+3\gamma_2)(1+2\gamma_1)}. \tag{6.68}$$

The fundamental evolution system is then symmetric-hyperbolic so long as the following inequalities are satisfied:

$$-\tfrac{5}{3} < \gamma_2 < 0 \tag{6.69}$$

$$4\gamma_2 + (1+2\gamma_1)(5+3\gamma_2) \neq 0. \tag{6.70}$$

Constraint damping requires that the rates r_i of Eqs. (6.62) – (6.65) be positive. This in turn requires that $\Gamma > 0$ and that

$$0 < 1 + 2\gamma_1 < v_3^2. \tag{6.71}$$

For the numerical simulations presented in the next section, $\gamma_1 = -1/4$. The parameter $\Gamma := (1/2)(2 - \gamma_3 + 2\gamma_4)$ can be expressed in terms of γ_2 using the above expressions for γ_3 and γ_4:

$$\Gamma = \frac{5+3\gamma_2}{4\gamma_2+(5+3\gamma_2)(1+2\gamma_1)} = \frac{10+6\gamma_2}{5+11\gamma_2}, \tag{6.72}$$

where the last equality is restricted to the case $\gamma_1 = -1/4$. In the allowable region for γ_2, Γ can be set equal to any value greater than 2. Here we choose $\Gamma = 5/2$.

The various parameters, and the associated growth rates, come out to:

$$\gamma_0 = \frac{1}{2}, \tag{6.73}$$

$$\gamma_1 = -\frac{1}{4}, \tag{6.74}$$

$$\gamma_2 = -\frac{5}{43}, \tag{6.75}$$

$$\gamma_3 = -\frac{43}{10}, \tag{6.76}$$

$$\gamma_4 = -\frac{52}{80}, \tag{6.77}$$

$$r_0 = \gamma_5, \tag{6.78}$$

$$r_1 = \frac{5}{4}\gamma_5, \tag{6.79}$$

$$r_2 = \frac{5}{4}\gamma_5, \tag{6.80}$$

$$r_3 = \frac{5}{8}\gamma_5. \tag{6.81}$$

These parameters satisfy all the necessary conditions for constraint damping in perturbations of flat spacetime, as well as those for symmetric-hyperbolic propagation of the fundamental evolution fields. Unfortunately, these parameters do not satisfy all of the necessary conditions for symmetric-hyperbolic constraint propagation. In [24] it was shown that when the adjustable characteristic speeds are all set to unity, the symmetric hyperbolicity conditions on the fundamental and constraint evolution systems collude to require that $1 + 2\gamma_1 < 0$, a direct conflict with our damping conditions. Unfortunately, this conflict does not appear to be an artefact of our condition that all adjustable characteristic speeds are equal to one. Monte Carlo searches over the entire available parameter space have not provided us with any examples of systems with constraint damping along with symmetric-hyperbolic propagation of the fundamental and constraint fields.

In principle, this conflict is very serious. At timelike boundaries of the simulation domain, conditions must be imposed on fields entering the computational grid. These boundary conditions should be compatible with the constraint equations. In [24], such boundary conditions were presented. These conditions control the growth of a certain norm of the constraint fields. In the case of the parameters used here, this norm is not positive-definite, so control of the norm does not necessarily imply control of the constraint fields themselves.

In practice, the damage done by this conflict can only be assessed with numerical simulations. While the constraint evolution is not symmetric-hyperbolic, it is strongly hyperbolic, so the boundary conditions of [24] can still be applied, even if they may not have all of the desired effects. In fact, the numerical results of the following section demonstrate that constraint-preserving boundary conditions are quite effective in these simulations. Perhaps this can be explained heuristically by the fact that the "timelike" degree of freedom in the constraint evolution (the one whose viola-

tions could compensate, in the indefinite norm, for violations of the other constraints) is very well controlled by the constraint damping.

It should also be noted that without the constraint damping terms, the particular parameter set used here leads to very unstable evolutions. In the following section, we will not make comparisons with the undamped case, $\gamma_5 = 0$, as those cases immediately become unstable. This could be due, in part, to the lack of symmetric-hyperbolic constraint evolution. At any rate, when the constraint damping terms are included, the evolutions become remarkably stable.

6.7 Numerical tests

The following numerical tests were carried out using the Spectral Einstein Code developed over the last few years by the numerical relativity groups at Cornell and Caltech. The code uses multidomain pseudospectral collocation methods to resolve the fields in space with exponential accuracy. Integration in time is implemented by the method of lines, using in this case a fourth-order Runge-Kutta scheme. More details on this code and its remarkable accuracy can be found in [9] and references therein.

The spectral representation of the computed fields is done in accordance with the topology of the spatial domain. The present simulations are of a single Schwarzschild black hole, in Kerr-Schild [16] coordinates. The spatial domain is made up of a family of concentric thick spherical shells. The fields are therefore resolved into spherical harmonics in the angular directions, multiplied by Chebyshev polynomials in the radial direction. The innermost boundary is inside the black hole horizon, so no boundary condition is needed there. At the outermost boundary, the constraint-preserving boundary conditions presented in [24] are used. As in [24], tensor spherical harmonic components of the four highest l values are discarded after each time step. No filtering appears to be necessary in the radial direction.

Figures 6.1 and 6.2 demonstrate the stability and exponential convergence of these simulations. Figure 6.1 is a plot of the error norm:

$$||\delta u||^2 := \int \left(\delta g^{ij}\delta g_{ij} + \delta K^{ij}\delta K_{ij} + \delta D^{kij}\delta D_{kij}\right) dV, \tag{6.82}$$

measuring the difference between the computed solution and the reference Kerr-Schild geometry. Figure 6.2 shows a positive-definite norm of the constraint fields:

$$||\mathcal{C}||^2 := \int \left(\mathcal{C}^2 + \frac{1}{3}\mathcal{C}^i\mathcal{C}_i + \frac{1}{18}\mathcal{C}^{kij}\mathcal{C}_{kij} + \frac{1}{18}\mathcal{C}^{klij}\mathcal{C}_{klij}\right) dV. \tag{6.83}$$

We normalize these quantities, dividing by norms that involve similar terms, but that should not

be expected to vanish. The error norm is divided by the overall solution norm:

$$||u||^2 := \int \left(g^{ij} g_{ij} + K^{ij} K_{ij} + D^{kij} D_{kij} \right) dV, \tag{6.84}$$

and the constraint norm is divided by a similar norm of the first derivatives of the computed fields:

$$\begin{aligned} ||\partial u||^2 \quad := \quad & \int (g^{kc} g^{ia} g^{jb} \partial_k g_{ij} \partial_c g_{ab} \\ & + g^{kc} g^{ia} g^{jb} \partial_k K_{ij} \partial_c K_{ab} \\ & + g^{ld} g^{kc} g^{ia} g^{jb} \partial_l D_{kij} \partial_d D_{cab}) dV. \end{aligned} \tag{6.85}$$

All indices are raised and lowered with the computed metric g_{ij}.

The inner (excision) boundary is at $1.9\,M$, and the outer boundary is at $41.9\,M$. This domain is divided into eight subdomains, each of coordinate thickness $5\,M$. This is the same domain used in [24]. Note that the convergence stops at the highest resolution presented here, overtaken by exponential growth that is not yet apparent in the constraint fields shown in Fig. 6.2. In [24], a "gauge instability" was mentioned, associated with one particular boundary condition. Presumably, this is the same instability apparent in Fig. 6.1, in which case it could be expected that convergence would improve as the location of the outer boundary is moved farther into the asymptotic regime.

As a test of this hypothesis, the highest-resolution run in Fig. 6.1 was repeated on larger domains, keeping resolution fixed but adding extra subdomains to place the outer boundary at coordinate radii 61.9 M, 81.9 M, 101.9 M. Figure 6.3 demonstrates the improvement in the overall error norm. Least-squares fitting of the data in that plot show that the late-term growth in this error occurs exponentially on a timescale proportional to the square of the coordinate position of the outer boundary. Figure 6.4 shows the growth of constraint energy in these simulations. Until an exponential instability sets in, apparently triggered by the overall loss of accuracy of the simulation, the constraint fields grow roughly as the square root of coordinate time. On the largest domain, this slow growth persists beyond 15,000 M, when exponential growth takes over at a rate that would allow the simulation to persist until nearly 50,000 M.

It is of some interest to verify the effectiveness of the constraint-preserving boundary conditions used in these simulations. As noted in the previous section, since the characteristic matrices of the constraint evolution system are symmetric only with respect to a Lorentzian norm, there is no reason to expect these conditions to control the influx of constraint violations. In Fig. 6.5, the simulation with $R_{max} = 41.9$ and $N_r = 17$ (in each subdomain) is repeated using conventional boundary conditions. These boundary conditions freeze the incoming characteristic fields of the fundamental evolution system to their initial values. These "freezing" boundary conditions control a positive-definite norm of the fundamental evolution fields, so the initial boundary value problem is known

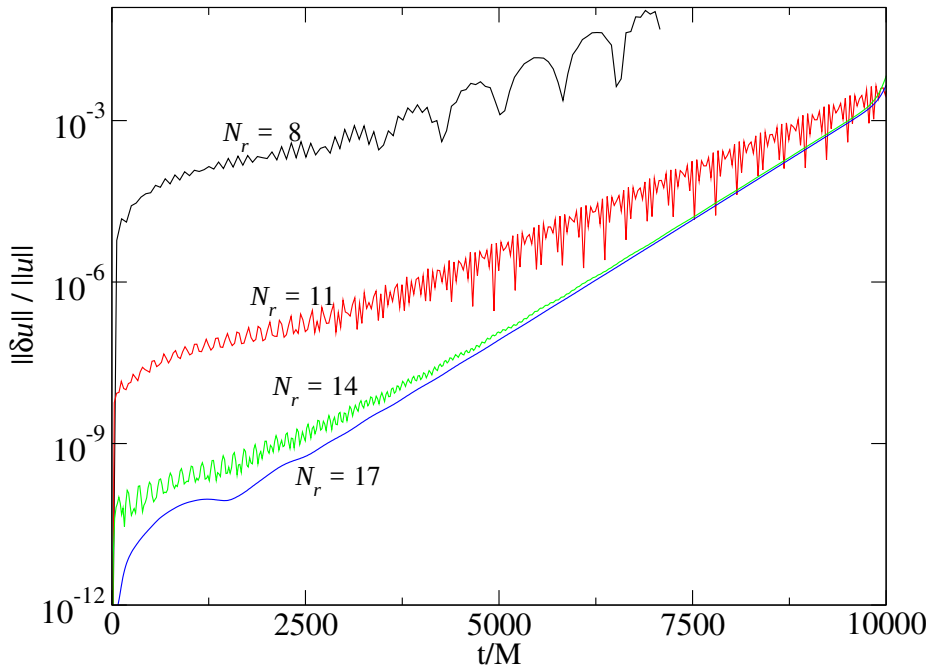

Figure 6.1: Norm of the error $||\delta u||/||u||$, relative to the reference solution, on a fixed domain extending from minimum coordinate radius $1.9\,M$ to maximum $41.9\,M$. The domain is broken into eight shells each of thickness $5\,M$ and radial resolution N_r, chosen on four different runs as $N_r = 8, 11, 14, 17$. The constraint damping terms presented in all of these simulations have $\gamma_5 = 0.6$.

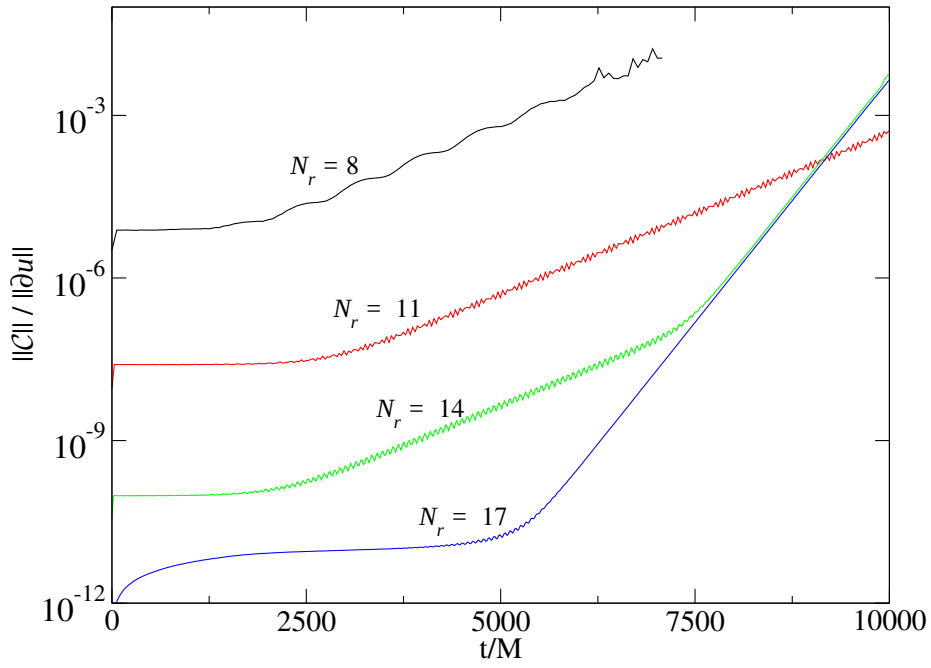

Figure 6.2: Constraint norm $||\mathcal{C}||/||\partial u||$ for the same runs plotted in Fig. 6.1

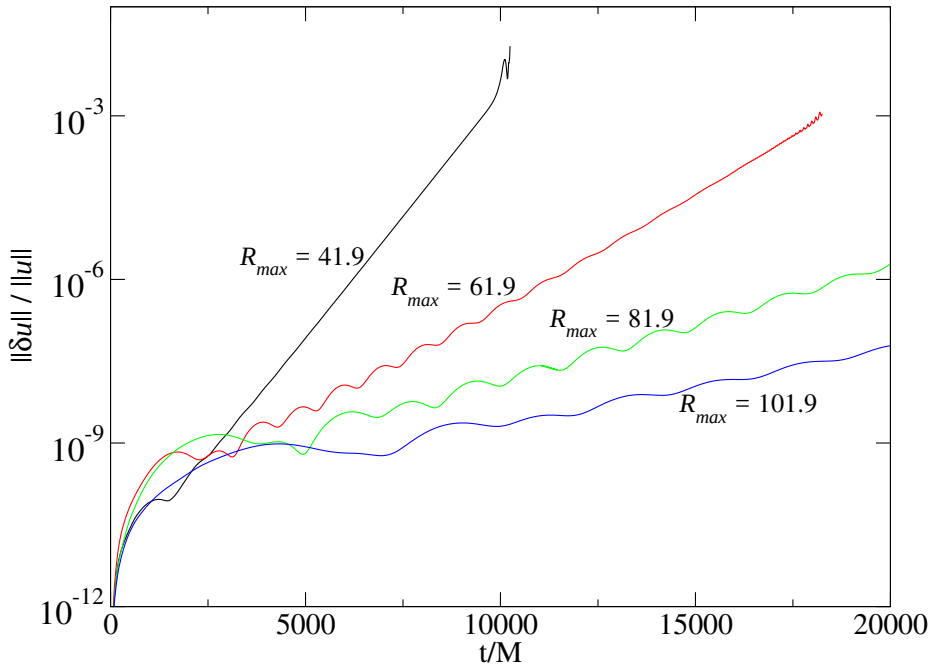

Figure 6.3: Error norm $||\delta u||/||u||$ for runs in the constraint-damped system with outer boundary at $r = 41.9\ M, 61.9\ M, 81.9\ M, 101.9\ M$. The long-term growth of the error norm occurs exponentially on a timescale proportional to the square of the coordinate position of the outer boundary.

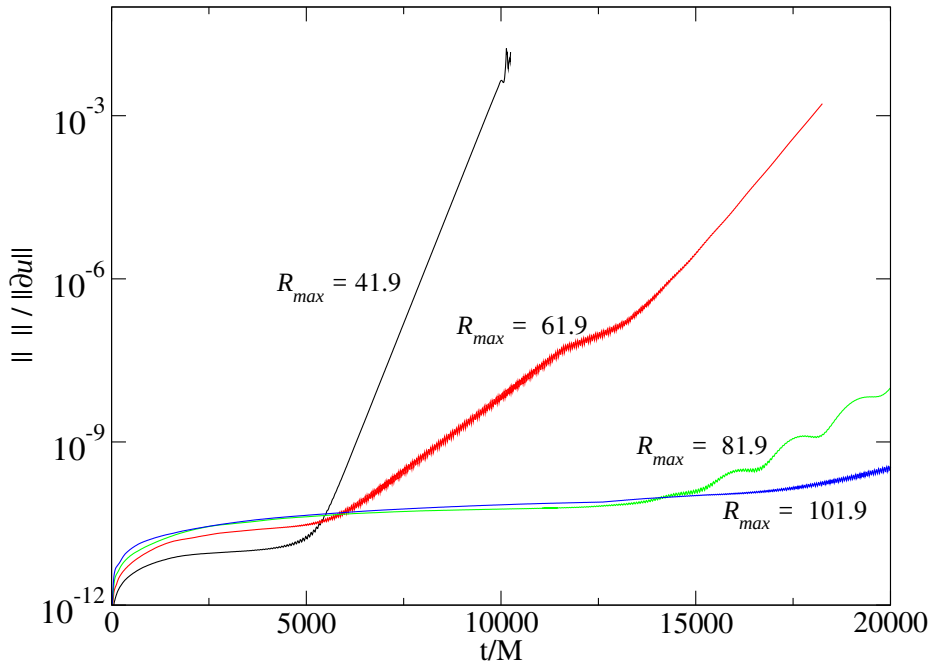

Figure 6.4: Constraint norm $||\mathcal{C}||/||\partial u||$ of the same runs as those in Fig. 6.3. The constraints grow as $t^{1/2}$ until eventually driven exponentially by the overall loss of accuracy demonstrated in Fig. 6.3.

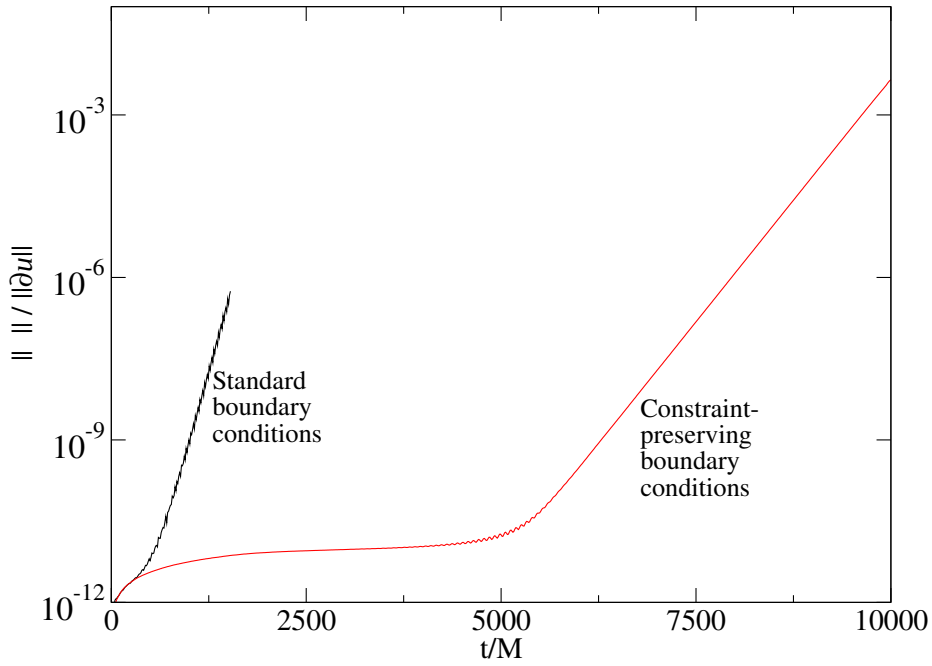

Figure 6.5: Constraint norm $||\mathcal{C}||/||\partial u||$ of a black hole simulation with $R_{max} = 41.9$, $N_r = 17$ (in each of eight subdomains), and two different boundary conditions.

to be well-posed by standard theorems. However, the figure clearly demonstrates the superiority of the constraint-preserving boundary conditions in this context, not only for constraint satisfaction, but for overall stability. Perhaps the effectiveness of the constraint preserving conditions is not robust, perhaps it will fail when the conditions are applied in more dynamical spacetimes. This possibility is an important avenue for further investigation — if this stability is found not to be robust, then either the spatial domain will need to be compactified to remove timelike boundaries, or further modification of the KST system will be needed to combine the constraint damping effects outlined here with truly symmetric hyperbolic constraint propagation.

6.8 Discussion

A generalization of the five-parameter KST systems was introduced, for use in numerical relativity. The added parameter γ_5 supplies a timescale on which exponential damping can occur (or growth, if parameters are not chosen carefully). The hyperbolicity of the fundamental and constraint evolution systems is not changed by this modification, but the effect that the constraint damping has on perturbations of flat spacetime is partly dependent on the same parameters that determine hyperbolicity. Parameters can be chosen such that all constraint modes are stable in perturbations of

flat spacetime, but not when the constraint fields are required to evolve in a symmetric-hyperbolic manner. Nevertheless, single black hole simulations using constraint-preserving boundary conditions are convergent, and what instabilities exist appear to be dominated by constraint-satisfying modes, associated with a gauge instability in the outer boundary condition.

6.9 Acknowledgments

I thank Lee Lindblom for extensive discussions and advice, and also Harald Pfeiffer and Mark Scheel, for help on the manuscript and for assistance on the use of their code. Michael Boyle provided access to some input files and numerical results of [9], which were of great help in debugging and understanding the numerical issues. The numerical calculations presented in this paper were performed with the Caltech/Cornell Spectral Einstein Code (SpEC) written primarily by Lawrence E. Kidder, Harald P. Pfeiffer, and Mark A. Scheel. This work was supported in part by NSF grants PHY-0099568, PHY-0244906, PHY-0601459, and DMS-0553302; NASA grants NAG5-12834 and NNG05GG52G; and a grant from the Sherman Fairchild Foundation. Some of the numerical calculations leading to this paper were performed with the Tungsten cluster at NCSA.

Bibliography

[1] A. M. Abrahams, G. B. Cook, S. L. Shapiro, and S. A. Teukolsky. Solving Einstein's equations for rotating spacetimes: Evolution of relativistic star clusters. *Phys. Rev. D*, 49:5153–5164, 1994.

[2] A. M. Abrahams and C. R. Evans. Trapping a geon: Black hole formation by an imploding gravitational wave. *Phys. Rev. D*, 46:R4117–R4121, 1992.

[3] A. M. Abrahams and C. R. Evans. Critical behavior and scaling in vacuum axisymmetric gravitational collapse. *Phys. Rev. Lett.*, 70:2980–2983, 1993.

[4] Miguel Alcubierre, Bernd Brügmann, Peter Diener, Michael Koppitz, Denis Pollney, Edward Seidel, and Ryoji Takahashi. Gauge conditions for long-term numerical black hole evolutions without excision. *Phys. Rev. D*, 67:084023, 2003.

[5] M. Anderson and R. A. Matzner. Extended lifetime in computational evolution of isolated black holes. *Found. Phys.*, 35:1477–1495, 2005. gr-qc/0307055.

[6] R. Arnowitt, S. Deser, and Charles W. Misner. The dynamics of general relativity. In *Gravitation: An Introduction to Current Research*, L. Witten, Ed., Wiley, New York, 1962, pages 227–265.

[7] John G. Baker, Joan Centrella, Dae-Il Choi, Michael Koppitz, and James van Meter. *Phys. Rev. Lett.*, 96:111102, 2006.

[8] John G. Baker, Joan Centrella, Dae-Il Choi, Michael Koppitz, and James van Meter. *Phys. Rev. D*, 73:104002, 2006.

[9] Michael Boyle, Lee Lindblom, Harald P. Pfeiffer, Mark A. Scheel, and Lawrence E. Kidder. Testing the accuracy and stability of spectral methods in numerical relativity. *Phys. Rev. D*, 75:024006, 2007.

[10] Othmar Brodbeck, Simonetta Frittelli, Peter Hübner, and Oscar A. Reula. Einstein's equations with asymptotically stable constraint propagation. *J. Math. Phys.*, 40(2):909–923, February 1999.

[11] Bernd Brügmann, José A. González, Mark Hannam, Sascha Husa, Ulrich Sperhake, and Wolfgang Tichy. Calibration of moving puncture simulations. 2006. gr-qc/0610128.

[12] Gioel Calabrese, Jorge Pullin, Olivier Sarbach, Manuel Tiglio, and Oscar Reula. Well posed constraint-preserving boundary conditions for the linearized Einstein equations. *Commun. Math. Phys.*, 240:377–395, 2003.

[13] Manuella Campanelli, Carlos O. Lousto, Pedro Marronetti, and Yosef Zlochower. Accurate evolutions of orbiting black-hole binaries without excision. *Phys. Rev. Lett.*, 96:111101, 2006.

[14] Manuella Campanelli, Carlos O. Lousto, and Yosef Zlochower. *Phys. Rev. D*, 73:061501(R), 2006.

[15] Manuella Campanelli, Carlos O. Lousto, and Yosef Zlochower. *Phys. Rev. D*, 74:041501, 2006. gr-qc/0604012.

[16] S. Chandrasekhar. *The Mathematical Theory of Black Holes*. Oxford University Press, New York, 1983.

[17] Matthew W. Choptuik. Universality and scaling in gravitational collapse of a massless scalar field. *Phys. Rev. Lett.*, 70(1):9, January 1993.

[18] Matthew W. Choptuik, Eric W. Hirschmann, Steven L. Liebling, and Frans Pretorius. An axisymmetric gravitational collapse code. *Class. Quantum Grav.*, 20:1857–1878, 2003.

[19] Matthew W. Choptuik, Eric W. Hirschmann, Steven L. Liebling, and Frans Pretorius. Critical collapse of the massless scalar field in axisymmetry. *Phys. Rev. D*, 68:044007, 2003.

[20] Carsten Gundlach, Gioel Calabrese, Ian Hinder, and Jose M. Martin-Garcia. Constraint damping in the Z4 formulation and harmonic gauge. *Class. Quantum Grav.*, 22:3767–3774, 2005.

[21] Carsten Gundlach and Jose M. Martin-Garcia. Well-posedness of formulations of the Einstein equations with dynamical lapse and shift conditions. *Phys. Rev. D*, 74:024016, 2006.

[22] Michael Holst, Lee Lindblom, Robert Owen, Harald P. Pfeiffer, Mark A. Scheel, and Lawrence E. Kidder. Optimal constraint projection for hyperbolic evolution systems. *Phys. Rev. D*, 70:084017, 2004.

[23] L. E. Kidder, M. A. Scheel, and S. A. Teukolsky. Extending the lifetime of 3d black hole computations with a new hyperbolic system of evolution equations. *Phys. Rev. D*, 64(6):064017, Sep 2001.

[24] Lawrence E. Kidder, Lee Lindblom, Mark A. Scheel, Luisa T. Buchman, and Harald P. Pfeiffer. Boundary conditions for the Einstein evolution system. *Phys. Rev. D*, 71:064020, 2005.

[25] Lee Lindblom and Mark A. Scheel. *Phys. Rev. D*, 66:084014, 2002.

[26] Lee Lindblom and Mark A. Scheel. Dynamical gauge conditions for the Einstein evolution equations. *Phys. Rev. D*, 67:124005, 2003.

[27] Lee Lindblom, Mark A. Scheel, Lawrence E. Kidder, Robert Owen, and Oliver Rinne. A new generalized harmonic evolution system. *Class. Quantum Grav.*, 23:S447–S462, 2006. Chapter 5 of this thesis.

[28] Frans Pretorius. Evolution of binary black hole spacetimes. *Phys. Rev. Lett.*, 95:121101, 2005.

[29] Frans Pretorius. Numerical relativity using a generalized harmonic decomposition. *Class. Quantum Grav.*, 22:425–452, 2005.

[30] Oliver Rinne. *Axisymmetric Numerical Relativity*. PhD thesis, University of Cambridge, 2005. gr-qc/0601064.

[31] Mark A. Scheel, Lawrence E. Kidder, Lee Lindblom, Harald P. Pfeiffer, and Saul A. Teukolsky. Toward stable 3d numerical evolutions of black-hole spacetimes. *Phys. Rev. D*, 66:124005, Dec 2002.

[32] Mark A. Scheel, Harald P. Pfeiffer, Lee Lindblom, Lawrence E. Kidder, and Saul Teukolsky. Solving einstein's equations with dual coordinate frames. *Phys. Rev. D*, 74:104006, 2006.

[33] F. Siebel and P. Hübner. On the effect of constraint enforcement on the quality of numerical solutions in general relativity. *Phys. Rev. D*, 64:024021, 2001.

[34] R. F. Stark and T. Piran. Gravitational-wave emission from rotating gravitational collapse. *Phys. Rev. Lett.*, 55:891–894, 1985.

[35] John M. Stewart. The cauchy problem and the initial boundary value problem in numerical relativity. *Class. Quantum Grav.*, 15:2865–2889, 1998.

[36] James R. van Meter, John G. Baker, Michael Koppitz, and Dae-Il Choi. How to move a black hole without excision: gauge conditions for the numerical evolution of a moving puncture. *Phys. Rev. D*, 73:124011, 2006.

[37] Hwai-Jang Yo, Thomas W. Baumgarte, and Stuart L. Shapiro. *Phys. Rev. D*, 66:084026, 2002.

[38] James W. York, Jr. Kinematics and dynamics of general relativity. In *Sources of Gravitational Radiation*, Larry L. Smarr, Ed., Cambridge University Press, Cambridge, England, 1979, pages 83–126.

Chapter 7

The spin of dynamical black holes

7.1 Introduction

The previous chapters of this thesis have described efforts for stabilizing numerical relativity simulations, i.e. for removing some of the deep numerical and mathematical instabilities that have prevented the codes from becoming robust tools for the study of generic astrophysical processes. In recent years, the field finally seems to have made this transformation. This claim is evidenced by the sheer number of research groups that are finally able, using various computational and mathematical techniques, to carry out accurate simulations of binary black hole coalescence, free of any approximations except numerical discretization [18, 8, 9, 10, 4, 5, 19, 7]. The time has come for us to *use* numerical relativity to investigate the physics of binary black holes.

One interesting target for physical investigation is the interaction between the spin angular momenta of the black holes and the orbital angular momentum of the overall binary system. Several groups have recently investigated equal mass spinning black-hole binaries, with the goal of understanding spin-orbit coupling, and the recoil that can be caused by asymmetric gravitational wave emission [10, 11, 12, 15, 16]. These exciting results deserve independent confirmation and extension, and the Caltech/Cornell pseudospectral code should be able to do so with astonishing accuracy. This chapter is meant to report work in progress intended to make it feasible for us to do so.

The first problem that arises when considering spin in numerical relativity is the very question of what is meant by the term. Concepts such as energy and momentum are notoriously delicate in general relativity, with widely understood rigorous definitions available only by integrals at spatial or null infinity [17, 21, 20]. To discuss the spin of *individual* black holes in a binary configuration, rather than that of the spacetime as a whole, a *quasilocal* construction is needed.

The literature on quasilocal charges in general relativity is vast and somewhat contentious, so I will refrain from the futile attempt to summarize it here. In numerical relativity, two approaches to computing spin have recently found widespread use. If the black holes are reasonably well

isolated from one another, such that tidal deformations can be ignored, then the ratio of equatorial to polar circumferences provides a rough estimate of the spin of a black hole horizon [1]. In late inspiral, when tidal deformations can no longer be neglected, and in cases where the equatorial and polar circumferences are not clearly defined, one must move on to something more precise. The prescription employed in essentially all of the recent literature was first given (to my knowledge) by Brown and York [6], and later reappeared in the formalism of apparent and dynamical horizons [2, 3]. This is:

$$J = \oint K_{ij} \varphi^i n^j dA, \tag{7.1}$$

where the integral is carried out on an apparent horizon, K_{ij} is the extrinsic curvature of the spatial slice in spacetime, n^j is the outward-pointing unit normal of the horizon in the spatial slice, and φ^i is a vector field that is tangent to the horizon and generates rotations. This charge is conserved (in vacuum) if φ^i is a Killing vector field.

The question of precisely what vector field should be used for $\vec{\varphi}$ is centrally important to any use of (7.1). Obviously if rotational Killing vectors exist, these are the preferred choices. Perfectly round two-spheres carry a three-dimensional vector space of rotational Killing fields, from which one might hope to recover something like the familiar three-dimensional spin "vector" in the encompassing space. Dynamical horizons, however, are almost never perfectly spherical. Even the equilibrium Kerr black hole does not have horizon slices with metric-sphere geometry when the spin is nonzero. In a binary configuration the situation is even worse, for example each hole will raise a tidal bulge on its partner. A well-defined prescription is needed, to find three "generalized rotation generators," vector fields tangent to any given topological two-sphere, that reduce to the Killing vector fields when they exist.

7.2 Approximate Killing vectors

In [13], Dreyer et al. introduce a method for defining approximate Killing vector fields based upon the Killing transport equations:

$$\nabla_A \varphi_B = L_{AB}, \tag{7.2}$$

$$\nabla_A L_{BC} = R^D{}_{ABC} \varphi_D, \tag{7.3}$$

where uppercase Latin indices are tangent to the two-sphere, ∇ is the metric-compatible covariant derivative on the two-sphere, and $R^D{}_{ABC}$ is its Riemann curvature tensor. It is straightforward to show that if $\vec{\varphi}$ is a Killing vector field, then it must satisfy this system of equations. Therefore if the value of a Killing vector field (and its first derivatives) is known at any one point, it can be found at any other point by a path integral of this system of equations. However, if $\vec{\varphi}$ is not truly a Killing

vector field, then the result of this integral will be path dependent. The method of Dreyer et al. is (roughly speaking) to choose initial data for this line integral that minimize the change in a vector as it is transported around a closed path, call this an "approximate Killing vector," and integrate along a network of paths covering the rest of the numerical grid. This method is remarkably clever, simple to implement in a numerical code, and it will indeed find a true Killing vector when one exists. However I find myself troubled by the question of how strongly the result will depend on the choice of paths, and by the nonsmoothness that will necessarily arise when the paths close.

I am investigating a more direct and geometrically inspired definition of an approximate Killing vector. Killing's equation,

$$\nabla_{(A}\varphi_{B)} = 0, \tag{7.4}$$

can be decomposed into two different pieces:

$$\sigma_{AB} = 0, \tag{7.5}$$

$$\Theta = 0, \tag{7.6}$$

where $\sigma_{AB} := \nabla_{(A}\varphi_{B)} - (1/2)g_{AB}\nabla^C\varphi_C$ is called the "shear" of $\vec{\varphi}$ and $\Theta := \nabla^C\varphi_C$ is called the "expansion." An approximate Killing vector might then be defined as a vector field that minimizes the integral:

$$\oint \left(\alpha\sigma_{AB}\sigma^{AB} + \beta\Theta^2\right) dA, \tag{7.7}$$

where α and β are parameters to allow us to fix the relative importance of expansion and shear. Our task is easier if we let one of these parameters be much greater than the other. That is, if there is a space of shear-free vector fields, we could minimize expansion within that space, or alternatively we could minimize the shear within the space of expansion-free vector fields.

The first of these strategies, looking for vector fields with zero shear and minimum expansion, is mathematically enticing. This is because the condition $\sigma_{AB} = 0$ is conformally invariant, and in two dimensions all smooth manifolds are conformally flat. Thus the problem of finding shear-free vector fields on a topological two-sphere can be reduced to finding them on a flat plane (and then imposing appropriate regularity conditions at infinity to make these fields smooth when the plane is curled back into a spherical topology).

On the other hand, Ashtekar and Krishnan [3], have shown that when spin is computed on a dynamical horizon using (7.1), the result is gauge invariant[1] if and only if $\vec{\varphi}$ is expansion-free. For this reason, I now focus on fields with zero expansion, and minimum shear.

[1] "Gauge," in this case, refers to the freedom of slicing the spacetime. A dynamical horizon assumes a fixed slicing of the horizon worldtube, but it is independent of how this slicing extends off the worldtube.

Consider the one-form χ_A satisfying:

$$\varphi^A = \epsilon^{AB}\chi_B, \tag{7.8}$$

where ϵ_{AB} is the antisymmetric Levi-Civita tensor on the two-surface. The zero-expansion condition is equivalent to the condition that:

$$\nabla_{[A}\chi_{B]} = 0. \tag{7.9}$$

This condition is immediately satisfied by letting

$$\chi_A = \nabla_A z, \tag{7.10}$$

for some smooth function z on the two-sphere. There are as many expansion-free vector fields,

$$\varphi^A = \epsilon^{AB}\nabla_B z, \tag{7.11}$$

as there are smooth functions z on the two-sphere.

Our task is now to find vector fields of the form (7.11) for which the integral of $\sigma_{AB}\sigma^{AB}$ is minimum. A straightforward calculation involving repeated integration-by-parts shows that this integral can be written in the form:

$$\oint \sigma_{AB}\sigma^{AB}dA = \oint zHzdA, \tag{7.12}$$

where H is a self-adjoint fourth-order differential operator:

$$Hz := \Delta^2 z + R\Delta z + (\nabla^A R)(\nabla_A z), \tag{7.13}$$

Δ is the Laplacian on the (not-necessarily round) two-sphere, and R is the Ricci scalar curvature of the two-sphere.

7.3 Normalization

We can now go about the variational problem of finding the function z that minimizes the integral (7.12), but we must be careful that the process does not simply land on the uninteresting minimum $z = 0$. To avoid this, we use a Lagrange multiplier λ to restrict the minimization to cases for which z satisfies some normalization condition.

Consider the case when the two-surface is a round unit sphere. The three "true" rotation Killing

vectors are generated from functions z equal to the three real $l = 1$ spherical harmonics. These spherical harmonics are normalized such that

$$\oint z^2 dA = 1. \tag{7.14}$$

If we accept this normalization condition for z in more general situations, then the integral that we want to minimize is:

$$I := \oint zHz dA + \lambda \left(\oint z^2 dA - 1 \right). \tag{7.15}$$

Minimizing with respect to the constant λ yields the normalization condition. Minimizing with respect to the function z yields an eigenvalue problem:

$$Hz = \lambda z, \tag{7.16}$$

or, recalling the definition of H,

$$\Delta^2 z + R\Delta z + (\nabla^A R)(\nabla_A z) = \lambda z. \tag{7.17}$$

It must be noted that the condition $\oint z^2 dA = 1$ is just one of many normalization conditions that one could choose to impose. It might be more sensible to place the normalization directly on $\vec{\varphi}$, asking that $\oint \varphi_A \varphi^A dA$ take the same value that it does on the unit sphere. This alternate normalization condition turns out to result in a *generalized* eigenvalue problem:

$$\Delta^2 z + R\Delta z + (\nabla^A R)(\nabla_A z) = \lambda \Delta z. \tag{7.18}$$

One issue to consider when choosing the normalization condition is the orthogonality of the resulting vector fields. Consider two vector fields $\vec{\varphi}_1$ and $\vec{\varphi}_2$ that result from functions z_1 and z_2, which are taken to satisfy (7.18) for respective eigenvalues λ_1 and λ_2. Due to the fact that $\epsilon^{AC}\epsilon^{BD} g_{BD} = g^{AB}$, it follows that:

$$\vec{\varphi}_1 \cdot \vec{\varphi}_2 = \vec{\nabla} z_1 \cdot \vec{\nabla} z_2. \tag{7.19}$$

It then follows that:

$$\begin{aligned}
\lambda_1 \oint \vec{\varphi}_1 \cdot \vec{\varphi}_2 dA &= \lambda_1 \oint \vec{\nabla} z_1 \cdot \vec{\nabla} z_2 dA && (7.20)\\
&= -\lambda_1 \oint z_2 \Delta z_1 dA && (7.21)\\
&= -\oint z_2 H z_1 dA && (7.22)\\
&= -\oint z_1 H z_2 dA && (7.23)
\end{aligned}$$

$$= -\lambda_2 \oint z_1 \Delta z_2 dA \tag{7.24}$$

$$= +\lambda_2 \oint \vec{\nabla} z_1 \cdot \vec{\nabla} z_2 dA \tag{7.25}$$

$$= \lambda_2 \oint \vec{\varphi}_1 \cdot \vec{\varphi}_2 dA, \tag{7.26}$$

where we have integrated by parts on two occasions and employed the self-adjointness of H. We've just shown that

$$(\lambda_1 - \lambda_2) \oint \vec{\varphi}_1 \cdot \vec{\varphi}_2 dA = 0. \tag{7.27}$$

Thus, vector fields resulting from (7.18) with different eigenvalues are (on average) orthogonal. If this ritual is repeated for the simpler problem, (7.17), the result is the less geometrically significant

$$(\lambda_1 - \lambda_2) \oint z_1 z_2 dA = 0. \tag{7.28}$$

An even more ambitious normalization condition would be to ask that the vector field $\vec{\varphi}$ equal the coordinate basis vector ∂_ϕ in some spherical coordinate system on the sphere. This is tantamount to requiring that the operator $\varphi^A \partial_A$ differentiate functions with respect to a parameter whose value changes by exactly 2π around each of the closed orbits of $\vec{\varphi}$. This amounts to a one-parameter family of conditions restricting the shear minimization, as opposed to the individual overall normalization conditions leading to (7.17) and (7.18). So this generalized spherical coordinate system would likely come at the expense of some shear.

7.4 Choosing the approximate Killing vectors

Now that we have laid down a few mathematical structures, let us take a moment to describe how they can be employed to define the three generalized rotation generators of a deformed sphere. For simplicity, let us focus on the normalization condition, $\oint z^2 dA = 1$, resulting in Eq. (7.17).

Consider the case when our surface is geometrically a unit two-sphere, for which the scalar curvature is constant, $R = 2$. Eq. (7.17) reduces to:

$$\Delta^2 z + 2\Delta z = \lambda z. \tag{7.29}$$

The eigenfunctions for this equation are simply the spherical harmonics Y_{lm}, and the eigenvalues are:

$$\lambda = [l(l+1)]^2 - 2\, l(l+1). \tag{7.30}$$

the eigenvalue λ vanishes for $l = 0$ or $l = 1$. The $l = 0$ eigenfunction is a constant, so the resulting vector field $\vec{\varphi}$ vanishes. This continues to be the case for deformed spheres, on which $z = \text{const.}$

continues to be an eigenfunction with vanishing eigenvalue. The remaining $\lambda = 0$ eigenfunctions on the unit sphere, $l = 1$ spherical harmonics, provide (taking real and imaginary parts) vectors $\vec{\varphi}$ equal to the three standard rotation generators on the unit two-sphere. The motivation for choosing eigenfunctions with the smallest value of λ goes beyond this analogy with the case of the unit sphere. If we multiply both sides of (7.16) by z, integrate over the sphere, and apply the normalization condition, then (recalling (7.12)) the significance of the Lagrange multiplier becomes clear:

$$\lambda = \oint zHzdA = \oint \sigma_{AB}\sigma^{AB}dA. \tag{7.31}$$

The value of λ is equal to the integrated, squared shear of the vector field. Choosing fields with minimum λ amounts to choosing the minimum-shear vector fields that we have sought.

In summary, to find the three generalized rotation generators, we first find the three eigenfunctions z satisfying (7.17) that are nonconstant and have eigenvalues λ that are nearest to zero. The generalized rotation generators are then defined by (7.11). The same prescription can be applied with Eq. (7.18) if one prefers its normalization condition.

7.5 Numerical results

The eigenvalue problems (7.17) or (7.18) that are used to define the generalized rotation generators would be extremely difficult to solve analytically for any surface of nonconstant curvature. Luckily this thesis is concerned with *numerical* relativity, so we should allow ourselves the help of a numerical code. I have written a simple code that solves a discretized version of (7.17) to find the generalized rotation generators of an arbitrary topological two-sphere. This discretization is carried out using the finite-difference method, where the field z is defined on a fixed coordinate grid. At each grid point, derivatives are approximated using differences of the values of z at the given grid point and its neighbors. This reduces the function-space eigenvalue problem (7.17) to a conventional vector-space eigenvalue problem, where the eigenvector is an array whose elements are the values of z on the grid points[2]. This matrix eigenvalue problem is then solved using standard LAPACK [14] routines. As a warmup for the fourth-order problem (7.17), I wrote code for a simpler second-order problem. This code could be useful in its own right for analyzing numerical relativity simulations, so I discuss it now.

[2]Far more accurate results can probably be obtained using a pseudospectral discretization, as in the code used for numerical results in chapters 4 – 6. I am in the process of implementing routines for approximate rotation generators in this larger code, and I plan to use pseudospectral discretization for this.

7.5.1 Generalized spherical harmonics

The simple eigenvalue problem

$$\Delta y = \Lambda y, \tag{7.32}$$

where again Δ is the Laplacian on the deformed sphere and Λ is some constant eigenvalue, defines the geometrically natural generalization of spherical harmonics for deformed spheres. The generalized spherical harmonics, y, could be of some use in studying the dynamics of coalescing black holes. For example, the tidal bulge raised on each hole by the pull of its partner can be studied with multipoles of the scalar curvature of each horizon surface, where the multipoles are projected out using the harmonics y as basis functions. Aside from the possible scientific uses for this eigenvalue problem, there is also the simple fact that Eq. (7.32) provides an ideal warm-up problem for (7.17) or (7.18).

I have written second-order accurate finite-difference routines to solve the discretized version of (7.32). The second-order convergence of this code is demonstrated in figures 7.1 and 7.2, where the surface is an ellipsoid defined by the following embedding in flat space:

$$X^2 + 2Y^2 + 3Z^2 = 1. \tag{7.33}$$

Figure 7.1 demonstrates the convergence of the lowest few eigenvalues Λ. Figure 7.2 demonstrates the convergence of the associated spherical harmonics y_Λ.

7.5.2 Generalized rotation generators

Now we turn our attention back to the problem of generalized rotation generators. The geometrically-preferred normalization condition, placed directly on the vector field rather than on the function z, leads to (7.18), a generalized eigenvalue problem. LAPACK includes routines for such generalized eigenvalue problems, but for the time being I have opted for the simpler problem (7.17), that can readily be implemented in the same code used for spherical harmonics.

Figure 7.3 demonstrates the convergence of the lowest three eigenvalues λ on the same ellipsoid used above. More resolution has been necessary to fully resolve this problem, grids as fine as 70×70, possibly due to the fact that the equation involves fourth-order derivatives. The convergence of the function z is demonstrated in Fig. 7.4.

7.6 Work in progress

Now that I have implemented code to solve the eigenvalue problems for generalized spherical harmonics and rotation generators, I am working on making it a part of our group's main numerical

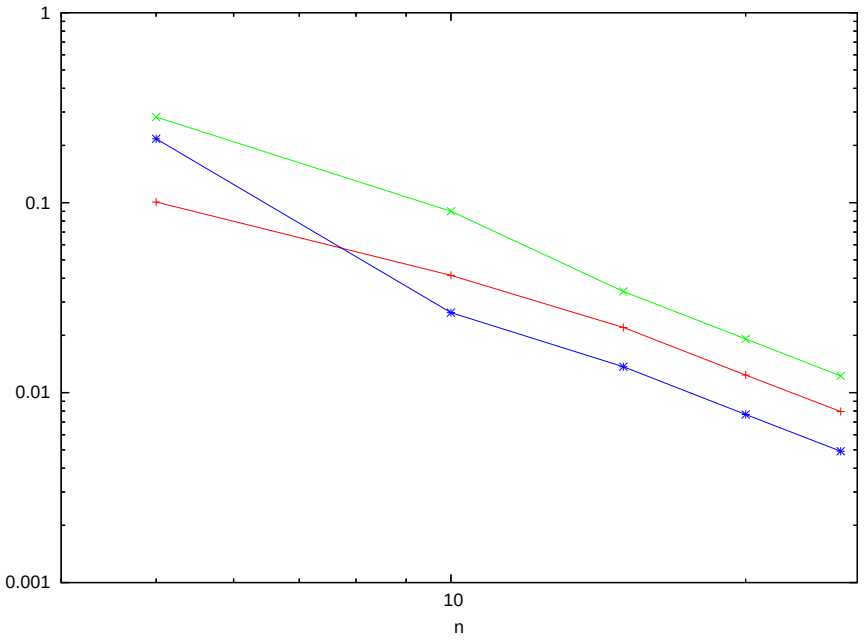

Figure 7.1: Difference between the computed eigenvalue for an $n \times n$ grid and a $2n \times 2n$ grid for the problem of generalized "$l = 1$" spherical harmonics. Data points are at $n = 5, 10, 15, 20, 25$. The scaling is logarithmic on both axes, and the apparent $1/n^2$ dependence confirms the second-order convergence of the code.

relativity code. Along the way, I am implementing spectral discretizations of the operators.

I have also written sections of the numerical relativity code to compute the integral (7.1) for any given vector field $\vec{\varphi}$. I have tested this so far using coordinate rotation vectors, and have found it to accurately compute the spin of analytic Kerr black holes. I have also applied this code to recent binary black hole results generated by Harald Pfeiffer, and have found results that appear to be consistent with those reported in [11], that horizon viscosity is not strong enough to pull certain initially-nonspinning binary configurations into corotation. This work is still preliminary, though, so I will not report it in any more detail.

I also intend to collaborate with Geoffrey Lovelace on two projects in the near future. Using rapidly-spinning black hole metrics for conformal data, he hopes to compute binary black hole initial data of higher spin than has yet been accomplished in the field. We are also interested in studying the tidal structure of binary black holes in the late stages of coalescence, for instance the question of how strongly the presence of each black hole deforms the apparent horizon of its partner, and the phase lag of these tidal bulges caused by the rotation of the system.

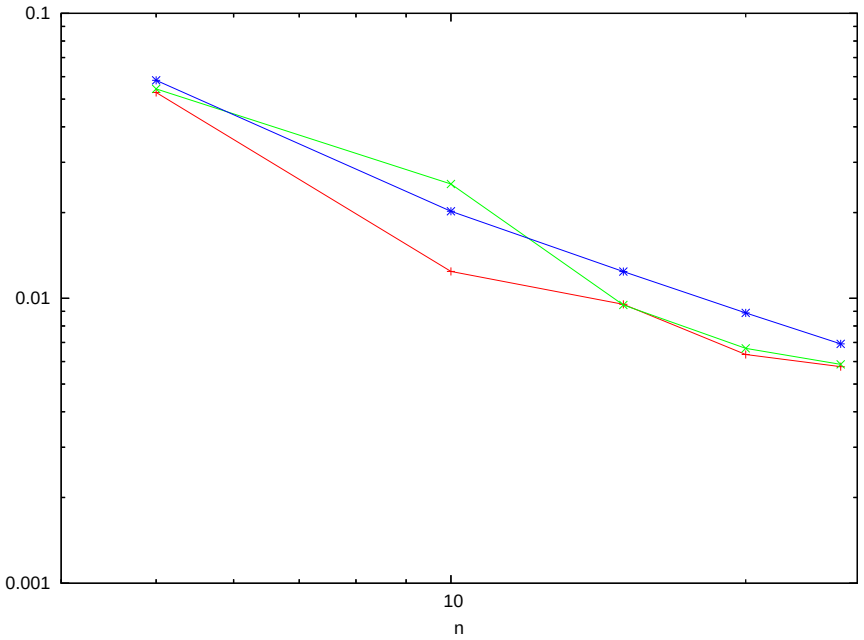

Figure 7.2: L_2 norm $||\delta y||_2 := \left[\oint (y_{2n} - y_n)^2 dA\right]^{1/2}$, of the difference between the computed harmonic y on an $n \times n$ grid and a $2n \times 2n$ grid for the problem of generalized "$l = 1$" spherical harmonics. Data points are $n = 5, 10, 15, 20, 25$. The scaling is logarithmic on both axes. Convergence appears to be slightly slower than $1/n^2$; this may be due to interpolation errors, or perhaps errors from the coordinate singularities at the poles.

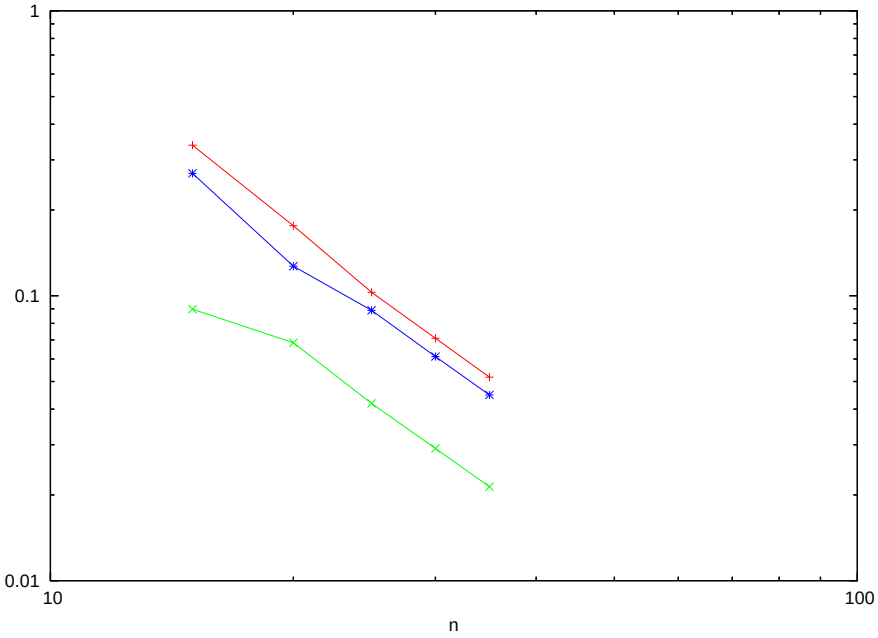

Figure 7.3: Difference between the computed eigenvalue λ for an $n \times n$ grid and a $2n \times 2n$ grid for the problem of generalized rotation generators. The scaling is logarithmic on both axes, and the error converges as $1/n^2$. The plot includes values for $n = 15, 20, 25, 30, 35$.

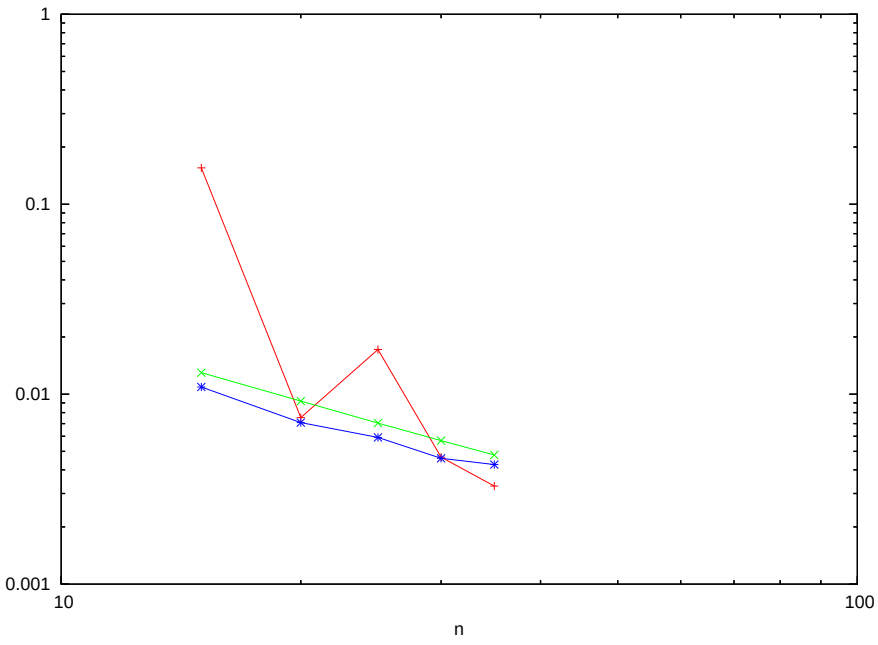

Figure 7.4: L_2 norm of the difference between the computed generating function z for generalized rotation generators on an $n \times n$ grid and a $2n \times 2n$ grid for $n = 15, 20, 25, 30, 35$. Convergence again appears to be slightly shallower than $1/n^2$. The wildly varying red curve relates to a solution for which the eigenvalue is small (apparently converging to approximately $\lambda \sim .095$), and there appears to be an issue with the near degeneracy of this eigenvalue with the $\lambda = 0$ eigenvalue corresponding to $z = \text{const}$. The variations of the red curve, therefore, may be due to ill conditioning of the eigenvector calculation.

Bibliography

[1] Miguel Alcubierre, Bernd Brügmann, Peter Diener, F. Siddhartha Guzman, Ian Hawke, Scott Hawley, Frank Herrmann, Michael Koppitz, Denis Pollney, Edward Seidel, and Jonathan Thornburg. Dynamical evolution of quasi-circular binary black hole data. *Phys. Rev. D*, 72:044004, 2005.

[2] Abhay Ashtekar, Christopher Beetle, and Jerzy Lewandowsky. Mechanics of rotating isolated horizons. *Phys. Rev. D*, 64:044016, 2001.

[3] Abhay Ashtekar and Badri Krishnan. Dynamical horizons and their properties. *Phys. Rev. D*, 68:104030, 2003.

[4] John G. Baker, Joan Centrella, Dae-Il Choi, Michael Koppitz, and James van Meter. *Phys. Rev. Lett.*, 96:111102, 2006.

[5] John G. Baker, Joan Centrella, Dae-Il Choi, Michael Koppitz, and James van Meter. *Phys. Rev. D*, 73:104002, 2006.

[6] J. David Brown and James W. York. Quasilocal energy and conserved charges derived from the gravitational action. *Phys. Rev. D*, 47:1407–1419, 1993.

[7] Bernd Brügmann, José A. González, Mark Hannam, Sascha Husa, Ulrich Sperhake, and Wolfgang Tichy. Calibration of moving puncture simulations. 2006. gr-qc/0610128.

[8] Manuella Campanelli, Carlos O. Lousto, Pedro Marronetti, and Yosef Zlochower. Accurate evolutions of orbiting black-hole binaries without excision. *Phys. Rev. Lett.*, 96:111101, 2006.

[9] Manuella Campanelli, Carlos O. Lousto, and Yosef Zlochower. *Phys. Rev. D*, 73:061501(R), 2006.

[10] Manuella Campanelli, Carlos O. Lousto, and Yosef Zlochower. *Phys. Rev. D*, 74:041501, 2006. gr-qc/0604012.

[11] Manuella Campanelli, Carlos O. Lousto, and Yosef Zlochower. Spin-orbit interactions in black-hole binaries. *Phys. Rev. D*, 74:084023, 2006. astro-ph/0608275.

[12] Manuella Campanelli, Carlos O. Lousto, Yosef Zlochower, Badri Krishnan, and David Merritt. Spin flips and precession in black-hole-binary mergers. gr-qc/0612076.

[13] Olaf Dreyer, Badri Krishnan, Eric Schnetter, and Deirdre Shoemaker. Introduction to isolated horizons in numerical relativity. *Phys. Rev. D*, 67:024018, 2003.

[14] E. Anderson et al. *LAPACK Users' Guide*. Society for Industrial and Applied Mathematics, Philadelphia, 1999.

[15] Frank Herrmann, Ian Hinder, Deirdre Shoemaker, Pablo Laguna, and Richard Matzner. Gravitational recoil from spinning binary black hole mergers. 2007. gr-qc/0701143.

[16] Michael Koppitz, Denis Pollney, Christian Reisswig, Luciano Rezzola, Jonathan Thornburg, Peter Diener, and Erik Schnetter. Getting a kick from equal-mass binary black hole mergers. 2007. gr-qc/0701163.

[17] Charles W. Misner, Kip S. Thorne, and John Archibald Wheeler. *Gravitation*. Freeman, New York, New York, 1973.

[18] Frans Pretorius. Evolution of binary black hole spacetimes. *Phys. Rev. Lett.*, 95:121101, 2005.

[19] Mark A. Scheel, Harald P. Pfeiffer, Lee Lindblom, Lawrence E. Kidder, and Saul Teukolsky. Solving Einstein's equations with dual coordinate frames. *Phys. Rev. D*, 74:104006, 2006.

[20] John Stewart. *Advanced General Relativity*. Cambridge University Press, 1991.

[21] Robert M. Wald. *General Relativity*. University of Chicago Press, 1984.